**Proceedings of:**

# *Silicon Machining*

## *1998 Spring Topical Meeting*

*April 13-16, 1998*
*LaPlaya Hotel*
*Carmel-by-the-Sea, California*

*The American Society for Precision Engineering (ASPE) is a multidisciplinary professional and technical society concerned with research and development, design, manufacture and measurement of high accuracy components and systems. ASPE activities encompass relevant aspects of mechanical, electronic, optical and production engineering, physics, chemistry, and computer and materials science. Membership is open to anyone interested in any aspect of precision engineering.*

*Founded in 1986, ASPE provides a new focus for a diverse but important community. Other professional organizations have covered aspects of precision engineering, always as a sideline to their principal goals. ASPE is based on the core of generic concepts necessary to achieve precision in any application; independent of discipline, ASPE intends to be the focus for precision technology — and to represent all facets from research to application.*

*ASPE — The American Society for Precision Engineering*
*301 Glenwood Avenue, Suite 205*
*P.O. Box 10826*
*Raleigh, NC 27605-0826*
*Phone (919) 839-8444 Fax (919) 839-8039*

# *Preface*

*This book comprises the proceedings of the 1997 Spring Topical Meeting. The contributions reflect the authors' opinions and are published as presented to ASPE, without change. Their inclusion in this publication does not necessarily constitute endorsement by the ASPE, or its editorial staff.*

*Individual readers of this book and nonprofit libraries acting for them are permitted to make fair use of the material contained in this book to be used in teaching or research; provided they copy said paper in total, as written by the author. Permission is granted to quote excerpts from the scientific or technical works in this book with proper acknowledgment of the source to include: the author's name, the book name, and the ASPE tag line. Reproduction of figures and tables is likewise permitted from the contents of this book, provided that the same acknowledgment of the same source and content is printed.*

*Any other type reproduction, systematic copying or multiple reproduction of any material in this book is expressly prohibited except with the written permission of the ASPE editorial staff, addressed to the Society's headquarters.*

*ISBN 1-887706-19-4*

*1998*

*American Society for Precision Engineering*
*301 Glenwood Avenue, Suite 205*
*Raleigh, NC 27603*

*Printed in the United States of America*

# *1998 Spring Topical Meeting*

## *Contents*

*Preface* . . . . . *ii*

*Contents* . . . . . *iii*

*Program* . . . . . *iv*

*Foreword* . . . . . *v*

*Technical Paper Index* . . . . . *vi-viii*

*Technical Papers* . . . . . *3-129*

*Author Index* . . . . . *131*

# 1998 Spring Topical Meeting

## Meeting Schedule

| Monday, April 13 | | Tuesday, April 14 | Wednesday, April 15 | Thursday, April 16 |
|---|---|---|---|---|
| | 7:30 | REGISTRATION AND CONTINENTAL BREAKFAST | | |
| | 8:30 | SESSION 1-A SILICON AS A MATERIAL | SESSION IV POLISHING | SESSION VI APPLICATIONS AND METROLOGY |
| | 10:00 | | | |
| | | BREAK | | |
| | 10:30 | SESSION 1-B SILICON AS A MATERIAL | SESSION V TURNING AND GRINDING | SESSION VII MACHINE DESIGN |
| | 12:00 | | | |
| | | LUNCH | LUNCH | LUNCH |
| | 1:00 | SESSION II MATERIAL PROPERTIES | OPEN FOR DISCUSSIONS | SESSION VIII WRAP-UP |
| | 2:30 | | | |
| | | BREAK | | |
| | 3:00 | SESSION III TOOL/WORKPIECE INTERACTIONS | | |
| | 4:30 | | | |
| ON-SITE REGISTRATION | 5:00 | OPEN EVENING | | |
| | 7:00 | | POSTER SESSION AND REFRESHMENTS | |
| | 9:30 | | | |

# *Foreword*

*The silicon machining spring topical meeting will provide a forum for experienced and knowledgeable individuals and organizations involved in the production of precision crystalline silicon parts, optics and electronics to share their experience, compare approaches and results, and discuss research and development needs within this focused program area.*

*The key objective of this meeting is to bring together specialists and practitioners from industry, government and academia to provide a forum for the exchange of ideas about the technical aspects of silicon machining. The presentations will cover a broad range of technologies and highlight potential areas for future development.*


***Organizing Committee***
***of the 1998 Spring Topical Meeting***

*Co-Chairs:*
*Daniel C. Thompson, Lawrence Livermore National Laboratory*
*John A. Patten, University of North Carolina at Charlotte*

*Members:*
*Kenneth L. Blaedel, Lawrence Livermore National Laboratory*
*Chris J. Evans, National Institute of Standards and Technology*
*Hiroshi Hashimoto, Kanagawa Institute of Technology*
*Michael Kerstan, Wacker Siltronic AG*
*Robert E. Parks, Optical Perspectives Group*
*Ronald O. Scattergood, North Carolina State University*
*John P. Schaefer, Texas Instruments*

# Technical Paper Index

## Session I-A
## Silicon As a Material
*Tuesday, April 14, 8:30 a.m. - 10:00 a.m.*

*Session Chair: Daniel C. Thompson (Lawrence Livermore National Laboratory)*

***Welcome Remarks***


1. ***Silicon (Invited Paper)***
   *W. A. Goodman (Schafer Corporation)* . . . . . *page 3*
2. ***Silicon as an IR Optical Material (Invited Paper)****
   *D. J. Neil (Raytheon Systems)*


## Session I-B
## Silicon As a Material
*Tuesday, April 14, 10:30 a.m. - 12:00 p.m.*

*Session Chair: Daniel C. Thompson (Lawrence Livermore National Laboratory)*


1. ***Silicon as a Mirror Material (Invited Paper)****
   *L. H. Skolnik (Department of Defense)*
2. ***Silicon Integrated Circuit Technology: Engine for the Electronics Industry (Invited Paper)***
   *S. Knight (Nat'l Institute of Standards and Technology)* . . . . . *page 10*
3. ***Silicon as a MEMS Material (Invited Paper)****
   *D. R. Ciarlo (Lawrence Livermore National Laboratory)*


## Session II
## Material Properties
*Tuesday, April 14, 1:00 p.m. - 2:30 p.m.*

*Session Chair: Michael Kerstan (Wacker Siltronic AG)*


1. ***Deformation of Silicon by Shear Flow or Phase Transition***
   *J. C. Lambropoulos, S. J. Burns, K-H. Chen, S. D. Jacobs (University of Rochester)* . . . . . *page 11*
2. ***The Anomalous Behavior of Silicon During Nanoindentation****
   *G. M. Pharr (Rice University)*
3. ***Surface Amorphization of Machined Silicon (Invited Paper)***
   *K. E. Puttick, C. Jeynes (University of Surrey), and A. E. Gee (Cranfield University)* . . . . . *page 15*


## Session III
## Tool/Workpiece Interaction
*Tuesday, April 14, 3:00 p.m. - 4:30 p.m.*

*Session Chair: John A. Patten (University of North Carolina at Charlotte)*


1. ***Thermal Modeling of Silicon Machining: Issues and Challenges***
   *H. A. Abdel-Aal, S. T. Smith (University of North Carolina at Charlotte)* . . . . . *page 19*
2. ***Process Characterization for $CO_2$ Laser Cutting of Silicon Using Four-point Bend Testing and LEFM****
   *F. M. Mess, C. Narayanan (Lucent Technologies, Inc.), and S. Danyluck (Georgia Institute of Technology)*
3. ***Anisotropy of Scratching and Indentation Fracture of Single Crystal Silicon****
   *K. E. Puttick (University of Surrey)*


** Abstract not available at press time*

## *Session IV*
## *Polishing*
*Wednesday, April 15, 8:30 a.m. - 10:00 a.m.*

*Session Chair: Robert E. Parks (Optical Perspectives Group)*


1. ***High-performance Dry Mechanochemical Polishing of Si Wafer Using Soft $BaCO_3$ Abrasive***
   *N. Yasunaga, M. Takashina, T. Inoue (Tokai University), and S. Tanaka, Y. Yamamoto (Sumitomo-Osaka Cement Co., Ltd.)* . . . . . page 24
2. ***On the Lapping and Polishing of Silicon****
   *C. J. Evans, M. L. McGlauflin (Nat'l Institute of Standards and Technology), R. E. Parks (Optical Perspectives Group), and D. J. Roderick (Rodel, Inc.)*
3. ***The Effect of Fluids on the Ductile Response of Silicon During Abrading***
   *J. A. Patten (University of North Carolina at at Charlotte)* . . . . . page 28


## *Session V*
## *Turning and Grinding*
*Wednesday, April 15, 10:30 a.m. - 12:30 p.m.*

*Session Chair: Hiroshi Hashimoto (Kanagawa Institute of Technology)*


1. ***Ultraprecision Grinding and Single Point Diamond Turning of Silicon Wafers and their Characterization***
   *M. Kerstan, A. Ehlert, A. Huber, D. Helmreich (Wacker Siltronic AG), and J. Beinert, W. Döll, M. G. Schinker (Fraunhofer Institut für Werkstoffmechanik)* . . . . . page 32
2. ***Epistemology and Abduction in Shear(ductile)-mode Grinding of Brittle Materials (Invited Paper)***
   *H. Hashimoto, K. Imai (Kanagawa Institute of Technology)* . . . . . page 36
3. ***Traverse Grinding Characteristics of Resin Bond Diamond Wheel with New Profile in Precision Grinding of Silicon Wafers***
   *M. Daito (Nissin Machine Works), A. Kanai (Ashikaga Institute of Technology), and M. Miyashita (Nano-Tec Associates)* . . . . . page 40
4. ***An Empirical Survey on the Influence of Machining Parameters in Diamond Turning of Large Single Crystal Silicon Optics***
   *C. K. Syn, D. A. Krulewich, P. J. Davis, P. C. DuPuy, M. A. Wall, K. L. Blaedel (Lawrence Livermore National Laboratory), and M. R. McClellan (Schafer Corporation)* . . . . . page 44


## *Poster Session*
*Wednesday, April 15, 7:00 p.m. - 9:30 p.m.*


1. ***Cost Effective Edge Machining of Silicon Wafers to Minimize the Polishing Process***
   *M. J. Ball, K. Carlisle, M. A. Stocker (Cranfield Precision)* . . . . . page 50
2. ***Ductile to Brittle Transition Investigated by Plunge-cut Experiments in Monocrystalline Silicon***
   *E. Brinksmeier, W. R. Preuß, O. Riemer, R. Malz (Universität Bremen)* . . . . . page 55
3. ***Cutting Fluid Study for Single Crystal Silicon***
   *D. Chargin (Lawrence Livermore National Laboratory)* . . . . . page 59
4. ***Monitoring Brittle/Ductile Material Removal Mechanisms in Micro-machining Using Wavelet Packet Analysis and Green's Function Solutions of AE Signals***
   *X. Chen, D. A. Dornfeld (University of California at Berkeley)* . . . . . page 63
5. ***Material Removal Rate vs. Power in Silicon Wafer Dicing***
   *H. Eshel, I. Weisshaus (Kulicke & Soffa Industries)* . . . . . page 67
6. ***Superpolishing by a Tin Polisher***
   *H. Gao, B. Chen, J. Cao (State Key Laboratory of Applied Optics)* . . . . . page 72
7. ***Silicon Spheres for Gravity Probe B Experiment***
   *F. Marcelja, G. M. Keiser (Stanford University)* . . . . . page 74


** Abstract not available at press time*

8. **TEM Results from a Multi-parameters Single-point Diamond Turning Study on Single Crystal Silicon***
*M. R. McClellan, S. C. Faulk, K. R. Shillito (Schafer Corporation)*

9. **Investigation of the Relationship Between Preston's Coefficient and Friction Coefficient in Chemical Mechanical Polishing (CMP) of Silicon**
*Y. Moon, D. A. Dornfeld (University of California at Berkeley)* . . . . . page 78

10. **Mechanical Properties and Relationship to Process Performance of the Polishing Pad in Chemical Mechanical Polishing (CMP) of Silicon**
*Y. Moon, I. Park, D. A. Dornfeld (University of California at Berkeley)* . . . . . page 83

11. **Cutting Tool Edge Radius and Depth of Cut Influence on the Generation of the High Pressure Phase Transformation During Ductile Machining**
*J. A. Patten (University of North Carolina at Charlotte)* . . . . . page 88

12. **Evaluation of Effective CMP Conditions by Estimation of Pressure Distribution on Semiconductor Wafer**
*Y. Sasaki, H. Aoyama, I. Inasaki (Keio University), and H. Miyairi, H. Shibaya (Mitsubishi Materials Corporation)* . . . . . page 92

13. **Pressure Distribution at the Silicon/Polishing Pad Interface**
*L. Shan, J. Levert, S. Danyluk (Georgia Institute of Technology)* . . . . . page 96

## *Session VI*
## *Applications and Metrology*
### *Thursday, April 16, 8:30 a.m. - 10:00 a.m.*

*Session Chair: Chris J. Evans (National Institute of Standards and Technology)*

1. **High Resolution X-ray Measurements for Surface and Sub-surface Silicon Characterization***
*M. S. Goorsky (University of California at Los Angeles)*

2. **Fabrication of 1KG Single Crystal Silicon Super-precision Spheres (Balls) for the Avogadro's Experiment**
*A. J. Leistner (CSIRO Telecommunications and Industrial Physics)* . . . . . page 101

3. **Acoustic Emission Sensing as a Tool for Manufacturing Process Control (Invited Paper)**
*D. A. Dornfeld (University of California at Berkeley)* . . . . . page 105

## *Session VII*
## *Machine Design*
### *Thursday, April 16, 10:30 a.m. - 12:00 p.m.*

*Session Chair: Kenneth L. Blaedel (Lawrence Livermore National Laboratory)*

1. **Design Concept of Multi-wire Saw for 400mm Diameter Silicon Ingot Slicing**
*H. Oishi, K. Asakawa, J. Matsuzaki (Super Silicon Crystal Research Institute Corporation)* . . . . . page 109

2. **Development of an Ultraprecision Grinding Machine for Super-large and Super-flat Silicon Wafer—Proposal of Trigonal Prism Type Pentahedral Structure**
*K. Abe, S. Okawa (Super Silicon Crystal Research Institute Corporation), and Y. Koma, K. Arai (DISCO Corporation)* . . . . . page 113

3. **Ductile Mode Cutting of Silicon Microparts**
*T. Hellmold, J. Zeadan, L. P. Ruhbach, H. H. Gatzen (Hanover University)* . . . . . page 117

## *Session VIII*
## *Wrap-up*
### *Thursday, April 16, 1:00 p.m. - 2:30 p.m.*

*Session Chair: John A. Patten (University of North Carolina at Charlotte) and Daniel C. Thompson (Lawrence Livermore National Laboratory)*

1. **Technical Details of Silicon Machining Behavior from a Diamond Toolmaker's Perspective**
*G. A. Kim (Edge Technologies, Inc.)* . . . . . page 122

2. **Proposal to the Science Foundation (NSF) to Research Silicon Machining**
*J. A. Patten (University of North Carolina at Charlotte)* . . . . . page 126

3. **Conference Summary and Discussion**

# Technical Papers

# SILICON

William A. Goodman
Schafer Corporation
26565 West Agoura Road, Suite 202
Calabasas, CA 91302

I would like to welcome you all to the first Topical Meeting on Silicon Machining organized by the American Society for Precision Engineering. The goal of this meeting is to exchange ideas regarding this critical technology, and hopefully to define the direction of future research. To this intent and purpose, the co-chairpersons, Dan Thompson of the Lawrence Livermore National Laboratory and John Patten of the University of North Carolina-Charlotte, have assembled an impressive array of specialists and practitioners on the technical aspects of silicon machining from industry, government, and academia. I am honored to have the privilege of presenting to this group of experts this background paper which discusses "Silicon" as a material.

In order to fully appreciate the importance of silicon as a material a short history refresher is merited. Two distinct, yet related "Industrial Revolutions" took place during the latter halves of the 18th and 19th centuries. Fueling both of these revolutions were inventions. In particular, the 18th century Industrial Revolution was attributed to inventions for the cotton and transportation industries. Key inventions for the manufacture and production of cotton included the "flying shuttle" for cutting cotton (1733)[1], the spinning jenny and the water-powered frame for providing yarn to the weaver (1764)[2], the cotton gin for cleaning cotton (1793)[3], and the power loom for cutting and spinning cotton yarn (1785-1790)[4]. The key transportation technology that rolled out in the late 1700's was the steam engine[5]. The steam engine allowed people to move large distances in shorts amount of time, and was the enabling technology which allowed new cities to be established in open spaces.

The 19th century Industrial Revolution proved more drastic than the first, not only in inventions, but in social and government policies and reforms. Art and culture flourished and was transformed into many different and unique styles. The second industrial revolution utilized the power of electricity to further develop technology and improve the standard of living. Michael Faraday, a British scientist, demonstrated the production of electric current, a concept and principle which is still in use today[6]. Electricity powered machines, provided light, and improved communications. Technology development led to the discovery of radio waves, allowing information to be transmitted over long distances in virtually no time at all. The telephone and telegraph became the first communication devices used by the general public. Most historians generally culminate the 2nd Industrial Revolution with the invention of the internal combustion engine and the emergence of powered flight.

We are currently in a 3rd Industrial Revolution, which began somewhere between the start of World War II and the middle of the 20th century. Future historians should note many key inventions from this period: jet engines[7], radar[8], atomic energy[9], lasers[10], computers[11], television[12], the world wide web, etc., all of which have made dramatic impacts on the quality of life. But they would be amiss if they cited any of these inventions as the key invention of the 20th century, a title which rightfully should belong to the silicon transistor[13], first announced at the Conference on Electron Devices held at the University of Michigan in 1950. Silicon transistors are found in all of these other inventions, and most other products of "The Information Age" which require electronic components. As one company's advertising campaign says: "We don't make these products, we make them better". An so it is with silicon.

The five most abundant elements in the atmosphere, rivers, lakes, oceans and earth's crust are: oxygen (49.5%), silicon (25.8%), aluminum (7.5%), iron (4.7%), and calcium (3.4%). Although second on the list in abundance, elemental silicon is not found in nature. Rather, it is most often found in the form of silicon dioxide ($SiO_2$), more commonly known as silica or quartz. Gay-Lussac and Thénard first produced elemental silicon in 1811 by reducing silicon fluoride with potassium. In 1817 Berzelius observed the new element as a precipitate in cast iron, and successfully separated it in 1823 by reducing potassium fluosilicate with metallic potassium. Today, metallurgical grade silicon (98% Si) is made by reducing sand ($SiO_2$) in an electric arc furnace. High purity polycrystalline semiconductor-grade silicon is produced from silane or chlorosilanes in a chemical vapor reactor.

High purity single crystal silicon ingots can be grown via the floating-zone or Czochralski techniques using polycrystalline silicon as the source material.

The Czochralski growth process is the major source of single crystal silicon for the semiconductor and optics industries. The semiconductor industry is currently scaling to process technology based on 300 mm diameter silicon wafers. Silicon Casting Inc. (Rancho Cordova, California) has grown single crystal silicon ingots up to 500 mm in diameter for certain laser optics applications. It is of great interest to both the semiconductor and optics industries to develop precision machining technologies for these large diameter substrates which produce finished surfaces that do not require the time and labor intensive procedures of mechanical lapping and polishing, or post-polishing. Consequently, ductile grinding and single point diamond turning (SPDT) of silicon in the ductile regime are two areas of intense study. Equally important are tool/workpiece interactions, machine design, and silicon material properties. This paper focuses on the properties of as-grown Czochralski silicon from large-diameter boules.

Single-crystal silicon ingots grown by the Czochralski method are known to exhibit a range of material values from ingot to ingot. The reasons for this variation stem from the growth and processing history of the boule. These variations are important because material properties such as the thermal conductivity and bulk absorption coefficient determine the heating response of optical substrates. Substrate heating causes distortion of the optics surface, which in turn degrades the quality of a transmitted or reflected laser beam. Also, the thermal history and processing of the material can result in the formation of point defects such as dislocations, stacking faults and oxide precipitates which could potentially have an adverse impact on electrical behavior or machining operations. Therefore, it is important to understand the growth process, chemistry, and history of the boule.

## 1. CRYSTAL GROWTH

The Czochralski growth process, depicted in Figure 1.1, begins by melting highly pure polycrystalline silicon in a quartz crucible. The concentric crucible and heating element create vertical and radial thermal gradients in the melt. The boule is pulled from a single-crystal seed that is introduced to the center surface of the melt, the site of the lowest temperature. Once the seed and melt reach thermal equilibrium, the heat flux is reduced to obtain undercooling in the melt. The seed is now pulled from the melt, and the associated latent heat of solidification conducts into the crystal which cools via radiation and convection. Often, as is the case with the large diameter silicon used in this research, the crucible and pulling apparatus are counter-rotating, such that complex convection flow patterns such as those in Figure 1.2 are set up in the melt. Oxygen and any other impurities or dopant additives in the quartz crystal dissolve into the melt and are dispersed by these currents.

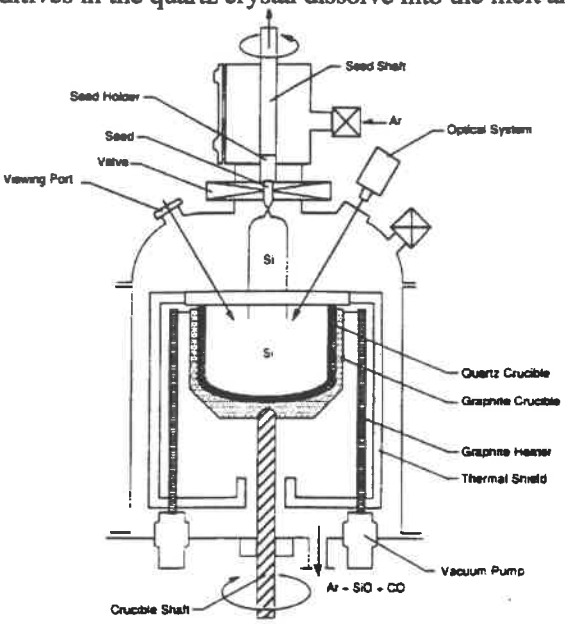


Figure 1.1 Schematic of Czochralski Puller Figure [14]

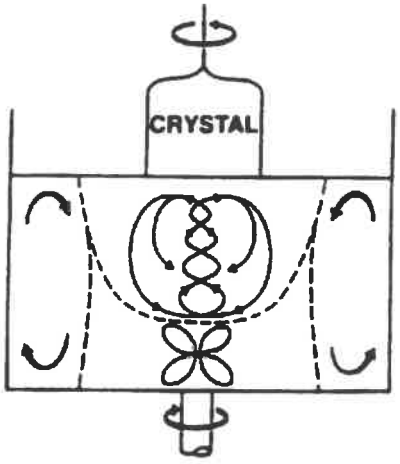


1.2 Convection Flow Pattern for Counter Rotation of Crystal and Crucible [14]

The growth process is a progressive freezing of the liquid silicon melt at the boundary layer interface between the solid crystal phase and the liquid phase. The impurity or dopant concentration at the interface varies with the fraction of the melt which has solidified and the value of the equilibrium distribution or segregation coefficient, $K_o$. The segregation coefficient is defined as the ratio of the impurity concentration in the solid phase to that in the liquid phase. Impurities accumulate at the interface for values of $K_o$ less than unity, and are depleted from the interface when $K_o$ is greater than unity (see Figure 1.3). Thus, the thickness of the boundary layer interface influences the concentration gradient of the impurity between the two phases, hence influencing the distribution of the impurity in the crystal.[14] The impurity concentration is further influenced by transient heat transfer considerations during the growth process, which cause the crystal to grow in a non-equilibrium condition. Impurities or dopants in the melt experience an actual distribution which differs from the equilibrium value, and this is known as the effective distribution or effective segregation coefficient. The effective segregation coefficient is therefore a function of the growth rate.

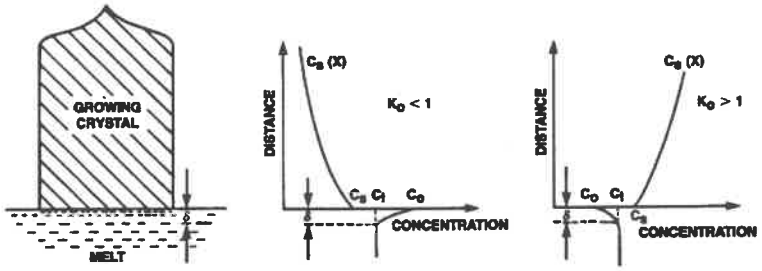


Figure 1.3 Impurity Concentration in the Melt and Crystal (Ref. 8)

During growth from the melt, the growth rate fluctuates on a microscopic scale although the crystal pull rate is maintained at a constant value. Since the effective segregation coefficient is a function of the growth rate, the fluctuating growth rate leads to impurity concentration striations in the crystal. Growth fluctuations can occur if the rotating crystal is off-center from the concentric melt isotherms.[14] This results in rotation striations. Growth fluctuations may also result from melt temperature instabilities. These cause thermal striations.[1] Minor instability in the furnace temperature or turbulent flow in the melt are common causes of thermal striations.

It should now be clear that the crystal growth process is quite complex. Heat transfer and fluid dynamics in the melt strongly influence the quantity and distribution of impurities in the melt and crystal. Consequently, these considerations also impact the material properties. The processing conditions and thermal history at the atomic scale also have an influence on the material properties.

## 2. ANNEALING SILICON FOR OPTICAL APPLICATIONS

Wafer vendors for the semiconductor industry typically stress relieve silicon by annealing at a temperature of 1080 °C.[15] Annealing at this temperature also provides the beneficial effect of intrinsic gettering. Intrinsic gettering is the removal of undesirable metallic impurities near the surface of the wafers (where the integrated circuit devices are made) to the bulk of the wafer (the substrate portion) through reaction with oxide precipitates in the bulk of the wafer.[16] That is, the native or intrinsic oxide precipitates getter the impurities, much like titanium pellets are used to getter the stray oxygen in vacuum furnaces. Although this annealing procedure may benefit semiconductor users, it probably is not in the best interest for optical silicon users.

The literature is quite unanimous in reporting that oxygen precipitation occurs in Czochralski grown single crystal silicon between the temperature range ~900-1100 °C.[17,18] The literature is also quite clear in reporting that oxide precipitates reduce the upper yield strength of the material by up to a factor of 5 as the result of producing lattice damage and strain.[15] The oxide precipitates have the generic chemistry $SiO_x$, commonly known as sand, and depending on time at temperature, can grow to sizes of more than several microns. These particulate sizes are on the same order of magnitude as infrared laser wavelengths, and would have a deleterious effect on SPDT operations. The oxide of silicon is harder than the parent silicon and would cause higher mechanical tool wear, thus impacting track length, surface finish, and sub-surface damage (SSD). Hence, the author strongly

recommends that the maximum anneal temperature for stress relieving optical substrates be no greater than 850 °C to avoid oxygen precipitation. This temperature is well above the 600 °C temperature cited in the literature as the onset of plasticity.[15]

The majority of phase transformations that occur in the solid state (for any material) take place by thermally activated atomic movements. The transformations that occur in Czochralski silicon, an "alloy" of silicon and oxygen, are a part of this majority. The silicon-oxygen phase transformations involve a temperature change from a single-phase region of the binary phase diagram to a region where one or more phases are stable. The thermal history resulting from the growth process of the silicon ingot plays a major role in determining which species will form and disappear (often simultaneously) upon subsequent annealing at different temperatures. The reactions that take place are all known as diffusion controlled reactions, or diffusional transformations. The reaction of primary interest for silicon optics fabrication is the precipitation reaction, which involves the formation of a phase with different composition than the matrix, a transformation which requires long-range, thermally activated diffusion.

The following provide a general summary of the key annealing ranges for Czochralski silicon:

**350-450 °C (Thermal Donor Generation Anneal):** In this temperature range interstitial oxygen, $O_i$, atoms are able to diffuse and agglomerate. When 3 to 5 $O_i$ atoms cluster together and a Si atom is removed from a lattice position, the cluster becomes electrically active by giving up 2 electrons.[19] Thus the oxygen thermal donor is a double donor. The thermal donor cluster is of sub-critical size to nucleate a precipitate. More will be said regarding critically sized nuclei and precipitates shortly.

**500-600 °C (Donor Kill Anneal):** In this temperature range additional atoms of $O_i$ join the thermal donor (the process of nucleation) such that more than 5 $O_i$ atoms are present in the cluster. The cluster attains a neutral charge by accepting back two free electrons from the Si matrix. When this occurs, the donor is said to have been killed.[20]

**600-900 °C (Typically 1st Step of a 2 Step Oxidation/ Precipitation Anneal):** In this temperature range the process of homogeneous nucleation accelerates. $O_i$ atoms within the Si matrix diffuse together to form small volumes with a composition $SiO_x$, where $1<x<2$.[21] The $O_i$ atoms may join with the pre-existing donor or killed-donor clusters to form nuclei with radii large enough to be able to grow into bonified precipitates. An $Si/SiO_x$ interface is created during this process and this leads to an activation energy barrier. The free energy change, $\Delta G$, of nucleation has three contributions:

1. At temperatures where the $SiO_x$ phase is stable, the creation of a volume V of $SiO_x$ will cause a volume free energy *reduction* of $V\Delta G_v$.
2. Assuming that the $Si/SiO_x$ interface is isotropic, the creation of an area A of interface causes an *increase* in the free energy $A\gamma$, where $\gamma$ is the interfacial free energy.
3. The transformed volume of $SiO_x$ is greater than the volume of Si matrix replaced, and this gives rise to a misfit strain energy $\Delta G_s$ per unit volume of $SiO_x$.

Summing all these changes gives the total free energy change:

$$\Delta G = -V\Delta G_v + A\gamma + V\Delta G_s \quad (1)$$

If the nuclei are assumed to be spherical with a radius r, then Equation 1 can be written:

$$\Delta G = -(4/3)\pi r^3(\Delta G_v - \Delta G_s) + 4\pi r^2\gamma \quad (2)$$

Equation 2 is plotted as a function of r in Figure 1.4. Note that the effect of the misfit strain energy is to reduce the effective driving force for the transformation to $(\Delta G_v - \Delta G_s)$. Differentiation of Equation 2 gives:

$$r^* = 2\gamma/(\Delta G_v - \Delta G_s) \quad (3)$$

$$\Delta G^* = 16\pi\gamma^3/3(\Delta G_v - \Delta G_s)^2 \quad (4)$$

which defines the expressions for the critical radius size and the free energy of the activation energy barrier which must be surpassed in order for a nuclei to grow to become a precipitate. The rate of homogeneous nucleation is dependent upon the diffusion process, which as noted above, is a temperature activated process and thus has Arrhenius behavior. Consequently the nucleation rate is temperature dependent and has the form:

$$N_{hom} = \omega C_o \exp(-\Delta G_m/kT)\exp(-\Delta G^*/kT) \quad (5)$$

where $\omega$ is a factor that includes the vibration frequency of the atoms and the area of the critical nucleus, $C_o$ is the number of atoms per unit volume in the phase, and $\Delta G_m$ is the activation energy for atomic migration (diffusion) per atom. The main factor which controls $\Delta G^*$ is the driving force for precipitation $\Delta G_v$.

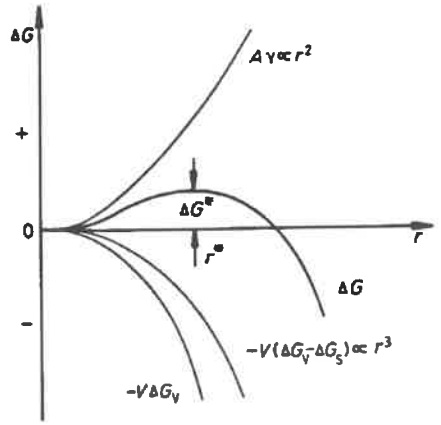


Figure 1.4 The variation of the Total Free Energy, $\Delta G$, with r for homogenous nucleation, and the activation energy barrier $\Delta G^*$

In this temperature range pre-existing nuclei (from the thermal history of the growth process) may grow to above the critical size and form *many small precipitates typically with a ribbon or platelike morphology.*[21] *These small precipitates are much more preferential from an optical standpoint to the large precipitates that arise from the 2nd step of the oxidation/precipitation anneal.*

**900-1100 °C (Typically 2nd Step of a 2 Step Oxidation Anneal):** In this temperature range oxygen precipitates which strain the Si matrix are formed.[21] Critical sized nuclei grow at the expense of dissolution of sub-critical nuclei, and continued annealing at these temperatures results in growth and coarsening of the precipitates by the mechanism of Ostwald ripening. Ultimately, large, coarse octahedral precipitates results with continued annealing in this temperature range.[22] This process is highly desired by the semiconductor industry because the precipitates are electrically active and act as intrinsic gettering sites for device killing contaminants such as Fe and Cu. *From a semiconductor viewpoint, the decrease in wafer yield strength by up to a factor of 5 (due to the strain) is acceptable when compared with the increase in device yield per wafer that is garnered by gettering the contaminants. From an optical standpoint we would not like to see the yield strength of the silicon decrease by a factor of 5, nor have large coarse oxide precipitates which could significantly increase tool wear and decrease track length during single point diamond turning.*

**1200-1350 °C (Oxidation Dispersion Anneal):** Annealing in this temperature range dissolves any oxide precipitates, thermal donors, or other clusters and returns oxygen atoms to their interstitial state.[23] A rapid quench insures that no re-nucleation or precipitation occurs. This temperature range can also completely remove strain from the material, but the key is to uniformly cool down the part to prevent unfavorable thermal gradients which are the source of plastic strain in the first place. Plastic deformation in silicon occurs at temperatures over 600 °C as discussed in the body of the paper.

## REFERENCES AND CITATIONS


1.) The flying shuttle was invented and patented in England in 1733 by John Kay.
2.) The spinning jenny was invented and patented in England in 1764 by James Hargreaves.
3.) The cotton gin was invented and patented in the United States in 1793 by Eli Whitney.

4.) The power loom was invented in England between 1785-1790 by Edmund Cartwright.
5.) The steam engine was developed over a period of about a hundred years by three British inventors. The first crude steam powered machine was built by Thomas Savery, of England, in 1698. Thomas Newcomen, also of England, built a machine where the steam actually pushed a movable piston in one direction. In 1763, James Watt, a Scottish engineer, figured out a way to push a piston back and forth in its cylinder. And more importantly, he found out a way to make this back-and-forth motion turn a wheel. By using a "crankshaft," the steam engine could produce circular motion.
6.) On 29th August 1831, using his "induction ring", Faraday made one of his greatest discoveries - electromagnetic induction: the "induction" or generation of electricity in a wire by means of the electromagnetic effect of a current in another wire. The induction ring was the first electric transformer. In a second series of experiments in September he discovered magneto-electric induction: the production of a steady electric current. To do this, Faraday attached two wires through a sliding contact to a copper disc. By rotating the disc between the poles of a horseshoe magnet he obtained a continuous direct current. This was the first generator.
7.) Sir Frank Whittle, English patent for jet engines, "A reaction motor suitable for aircraft propulsion", 1932.
8.) Sir Robert Watson-Watt, with the help of his assistant Arnold Wilkins, drafted, in February 1935, a report titled "The Detection of Aircraft by Radio Methods". This was presented to the newly formed committee for the scientific survey of air defense, chaired by Sir Henry Tizard, and on 26th of February 1935 a trial took place using the BBCs short-wave (about 50 meters wavelength) radio transmitter at Daventry against a Heyford Bomber.
9.) Albert Einstein predicted that mass could be converted into energy; this was later confirmed in 1932 by two scientists named John D. Crockfort and Ernest R. Walton. Fission was discovered in 1938.
10.) Gordon Gould has said that his first ideas for the laser 'came in a flash' one night in 1957. He wrote these down in a notebook entitled "Some rough calculations on the feasibility of a LASER: Light Amplification by Stimulated Emission of Radiation," the first use of this acronym for the now familiar name. However, because he misunderstood an attorney's advice, he didn't file for a patent until 1959, after other laser researchers had already filed. The patents were "Optically Pumped Laser Amplifiers; Light Amplifiers Employing Collisions to Produce a Population Inversion" , Patent Nos. 4,053,845; 4,704,583
11.) George R. Stibitz is internationally recognized as the father of the modern digital computer, "Complex Computer", Patent No. 2,668,661.
12.) Louis W. Parker invented the intercarrier sound system for television sets, "Television Receiver", Patent No. 2,448,908.
13.) Physicists John Bardeen, William B. Shockley, and Walter Brattain shared the 1956 Nobel Prize for jointly inventing the transistor, a solid-state device that could amplify electrical current. The transistor performed electronic functions similar to the vacuum tube in radio and television, but was far smaller and used much less energy. The transistor became the building block for all modern electronics and the foundation for microchip and computer technology. The patents were: "Semiconductor amplifier; Three-electrode circuit element utilizing semiconductive materials", Patent Nos. 2,502,488; 2,524,035
14.) H. Ming Liaw, *Handbook of Semiconductor Silicon Technology*, edited by W. O'Mara, R.B. Herring, and L.P. Hunt, (Noyes Publications, New Jersey, 1990), pp. 110-117.
15.) D. Bornside, T. Kinney, and R. Brown, "Minimization of Thermoeleastic Stresses in Czochralski Grown Silicon", Proc. Of the 2nd Symp. On Defects in Silicon, Ed. W. Murray Bullis, Ulrich Gosele, and Fumio Shimura, (The Electrochemical Society, New Jersey, 1991).
16.) B. Goldsmith, L. Jastrzebski, and R. Soydan, "Defects in Silicon", Ed. W. Murray Bullis and L.C. Kimerling (The Electrochemical Society, New Jersey, 1983), p. 142.
17.) H. D. Chiou, Solid State Technology, p. 77, 1987.
18.) N. Inove, K. Wada, and J. Osaka, in Semiconductor Silicon 1981, ed. H.R. Huff, R.J. Kriegler, and Y. Takeishi (Electrochemical Society, Princeton, New Jersey,(1981) p. 282.
19.) A Kanamori, "Annealing Behavior of the oxygen donor in silicon", Appl. Phys. Lett.,34, 287-289 (1979).
20.) W.C. O'Mara, J.E. Parker, P. Butler, and A.Gat, "Investigation of short time donor annihilation in silicon", Appl. Phys. Lett., **46**, 299-301 (1985).
21.) H. Bender, Phys. Stat. Sol. (a) **86**, 245 (1984).

22.) A. Bourret, "Transmission electron microscope studies of O, C, N precipitation in crystalline silicon", Mat. Res. Soc. Symp. Proc., **59**, 223-235, (1986).
23.) L. Jastrzebski, P. Zanzucchi, D. Thebault, and J. Lagowski, "Method to measure the precipitated and total oxygen concentration in silicon", J. Electrochem. Soc., **129**, 1638-1641 (1982).

# SILICON INTEGRATED CIRCUIT TECHNOLOGY: ENGINE FOR THE ELECTRONICS INDUSTRY

**Stephen Knight**
Office of the Microelectronics Program
National Institute of Standards and Technology
Gaithersburg, MD 20899

The explosive growth of the electronics industry over the past half-century has been fueled by sustained productivity improvements in magnetic memory technology, optoelectronics technology, and most significantly, semiconductor technology.

In this talk I will discuss briefly these productivity improvements, sketch early semiconductor technology development, and then focus on the unique properties of silicon and how these properties have contributed to the remarkable development of silicon integrated circuit technology. The enormous productivity improvements in silicon have come at the expense of ever-increasing technological complexity, which has had and will continue to have profound effects on the structure of the semiconductor industry. I will discuss these effects from a historical perspective, and close with my predictions of the future of the industry.

# DEFORMATION OF SILICON BY SHEAR FLOW OR PHASE TRANSITION

John C. Lambropoulos,[1, 2, 3, 4] Stephen J. Burns,[1, 2]
Kang-Hua Chen,[1, 3] and Stephen D. Jacobs[1, 2, 3]

[1] Department of Mechanical Engineering, [2] Materials Science Program,
[3] Center for Optics Manufacturing, and [4] Laboratory for Laser Energetics
University of Rochester
Rochester, NY 14627

**ABSTRACT** Processing of semiconductors, including machining, grinding, or polishing, involves thermomechanical deformation of a thin surface layer, thus coupling temperature and stress fields. Si, Ge, and other III–V semiconductors, exhibit complex constitutive laws coupling mechanical deformation with an evolving microstructure, typically dislocation density or coordination number. Irreversible shear flow and phase transitions are induced by combined stresses and temperatures. We discuss constitutive laws applicable to the machining of silicon.

1. **SHEAR FLOW** Several constitutive models used may be used to describe deformation of Si under coupled temperature and stresses. The first model corresponds to steady–state high temperature exponential creep [Myshlyaev et al., 1969]

$$\varepsilon^{cp} = A \exp\left( - \frac{U_0 - V_0 \sigma}{R_g T_m} \frac{1}{\phi} \right) \qquad \phi = T/T_m$$

We may also use power–law creep [Frost and Ashby, 1982; Lambropoulos et al., 1983]

$$\varepsilon^{cp} = \varepsilon_0 \frac{1}{\phi} \exp\left[ - \left( \frac{Q}{R_g T_m} \right) \left( \frac{1}{\phi} - 1 \right) \right] \left( \frac{\sigma}{\sigma_0} \right)^n$$

where $\varepsilon_0$ is strain rate at the melting point and applied stress $\sigma_0$. In machining Si a given material particle experiences continuously varying stress and temperature fields, contrary to the basic premise of steady–state (constant stress and temperature, non–evolving microstructure).

On the other hand, the Haasen–Alexander model [Haasen, 1962; 1964; Alexander & Haasen, 1968; Yonenaga & Sumino, 1978; Suezawa et al., 1979; George & Rabier, 1987; Rabier & George, 1987] uses the Orowan equation $d\gamma/dt = N\, b\, v$ with the stress dependence of the dislocation velocity

$$v = v_0 \left( \frac{\tau_{eff}}{\tau_0} \right)^m \exp\left( - \frac{Q}{R_g T} \right), \qquad \tau_{eff} = \tau - A\sqrt{N}$$

$\tau_{eff}$ is effective shear stress, smaller than applied shear stress $\tau$ due to back stress $A\sqrt{N}$ of existing dislocations (dislocation density N.) The model is completed by also specifying a rate of dislocation multiplication. Using cross–slip as the mechanism for multiplication, $dN/dt = K_1\, N\, v\, \tau_{eff}$.

The constitutive model of Alexander–Haasen does not allow for dislocation annihilation, significant at high temperatures. A simple model of dislocation climb and annihilation, superposed to generation by cross slip, gives for the net generation rate

$$dN/dt = \dot{N} = K_1\, N\, v\, \tau_{eff} - K_2 N^p \tau_{eff} \qquad 1 < p < 2.$$

Data for constants describing the deformation of Si, as well as Ge and other III–V semiconductors, are summarized in Lambropoulos and Wu [1996]. Specifically for Si, see Patel and Chaudhuri [1963], Suezawa et al. [1979], Schroter [1983], Siethoff [1992], Sumino and Yonenaga [1993].

We apply this constitutive relation to study dislocation generation in the transient heating of a thin Si wafer by a laser beam. The beam is turned on at time t=0, and has a gaussian spatial distribution $\exp(-r^2/a^2)$, where r measures from the center of the heated region, and a is the thermal radius. The wafer is assumed thin, so that only stresses $\sigma_{rr}(r,t)$ and $\sigma_{\theta\theta}(r,t)$ develop in its plane. We measure time in units of $t_0 = a^2/D$, D being the high–temperature thermal diffusivity of Si, and temperature in units of $T_0 = P/(\pi\, H\, k)$, where P is deposited power, H is wafer thickness, and k its thermal conductivity (25 W $m^{-1}$ $K^{-1}$ at high temperatures). Prior to heating, we assume a uniform initial dislocation density $N_0$ within the wafer.

Fig. 1 shows the evolution of dislocation density N in the wafer center for three different initial dislocation densities (low $N_0$, medium $N_0$, high $N_0$). It is seen that the evolution consists of three stages. Initially, an incubation stage where the dislocation density remains constant at its initial value while temperature and the corresponding thermal stresses increase. Then, there is a period of rapid rise in dislocation density, and finally a saturation stage where the dislocations have increased to such a density that the applied thermal stresses are counteracted by the internal stress field of the existing dislocations. The dislocation density increases when the thermal wave has swept past the vicinity of the beam, and the resulting creep strain rate shows a profile similar to the dislocation density. Initially, creep strain rates are driven by the presence of the stresses at low temperatures and at the initial (constant) dislocation density, then the temperature increases sufficiently for dislocation density to increase rapidly, and finally the existing dislocations shield the wafer from the applied thermal stresses.

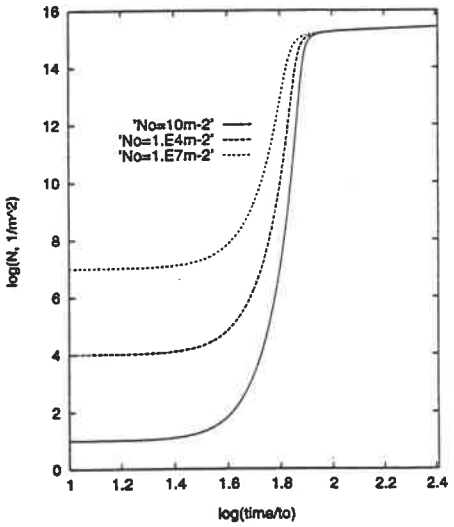


FIG. 1 Evolution of dislocation density N with time in the center of a thin silicon wafer heated by a laser beam. The thermal radius of the beam is a. For a thermal radius a = 100 μm, the time $t_0$ = 1 ms. For a deposited power P of about 31 W, $T_0$ = 800 K.

**2. PHASE TRANSITION** Under large compressive stress covalent solids may undergo a stress–induced phase transformation. Specifically, compression causes insulators and semiconductors to become metallic when the concentration of atoms reaches a critical value [Herzfeld, 1927]. Thus, volumetric compression criteria to describe this transition have been proposed (about 22% reduction in volume for Si). Significant shear stress may affect the pressure required for such a phase transition. Minomura and Drickamer [1962] reported finding a large drop in the electrical resistance of crystalline Si resulting from compression at about 13 GPa using an opposed anvil method. When large shear or uniaxial stresses were present, the change occurred at 8–9 GPa. Gupta and Ruoff [1980] found that high pressures (in a diamond indenter) caused a phase transition with the electrical resistance significantly decreasing at pressures in the range 8–12 GPa. The pressure values depended on the orientation of the Si wafer. Gupta and Ruoff observed that different Si wafer orientations created different stress states, involving different levels of shear stress, and that different dislocation densities may also have affected electrical resistivity.

More recently, Gilman [1993] argued that microscopic shear strains may be more important than volumetric dilatations in describing pressure–induced phase transition from the semiconducting to the metallic state. As a result, uniaxial compression (combining both hydrostatic and shear stresses) induces the transition to the metallic state at much lower stresses than purely hydrostatic compression. This observation is in agreement with the measurements of Wentorf and Kasper [1963], who confirmed the importance of shear stresses. In Gilman's words [1993]:

> "If it is accepted that shear can induce metallization, there are implications for many situations that do not appear to have been appreciated in the past. These include ...the core structures of dislocations and dislocation dipoles. the mechanisms of machining and grinding, mode–III crack propagation, reversible compression–induced transitions in silicate–like frameworks, impacts and shock fronts, and indentations."

Gilman observed that the opposite also may occur, i.e. insulization of metals under large tensile strains.

Similar phenomena have been observed in the irreversible phase transformation of fused silica upon compression in the range 2–16 GPa. In this transformation, the Si coordination number increases from 4 to 6, and there is a permanent volume change (densification), in addition to shear flow. Under pure pressure, the transformation in amorphous $SiO_2$ occurs at about 14–15 GPa, with this value reduced to 2–3 GPa in the presence of large shear stresses. For a review of stress–induced densification in amorphous $SiO_2$, see Lambropoulos et al. [1996].

The issue of reversibility of the transition in Si is important: The data of Gupta and Ruoff [1980], for example, show that the electrical resistance does not immediately recover upon partial removal of the pressure. On the other hand, densification in amorphous $SiO_2$ is known to be irreversible upon removal of the pressure.

To model such transitions, in which pressure and shear stresses induce the phase transition, which itself may consist of volume changes as well as shear flow, we use a yield function

$$f(\sigma_{ij}) = -\alpha\sigma_m + (1-|\alpha|)\tau_e - \sigma_0$$

$\alpha$ is a material constant ($0 \le \alpha \le 1$) describing relative contributions of pressure and shear in inducing the phase transition, and $\sigma_0$ is a yield stress. $\sigma_m$ is mean stress $(\sigma_{11}+\sigma_{22}+\sigma_{33})/3$ (pressure $p=-\sigma_m$), and $\tau_e$ is equivalent shear stress $(s_{ij}s_{ij}/2)^{1/2}$ with $s_{ij}=\sigma_{ij}-\sigma_m\delta_{ij}/3$ the deviatoric stress. For pure hydrostatic pressure $\sigma_{11}=\sigma_{22}=\sigma_{33}=-p$, then $\sigma_m=-p$ and $\tau_e=0$. For pure shear stress $\sigma_{12}=\sigma_{21}=\tau$, then $\sigma_m=0$ and $\tau_e=|\tau|$.

With continued loading, we assume that permanent strains are not affected by loading rate, but only by increments in applied stresses. Thus, permanent strains evolve by a flow rule

$$d\varepsilon_{ij}^{p} = d\lambda \frac{\partial g}{\partial \sigma_{ij}}, \quad g(\sigma_{ij}) = -\alpha' \sigma_m + (1 - |\alpha'|)\tau_e$$

$g(\sigma_{ij})$ is the flow potential, and $d\lambda$ is a proportionality constant. $d\lambda=0$ if $f(\sigma_{ij})<0$, and $d\lambda>0$ when $f(\sigma_{ij}) = 0$. Constant $\alpha'$ generally differs from $\alpha$. In the special case $\alpha = \alpha'$, permanent strain increment is normal to the yield function in stress space. The issue of normality is important in stress–induced phase transitions. When $\alpha \neq 1$, shear stresses facilitate densification by lowering the required level of pressure ($-\sigma_m$). If $\alpha' = 1$, the resulting deformation consists of densification only without any shear flow.

We examined the deformation patterns created by stress–induced phase transition by using the nonlinear finite element code Abaqus to model axisymmetric indentation of a rigid, conical indenter into a half–space of silicon, here assumed isotropic. The indenter was loaded with a normal force increasing from 0 to $P_{max}$ and then decreasing back to 0. In particular, we have concentrated on identifying the effects of the constant $\alpha$ coupling shear and hydrostatic stresses on the resulting deformation patterns and stress levels under maximum load $P_{max}$ as well as on the residual stresses and deformation. In this initial study we have assumed that normality is satisfied ($\alpha = \alpha'$).

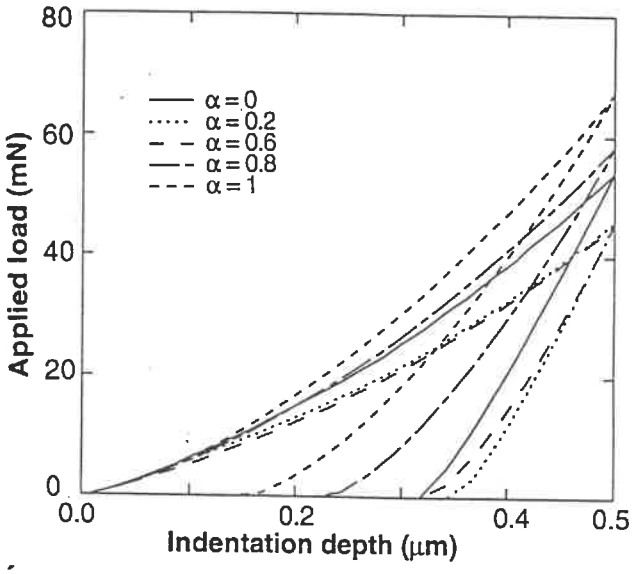


FIG. 2 Computed load–displacement curves for indentation of a half–space (E = 160 GPa, $\nu$ = 0.25, $\sigma_0$ = 5 GPa) by a rigid, conical indenter (cone angle $2\psi$ = 120°, tip radius $R_{tip}$ = 1 μm). Parameter $\alpha$ couples hydrostatic pressure to shear stress. $\alpha$ = 0 corresponds to an ideal elastic–perfectly plastic solid in which plastic deformation consists only of shear flow and is induced only by shear stress (i.e. von–Mises type of shear flow.)

Fig. 2 shows dependence of computed load–displacement curves on parameter $\alpha$ coupling pressure and shear stress. Small $\alpha$ implies that the same indentation depth is reached at lower loads (i.e. softer material). $\alpha$ in the range $0.5 \le \alpha \le 1$ implies larger loads for the same depth of penetration (i.e. harder material). Fig. 3 shows the deformation pattern while the load is at its maximum value $P_{max}$, and the residual deformation pattern. Small values of $\alpha$ lead to a pile–up in the periphery of the contact zone between the indenter and the material. For larger values of $\alpha$ the pile–up is not observed, and the residual depth of penetration is significantly lower.

Fig. 4 shows contours of the radial stress component $\sigma_{rr}$ (parallel to the free surface) when the applied load is at $P_{max}$ for the two cases $\alpha$ = 0 (pure shear flow activated by shear stress only) and $\alpha$ = 1 (pure hydrostatic compression activated by pure pressure only). For $\alpha$ = 0, it is seen that the stress near the surface is compressive, but becomes tensile below the surface. The opposite is the case for $\alpha$ = 1: Large tensile stresses are localized near the indenter, but the area below is under compression.

In this initial model of Si phase transition, we neglected any rate or temperature contributions which are known to affect the transition. Such effects are naturally included in the Haasen–Alexander model of dislocation generation. We are currently developing a unified framework by which both dislocation generation and stress–induced transitions can be described, with the goal of understanding the material removal mechanisms in polishing and microgrinding Si, and the generation and evolution of surface roughness, subsurface damage, and grinding–induced residual stresses.

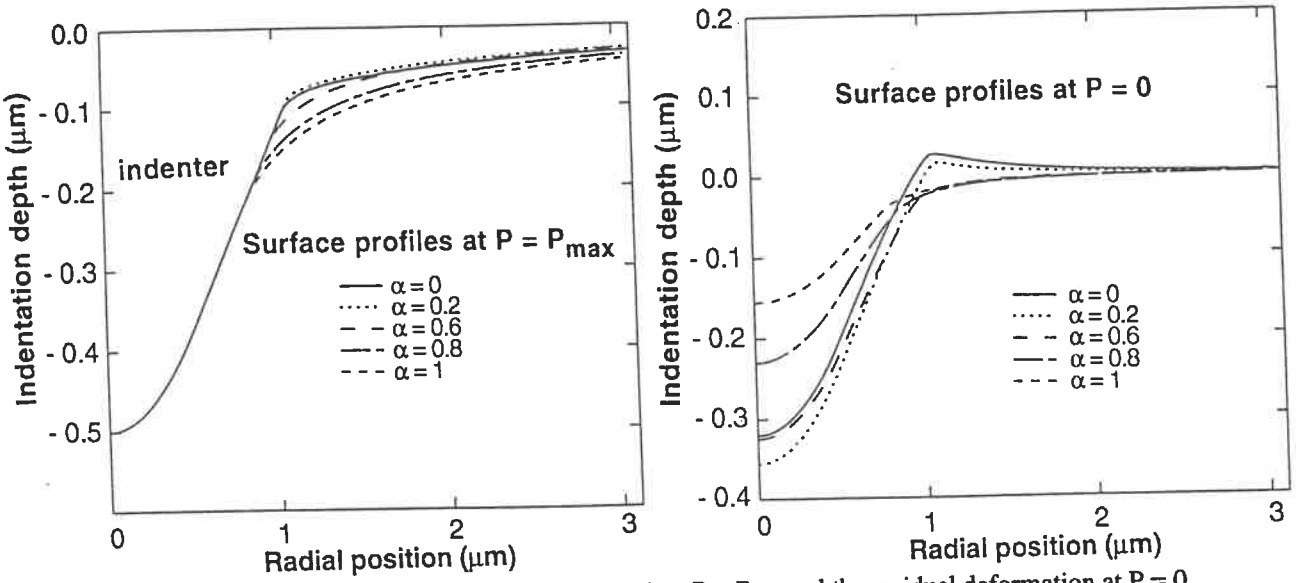


FIG. 3 Deformation pattern under rigid indenter when $P = P_{max}$ and the residual deformation at $P = 0$.

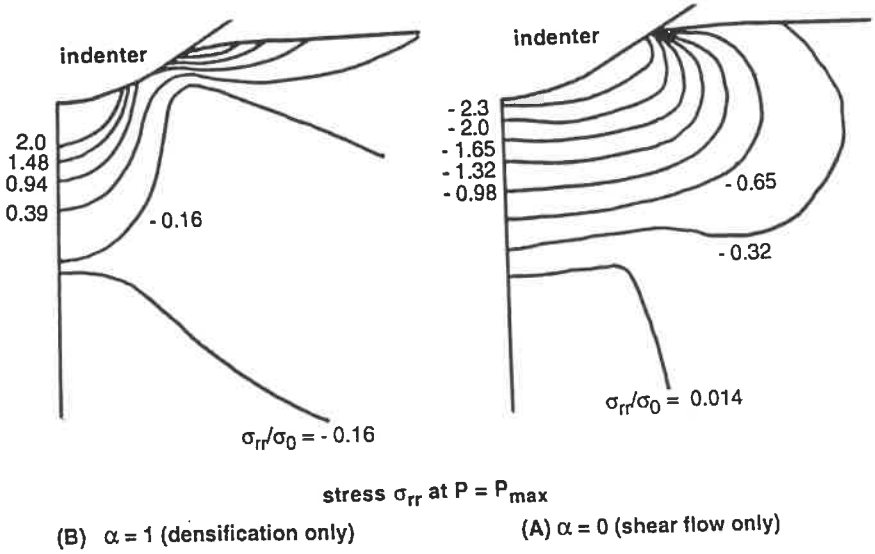


FIG. 4 Contours of radial stresses ($\sigma_{rr}/\sigma_0$) under rigid indenter for pure shear constitutive law ($\alpha = 0$) and pure hydrostatic compression constitutive law ($\alpha = 1$). The applied load is at $P = P_{max}$. Yield stress $\sigma_0 = 5$ GPa.

## REFERENCES


H. Alexander and P. Haasen, Solid State Phys. **22**, 28 (1968).
H. J. Frost and M. F. Ashby, *Deformation Mechanism Maps* (Pergamon Press, New York, 1982), p. 71.
A. George and J. Rabier, Revue Phys. Appl. **22**, 941 (1987).
J. J. Gilman, Phil. Mag. **B67**, 207, (1993).
M. C. Gupta and A. L. Ruoff, J. Appl. Phys. **51**, 1072 (1980).
P. Haasen, Z. Phys. **167**, 461 (1962).
P. Haasen, Discussions of the Faraday Soc. **38**, 191 (1964).
K. F. Herzfeld, Phys. Rev. **29**, 701 (1927).
J. C. Lambropoulos, J. W. Hutchinson, R. Bell, B. Chalmers, & J. Kalejs, J. Crystal Growth **65**, 324 (1983).
J. C. Lambropoulos and C.-H. Wu, J. Mater. Res. **11**, 2163 (1996).
J. C. Lambropoulos, Su Xu, andTong Fang, J. Amer. Ceram. Soc. **79**, 1441 (1996).
S. Minomura and H. G. Drickamer, J. Phys. Chem. Solids **23**, 451 (1962).
M. M. Myshlyaev, V.I. Nikitenko, and V.I. Nesterenko, phys. stat. sol. **(a) 36**, 89 (1969).
J. R. Patel and A. R. Chaudhuri, J. Appl. Phys. **34**, 2788 (1963).
J. Rabier and A. George, Revue Phys. Appl. **22**, 1327 (1987).
W. Schroter, H. G. Brion, and H. Siethoff, J. Appl. Phys. **54**, 1816 (1983).
M. Suezawa, K. Sumino, and I. Yonenaga, phys. stat. sol. **(a) 51**, 217 (1979).
K. Sumino and I. Yonenaga, phys. stat. sol. **(a) 138**, 573 (1993).
I. Yonenaga and K. Sumino, phys. stat. sol. **(a) 50**, 685 (1978).
R. H. Wentorf, Jr. and J. S. Kasper, Science **139**, 338 (1963).

# SURFACE AMORPHIZATION OF MACHINED SILICON

**Keith Puttick, Chris Jeynes (University of Surrey, Guildford, UK GU2 5XH)**
**Tony Gee (Cranfield University, Cranfield, UK MK43 0AL)**

## 1. Introduction

The layer of amorphous material observed on the surface of machined silicon by TEM (Puttick et al 1994, Shibata et al 1994) and by Rutherford backscattering (RBS) by Jeynes et al (1996) undoubtedly represents the irreducible minimum of surface damage inflicted by machining. It is also of scientific interest in other contexts, since it constitutes the clearest evidence yet for the existence of the layer of amorphous material said to be present on the surface of all polished crystals (Beilby 1903): moreover, it appears to be a new way of making amorphous silicon, a material with useful photovoltaic properties. However, the route by which the originally perfect crystal is transformed into the glassy state is still not clear, and this paper attempts to summarize the generally agreed known facts and to draw from them a tentative model at least qualitatively self-consistent.

We need to emphasize to begin with that precise quantitative knowledge regarding the pressure and temperature beneath the tool tip is not at present available, and estimates can be made only of probable upper and lower limits. In particular, we are uncertain of the true values of the coefficient of friction, the hardness and the true contact area of the tool under the conditions of machining, and of the boundaries of any metastable phases in the pressure-temperature diagram (itself not completely beyond dispute).

## 2. Theories of Contact Amorphization

Existing ideas of the crystalline-amorphous (c/a) transition originate in the observation by Clarke et al (1992) that amorphous silicon ($Si_a$) is formed by indentation. Under load they found that the electrical conductivity increased dramatically, prompting the suggestion that a transformation had occurred under the hydrostatic pressure beneath the indenter from the diamond cubic α to the metallic β-Sn structure, and on rapid unloading had reverted, not to the α phase but to a metastable amorphous state. Alternatively, they proposed that the local pressure exceeded the metastable extension of the liquidus line in the equilibrium diagram, which could occur at a level of about 36 GPa.

We believe that neither hypothesis is completely consistent with experimental results. However, the evidence regarding silicon should certainly be considered in the context of a body of older work that amorphization is present on polished surfaces of a range of metals (Bowden and Tabor 1967).

## 3. Hydrostatic Pressure during Indentation

In this and the following sections we attempt to delineate the probable area of the silicon pressure-temperature (P-T) phase diagram within which machining operates, as shown in Fig. 1. These calculated bounds are necessarily based on the values for indentation.

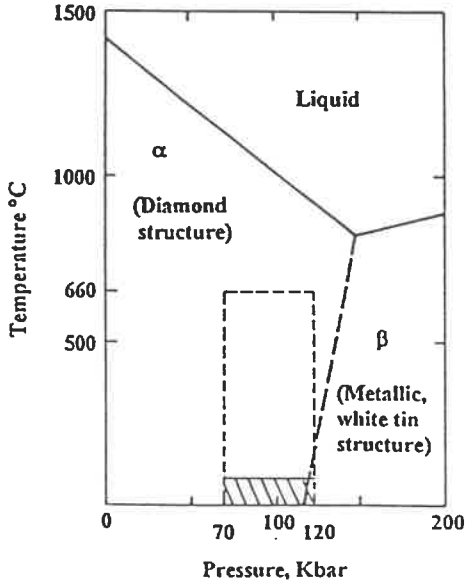


Fig. 1 P-T phase diagram of silicon, showing probable limits to tool tip conditions during nanomachining (dotted line) and in low speed regimes (hatched area)

### 3.1 Maximum Hydrostatic Pressure

The greatest local hydrostatic pressure which can be sustained by a crystal is reached when the associated shear stress $\tau$ attains the level at which dislocations are nucleated in the lattice. This has been found both theoretically and experimentally to be about 0.03 of the shear modulus g (e.g. Hull 1964) which gives $\tau \cong 2.36$ GPa. Now the relation between the maximum local pressure p and the uniaxial yield stress Y of a plastic-elastic solid is that for a pressurized spherical cavity in the interior of a solid (Hill 1950):

$$p = \frac{2Y}{3}\left\{1 + \ell n \frac{E}{3(1-\nu)Y}\right\} \tag{1}$$

where E is Young's modulus and $\nu$ Poisson's ratio.

Taking $E = 2 \times 10^{11}$ Nm$^{-2}$, $\nu = 0.27$, $Y = 2\tau = 4.72 \times 10^{9}$ Nm$^{-2}$[†] the maximum pressure is

$p_m = 12.4$ GPa = 124 kilobars (kb)

This is the greatest local pressure which the lattice can resist: it remains to consider the actual value beneath an indentation.

### 3.2 Indentation Pressure

It was pointed out by Studman et al (1979) that the hydrostatic pressure in indentation is less than the measured hardness H, because the stress below the indenter is not purely hydrostatic. Their expression is

$$H = CY + \frac{2Y}{3}\left\{1 + \ell n \frac{E}{3(1-\nu)Y}\right\} \tag{2}$$

where C = 0.5 for pointed and 0.3 for spherical indenters.

Thus

$$p = H - CY \tag{3}$$

For example, Puttick and Hosseini (1981) found the microhardness of (111) silicon to be 12.5 GPa at a load of 0.02N, but according to (3) the actual hydrostatic pressure was ~ 112 kb.

A lower limit to the hydrostatic pressure may be calculated from (3) by using the lower values[‡] of H ~ 9 GPa observed at higher loads. This gives $Y \cong 3$ GPa, and from (2) and (3) p ~ 7.5 GPa. We may reasonably place the probable limits to the pressure between 70 kb and 120 kb, as shown in Fig. 1.

## 4. Surface Temperature

We believe that the surface temperature in our experiments is low (< 100°C) though existing models of thermal effects cannot be considered to be accurate to better than an order of magnitude due to the inherent uncertainties in the parameters of friction and hardness under machining conditions. We therefore consider only values based on the contact between flat sliders of radius a, providing expressions of the form

$$\Delta T_m = \frac{\alpha \mu HVa}{K} \tag{4}$$

where $\mu$ is the coefficient of friction, V velocity, K thermal conductivity and $\alpha$ a numerical constant depending on the details of the model. For example, in the formulation of Archard (1959) $\alpha \cong 0.62$ f where f is the fraction of heat generated at the interface conducted into the workpiece. f may be taken to be $\sim\left(1 + \frac{(K\rho C)_p}{(K\rho C)_a}\right)^{-\frac{1}{2}} \cong 0.32$ (Ramanath and Shaw 1988) in our experiments, where $(K\rho C)$ refers to the conductivity, density $\rho$ and specific heat C respectively

---

[†]Ruoff (1979) gives Y = 4.33 GPa

[‡]The exact size of microhardness impressions becomes difficult below loads of about 0.05 N due to the surface distortion by plastic flow. In the range 0.02 – 0.14 N the hardness falls from 12.5 GPa to 9 GPa.

of diamond and silicon. In the work of Puttick et al (1994)

$$V_{max} = 3ms^{-1}, \quad H_{max} = 1.25 \times 10^{10} Pa, \quad a = 2\mu m, \quad K_{Si} = 124, \quad \mu = 0.2$$

we find $\Delta T_m \cong 24$ °C.

Apart from such calculations, we suggest that there is an upper limit to the temperature at which the metastable phase may be retained, set by the recrystallisation of the glass. Assuming that our surface layers are similar in character to those produced by ion bombardment or CVD, we expect this reversion to proceed above about 660 °C. (Stiffler et al 1992). However, it is clear from the work on indentation and slow speed scratching as well as machining that amorphization in general may take place at low speeds and temperatures.

**5. Viscosity of the Amorphized Layer**

A potentially important observation by Whitmore (1994) on machined surfaces and by Minowa and Sumino (1992) on scratches on silicon is that the surface of the amorphous phase is smoother than the amorphous-crystalline interface. In grinding particularly, relatively deep grooves are found to be completely filled with $Si_a$, although the interface shows clear evidence of tearing and plucking by the abrasive grain. Re-entrants and cracks have been wholly or partly filled with amorphous solid.

We believe that this effect can be explained only in terms of fluid flow subsequent to the passage of the tool or grain: the amorphized material has retained enough fluidity in an ensuing short interval to allow the surface to relax, in the way qualitatively envisaged by Beilby (1903). This interval is roughly $\frac{b}{V}$, where b is the size of the slider. Thus the relaxation time $t_r \leq \frac{b}{V}$, or about $10^{-6}$s. Now the viscosity $\eta \cong Gt_r$ (cf e.g. Champion and Davy 1944) and if we identify G with the shear modulus for the crystalline solid $\eta \sim 10^5$ Nsm$^{-2}$. This is well below the glass transition as usually defined ($t_r = 10^4$s) and so the material behind the tool seems to be behaving as a supercooled liquid with Newtonian viscosity. More attention is required to this property of the surface layer.

**6. Discussion**

We may now summarize our conclusions and speculations so far in terms of the possible pressure and temperature conditions at the tool tip during nanomachining of silicon:

(i) The hydrostatic pressure lies between 125 kb and 70 kb.

(ii) Plastic deformation proceeds by athermal generation of dislocations in the crystal lattice. The temperatures and strain rates at the diamond-silicon interface are such that this mechanism predominates in all machining regimes. The pressure is accordingly not a significant function of speed

(iii) The temperature lies between 20 °C and 700 °C., but is probably < 100 °C in our experiments.

(iv) Amorphization is observed under all machining conditions

(v) The amorphous material in the vicinity of the tool behaves as a supercooled liquid.

The probable areas of the P-T diagram involved are indicated in Fig.1. If accepted as valid, these conditions clearly rule out the direct amorphization of the silicon by hydrostatic pressure, but are just consistent with the possibility of the $\alpha$ - $\beta$ transition. Nevertheless, the postulated reverse $\beta$ - $Si_a$ transformation seems implausible, given the lack of detailed thermodynamic justification and of any observation of retained $\beta$ phase in any experiment. We propose an alternative view, that the $Si_c \rightarrow Si_a$ transition is driven by the free energy of the high density of lattice defects induced by the very large shear strains, in the same way as amorphization is induced by ion implantation (Donovan et al 1983) or indeed by ball milling (Shen et al 1995). In the latter case it has been noted that the surface of nanocrystalline particles of silicon formed by milling were amorphous, and that the glassy phase recrystallized at a temperature of about 660 °C. There thus appears to be a glassy phase nucleated during any type of abrasion stable below this temperature, a hypothesis with important implications for other materials.

**References**


Archard J F, 1959 *Wear* **2**, 438

Beilby G T 1903 *Proc. Roy. Soc.* **A72**, 218-225

Bowden P and Tabor D 1967 *Friction and Lubrication* (London: Methuen & Co)

Carslaw H S and Jaeger J C 1959 *Conduction of Heat in Solids* (Oxford: Clarendon Press)

Clarke D R, Kroll M C, Kirchner P D, and Cook R F 1988 *Phys. Rev. Letters* **60**, 2156-2159

Champion F C and Davy N 1944 *Properties of Matter* (London: Blackie & Son)

Donovan E P, Spaepen F, Turnbull D, Poate J M and Jacobson D C 1985 *J. Appl. Phys.* **57**, 1795
Gerk A and Tabor D 1978 *Nature* **271**, 732
Hill R 1950 *Plasticity* (Oxford: Clarendon Press)
Hosseini M M 1981 *Ph. D. Thesis* (University of Surrey)
Hu J Z, Merkle L D, Menoni C S, and Spain I L 1986 *Phys. Rev.* **B34**, 4679
Hull D, 1964 *Introduction of Dislocations* (Oxford: Pergamon Press)
Jeynes C, Puttick K E, Whitmore L C, Gärtner K, Gee A E, Millen D K, Webb R P, Peel R M A, Sealy B J 1996 *Nuc. Inst. & Methods* **B118**, 431-436
Johnson K L 1985 *Contact Mechanics* (Cambridge University Press)
Minowa K and Sumino K 1992 *Phys. Rev. Letters* **69**. 320-322
Puttick K E and Shahid M A 1979 *phys. stat. sol.* (a) **54**, K95
Puttick K E, Jeynes C, Rudman M R, Gee A E and Chao C L 1992 *Semicond. Sci. Technol.* **7**, 255-259
Ramanath S and Shaw M C 1988 *ASME J. Eng. Industry* **110**, 15-18
Ruoff A L 1979 in: *High Pressure Science and Technology* (New York: Plenum)
Shen T D, Koch C C, McCormick T L, Nemanich R J, Huang J Y and Huang J G 1995 *J. Mater. Res.* **10**, 139-148
Shibata T, Ono A, Kurihara K, Makino E and Ikeda M 1994 *Appl. Phys. Lett.* **65**, 2553-5

# Thermal Modeling of Silicon Machining: Issues and Challenges

Hisham A. Abdel-Aal and Stuart T. Smith
Department of Mechanical Engineering
The University of North Carolina at Charlotte
Charlotte, N. C., 28223,
U. S. A.

**ABSTRACT**: This paper proposes a possible model for the machining of silicon (and semi-conductors) in general. The model is based on the so called "*enthalpy formulation*" of the Stefan problem. It is shown that such formulation may successfully encompass high localized stress machining processes ( e.g. turning) especially when coupled to a comprehensive thermodynamic analysis that quantifies the energetics of the phase transformations induced by machining.

## Introduction

Fundamentally, there are four problems encountered in the thermal analysis of processes that are associated with phase transformation:

1- the strength and distribution of the heat source generated, which relates to the material removal mechanisms and the nature of subsurface damage introduced by the chip extrusion mechanism,

2 -the convection of cooling media, which reflects the effects of a coolant,

3- the thermal properties of the tool-workpiece combination and there respective change as a function of the temperature rise encountered at the tool-work piece contact spot. This would reflect mainly on the division of the process heat between the chips, work piece and the tool.

4- the relative speed between the chip-work piece and the tool, this reflects on the amount of heat added due to the nominal contact forces ( friction-induced heat) as compared to the heat of formation or latent heat of phase transformation.

Therefore a full exploration of the realistic effects of the key machining parameters on the course of the machining process relies greatly on an adequate modeling of the machining heat source. This in turn, dictates an adequate quantitative knowledge of the energetics of a specific Silicon machining process keeping in mind the fundamental differences between each process. Such differences may exclude the possibility of adopting a "*universal machining model*" that is adequate and applicable to any machining process involving a semi-conductor or a phase transformation in general.

This paper discusses the various information necessary to produce a credible thermal model of a silicon ( semi-conductor) machining process and the status of current available data. A model based on the enthalpy formulation of the Stefan problem is proposed. The model is based on expressing the heat equation in terms of the enthalpy of the pressure-induced phase transformations. As such, the enthalpy of each phase is treated as the sum of two components: the latent heat component which may be approximated by treating the data gathered from diamond anvil tests as P-V diagrams from which inferences of steady-state thermodynamics can be made and, a volumetric component that represents the step wise change in the internal energy of a given phase due to a corresponding step increase in temperature induced by frictional heat input. This quantity may be estimated from Hertzian contact theory as an upper bound ( the product of the relative sliding speed

and the Hertzian contact stress) and a heat of formation component that is induced by the structural transforms.

## 1. Phase transformations of Silicon

The phase transformations of Silicon ( and Semi-conductors in general) have been the focus investigation for quite some times. Early work [1,2] suggested that a phase change took place beneath the contact site which induced a semi-conductor to metallic like behavior. These propositions were later supported [3-6] by the suggestion that the so called " *pop-out event*" that occurs during unloading is a consequence of the phase transformation from Silicon-II to Silicon-III and it's accompanying volumetric expansion. It was found [7] that the semi-conducting behavior of silicon vanished when the pressure dependence of the dielectric behavior of the material becomes unstable. Such instability was found to occur at the so called " *Hertzian Field Transition Pressure*". The assessment of the pressure dependence of the phase transitions of silicon has beeen addressed by several authors, a summary of the phases and their respective "triggering" pressures is presented in table 1 [8,9]

**Table 1: Summary of the phase transformations undergone by Silicon and their respective characteristics**

| Pressure (GPa) | Phase | structure | $v_{phase}/v_I$ |
|---|---|---|---|
| $0 < P < 11$ | Si-I | diamond cubic | 1 |
| $11 < P < 13$ | Si-II | β-tin | 0.78 |
| $-8.5 < P < -10.8$ | Si-III | B. C. C. | 1.08 |

The energy associated with the formation of the different phases were estimated from the analysis of force-displacement diagrams obtained from indentation tests. To estimate these energies it is necessary to consider that the phase changes are adiabatic and that the complete unloading curve behaves elastically. These assumptions may not reflect accurately the true thermodynamic nature of the phase transformations. However, the current status of knowledge does not allow for examining these assumptions nor does it allow for the assessment of the margin of error (if any) introduced. In light of the above, the released energy may be found by integrating the areas under the respective load-displacement diagrams. A summary of the resulting energies is given in table 2.

**Table 2: Summary of the energy estimates associated with the phase transformations undergone by Silicon**

| Phase | absorbed energy *(KJ/mole)* |
|---|---|
| Si-*I* to Si-*II* | 38.3±2.7 |
| Si-*II* to Si-*III* | -8.31±0.71 |

## 2. A conceptual machining model

An adequate model of a silicon machining process encounters difficulties that are two-fold: on the one hand, there are several fundamental mechano-thermal differences between the different machining processes applied to silicon ( turning, polishing, grinding and, lapping). On the other hand, the current status of knowledge regarding the energetics of the phase transforms is limited. In particular, a reliable thermodynamic analysis of the phase changes encountered during loading and unloading is lacking. This, for instance, hinders the application of currently available mathematical models, that have been applied successfully to conventional machining [10, 11]. However, despite the inadequacy of information a conceptual model based on a generic Stephan problem with enthalpy formulation may be proposed.

### 2.1. enthalpy based formulation

The governing model equations following the classical theory of non-linear heat conduction in a domain $\boldsymbol{R}$ are given by,

$$\rho C_v(\Theta)\frac{\partial \Theta}{\partial t} = (k_{ij}\Theta_{,j})_{,i} + Q(x_i,t) \in \mathbb{R}\times(0,T) \qquad (1)$$

where $\rho$ is the mass density, $C_v$ is the specific heat, $k_{ij}$ is the symmetric thermal conductivity tensor, Q is the generated internal heat flow source per unit volume, and $\Theta$ is the temperature field.
Let $\Re$ be enclosed by a boundary surface

$$\partial\Re = \partial\Re_p \cup \partial\Re_q \qquad (2)$$

where $\partial\Re_p$ and $\partial\Re_q$ are non-overlapping subregions of $\partial\Re$ which consists of the prescribed temperature field boundary $\partial\Re_p$ and the natural flux boundary $\partial\Re_q$. The boundary and initial conditions are typically represented as,

$$\Theta = \Theta_p \quad \forall \ \partial\Re_p \qquad (3)$$

$$q_i n_i + q_s - h(\Theta - \Theta_n) = 0 \quad \forall \ \partial\Re_q \qquad (4)$$

and

$$\Theta(x_i,0) = \Theta_i \quad x_i \in \Re \qquad (5)$$

Equations (1)-(5) refer to unsteady nonlinear thermal field with temperature dependent thermo-

physical properties. The quantities $\Theta_s$ and $\Theta_h = h(\Theta - \Theta_h)$ represent surface heating per unit area and the rate of heat flux per unit area due to convection respectively on $\partial \Re_q$.

The evolution of the latent heat can be treated in terms of the thermo-physical properties which are temperature dependent. Introducing the enthalpy function $H$ which is defined as,

$$H = \int_{\theta_{ref}}^{\theta} \rho C(\theta) d\theta \tag{6}$$

Where $\Theta_{ref}$ is a reference temperature, for the Classical Stefan problem one can write:

$$H_{tot} = \sum_{i}^{n} \rho_i \mathcal{L}_i + \int_{\theta_{ref}}^{\theta} \rho C_{ph_i}(\theta) d\theta \qquad (i=1,2,3...j,....n) \tag{7}$$

where the subscript $I$ denotes a distinguished phase and $\mathcal{L}$ denotes the latent heat of the phase. Introducing the definition of the enthalpy in equation (1) the heat equation takes the form

$$\left(\frac{\partial H}{\partial \Theta}\right)\left(\frac{\partial \Theta}{\partial t}\right) = (k_{ij}\Theta_{,j})_{,i} + Q(x_i,t) \in \mathbb{R} \times (0,T) \tag{8}$$

It will be noticed that in order a obtain a solution for the equation, two essential quantities have to be well defined, the first is the rate of change of the enthalpy with temperature $\partial H/\partial \Theta$ (which implies a knowledge of the number and characteristics of all the phases present during machining)and the heat generation term $Q$ which reflects the nature of the subsurface deformation (stress-strains) within the machined volume. Equation (8) may be solved by implementing fixed grid techniques [11]. However, difficulties that are two fold may hinder a direct application of such techniques. The first is that the number and location of the interface fronts are not known *a priori* in general. The second being the coupling between the phase change and the evolution of the contact pressure between the tool and the work piece. This later difficulty may be treated by coupling a stress-strain solver to the heat equation solver and interchanging data. That is, feeding the step-by-step evolution of the contact stresses in the heat equation to determine the current phase of the work-piece and their respective temperatures.

Regardless of the numerical scheme utilized in a solver, reliable information pertaining to phase-change thresholds in terms of stress-temperature combinations is necessary to locate the phase boundaries. As such, tracking the phase fronts represents a profound numerical difficulty that is perpetuated by the lack of fundamental studies on the phase change of silicon under the coupled influence of stress and temperature rather than the lack of computational schemes. This situation is clearly intensified in the presence of transient phase fronts involving the existence of simultaneous multiple phase fronts. However, on the assumption that phase changes are fully characterized, the phase fronts may be tracked by replacing the phase change temperatures by,

$$\Theta^*_{ph_{i\to j}} = \Theta_{ph_{i\to j}} + \delta\theta \tag{9}$$

Where, $\Theta^*$ is an approximate temperature threshold for the change from phase $i$ to phase $j$, and $\delta\theta$ is a small incremental temperature field. Therein the interface positions may be interpolated upon in a straight forward manner employing the criterion

$$\left| \Theta_i - \Theta^*_{ph_{i\to j}} \right| < \tau_{tol} \tag{10}$$

where, $\tau$ is a user specified tolerance.

## Conclusions

A conceptual model for the machining of silicon ( and semi-conductors in general) was proposed. The model stems from the enthalpy formulation of the Stefan problem. An algorithm for the numerical solution of the resulting equations have been outlined. The numerical scheme is based on tracking the phase transformation interface. A process that relies on a thorough characterization of the phase transformation thresholds in terms of a combined stress-temperature parameter. Such characterization is currently unavailable. As such, the modeling problem is viewed to be a consequence of the lack of fundamental physical characterization, rather than perpetuated by the impedement of mathematical tools.

## References


1. N. A. Goryonova, A. S., Borshcherskii, and C. N., Tretiakov in *Physics of III-V compounds semi-conductors and Semi-metals*, Academic Press, san Diego, 1968, Ch. 1
2. I. V. Gridneva, Yu. V. Milman and V. I., Trefilev, *Phys. Status. Solidi* **9** (14) (1972) 177.
3. D. R. Clarke, M. C. Knoll, P.D., Kirchener, R. F., Cook, and B. J. Hockey, *Phys. Rev. Lett.* **21** (1988) 2156.
4. G. M. Pharr, W. C., Oliver and D. R., Clarke, *Scripta Metall* **23** (1989) 1949.
5. Idem, *J. Elect. Mater.* **19** (1990) 881.
6. G. M., Pharr, in " *Thin Films stresses and mechanical properties III*," W. D., Nix, ed, Material research Society Simposia Proceed., Pittsburgh, PA (1992) **239,** p 301.
7. J. J., Gilman, *J mater. Res.* **7** (1992) 535
8. E. R. Weppelmann, J. S. Field and M. V., Swain, *J. Mater. Sc.*, **30** (1995) 2455
9. E. R. Weppelmann, J. S. Field and M. V., Swain, *J. Mater. Res*, **8**,4, (1993) 830
10. L. Zhang and M. Mahdi, *Int. J. Mach. Tools Manufact.*, **35**, 10 (1995) 1397
11. N. D. Malmuth, *Int. J. Heat Mass Transf*, **19** (1976) 349.

# High-performance Dry Mechanochemical Polishing of Si Wafer Using Soft $BaCO_3$ Abrasive

N.Yasunaga*, M.Takashina*, T. Inoue*, S.Tanaka** and Y.Yamamoto**
*Tokai University, **Sumitomo-Osaka Cement Co.Ltd.

## 1 Introduction

In current polishing process of Si wafer prodution, great amount of chemical slurry of KOH solution mixed with $SiO_2$ fine powder or colloidal-silica is used and wasted. Not only from the economical consideration of slurry usage and disposition, but also from the ecological point of view, such chemical slurry should be decreased or eliminated if possible. One of the most innovatory solutions will be the introduction of dry polishing process instead of the current wet polishing. The authors have found that dry polishing of Si wafers can be effectively and stably operated by using fine $BaCO_3$ powder which is mechanically softer than Si and is able to mechanochemically and supersmoothly polish it remaining no mechanical damage on Si surface. This paper describes experimental results of Si wafer polishing ①by supplying loose $BaCO_3$ fine powder on conventional polishing pads and ②by rubbing with bonded $BaCO_3$ pellets, both on dry condition. These results have suggested that this dry polishing process will be effectively applicable to the next generation ultralarge-size Si wafer production.

## 2 The priciple of mechanochemical polishing

One of the authors has developed the mechanochemical polishing process (MCP) firstly for sapphire by using $SiO_2$ fine powder which is mechanically much softer than sapphire but chemically reactive with it[1]. At the real contact points solid state reaction would occurs between the work surface and the powder and the very small interfacial reaction products would be rubbed off during the sliding operation, as demonstrated in the machining model of Fig.1. Neither indentation nor scratching action of the powder would occur at the real contact area, because the abrasive powder softer than the work-material initially deforms, and therefor no mechanical damage can be introduced to the worked sapphire surfaces.

For mechanochemical polishing of Si wafers, $BaCO_3$ powder has been found to be the most suitable abrasive[2]. As an interfacial reaction product, existence of barium silicate in amorphous state has been detected and observed by X-ray and electron beam diffraction, XMA, XPS and TEM analyses.

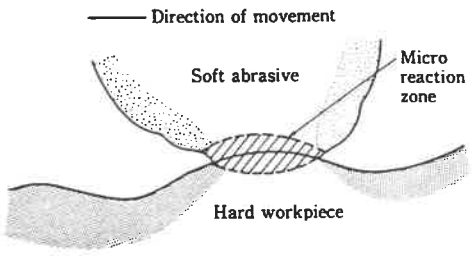


Fig.1 Mechanochemical polishing model

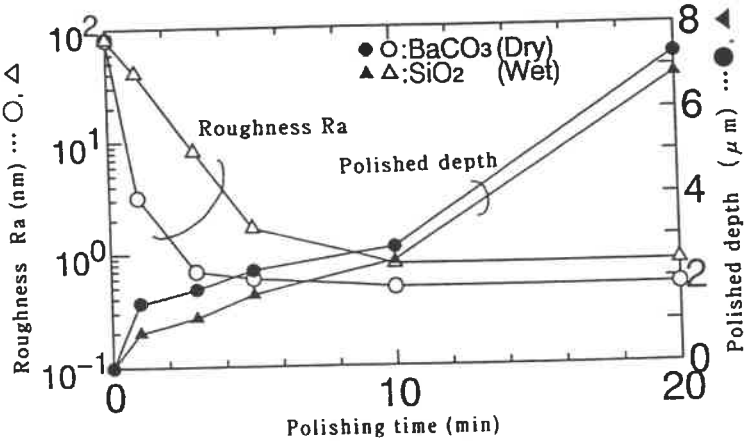


Fig.2 Polishing characteristics of $BaCO_3$ dry polishing compared with silica slurry polishing

## 3 Experimental procedures and results

### 3.1 Loose abrasive dry poloishing

In order to obtain fundamental data of loose abrasive dry polishing by 0.1 $\mu$ m $BaCO_3$ powder, 3 pieces of (100) Si wafers of 30 mm diameter were polished on a rotating 400 mm diameter polishing pad (SUBA800 which was supplied from Rodel-Nitta Ltd. and popularly used in the primary polishing process of current Si wafer production) under the conditions of the table revolution of 60 rpm and the pressures of 35 kPa. Wet polishing experiments using conventional silica slurry were also carried out under the same polishing conditions for comparison. Polished depth and surface roughness changes measured by a contact-type surface-roughness meter are shown in Fig.2, which indicates that dry polishing by $BaCO_3$ powder gives a removal rate about twice as high especially at the initial stage of the operation. This figure also shows that $BaCO_3$ dry polishing brings much more rapid improvement of surface roughness and better final roughness than the conventional silica slurry polishing does. AFM images shown in Fig.3 which were observed at the final stage of the polishing operation indicate a better feature on the surface polished by $BaCO_3$ powder.

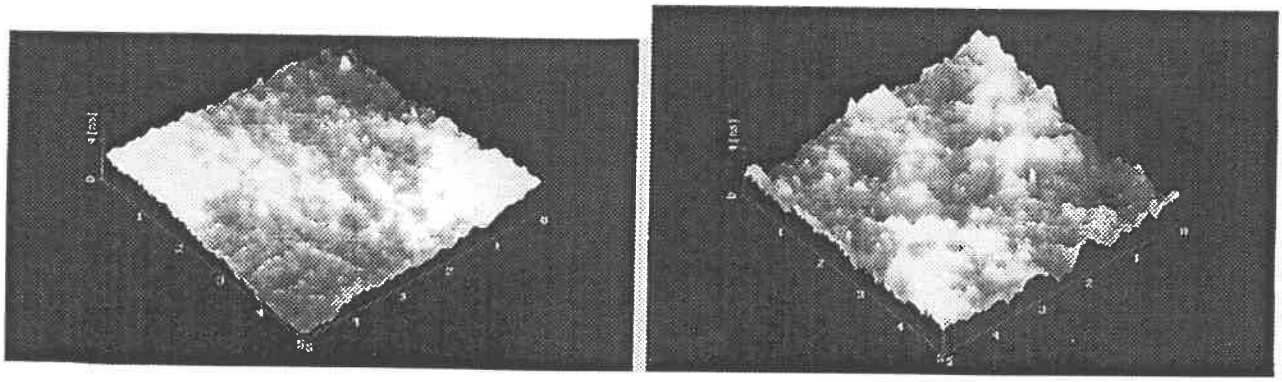

polished by 0.1 $\mu$ m $BaCO_3$ powder on dry condition

polished by silica slurry in KOH solution (pH 10.5)

Fig.3 Comparison of AFM images of the Si wafer surfaces polished at 35 kPa

#2000 diamond wheel grinding

Dry polishing by 0.1 $\mu$ m $BaCO_3$ powder

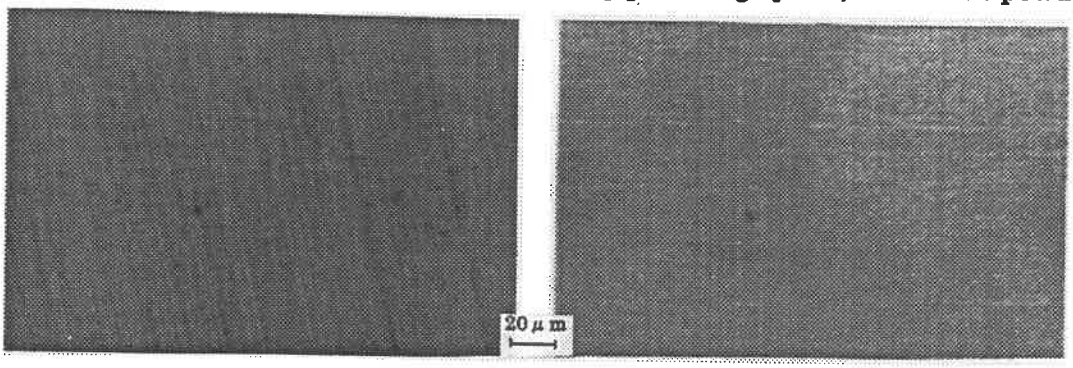


Optical microscopic observation

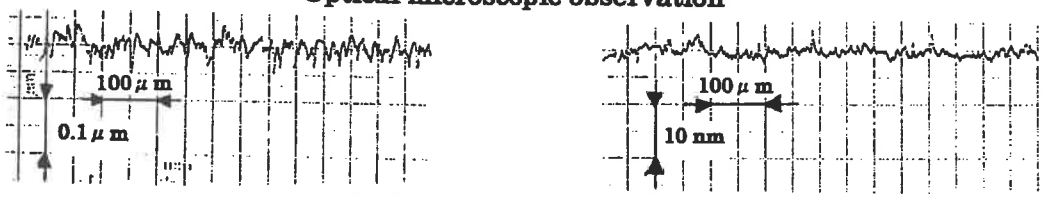


Surface roughness

Fig.4 Surface features of ground and polished 300 mm wafers

Dry polishing by the same loose $BaCO_3$ powder was further applied to finish next generation large size 300 mm wafers on a vertical-spindle／rotary-table type grinding machine. After fine grinding by #2000 diamond cup-wheel with the feed rate of 10 $\mu$ m/min, a polishing disk of the same coupling structure and diameter with the cup-wheel was attached to the spindle in stead of the wheel. The polishing pad SUBA800 was pasted on the disk surface and vertically fed and pressed the ground wafer, which was then polished by 0.1 $\mu$ m $BaCO_3$ powder on dry condition at the disk revolution of 300 rpm and the table revolution of 60 rpm. It was confirmed that the whole surface was uniformly polished to a smooth mirror surface after only 2 $\mu$ m depth removal within 5 minutes operation. Surface roughness and optical microscopic views before and after the polishing operations were compared in Fig.4. Slight stripes seen on the polished surface would be derived from the kinematic directionality of the polishing pad against the wafer and would be eliminated in the practical operation by changing the rotational conditions in process.

### 3.2 Bonded abrasive dry polishing

MCP pellets of 0.4 $\mu$ m $BaCO_3$ powder bonded by phenol-resin were formed under various sintering conditions of powder size (0.4～1.3 $\mu$ m), bond stuff (liquid-type or powder-type), mixing ratios (95～80 wt.% $BaCO_3$ + 5～20 wt.% resin), sintering pressures (30～90 MPa) and temperatures(r.t.～200℃). Polishing performances of the pellets of 10 mm diameter were examined by sliding tests, where each pellet was pressed on a circular track of a rotating Si wafer under the load of 9.8 N. Specific polished volumes (polished volumes per unit sliding distance and load) and polishing ratios (ratios of polished volumes of the Si wafer to worn volume of the abrasive pellet) were calculated through measuring the volume of the grooved track. Table 1 shows examples of polishing performances of various pellets sintered under the conditions of the pressure of 30 MPa , the temperature of 150℃ and the sintering time of 40 minutes. It is recognized that higher polishing rates can be obtained from the pellets of high powder density of 95 wt.% which was sintered with liquid-type phenol-resin. For example, in the case of ② in Table 1, the polishing rate obtained corresponds to such high performance that a lapped and etched Si wafer could be polished up to a smooth mirror surface in a few minutes, assuming that the whole wafer surface were uniformly pressed on a large-size bonded abrasive plate under the same polishing pressure of 0.12 MPa.

Table 1 Polishing performance by phenol resin bond $BaCO_3$ pellets

| Type of phenol resin bond | | Grain size of $BaCO_3$ powder ($\mu$ m) | Mixing tratio BaCO3 : bond | Polishing pressure (MPa) | Specific polished volume ($\mu m^3$/MPa·m) | Polishing ratio |
|---|---|---|---|---|---|---|
| Powder type | | 1.3 | 90 : 10 | 0.24 | $4.8 \times 10^6$ | 0.42 |
| | | | 95 : 5 | | $5.4 \times 10^6$ | 0.03 |
| Liquid type | ① | 1.3 | 95 : 5 | 0.12 | $10.8 \times 10^6$ | 0.03 |
| | | 1.1 | | | $6.4 \times 10^6$ | 0.1 |
| | | 0.4 | | | $26.2 \times 10^6$ | 0.08 |
| | ② | 0.4 | | | $26.2 \times 10^6$ | 0.06 |
| | ③ | 1.1 | | | $14.6 \times 10^6$ | 0.52 |

Further polishing experiments were tried on a sequential grinding-polishing machine[3] recently developed by us, in order to confirm if the whole surface of 125mm diameter wafer could be polished up on dry condition by using a cup-wheel made of these pellets. For this experiment, a polishing wheel of 100 mm diameter was prepared which sets 20 pieces of $BaCO_3$ pellets around its periphery as seen in Fig.5. After grinding the 125mm wafer by #800 diamond cup-wheel, the grinding wheel was exchanged for the polishing wheel and then dry

polishing was sequentially operated. Figure 6 is a snapshot of the polishing operation. The polishing wheel was so set that the polishing pellets passed through the center of the rotating Si wafer. Figure 7 shows surface roughness near the center of the wafer and shape profile near the periphery edge after the dry polishing of about 5 $\mu$m, compared with the case of conventional wet polishing on the pad SUBA 800. It is clearly seen that polishing by $BaCO_3$ pellets gives the level roughness but extremely sharp edge-shape.

## 4 Conclusion

Mechanochemical dry polishing of Si wafers by $BaCO_3$ powder was tried in loose abrasive style and bonded abrasive style. It was found that in both cases Si wafers can be polished with high efficiency and high quality. In order to keep the manufacturing environment clean, introduction of these kinds of dry polishing should be more positively promoted as desirable future processes.

## References


1) N.Yasunaga et al. : Proc.1st Inern. Conf. Prec. Engg., Tokyo(1974)32
2) N.Yasunaga et al. : NBS Special Publication No.562, (1979)171
3) N.Yasunaga et al. : Proc. from ASPE Spring Topical Meeting, (1996)29


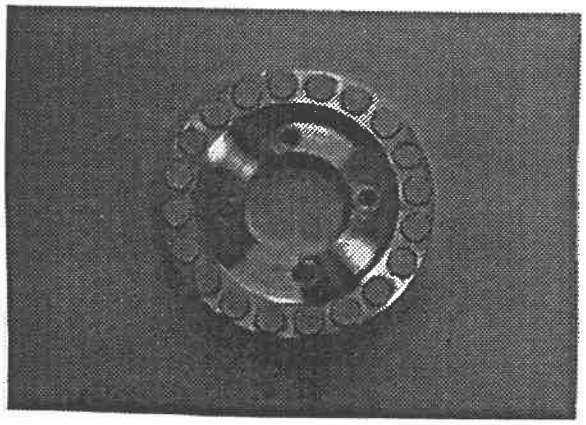

Fig.5 A polishing wheel made of BaCO3 pellets

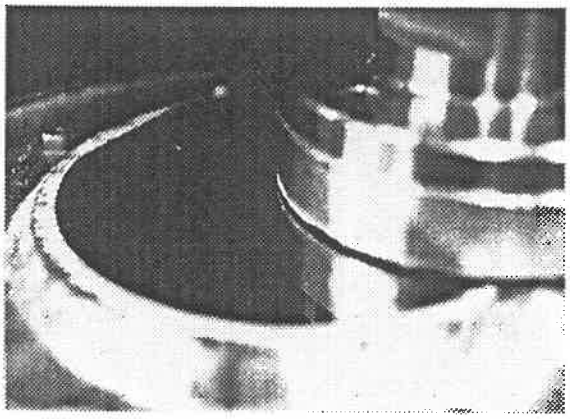

Fig.6 Dry polishing operation by the polishing wheel

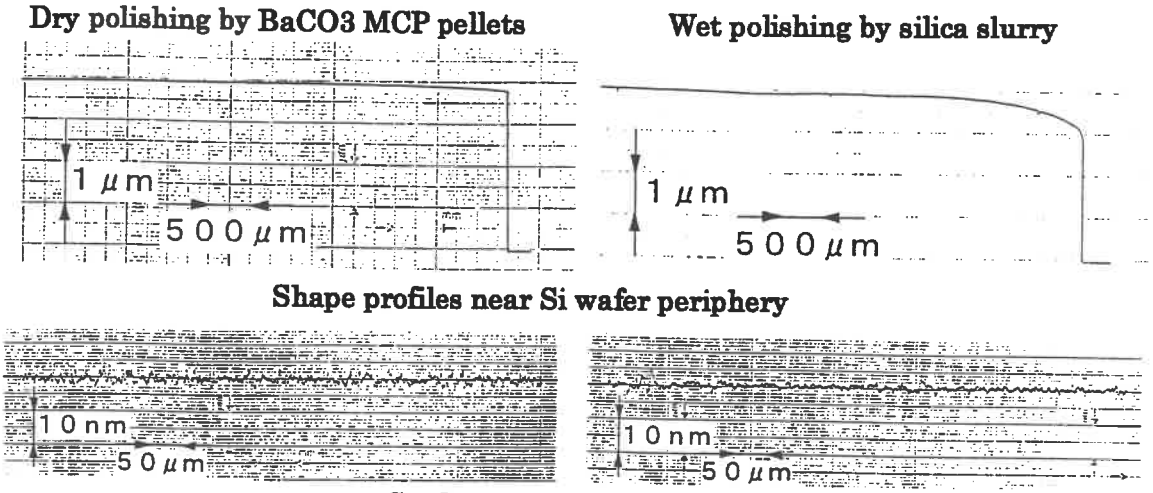


Fig.7 Comparison of polishing features

# The Effect of Fluids on the Ductile Response of Silicon during Abrading

John Patten
University of North Carolina Charlotte

**Abstract:** The fluid environment is a process variable during silicon machining. In addition to lubrication, fluids act as coolants to reduce the temperature generated during material deformation and removal. Chemistry of the fluid is also an important process parameter. The fluid chemistry has been shown to promote or inhibit fracture during processing, resulting in rough and smooth surfaces respectively. Cutting fluid chemistry has been shown to effect the resultant material removal rate during machining processes. Generally, this variation is a function of the dominant material removal mechanism. If fracture dominates, high material removal rates are expected. Tool wear can also be effected by all three fluid characteristics, i.e. lubricating, cooling and chemical activity. This paper reports on results from an experimental program conducted to address the effect of fluids on the hardness of silicon during abrasion processes such as polishing. A number of commercial polishing slurries have been tested to determine their relative influence during deformation of silicon. These polishing slurries have been compared to dry (room air) abrasion and deionized water. It was anticipated that the polishing slurries would soften the silicon surface resulting in higher material removal rates. This model is consistent with the accepted chemical-mechanical-polishing (CMP) model. However, indentation and abrasion (scratching) tests indicate that these polishing slurries produce an apparent increase in hardness, which should lead to reduced material removal rates. This finding, which is in direct conflict with present process models, has been supported by nano-indentation studies. Further, at low loads water appears to produce the same apparent increase in hardness as the polishing slurries. At higher loads, the slurries and dry conditions produce a ductile response and water produces brittle fracture.

Keywords: Silicon, fluids, hardness, indenting, scratching

**Introduction:** The literature is abundant with studies on the influence of fluids during mechanical contact processes, such as friction (Levert, 1996) and machining (Chargin, 1998). Many different fluid environments have been evaluated in combination with numerous materials and contact loading geometries. For silicon machining, water is widely used as a coolant for grinding and SPDT. Polishing slurries, which add a mechano-chemistry action, are used in semiconductor manufacturing. In addition to these wet environmental conditions, dry silicon machining is often employed in laboratory investigations and fundamental studies, such as with indenting, scratching and machining experiments. The conditions involving water and dry (air) machining of silicon appear to be consistent and straightforward,

if perhaps not completely understood. Water in addition to providing cooling, during grinding and SPDT, appears to facilitate fracture during brittle material removal. The combined effect of cooling and higher material removal rates results in greater throughput and increased tool life. However, the resultant surface finish and sub-surface damage are degraded. When experiments are performed with dry cutting conditions, ductile machining can be achieved. Ductile material removal is possible with sharp tools, small depths-of-cut and negative rake angle tools. Ductile regime machining can produce smooth surfaces, but it also results in sub-surface damage involving dislocations and phase transitions. Ductile material removal rates are low, and tool life is short, when machining in air. Fluid environments, involving cutting fluids, lubricants, coolants and chemical mechanisms, are far more complicated to evaluate. It is these areas that the present work attempts to evaluate. Polishing slurries have been tested during indenting and scratching experiments to define the relative influence of these solutions compared to similar tests with water and air. The ductile and brittle response associated with these fluids is of interest. This work is primarily concerned with the ductile nature of the deformation.

**Theory:** Fundamental to this work are two well documented theories associated with ductile material removal during machining (SPDT, grinding, polishing and lapping). First, high pressure phase transformations occur which convert the brittle semiconductor into a ductile metal (Hamann, 1957). Second, the CMP process involves a chemical softening of the surface which facilitates material removal. There is the possibility that these two process mechanisms can interact. Gilman (1996) provides a theory to evaluate this condition. His thesis is that chemical reactions can be triggered by mechanical forces. Also, much literature exists which suggest that the ductile nature associated with silicon machining is due to thermal mechanisms. Most of this latter body of information is based upon grinding conditions involving high speed or high cutting velocities. However these conditions to not apply to ductile processes such as SPDT, polishing and lapping.

**Experimental Method:** Two experimental programs are reported herein. The first involved a series of scratch test and the second were nanoindentations. Polished silicon wafers, (100) N-type Arsenic Doped, 0.005 ohms-micrometer, were used in all of the experiments. The fluid environment included the following: Dry - room air, deionized water and polishing slurries.

**Scratch Tests:** The scratch tests were conducted on a Mahr Profilometer to which various loads were applied to the stylus. The nominal load with no additional weight, is approximately 0.7 mN force. Weights of approximately 5 mN and 10 mN were tested. Scratch lengths were 60 mm and the scratch speed was 0.5 mm/s. Scratches were made in the [010] and [001] directions. The interaction of these scratches provides additional insight into the resultant deformations. The diamond stylus of the

profilometer has a nominal radius of 2 micrometers. For each fluid environment two (perpendicular) scratches were created, evaluated, and measured. All of the fluids puddle on the surface and seemed to have minimal wetting effect. Immediately after the scratches were made the wafers were cleaned and dried. For the scratches made in deionized water the wafers were blown dry with compressed air and then dried with nitrogen. For the wafers treated with polishing slurries, additional cleaning/rinsing was required to completely remove the resultant surface film. The wafers scratched with polishing slurries were rinsed in deionized water, then put into an ultrasonic deionized water rinse bath for five minutes, followed by nitrogen drying.

**Nanoindentations:** These tests were conducted to compare to the anomalous behavior discovered with the scratch test which suggested an apparent increase in the hardness of the silicon in the presence of water or polishing slurries. For this series of experiments a Digital Instruments (DI) AFM was fitted with a DI nano-indenter. As with the scratches, a comparison was made between dry, deionized water and the polishing slurries to determine any relative change due to the fluid environment. In these tests, a drop of fluid was put on the silicon surface, the nanoindentation was made (in the fluid) and the indent was immediately imaged with the same tip that made the indent (in-situ). For the wet fluid environments, the cantilever was submerged in the fluid. For the nanoindentation work, since the cantilever was submerged in the fluid, the measured response is sensitive to the change in the optical path length of the laser beam used to determine displacement (and thus force). Work is currently under way to assess this effect.

**Results:** The hypothesis that the polishing slurries would soften the silicon surface, during both the scratch and indent tests, was not confirmed. Rather, the silicon experienced an "apparent increase in hardness" due to the presence of the polishing slurries. The relative hardness of silicon and its response to the various fluid environments was based upon post process measurements of the scratch or indent geometry. The scratch geometry was profiled and the depth, width and pile-up measured with a AFM (Tencor-Park Scientific). The scratches produced with the slurries were shallower and narrower that the ones created in air at the same load. The smooth continuous regular shape and pile-up along the edges of the scratches, is indicative of ductile material deformation. No chipping or cracking was observed in these ductile scratches when imaged in the AFM. For the nanoindents the dry test resulted in a penetration depth of 5 nm while the indentations with the fluids (water and slurries ) were approximately 2 nm deep (Jarausch, 1997). The wet indents were shallower than the dry indents, consistent with the scratch test results.

**Analysis of Results:** It is understood that the high pressure phase transformation of semiconducting silicon to metallic silicon is responsible for the ductile behavior of this material during indenting, scratching and machining. The apparent change

in hardness, experienced during these fluid tests, could be caused by the fluid's effect on this transition. The slurries may hinder or impede the phase transformation, which would lead to the observed results. At low loads, as in the nanoindentation, water behaved similarly to the slurries resulting in an apparent increase in hardness. At higher loads during scratching, water produced a brittle fracture response. This transition from a ductile-to-brittle response with increasing load is consistent with fracture mechanics models. A harder response equates to a more brittle response (when comparing the dry to water conditions this is consistent). However, the polishing slurries showed an increased hardness and increased toughness which is not consistent. This result may explain why polishing slurries are successful in material removal processes. If the slurries do create an increase in toughness this would lead to less brittle fracture and more ductile material removal resulting in smoother, less damaged surfaces, which is surely the case. The increase in hardness would have a similar beneficial result of less surface penetration of the tool or polishing particle causing decreased material deformation leading to decreased surface roughness.

**Conclusions:** The CMP model which includes a softening effect of the silicon surface does not correlate with the apparent increase in hardness realized during scratching and nanoindenting experiments conducted in the presence of polishing slurries and water. Further experimental and theoretical work is required to evaluate other process mechanisms which may influence the measured results. These include, surface energy effects (Johnson, 1989), optical path (in-situ AFM) changes (Jarausch, 1997) and phase transformations (Patten, 1996). Initially it was expected that the particle size would have an influence on the measured results, but this was never confirmed in the experiments. Future experiments with styli of controlled tip radii will be conducted to evaluate the effect of particle size as simulated by the stylus radius.

**References:**


Chargin, D, Cutting Fluid Study for Single Crystal Silicon, 1998 ASPE Spring Topical Meeting, Silicon Machining.

Gilman, John J., Mechanochemistry, Science ,1996, Vol. 274, 65.

Gilman, J.C., Chemical reactions at detonation fronts in solids, Phil Mag. B, 1995, Vol. 71, No. 6, 1057-1068.

Jarausch, K., Russell, P., Patten, J., Measuring the nanomechanical response of surfaces with an atomic force microscope, NCSU, Precision Engineering Annual Report

Levert, J., Baker, R., Mess, F., Danyluk S., In-Situ slurry film measurements for chemical-mechanical polishing, ASPE 1996,80

Hamann, S.D., Physico-Chemical Effects of Pressure, Butterworths Sci. Pub. London 1957

Johnson, K.L., Contact Mechanics, Cambridge, 1989.

Patten, J. High pressure phase transformation analysis and molecular dynamics simulations of single point diamond turning of germanium, Ph.D. dissertation, NCSU, 1996.

# Ultraprecision Grinding and Single Point Diamond Turning of Silicon Wafers and their Characterization

**M. Kerstan, A. Ehlert, A. Huber, D. Helmreich**
*(Wacker Siltronic AG, D-84479 Burghausen, Germany)*
**J. Beinert, W. Döll, M. Schinker**
*(Fraunhofer-Institut für Werkstoffmechanik, D-79108 Freiburg, Germany)*

## 1 Introduction

The conversion from 200 mm to 300 mm diameter silicon wafer in combination with increasing economical and quality requirements demands for new wafer preparation techniques. Part of the existing process steps will already pass their limits of technical capability, so new processes with innovative breakthrough technology and respective equipment have to be developed and integrated in forthcoming wafer manufacturing lines. For example conventional steps for wafer planarization and stock removal such as free floating lapping may be substituted by advanced grinding procedures. These techniques are expected to meet the very demanding goals for wafer geometry (site flatness ≤ 0.18 µm) and morphology (microroughness ≤ 5 Å, no subsurface damage (SSD)). Among the different grinding concepts presently under discussion and evaluation, recent advances in ultraprecision grinding and single point diamond turning (SPDT) make these techniques attractive in silicon wafer manufacturing due to a reduction of surface and subsurface damage. In particular under ductile mode machining conditions wafer surfaces almost free of damage in form of microcracks can be achieved.
Both wafer shaping techniques mentioned above have been compared with each other. The very new technology of ductile mode SPDT was improved and developed further with respect to technical applicability. The processing parameters have been optimized, especially under the aspect of economical manufacturing.
The wafers produced with either technique have been evaluated with respect to geometry, surface topography, roughness as well as depth and type of subsurface damage. Interferometry and atomic force microscopy (AFM) have been used for roughness measurements. Scanning infrared depolarization (SIRD), photothermal heterodyne inspection (PTH) and high resolution transmission electron microscopy (HRTEM) were employed for surface and subsurface damage evaluation.

## 2 Silicon Wafer Preparation

### 2.1 Ultraprecision Cup Wheel Grinding (CWG): Conventional and EPD Technique

Since many years cup wheel grinding is the dominating grinding technique in silicon wafer mass production. Fully automated systems are used as stand alone equipment without the need of complicated supply networks. They offer high wafer throughput and a broad variety of tools is available. With grinding equipment presently on the market all requirements with respect to wafer geometry can be achieved for todays design rules in IC manufacturing. For this study 200 mm and 300 mm wafers have been ground on a conventional cup wheel grinding system using standard parameter settings of wafer mass production. Cup wheels with two different mesh sizes of resin bonded diamonds, mesh 2000 and mesh 4000, respectively were employed.
Grinding with ultrafine abrasive particles (UAPG) is known since some years [1]. Originally EPD (electrophoretic deposition) has been applied to form pellets which can be used as grindstones mounted on to a cup wheel. First pellets consisted mainly of colloidal silica (abrasive) and sodium alginate (binding agent) and were soluble in water. Thus, grinding was possible in dry conditions only, leading to grinding machine pollution and strong tool wear. Further development of EPD pellets led to a second generation of pellets consisting of fumed silica (abrasive), plastic and other additives. This type of pellets has higher rigidity and is nonsoluble in water. First EPD grinding experiments were carried out on a standard CWG system equipped with EPD pellets mounted on to a standard cup wheel tool.

## 2.2 Single Point Diamond Turning (SPDT)

A new promising concept in wafer preparation is the ductile mode turning using a single point diamond tool [2]. This technique

- utilizes the plastification of the material under the influence of the extremely high compressive stresses underneath the diamond cutting edge,
- enables therefore a ductile machining of normally brittle materials like silicon,
- allows - combined with ultraprecision machining - the manufacturing of very plane surfaces and
- avoids contamination of the surface by metals, because the wafer is in contact with diamond (= pure carbon) and metal-free cooling liquid or lubricant only.

In ductile mode SPDT of silicon a diamond cutting edge with negative angle is moved across the surface under preparation. Within the cutting zone underneath the edge hydrostatic compressive stresses prevail to such an extent that a phase transformation from the (brittle) diamond-structure into the (ductile) metallic β-tin-structure can occur. All technological conditions, therefore, must be chosen in a way that this phase transformation takes place on the surface along the whole diamond trace.
In order to optimize the different machining parameters their interdependence and influence on the wafer surface quality were investigated, also under the aspect of economy. Relevant parameters are

- concerning the turning machine: stiffness, mechanical precision, vibrational behaviour,
- concerning the diamond-tool: geometry of the cutting edge, tool fixture, synthetic/natural diamond,
- concerning the turning process: infeed rate, depth of cut, cutting speed, coolants/lubricants.

Regarding the infeed rate resulted: under otherwise constant conditions the stock removal occurs in a ductile mode if the infeed rate V remains *below* a certain critical value $V_{crit}$, however, occurs in a brittle mode if V *exceeds* this critical value (fig. 1). $V_{crit}$ depends on the depth of cut: with increasing depth of cut , $V_{crit}$ first decreases and then approaches a constant value. The amount of this value depends on the above mentioned parameters. As a consequence relatively large depths of cut of several 10 µm can be realized in ductile mode regime so that sliced wafers with their rough surface can be prepared in one step to a semi-finished state where only polishing with reduced stock removal is needed.
Experiments showed that SPDT permits relatively high cutting speeds. Any dependence of $V_{crit}$ on the cutting speed was not observed in the investigated range up to 31 $ms^{-1}$. This enables short machining times needed in view of economy.

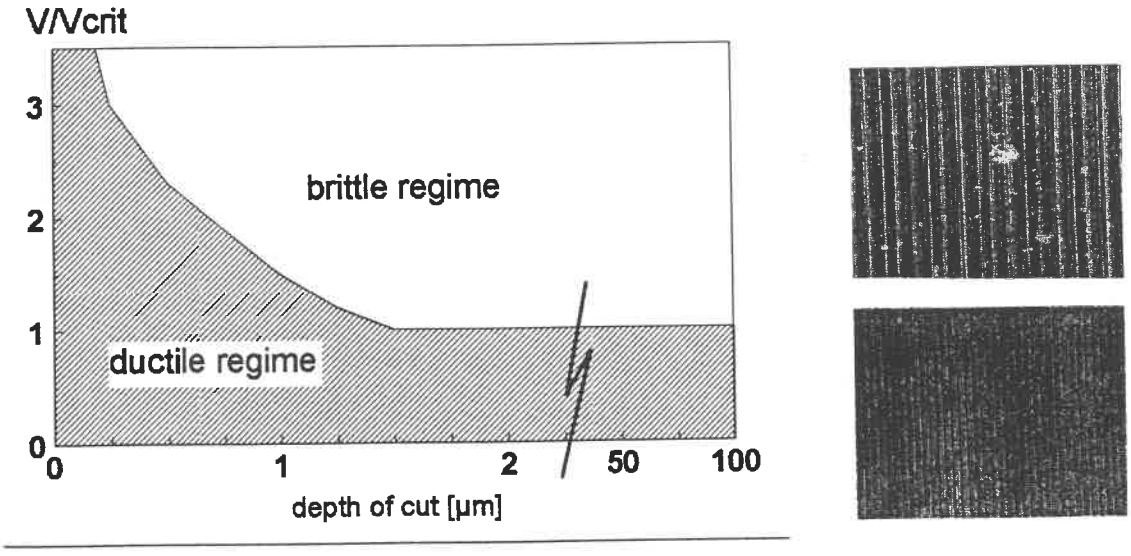


Fig. 1: ***left:*** $V_{crit}$ as a function of depth of cut,
***right:*** Micrographs of SPDT wafer surfaces: with infeed rate $V<V_{crit}$ the stock removal occurs ductile. Except machining tracks no structure is visible (bottom). With $V>V_{crit}$ the surface exhibits brittle fracture (top).

# 3 Silicon Wafer Characterization

## 3.1 Characterization Methods

### 3.1.1 Surface Morphology Characterization

Parameters describing the wafer surface morphology (appearance, microroughness) have been obtained with optical differential interference contrast (DIC) microscopy, microinterferometry and AFM mapping (2D rms values, size of scans: 100 X 100 $\mu m^2$). In addition geometrical measurements have been performed.

### 3.1.2. Wafer Damage Evaluation

The surface and subsurface damage was evaluated by means of SIRD and PTH, respectively.
The SIRD method is based on a principle of Lederhandler [3] -crystalline defects induce an optical birefringence in silicon normally to be optically isotropic- and has been first applied by Lundt et al. [4] for a quantification of silicon subsurface damage due to abrasive wafering operations.
Photothermal response measurement techniques are among the most sensitive methods in materials analysis because they are based on the coupling of optical phenomena (via the complex dielectric function) with the relaxation of a laser-induced electrical or thermal local nonequilibrium (relaxation and recombination of excited carriers). Many of the influencing optical, electrical and thermal properties are extremely sensitive to structural modifications at or beneath the surface of a wafer. In our study we employ a single-beam technique based on a two-frequency modulation of the laser beam. A detailed description of this principle and applications have been given in [5].

## 3.2 Results

General features of the machined wafers with respect to their roughness and damage are summarized in table 1.

| Table 1 | CWG mesh 2000 | CWG mesh 4000 | EPD Grinding | SPDT |
|---|---|---|---|---|
| Roughness (AFM) | 10 – 100 nm | 5 – 15 nm | 0.5 – 3 nm | 1 – 10 nm |
| SSD (SIRD) | 1 – 3.5 µm | 0.5 – 2 µm | < 0.2 µm | < 0.2 µm |
| SSD (PTH) | not measured | 8 – 10 µm | not measured | 0.2 µm |
| SSD (TEM) | 0.5 µm | 0.2 µm | not found | 0.06 µm |

### 3.2.1 Ultraprecision Cup Wheel Grinding: Conventional and EPD Technique

*Conventional CWG Wafers:* Due to the experimental limitations of the SIRD equipment only averaged values for SSD could be obtained. More detailed informations have been received from the PTH inspection, indicating the existence of local residual SSD sites even up to 8 - 10 µm in depth. In addition a PTH wafer mapping reveals an inhomogenity of defect distribution with a high level at the outer wafer area (deep reaching SSD sites) and a low level at wafer center.
A more detailed investigation of the crystallographic character of surface and subsurface damage due to CWG has also been performed with PTH and points to a triple zoning with an amorphous layer on the top of the wafer (layer thickness about 50 nm). The top layer is followed by a polycrystalline zone (layer thickness of about 130 nm) consisting of grain boundaries due to crystal blocking. A transition zone (layer thickness at least 160 nm) to the perfect silicon bulk material contains single end-of-range (EOR) defects.
In TEM investigations we obtained the following results for local spots: subsurface damage in fine CWG machined wafers consists of dislocation networks mainly, no fractures could be recognized in the TEM images. Depth of damage again depends on grain size of diamonds used in the grinding

wheel. The results confirm the assumption that fine CWG processes work predominantly in the socalled ductile mode of material removal.
*EPD wafers:* First results showed a mirror-like surface finish after short processing time. Only few scratches remained due to poor grinding wheel adjustment. No residual damage could be found with SIRD measurements and TEM analysis, respectively.

### 3.2.2 Single Point Diamond Turning

Wheras the roughness of SPDT wafers has a typical value of 2 nm, the depth of the machining traces due to the turning process is approximately 25-35 nm.
For this wafertype SIRD inspection has found not to be a suitable evaluation technique. Thus SSD analysis was performed using PTH inspection.
In contrast to CWG machined wafers, SPDT processed samples exhibit only a double zoning: an amorphous layer on the top (layer thickness <100 nm) is followed by a transition zone underneath. The latter is almost free of EOR defects and more homogeneous in lateral extension. The total amount of lattice disorder due to SPDT machining is about 200 nm depending on machining parameters such as the infeed rate and the conditions of the diamond tool, respectively. The PTH signals probably point to subsurface damage consisting of dislocation loops predominantly on a single slip system which is confirmed by TEM results. Thus in comparison to CWG the SPDT subsurface damage seems to be more ordered from the view of crystallography.

## 4 Summary / Conclusions

Two novel concepts of wafer preparation techniques have been compared: ultraprecision cup wheel grinding and single point diamond turning. The conventional CWG process described in this study represents the present technological stage in silicon wafer mass production. A promising development was started by applying a new tool generation to the standard CWG equipment: EPD cup wheels. In SPDT technique processing parameters have been optimized with regard to wafer quality and economical aspects.
CWG and SPDT machined silicon wafers have been evaluated with respect to wafer morphology and damage. For damage evaluation two noncontact and laser-based inspection methods, SIRD for a global detection of defects and PTH for the localization and classification of lattice imperfections have been coupled. PTH has been demonstrated to be an effective metrology tool for defect detection and process optimization.
SSD due to CWG has been found to be more complex and far-reaching as compared to the damage induced by SPDT machining. For SPDT wafers low roughness values, comparable to those obtained in stock removal polishing step, together with a very thin layer of damage consisting of an amorphous toplayer and dislocation networks below it, indicated an outstanding surface quality, suitable for subsequent polishing processes.
Besides the wafer quality, tool wear and wafer throughput for either technique will be of primary concern in future developmental work.

## 5 Literature


[1] Ikeno, J.; Tani, Y.; Sato, H.: „Nanometer Grinding using Ultrafine Abrasive Pellets – Manufacture of Pellets applying Electrophoretic Deposition", Annals of the CIRP, vol. 39, no. 1, pp. 7-10, (1990)

[2] Morris, J.C.; Callahan, D.L.; Kulik, J.; Patten, J.A.; Scattergood, R.O.: „Origins of the Ductile Regime in Single-Point Diamond Turning of Semiconductors", J. Am. Ceram. Soc., vol. 78, pp. 2015-2020, (1995)

[3] Lederhandler, S.R.: „Infrared Studies of Birefringence in Silicon", J. Appl. Phys., vol. 30, no. 11, pp. 1631-1638, (1958)

[4] Lundt, H.; Kerstan, M.; Weiss, R.: „Subsurface Damage Characterization of Silicon Wafers using Scanning Infrared Depolarization", Proc. of the Spring Topical Meeting of the American Society for Precision Engineering, Tuscon, pp. 42-45, (1993)

[5] Ehlert, A.; Kerstan, M.; Lundt, H.; Huber, A.; Helmreich, D.; Geiler, H.D.; Karge, H.; Wagner, M.: "Selected Applications of Photothermal and Photoluminescence Heterodyne Techniques for Process Control in Silicon Wafer Manufacturing", Opt. Eng., vol. 36, no. 2, pp. 446-458, (1997)

# Epistemology and Abduction[1)] in Shear(Ductile)-mode Grinding of Brittle Materials

Hiroshi Hashimoto, Kenichiro Imai
Kanagawa Institute of Technology
1030 Shimo-ogino Atsugi-shi Kanagawa, 243-0292, JAPAN

## 1.Introduction

In recent years, various brittle materials have made their appearance to serve the need of technologies such as electronics and optics. Especially, semiconductors have become more powerful and lower-priced, caused by an increase in the diameter of silicon wafers. In view of this fact, precision grinding has been recognized as one of the key technologies replacing lapping and polishing processes for brittle materials. However, very serious problems remain in productivity accuracy, especially in subsurface damages.

According to hypotheses of conventional grinding theory, when material removal proceeds, the wheel-active surface changes (including self-dressing), and as a result, grinding force increases. Therefore, dressings during the grinding process are needed. This theory was established primarily as it pertains to metal grinding, but has been also been applied to grinding of brittle materials, with the advent of silicon, ceramics, and glass.

This paper describes the epistemology of abduction processes obtained in our experiments in grinding brittle materials.

## 2. Epistemology obtained in experiments

### 2.1 Grinding method

A 4mm wide bronze bonded 3000 grit diamond wheel(Dia.100mm) was used to grind 50mm long, 3mm wide samples of optical glass BK7; an oil based grinding fluid was used. Wheel speed was 1500rpm and cross feed rate 150 mm/min. The depth of cut was set up at 2, 6, 10, 12 $\mu$m, (given stock removal rates of 0.9, 2.7, 4.5, 5.4 $mm^3$/min) and number of cuts (ie passes across the sa,ple) was 200. The wheel had been previously used in a grinding experiment with more than 500 passes at the depth of cut of 2 $\mu$m after truing , and was used in this experiment without further truing and dressing. Grinding forces were measured using four-axis quarts piezoelectric measuring instrument (Type9273 made by Kistler Co). Roughness measurements were made using a Surtronic 3P made by Rank Taylor Hobson Co.

### 2.2 Results

The following results were induced;

1)Normal grinding forces Fn are invariant throughout the processing.(shown in Figure 1) And, tangential forces Ft / Fn ratio is invariant at 0.08.

2)The forces are repeatable to a high degree of accuracy and given as deterministic function of wheel, workpiece and grinding conditions.(shown in Figure 2)

3)No residual material removal is left after wheel passing.

4)Roughness of wheel active surface is unchanged during process. (shown in Figure 3)

Therefore, a) dressing of wheel is not necessary during processing, b)depth of sub-surface damage is assumed to be almost uniform. And, we found that these results could be extended to other materials such as Pyrex and Zerodure.

### 2.3 Shear Mode Grinding Force Criteria

Above mentioned results [1)~4)] can not be derived from the conventional theory. From these experimental results, shear mode grinding force criterion was defined as the steady, invariant grinding force which is a repeatable deterministic function of shear mode grinding conditions including materials and grinding wheels. And, based on the criterion, various processing phenomena can now be established.

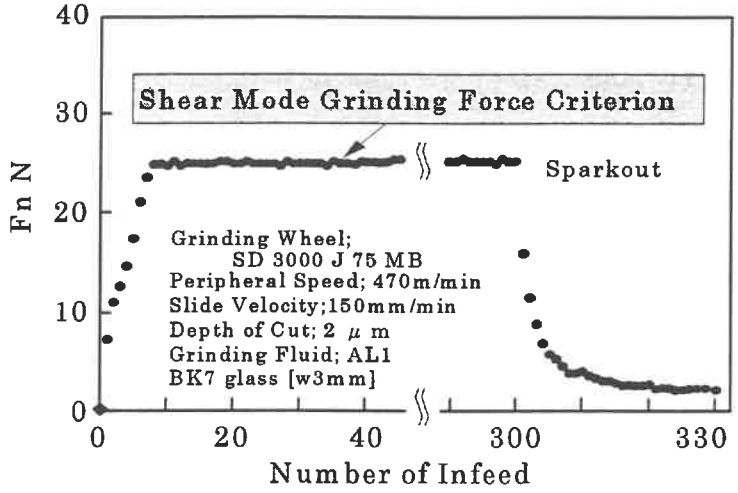


Figure 1 Shear mode grinding force criterion.

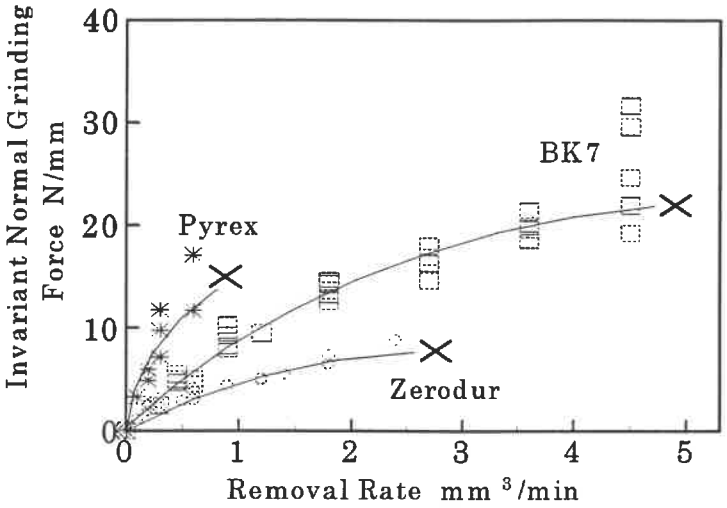


Figure 2 Invariant normal grinding Force at various materials

### 3.Introduction of ultrasonic assisted grinding

As described above, epistemology was ascertained to be fairly universal to some extent. However, the removal rate is limited by contact length of wheel to workpiece which might cause heat generation. For example, the normal grinding force when the depth of cut was further increased to 12 μ m is shown in figure4. Initially, the behavior is consistent with the results at lower depth of cut; after

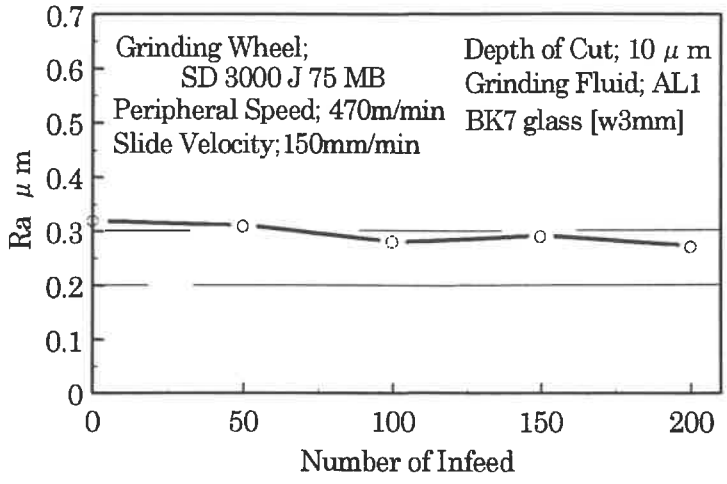


Figure 3 Wheel surface roughness Ra, when the grinding force is invariant

approximately 5 passes, the normal grinding force levels out at a steady state value, but after about 10 passes it starts to increase linearly, reading 200N at 16th cut. Grinding was almost impossible under theses conditions and grinding burn on the surfase occurs.(shown in Figure 5)

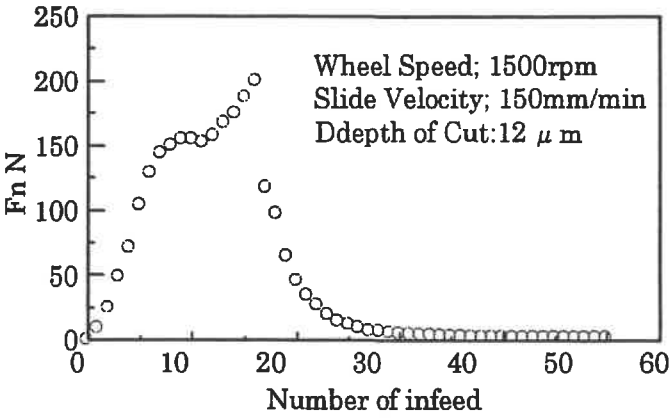


Fig.4 Change of normal grinding force of BK7.at 12 μm

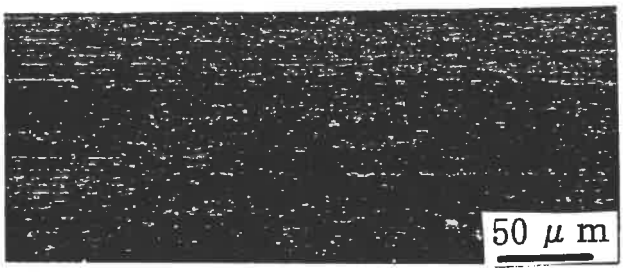


Fig.5 Ground surface with burning and cracking

In comparison with straight wheel grinding previously mentioned, cup wheel is commonly used in silicon wafers grinding. To overcome heat generation, we introduced 40kHz ultrasonic assisted grinding with cup wheel, we assumed vibration may let grinding fluid come into the contact area. In our experiments, a metal-bonded cup type wheel was used on a reconstructed surface grinding machine (Okamoto PSG-52DX) with a Professional Instrument's "Block-Head" type 4R. The ultrasonic spindle was installed under the air spindle. The frequency of the ultrasonic vibration is 40kHz and the amplitude is 2 μm. Batches of 10 × 25mm silicon wafer ([100] surface) were ground with ("ultrasonic vibration-assisted grinding") and without ultrasonic vibration ("conventional grinding'). The wheel rotation was changed to 2000 rpm, table speed was 100 mm/min and the depth of cut 0.5～14 μm/pass. The schematic illustration of grinding machine is shown in Figure 6 and the grinding conditions are shown in table 1. When using #3000 grit wheel, comparison of change of normal grinding force with and without ultrasonic vibration under 200 passes is shown in Figure 7. The normal grinding force of conventional grinding increased with passes and exceeded the value, produced by ultrasonic assisted grinding. On the other hand, the normal grinding force of grinding with ultrasonic vibration showed comparatively low value, but it was quite stable. Further, [tangential / normal] grinding force ratio was 0.05. This value is about

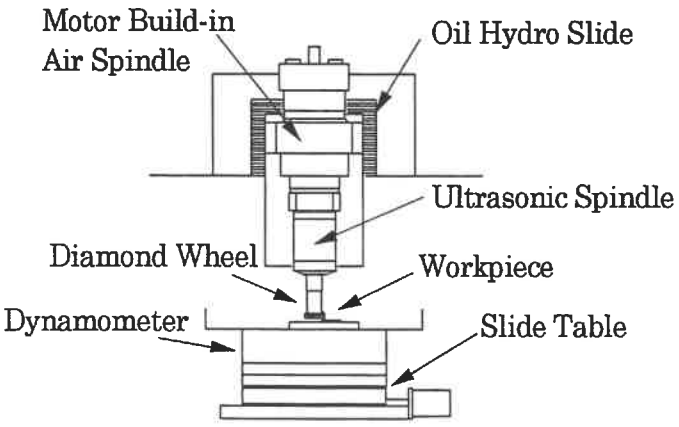


Fig.6 Schematic drawing of the grinding machine

one third compared with conventional grinding. And, we could produce shear-mode ground surface. (Figure 8) As a result of these experimental results, normal and tangential grinding forces of silicon wafer workpieces were found to be invariant and not limited by the increase of material removal.

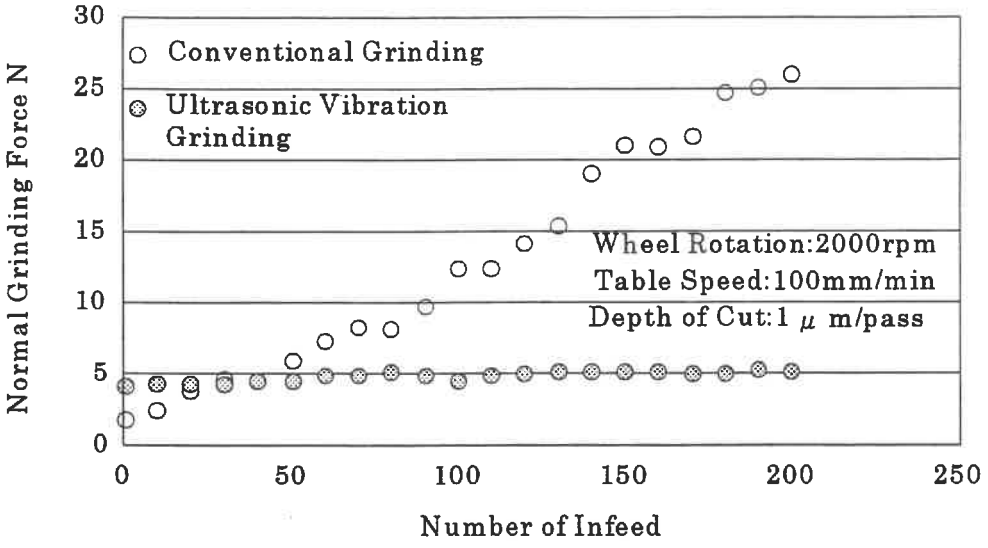


Figure 7 Comparison of normal grinding force with #3000 grid wheel

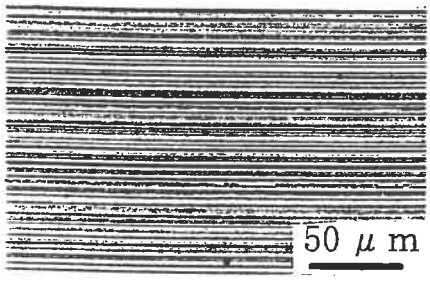


a) Conventional Grinding

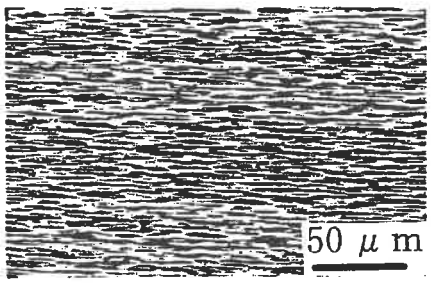


b) Grinding With Ultrasonic Vibration

Figure 8 Ground surfaces with both grinding method

## 4. Conclusion

The results obtained in our experiments were found to be universally applicable. Further, the possibility of a new theory was proved by ultrasonic-assisted grinding experiments. Thus, in comparison with conventional metal-grinding theory, a new epistemology of abduction in shear (ductile)-mode grinding theory of brittle materials as applied to electronics and optics, was demonstrated in this paper.

References

1)Willian H. Davis : Peirce's Epistemology, Martinus Nijihoff Publishings B.V. (1972).

# Traverse Grinding Characteristics of Resin Bond Diamond Wheel with New Profile in Precision Grinding of Silicon Wafers

Masamichi Daito*, Akira Kanai** and Masakazu Miyashita***

*Nissin Machine Works, **Ashikaga Institute of Technology, ***Nano-Tec Associates
**268 Omae, Ashikaga, Tochigi 326, Japan

## Abstract

In traverse grinding compared with plunge grinding, concepts of wheel depth of cut and grinding width are not clear in definition, and then grain depth of cut can not be defined. By introduction of new wheel profile -front and rear tapers-, the above two concepts are defined and also truing accuracy required to give them physical meaning is discussed. Requirement in workshop such as stock removal per traverse of 10 to 20 μm/pass and feed rate of 50 ~ 70 mm/min are achieved under the wheel depth of cut of 0.1 ~ 0.2 μm/rev by applying resin bond diamond wheel with soft binder and concentration of 100.

## 1. Introduction

In traverse grinding, wheel depth of cut and equivalent plunge grinding width can not be defined without assuming a wheel profile. In the present paper, a profile of wheel with front and rear taper for traverse grinding is proposed, and a traverse grinding characteristics of silicon wafers is discussed in terms of parameters -wheel depth of cut and equivalent grinding width- instead of a stock removal per traverse.

## 2. Proposal of wheel profile with front and rear tapers for traverse grinding and definition of wheel depth of cut and grinding width in equivalent plunge grinding

Fig. 1 shows a profile of wheel with front and rear tapers for traverse grinding. From the geometrical arrangement, wheel depth of cut $d$ and effective grinding width $w$ are defined as follows :

$$d = \frac{f}{N_w} \cdot \sin\delta, \quad w = \frac{D}{\sin\delta} \tag{1}$$

Considering a practice in workshop, such as D=10 ~ 20 μm/pass and d= 0.1 ~ 0.2 μm/rev., $\delta \approx 10^{-3}$ rad.

## 3. Truing accuracy required for generation of newly proposed wheel profile - ductile mode truing

For realizing Eq. (1), sufficiently close distribution of effective cutting points along the profile is required. Therefore, the following conditions are derived :

wheel profile accuracy ≤ wheel depth of cut (2)

wheel runout ≤ wheel depth of cut (3)

For achieving Eqs. (2) and (3), a ductile mode truing[1] in which diamond wheel is processed in ductile mode is to be introduced.

## 4. Proposal of combination wheel for achieving coarse and fine grinding by one traverse.

Fig. 2 shows a combination wheel composed of coarse and fine wheels and wheel profile. Fig. 2(b) is the revised profile for reduction of local wear at wheel edge.

## 5. Experimental results of traverse surface grinding of Si wafers

Fig. 3 is the ultraprecision and high stiffness horizontal spindle rotary table surface grinding machine[2] applied to the experiments and main specification.

5.1 Precision grinding with fine wheel profiled front and rear tapers / Fig. 4

5.2 Coarse and fine grinding by one pass with the combination wheel / Fig. 5 and 6

5.3 Effect of wheel contact stiffness on grinding performance

## 6. Conclusion

1. Conventional SD1500L100B has a limitation of grinding capability at most 2 μm/pass × 72 mm/min resulting from binder burning, excessive grinding load and stock residual.
2. SD 8/16 B with soft binder and concentration 100 has better grinding capability such as 15 μm/pass × 72 mm/min. The grinding load at 5 μm/pass × 72 mm/min is about one third compared with SD1500L100B at 2 μm/pass × 72 mm/min.
3. By introduction of front and rear tapers and combination wheel, 20 μm/pass × 50 mm/min at the wheel depth of cut 0.1 ~ 0.2 μm/rev is achieved.
4. The grinding accuracy and the grinding ratio at the above mentioned conditions are : Flatness : 0.2 ~ 0.3 μm/ϕ150, Surface finish : 12 ~ 16 nm $R_a$, Grinding ratio : ≈ 300.

**References :** (1) M. Miyashita, A. Kanai, F. Inaba, Strategies for truing/dressing technique and precision grinding performance of superabrasive wheel for brittle-material components, Proc. of SPIE, Vol. 3134 (1998), pp366-369

(2) M. Daito, A. Kanai and M. Miyashita, Design strategies of an ultraprecision surface grinding machine for ductile mode surface finishing of brittle materials, Proc. of ASPE Annual Meeting (1994), pp205-212

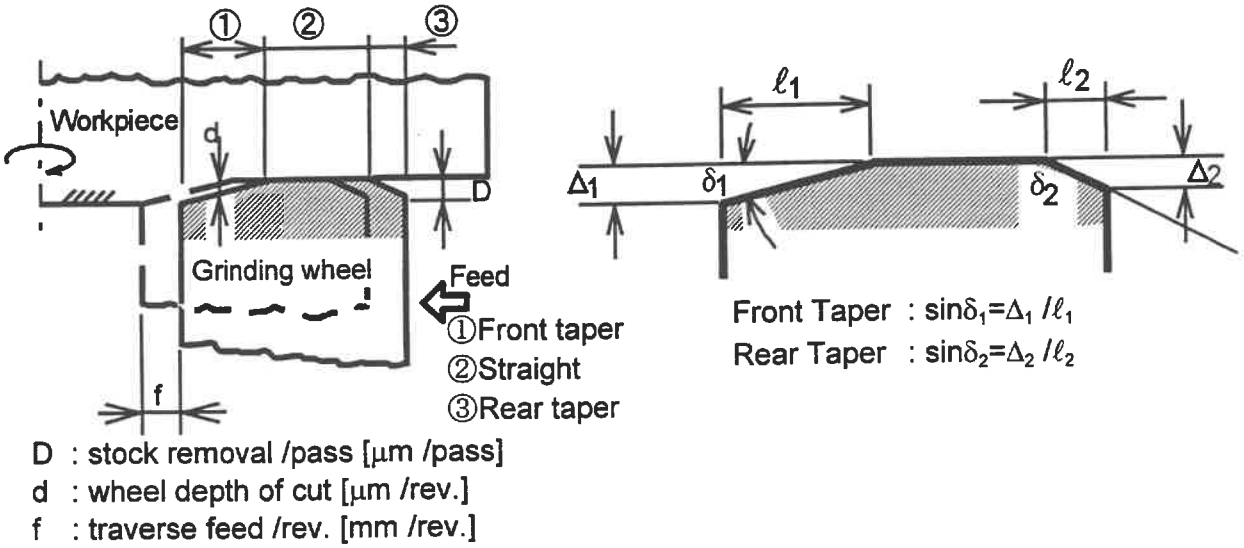


Fig.1 Grinding wheel with front and rear tapers for traverse grinding

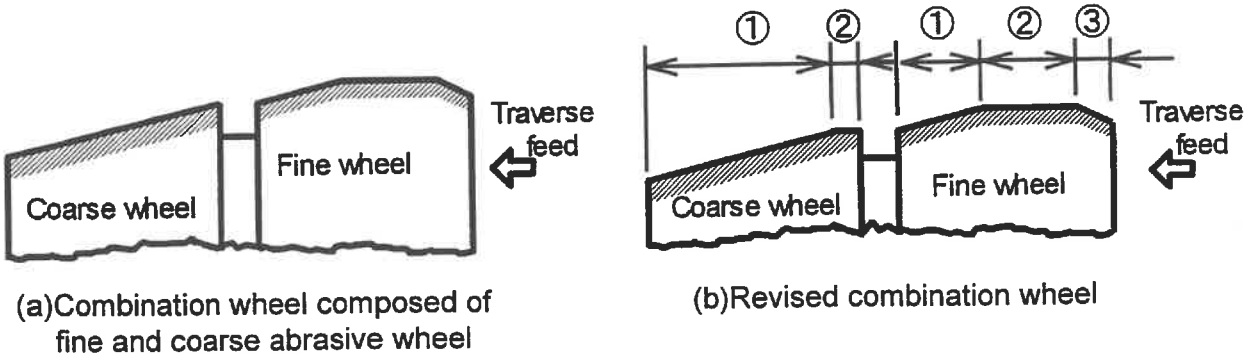


(a)Combination wheel composed of fine and coarse abrasive wheel

(b)Revised combination wheel

Fig.2 Combination wheel for coarse and fine grinding process by one traverse feed

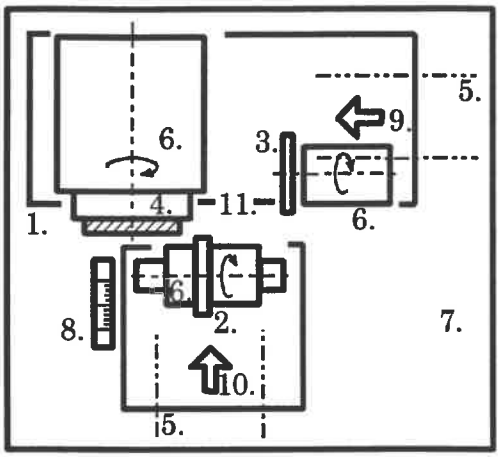


pecifications
1.Workpiece : silicon wafer or disc,ϕ150 350 rpm
2.Grinding wheel : ϕ175×20, 40mm
2100 rpm(1150 m/min)
3.Truing wheel : ϕ175×3 mm, SD200M
4.Vacuum chuck : ϕ200, 3 Kw
5.V-V plain bearing guideway
6.Wheel spindle : hydrostatic bearing
7.Low thermal expansion coefficient cast iron
8.Feedback linear scale : 0.01 μm
9.X axis : 0.01 μm/step
10.Z axis : 0.01 μm/step
11.Coolant : JIS W-1

Fig.3 Ultraprecision and high stiffness surface grinding machine[1]

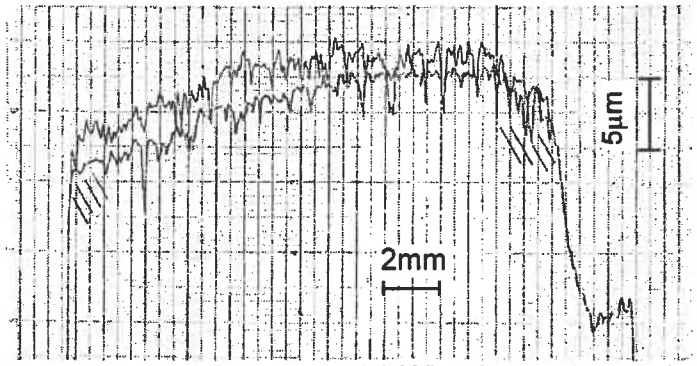


Grinding mode : traverse down grinding
Wheel velocity : 2100rpm
Stock removal : 5μm×25pcs (2.2cm³)
Work velocity : 350rpm
Feed : 72mm/min (0.2mm/rev)
Front taper : 7μm/9mm
Rear taper : 3μm/2.5mm
d=0.15μm/rev., w=7mm
G≈120

(a) Wheel wear for stock removal of 2.2cm³

(b) Grinding load of silicon wafer for 25pcs

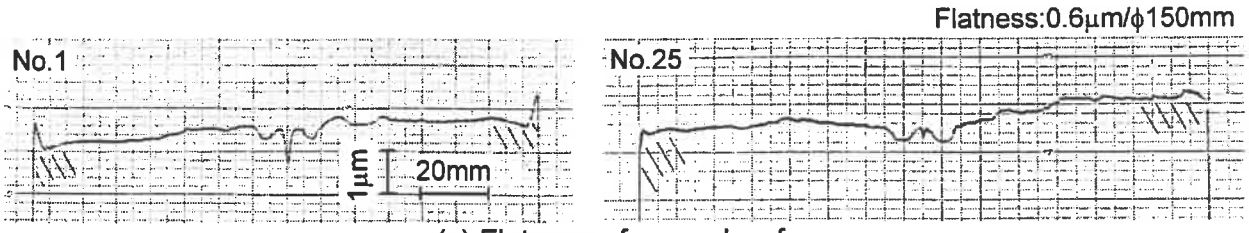


(c) Flatness of ground wafer

Fig.4 Traverse grinding characteristics of SD2/6B
with soft binder and concentration 100

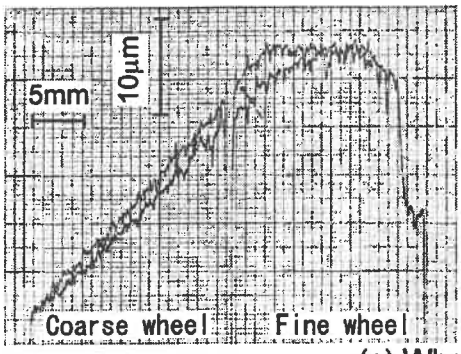


Same as Fig. 4(a) except :
Stock removal : 20μm×28pcs (10cm³)
Feed : 50mm/min (0.14mm/rev)
Coarse wh./Front taper : 22μm/20mm, SD8/16B
Fine wh./Front taper : 4μm/5mm, SD2/6B
Coarse wh./d=0.15μm/rev., w=15mm
Fine wh./d=0.15μm/rev., w=5mm
G≈300

(a) Wheel wear for stock removal of 10cm³

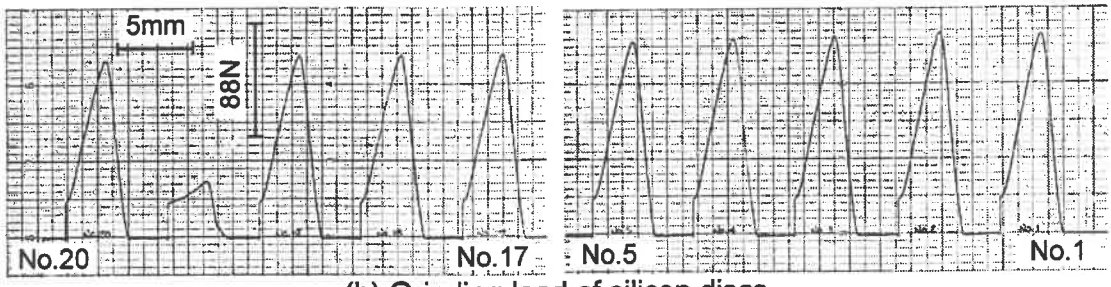


(b) Grinding load of silicon discs

Flatness:0.6~0.8μm/φ150mm

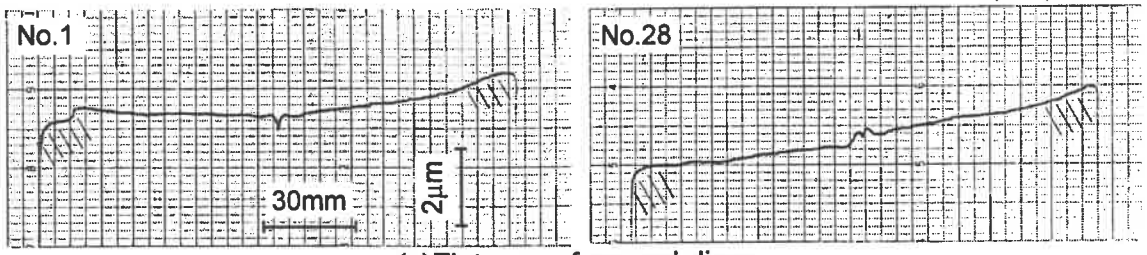


(c)Flatness of ground discs

Fig.5 Traverse grinding characteristics of combination wheel SD2/6B

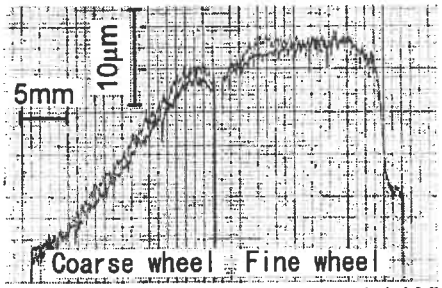


Same as Fig. 5(a) except :
Coarse wh./Front taper :25μm/17mm
Fine wh./Front taper :4μm/5mm
Coarse wh./d=0.21μm/rev., w=11mm
Fine wh./d=0.11μm/rev., w=4.4mm
G≈300

(a) Wheel wear for stock removal of 10cm³

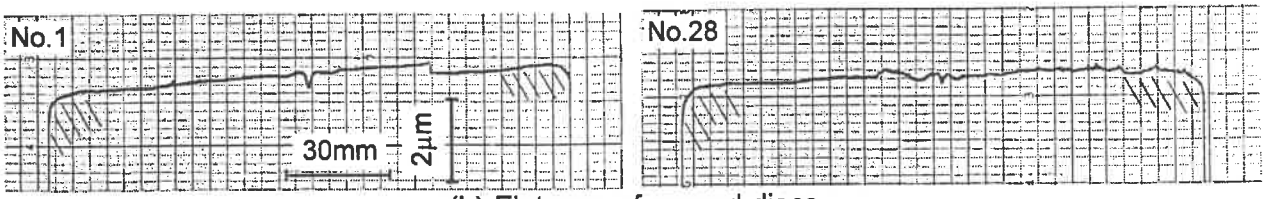


(b) Flatness of ground discs

Fig.6 Traverse grinding characteristics of revised combination wheel

# An Empirical Survey on the Influence of Machining Parameters in Diamond Turning of Large Single Crystal Silicon Optics

C. K. Syn, D. A. Krulewich, P. J. Davis, M. R. McClellan[†],
P. C. DuPuy, M. A Wall, and K. L. Blaedel
Lawrence Livermore National Laboratory, Livermore CA 94551
[†]Schafer Corp., Livermore CA 94550

## Abstract

A series of Si diamond turning tests was conducted to survey the influence of machining parameters on tool wear and subsurface damage (SSD) in long distance cutting. The survey test matrix was selected by an experimental design technique. The machining parameters included in the test matrix were two settings of depth-of-cut, feed rate, surface speed, tool radius, tool rake and tool skew, and three different fluids. Tool wear was measured by the amount of tool edge recession and wear volume, and subsurface damage was evaluated from the damage layer thickness observed by cross-sectional transmission electron microscopy. The results (within the limits of these experiments) shows that a large DOC produced the lowest SSD and tool wear; feedrate had a conflicting effect on the tool wear and SSD; skew angle also had a conflicting effect on SSD for two crystallographic orientations, [100] and [110]; the third cutting fluid had a significant effect on SSD; a high cutting speed did not affect SSD but shown to reduce tool wear.

## Introduction

Manufacturing of large, precision contoured single crystal silicon optics obviously requires machining of large surface areas. Diamond turning of the large surface areas poses a fundamental obstacle, since wear of the single point diamond tool dominates profiling errors and surface roughness as the cutting distance increases. The increased tool wear may also induce an increasing trend of surface and subsurface damage as the cutting distance extends.

Most of the literature on silicon diamond turning were concerned with ductile mode of material removal process in relatively short cutting distance and the related and subsurface damage in small optics[1-7]. Thus, it was decided to survey fundamental machining parameters and assess their influence on the tool wear and nature and extent of subsurface damage in long distance cutting associated with diamond turning of large silicon optics. The machining process input parameters to be surveyed were surface. The output parameters measured from the cutting experiments include tool wear, surface finish, and subsurface damage (SSD) along [100] and [110] orientations.

To select the experimental matrix, we used experimental design technique[8, 9]. The full factorial design requires 192 total experiments (considering two settings for depth-of-cut (DOC), feed rate, surface speed, tool radius, tool rake and tool skew, and three different fluids). Using experimental design techniques, we selected an optimal subset of 14 tests from the full factorial. In this subset of 14 experiments, more than one parameter was varied during each experiment in such a way that allowed for optimum analysis of the results from a statistical viewpoint. Using statistical techniques such as the correlation coefficient, residual mean squared error, and Mallows Cp statistic[9], we were able to determine which parameters affected tool wear, subsurface damage and surface finish within the tested parameter space. Once the influential parameters were identified, a response surface methodology[9] could be used to design a reasonable number of experiments to determine a predictive model.

## Experimental Procedure

**Turning tests:** A large single crystal silicon boule (CZP (100), 143.5 mm in diameter, and 254 mm in length) was prepared in damage-free condition by grinding, etching and diamond turning. Small witness samples of 25.4 mm in diameter and 6.35 mm thickness were prepared using a similar procedure. The axis of each witness sample was along the [100] direction, same as the boule's axis. 14 survey turning tests were performed on the boule using a preselected set of input parameters for each test as listed in Table 1. DOC and feedrate were adjusted such that the material removal occurred in ductile cutting rather than brittle fracture mode as suggested in the earlier studies[1-4]. After seven survey tests, the boule was re-prepared for the remaining seven tests by going through the grinding, etching and diamond turning sequence. Each survey test consisted of diamond turning of a 25.4 mm wide band around the boule first and then cutting two witness samples along [100] and [110] direction on each sample. The cutting of witness samples was performed to create a small diamond turned surface on the cylindrical surface of each witness sample and use them as samples for evaluation of surface and subsurface damages. Diamond turning required for the boule preparation and survey tests was all performed using the DTM II machine at the Lawrence Livermore National Laboratory (LLNL), the machine tool characteristics of which is similar to the LLNL's PERL machine[10]. Four diamond tools were used for the survey tests. The nose radius was 1.524 mm (0.060 inch) for two of the four tools and 0.762 mm (0.030 inch) for the other two. One of the two tools having identical nose radius was processed to have a built-in negative rake angle of -40°. After each survey test, the tool was resharpened for the later tests. Three cutting fluids used were (i) polyalkaline glycol (pg), (ii) a solution of polyalkaline glycol and water (pgw) and (iii) a solution of polyalkaline glycol, water, and tri-potassium phosphate (pgwp).

Table 1: Cutting parameters used in the survey tests

| *Exp. #* | *Cutting speed m/sec* | *Feed rate μ/rev* | *DOC μm* | *Nose radius mm* | *Rake angle degree* | *Skew angle degree* | *Cutting Fluid** | *Uncut chip thickness μm* | *Cutting time hr* | *Track length km* | *Material removed $mm^3$* | *Material removal rate, $10^{-3}$ $mm^3$/sec* |
|---|---|---|---|---|---|---|---|---|---|---|---|---|
| 1 | 3.81 | 1.27 | 5.08 | 1.52 | 0 | 0 | pg | 0.104 | 0.65 | 8.85 | 57.0 | 24.58 |
| 2 | 0.51 | 3.05 | 5.08 | 1.52 | -40 | 0 | pg | 0.218 | 2.02 | 3.69 | 57.0 | 7.87 |
| 3 | 0.51 | 3.05 | 1.02 | 0.76 | 0 | 40 | pg | 0.205 | 2.02 | 3.69 | 11.5 | 1.58 |
| 4 | 3.81 | 1.27 | 1.02 | 1.52 | 0 | 40 | pg | 0.065 | 0.65 | 8.85 | 11.5 | 4.92 |
| 5 | 0.51 | 1.27 | 1.02 | 0.76 | -40 | 40 | pg | 0.075 | 4.85 | 8.85 | 11.5 | 0.66 |
| 6 | 0.51 | 3.05 | 5.08 | 0.76 | 0 | 0 | pgw | 0.352 | 2.02 | 3.69 | 57.0 | 7.87 |
| 7 | 3.81 | 3.05 | 1.02 | 0.76 | -40 | 0 | pgw | 0.138 | 0.27 | 3.69 | 11.5 | 11.80 |
| 8 | 0.51 | 1.27 | 1.02 | 0.76 | 0 | 40 | pgw | 0.086 | 4.85 | 8.85 | 11.5 | 0.66 |
| 9 | 3.81 | 3.05 | 5.08 | 1.52 | 0 | 40 | pgw | 0.325 | 0.27 | 3.69 | 57.0 | 58.99 |
| 10 | 0.51 | 1.27 | 5.08 | 1.52 | -40 | 0 | pgw | 0.090 | 4.85 | 8.85 | 55.4 | 3.28 |
| 11 | 3.81 | 1.27 | 5.08 | 0.76 | 0 | 0 | pgwp | 0.147 | 0.65 | 8.85 | 57.0 | 24.58 |
| 12 | 0.51 | 1.27 | 1.02 | 1.52 | -40 | 0 | pgwp | 0.040 | 4.85 | 8.85 | 11.5 | 0.66 |
| 13 | 0.51 | 3.05 | 1.02 | 1.52 | 0 | 40 | pgwp | 0.145 | 2.02 | 3.69 | 11.5 | 1.58 |
| 14 | 3.81 | 3.05 | 5.08 | 0.76 | -40 | 40 | pgwp | 0.402 | 0.27 | 3.69 | 57.0 | 58.99 |

*pg: polyalkaline glycol; pgw: pg+water ; pgwp: pgw+ tri-potassium phosphate

**Evaluation of Tool Wear, Surface and Subsurface Damage:** Tool wear was measured by using the tool setting station mounted on the DTM II, which was equipped with an air bearing LVDT (linear voltage displacement transducer) probe. The probe swept around the nose of the

rotating tool. By taking the difference between the nose sweep data before and after each survey test, the tool nose recess due to wear could be measured. By superposing the difference on the initial tool nose profile, one could visualize the tool wear on the nose. Tool wear volume was obtained from calculating the volume between the wear land on the clearance face and the initial tool surface. The wear pattern was also examined using an optical microscope (OM) and scanning electron microscope (SEM). Surface finish of witness samples was inspected using a ZYGO laser interferometer. Surface quality and subsurface damage depth of the boule and witness samples were evaluated using interferometry, OM, SEM and transmission electron microscopy (TEM) techniques. Degree of surface damages was evaluated and ranked from the OM photographs taken from the representative areas of the surface damages. For TEM, the witness samples were sectioned transverse to the cutting direction so that the subsurface damage along the feed direction could be viewed and measured. Depth of the subsurface damage was measured directly from the TEM photographs.

## Results

**Experimental Test Results**: Results of measurement of the tool wear, surface damage, depth of SSD, and surface finish are listed in Table 2. Tool wear measurement and SEM of the used tools showed gradual and smooth tool edge recess wear and no fracture or breakage. TEM photograph in Fig. 1 shows SSD pattern developed in the [110] witness sample during the survey test #5. The damage layer is consisted of a thin amorphous layer[5] on the surface and underlying highly dislocated layer[5-7], which indicates that the diamond turning removed the material in a ductile cutting mode. The amorphous and dislocated layers shows a periodicity of 1.3 μm, reflecting the influence of the feedrate employed in the test.

Table 2: Summary of tool wear, subsurface damage and surface finish measurements

| *Exp #* | *Tool wear (edge recess) μm* | *Tool wear (volume) $\mu m^3$* | *Surface damage ranking (110)* | *Surface damage ranking (100)* | *Subsurface damage [110] μm* | *Subsurface damage [100] μm* | *RMS surface finish [110] nm* | *RMS surface finish [100] nm* |
|---|---|---|---|---|---|---|---|---|
| 1 | 0.64 | 78.31 | 13 | - | 0.45 | - | 6.65 | - |
| 2 | 0.17 | 3.95 | 1 | - | 0.10 | - | 8.05 | - |
| 3 | 0.50 | 29.17 | 8 | - | 1.35 | - | 8.20 | - |
| 4 | 0.32 | 14.13 | 6 | 7 | 2.20 | 0.80 | 13.56 | 5.41 |
| 5 | 0.61 | 71.32 | 1 | 5 | 2.30 | 0.60 | 16.38 | 10.16 |
| 6 | 0.23 | 4.46 | 2 | 9 | 0.30 | 0.75 | 6.38 | 5.61 |
| 7 | 0.07 | 0.28 | 5 | 3 | 0.90 | 0.90 | 17.78 | 24.18 |
| 8 | 0.77 | 89.24 | 1 | 5 | 1.00 | 1.00 | 12.50 | 16.87 |
| 9 | 0.14 | 1.74 | 2 | 4 | 0.90 | 0.50 | 9.02 | 12.01 |
| 10 | 0.13 | 2.02 | 14 | 15 | 1.60 | 0.80 | 2.54 | 1.57 |
| 11 | 0.44 | 21.94 | 16 | 17 | 5.00 | 5.00 | 5.28 | 9.42 |
| 12 | 0.52 | 60.78 | 11 | 13 | 5.00 | 2.00 | 227.94 | 138.58 |
| 13 | 0.43 | 28.84 | 18 | 18 | 1.00 | 1.00 | 37.95 | 71.35 |
| 14 | 0.11 | 1.03 | 12 | 10 | 0.60 | 0.50 | 24.44 | 20.50 |

Table 2 shows that cutting fluid #3 containing tri-potassium phosphate generated the highest level of surface damages, SSDs and the roughest surface finish. The surface finish variations of samples machined using fluids #1 and #2 were very small. It appears that the material removal by ductile cutting mode was achieved in those samples. SSD for the [110] orientation seems to be deeper than for the [100] orientation. Except a few cases of samples machined using the fluid #3,

samples with high surface damage rankings seem to show thinner subsurface damage layer. This may simply reflect that material removal by brittle fracture would not deform the subsurface layer. On the other hand, the material removal by ductile cutting will involve plastic deformation of the surface and subsurface to a large depth.

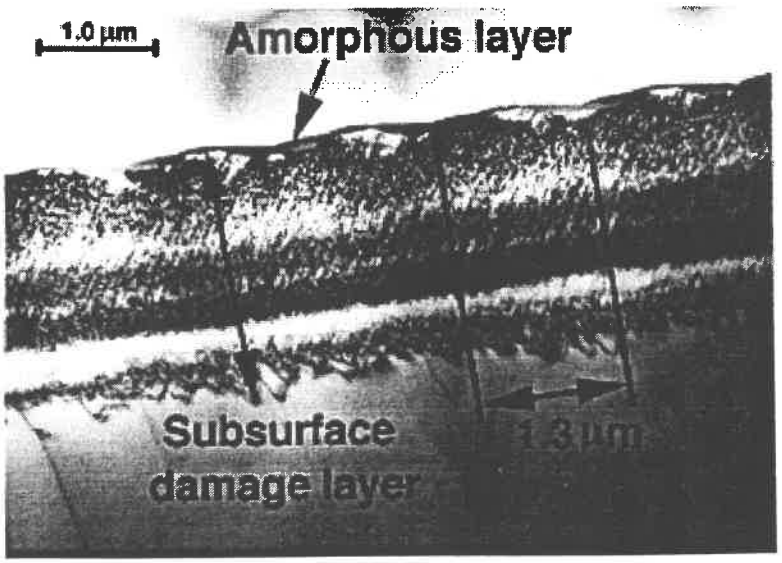


Fig. 1. TEM of [110] witness sample from survey test #5 showing subsurface damage structure.

## Statistical Analysis

Mallow's Cp statistic and the correlation coefficient method[8,9] was used to determine which parameters were significant. In general, there are two methods for selecting optimum models using the Cp statistic. The first approach dictates that we select the model with the minimum value for Cp, while the second approach dictates that we select the model with the Cp value that is closest to the number of terms. We also considered the adjusted $R^2$ statistic. The $R^2$ statistic, or the coefficient of multiple determination, is the square of the correlation between the measured values and the model estimated values normalized to fall between zero and one. When the number of terms in the model equal the number of measurements used to fit the model, the $R^2$ statistic will exactly equal one. As terms are added, the $R^2$ statistic (approximately) asymptotically approaches one. Alternatively, we have selected to use the adjusted $R^2$ statistic, where an adjustment has been made to the $R^2$ statistic to account for varying degrees of freedom. The adjusted $R^2$ statistic for the optimum model begins to approach one.

We considered the full model to be a linear function of the parameters

$$y = a_1 \cdot V + a_2 \cdot f_R + a_3 \cdot d_C + a_4 \cdot R_N + a_5 \cdot \alpha_R + a_6 \cdot \alpha_S + a_7 \cdot f_L \qquad (1)$$

where the output variable y was either sub-surface damage, surface finish, or tool wear normalized to track length. The $a_i$'s are the fitted coefficients for each term, and the symbols, V, $f_R$, $d_C$, $R_N$, $\alpha_R$, $\alpha_S$, and $f_L$ in the equation correspond to cutting speed, feedrate, DOC, tool nose radius, rake angle, skew angle, and cutting fluid, respectively. The range of values for these parameters are given in Table 1. Then, using the Cp statistic and the adjusted $R^2$ statistic along with engineering judgment, the subset model was selected.

With the exception of survey tests using the fluid #3, the surface finish variations were very small. Since the peak-to-valley surface finishes were smaller than the depth of SSD, the surface finish errors should be removed by the post-turning polishing process to remove SSD. Therefore, it was determined that surface finish was not a critical parameter and the diamond turning process should be optimized through observation of tool wear and SSD. Since the SSD and surface finish obtained from using fluid #3 were so drastically different from the other two fluids, it was difficult to develop a simple model that could describe all three fluids. Thus, the data from the four survey tests using fluid #3 were omitted for the analysis of sub-surface damage.

**Subsurface damage**: Definite differences was observed between the SSD for each orientation. as shown in Table 2. We therefore decided to model the two crystallographic orientations separately.

*[110] orientation*:: The optimum model with minimum Cp and Cp closest to the number of terms is the model with two terms, skew and depth of cut according to the Cp criteria. According to the adjusted $R^2$ statistic, the "best" model is either the three or four term model. Considering all these results and engineering judgment, we have selected the model containing three terms (skew angle, depth of cut, and feed rate) as the "best" model. A rapid feed rate, large DOC, and 0° skew angle produce the minimum SSD for orientation [110]. The remaining parameters, velocity, tool radius, rake angle, and fluid, do not significantly contribute to sub-surface damage.

*[100] orientation*:: Due to a set-up error, three data points for the SSD of orientation [100] are missing. Furthermore, it was decided to omit the results using Fluid #3 as explained above. With only seven data points, and the assumption that the same parameters were significant for [100] as those for [110], a similar relationship with an exception of the skew angle dependence between the previously determined parameters and the SSD was obtained. An important observation from this analysis is that the optimum skew angle may be different depending on the crystallographic orientation. In most turning operations, all crystallographic orientations will be machined and therefore the skew angle should be optimized to minimize the total SSD on all orientations. Furthermore, if we were to include one more parameter in the model, the next most significant parameter is rake angle. Similarly, to minimize SSD on [110], a 0° rake should be chosen, while a 40° negative rake should be chosen for [100]. These differences support the need for further investigation.

**Tool wear:** Since a drastic difference in tool wear was not observed for the different fluids as in SSD, all data, including data from experiments using Fluid #3, were used in the analysis. The experiments were designed so that each experiment removed an equal area of material. In that sense, the tool wear measurements were normalized to area, but normalizing the tool wear to track length rather than area was found to be more representative. According to the Cp criteria, the optimum model with minimum Cp and Cp closest to the number of terms is the model with two terms including velocity and rake angle. According to the adjusted $R^2$ statistic, the "best" model is either the two or three term model. Considering all these results and engineering judgment, we have selected the model containing three terms (velocity, depth of cut, and rake) as the "best" model. A rapid surface velocity, large DOC, and negative 40° rake angle produce the minimum SSD. The remaining parameters, feed rate, tool radius, skew angle, and fluid, do not significantly contribute to tool wear. However, a further analysis shows that a high cutting speed, low feedrate, negative rake and fluid #2 minimize the log of the tool wear volume normalized to the track-length, i.e. log(tool wear)/track length, indicating that feedrate has some impact.

## Concluding Remarks

Table 3 summarizes the significant cutting parameters affecting tool wear and SSD. The entry 'High' indicates that a large value for that parameter is beneficial, while the entry 'Low' indicates that a small value for that parameter is beneficial. The '1' and '2' entry for fluid #1 (polyalkaline glycol) and #2 a solution of polyalkaline glycol and water. Note that fluid #3, a solution of polyalkaline glycol, water, and tri-potassium phosphate, will not produce acceptable SSD. The results shows that a large DOC (within the limits of these experiments) produces the lowest SSD and tool wear. Feedrate may have a conflicting effects on the tool wear and SSD. None of the other parameters were significant for both tool wear and SSD. For SSD, there may be conflicting settings for the two crystallographic orientation for skew angle, although this result needs further investigation. These results are positive in the sense that a high velocity, and large depth of cut lead to shorter machining time.

The purpose of these screening experiments was to identify the cutting parameters that significantly affect the sub-surface damage and tool wear. These results cannot be extrapolated beyond the range of the experiments, nor can the fitted models be expected to perform within the extremes of the settings. The simple model chosen here assumed a linear fit between the extremes of the settings, and any experiments between the extremes have yet to be done. Since the effect may not be linear, the optimum setting may exist between the two extremes.

Table 3: Summary of Results

| *Parameter* | *Tool Wear* | *SSD [110]* | *SSD [100]* |
|---|---|---|---|
| Cutting Speed | High | --- | --- |
| Feedrate | Low | High | High |
| DOC | High | High | High |
| Tool nose radius | --- | --- | --- |
| Rake angle | High (negative) | --- | --- |
| Skew angle | --- | Low | High |
| Cutting fluid | --- | 1 or 2 | 1 or 2 |

Diamond turning of large optics will require significantly longer machining time. For the longer track length operations, the significant parameters will remain the same. However, the fitted models will not provide accurate predictions of tool wear and SSD as the track length is extended beyond the limits of the screening experiments. Therefore, the long track follow-on experiments should be performed to generate information that relates the increasing tool wear to SSD beyond the range of the screening experiments.

**Acknowledgment:**

This work was performed under the auspices of the U.S. Department of Energy by the Lawrence Livermore National Laboratory under Contract No. W-7405-ENG-48.

## References

1. C. K.Syn, J. S. Taylor, R. R. Donaldson, and S. Shimada, *Proc. JSPE 1988 Spring Meeting, Kawasaki, Japan, pp. 781-782.*
2. P. N. Blake and R. O. Scattergood, *J Am Ceram Soc, 1990, 73, 949-957.*
3. W. S. Blackley and R. O. Scattergood, *Prec Eng, 1991, 13, 95-103.*
4. M. Daito, A, Kanai, and M. Miyashita, *Int'l Progress in Precision Eng., eds. M. Bonis et al., Elsevier, pp. 331-334.*
5. T. Shibata, S. Fujii, E. Makino, and M. Ikeda, *Prec Eng, 1996, 18, 129-137.*
6. K. E. Puttick, L. C. Whitmore, C. L. Chao, and A. E. Gee, *Phil Mag A, 1994, 69, 91-103.*
7. R. R. Kunz, H. R. Clark, P. M. Nitishin, and M. Rothschild, *J Mater Res, 1996, 11, 1228-1237.*
8. G. E. P. Box, W. G. Hunter, and J. S. Hunter, *Statistics for Experimenters*, New York: John Wily & Sons, 1978.
9. N. R. Draper and H. Smith, *Applied Regression Analysis, 2nd Ed.*, New York: John Wily & Sons, 1981.
10. R. R. Donaldson and D. C. Thompson, *Annals CIRP, 1986, 35 (1).*

# COST EFFECTIVE EDGE MACHINING OF SILICON WAFERS TO MINIMISE THE POLISHING PROCESS

**M.J. Ball, K. Carlisle, M.A. Stocker**
Cranfield Precision (Division of Landis Lund, a UNOVA Company), Cranfield, Bedford, UK

## Introduction

The current move to 300mm silicon wafer technology presents new technical challenges at all stages of the integrated circuit fabrication process. The quality of prime wafers is of great importance, and here we describe recent work at Cranfield on an edge grinding process with the potential to dramatically reduce the need for subsequent edge polishing and etching in prime wafer production.

Wafer edge quality must be of the highest order to withstand damage from handling. Any chipping of the edge, no matter how small, will contaminate the process and could cause irreversible damage to the integrated circuitry during subsequent fabrication stages. Rapid Thermal Processing (RTP) can also cause pre-existing microscopic cracks from the grinding process to propagate as the wafer rapidly undergoes large temperature changes during deposition stages; sometimes resulting in total wafer breakage.

Generically speaking, current silicon wafer edge processing begins with fixed abrasive grinding using metal bonded diamond wheels to rough grind the diameter, orientation flat or notch, to the required size and edge form. This process produces a surface roughness of between 300 to 400nm RMS with 20μm, or more, sub-surface microcrack damage. Etching and free abrasive edge polishing is then used to remove the damaged layer, producing 2 to 5 nm RMS surface roughness. Since etching and polishing are time consuming, costly and have negative environmental implications, wafer manufacturers are looking for ways to reduce or eliminate these two processes. Whatever the solution, it should satisfy the goals of higher yield and lower cost.

Based on these requirements, and previous work at Cranfield which investigated the "ductile regime" grinding of brittle materials [1] , a machine and process have been developed to edge grind 200mm and 300mm silicon wafers.

## Machine Configuration

The Cranfield Precision Silicon Wafer Edge Grinder has been designed with the aid of finite element analysis to create a machine with high stiffness to weight ratio and good damping of parasitic structural vibrational modes. These characteristics are required to control the interaction between wheel and workpiece to a level compatible with high quality, low damage grinding.

Three air bearing spindles are mounted horizontally on the machine; workhead spindle, O/D grinding spindle and high speed notch grinding spindle. The O/D and notch grinding wheel spindles are mounted opposite to, and on either side of the workhead axis. Both are configured to feed in a radial direction, towards the workhead axis.

Wafers are transferred from the load station by robot handler and placed on an automated inspection station. Each wafer is centered, the orientation mark (notch or flat) located, and then transferred to the workhead vacuum chuck. The wafer's outside diameter is ground in a plunge mode using grooved peripheral O/D wheels (the wheel grooves having been previously formed on the machine to the required wafer edge profile). From the standoff position, a rapid search feedrate is used until an acoustic touch sensor detects contact between wheel and workpiece. Only then is a change to the slower grinding feedrate triggered, thus helping to reduce overall cycle time.

The same grooved O/D wheels are used to grind the orientation flat. A 4mm diameter wheel is used to grind the notch, and is grooved in the same manner as the O/D wheels. The wheel groove diameter is made small enough to allow generation of the required notch bottom radius. Either orientation flat or notch are ground in a contour creep feed mode, with the workhead and grinding wheel axes slaved together by CNC, in order to generate the required geometrical form.

After grinding, the wafer is returned to the inspection station where edge profile form accuracy and centering are measured, together with notch or orientation flat geometry.

Wheel conditioning and geometrical control of the cross-sectional edge profile is maintained through the use of a periodic in-situ wheel re-forming process. The forming interval is determined by the degradation in wafer edge profile, and quality of surface finish.

**The Grinding Process**

The O/D grinding process can be broken down into discrete grinding stages, from roughing to final finishing. The number of stages used depends upon the amount of material to be removed and quality of surface to be obtained. For the purposes of this paper, we shall look at a 3-stage process.

A typical three stage grinding process for incoming wafers with a square edge profile would be as follows:

1) Rough grind: Using a large grit size, the wafer is ground to approximately 0.3mm oversize on diameter. This stage is used for major stock removal and, generates a near net shape edge profile from the incoming wafer's square edges.

2) Semi-finish grind: Using an intermediate grit size, a further 0.2mm of material is removed from the diameter. This stage is intended to remove material efficiently,

without creating significant sub-surface damage, whilst at the same time further refining the edge profile to minimise uneven wear on the finish grinding wheel

3) Finish grind: Using a small grit size, approximately 0.1mm of material is removed on diameter to bring the wafer to target size, and generate the final surface.

Each of the three grinding stages produces a progressively smoother surface with consequently less sub-surface damage.

**Results**

Surface quality has been measured in terms of surface roughness and sub-surface damage. Surface roughness has been measured using the Rank Taylor Hobson Form Talysurf (Gaussian filter, 12*0.08mm cutoffs).

Sub-surface damage (SSD) in the form of micro-cracks has been assessed by Cranfield University using polishing and etching techniques [2] . A small segment of wafer is taken and mounted vertically in resin. The sample is lapped and polished so as to generate a flat (chord) on the wafer edge. An etch is used to reveal any micro-cracks which are then measured using an optical microscope. This method of polishing a chord along the wafer edge, serves to magnify any sub-surface microcracks by typically up to 30× for ease of observation. With knowledge of the original wafer diameter and the polished chord length, the true damage depth (perpendicular to the wafer edge) can be calculated.

Figures 1 to 3 show the sub-surface damage revealed by this technique for each of the three O/D grinding stages. One can clearly see the micro-cracks produced during rough and semi-finish grind (fig.1, & fig.2, respectively). Scale: 80μm ⊢——⊣

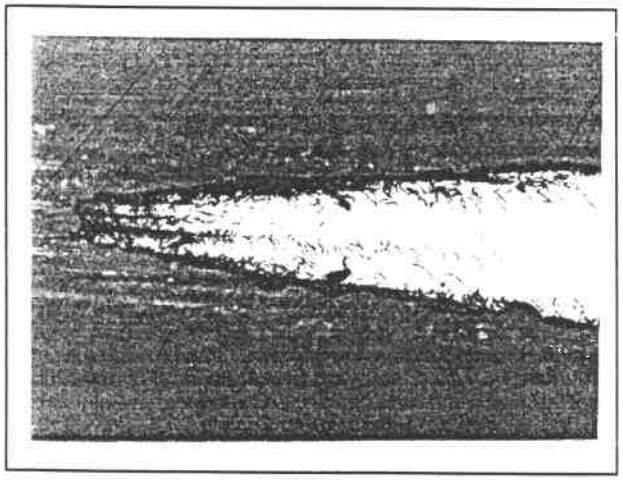

Fig1. Micrograph of SSD produced by ROUGH grinding

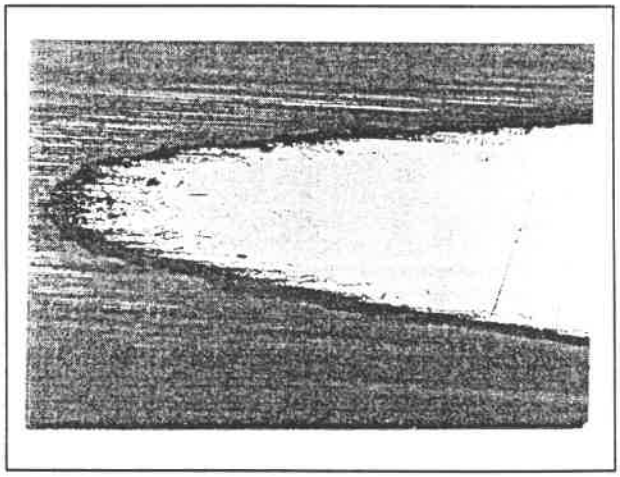

Fig2. Micrograph of SSD produced by SEMI-FINISH grinding

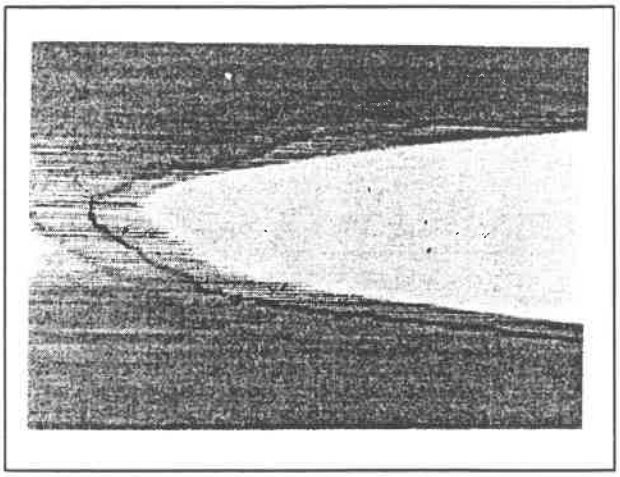

Fig3. Micrograph of SSD produced by FINISH grinding

Scale: 80μm ⊢——⊣

Figure 4. shows the relationship between sub-surface damage and surface roughness for a number of samples. The spread of roughness values was created by using a range of feedrates for each stage. Surface roughness for typical process feedrates is ~750nm RMS (roughing), ~200nm RMS (semi-finishing), and ~20-80nm RMS (finishing). As expected, the general trend is for increased sub-surface damage with increased roughness. Minimum sub-surface damage observed for the finish stage is typically <2μm.

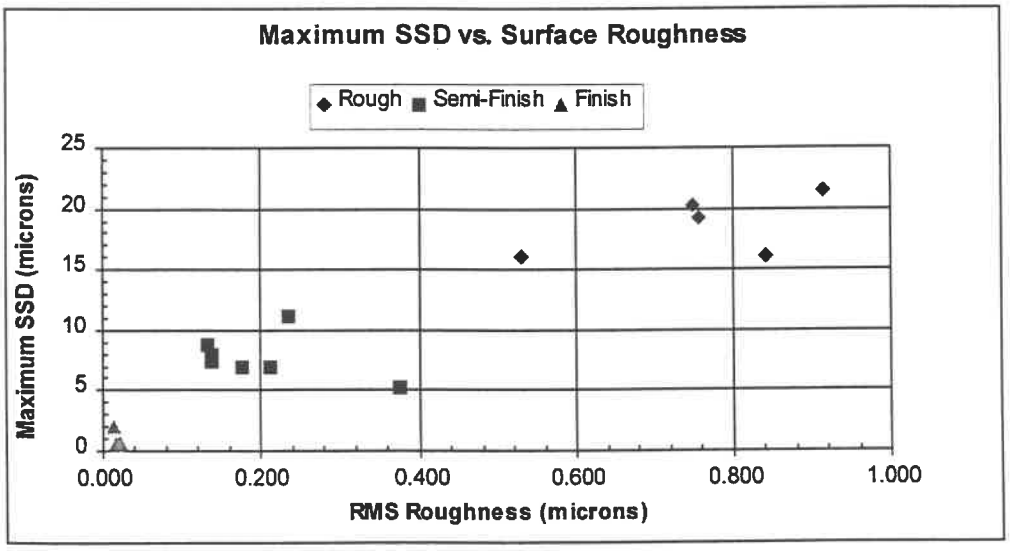


Fig 4. Relationship between SSD and surface roughness

Using the 3-stage O/D process, and including notch or flat grinding, cassette-to-cassette cycle times of approximately 180 seconds and 270 seconds have been achieved for 200mm and 300mm wafers respectively.

## Conclusions

The process described above, when implemented on the Cranfield Precision Silicon Wafer Edge Grinder, is capable of producing a high quality ground surface of 20-80nm RMS with typically <2μm sub-surface damage, with a reasonable throughput. This improved ground surface quality helps to reduce the requirement for further etching and polishing stages, thereby giving the potential for cost savings and a more environmentally compatible prime wafer fabrication process.

## References


[1] Carlisle.K, McKeown.P, Shore.P, Wills-Moren.W.J, "Ductile regime grinding of glass and other brittle materials by the use of ultra-stiff machine tools".

[2] SSD assessments were performed by Dr. Sue Impey & Mr A. Dyer, School of Industrial and Manufacturing Science, Cranfield University, U.K.

# Ductile to brittle transition investigated by plunge-cut experiments in monocrystalline silicon

Brinksmeier, E.; Preuß, W.; Riemer, O.; Malz, R.
Labor für Mikrozerspanung, Universität Bremen

## 1 Introduction

We have derived experimental data on the ductile to brittle transition from well defined cutting experiments using an inclined plunge-cut method [1] with continuously increasing uncut chip thickness (fig.1).

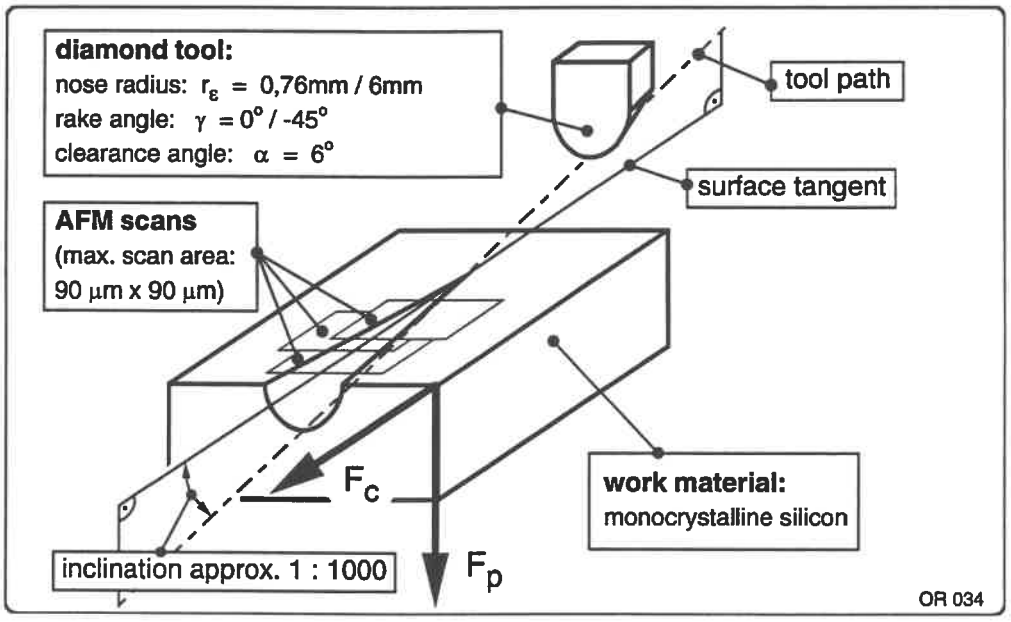


**Fig. 1:** Principle of plunge-cut experiments.

The plunge-cut experiments were performed on a Moore M18 Aspheric Generator at a constant cutting speed of 20 mm/min. We used four different diamond tools with nose radii of 6 mm and 0.76 mm and rake angles of 0° and -45°, respectively. The samples were diamond turned with a surface finish < 3 nm rms. The selected cutting directions were <100> on a {100}-surface and <22$\bar{1}$> on a {111}-surface. The crystallographic orientation was determined from Laue diagrams. In order to assure reproducibility, each plunge-cut was repeated three times.

## 2 Experimental results

The cutting forces were recorded with a Kistler 9251A piezo electric transducer. The groove topography was investigated with a Nomarski microscope and a Nanoscope III atomic force microscope. Although the details of ductile to brittle transition strongly depend on tool radius, rake angle and cutting direction, a general pattern was found comprising four regimes of material response. This pattern is shown schematically in the upper part of fig. 2. The first regime is governed by elastic response, identified by a steady increase of thrust force without any trace of damage detectable by Nomarski or atomic force microscopy. In the second regime, plastic deformation takes place, resulting in a change of interference contrast without change of topography. The third regime is characterized by ductile material removal, while the fourth regime is dominated by brittle fracture. The lower part of fig. 2 shows a typical force signal vs. cutting time.

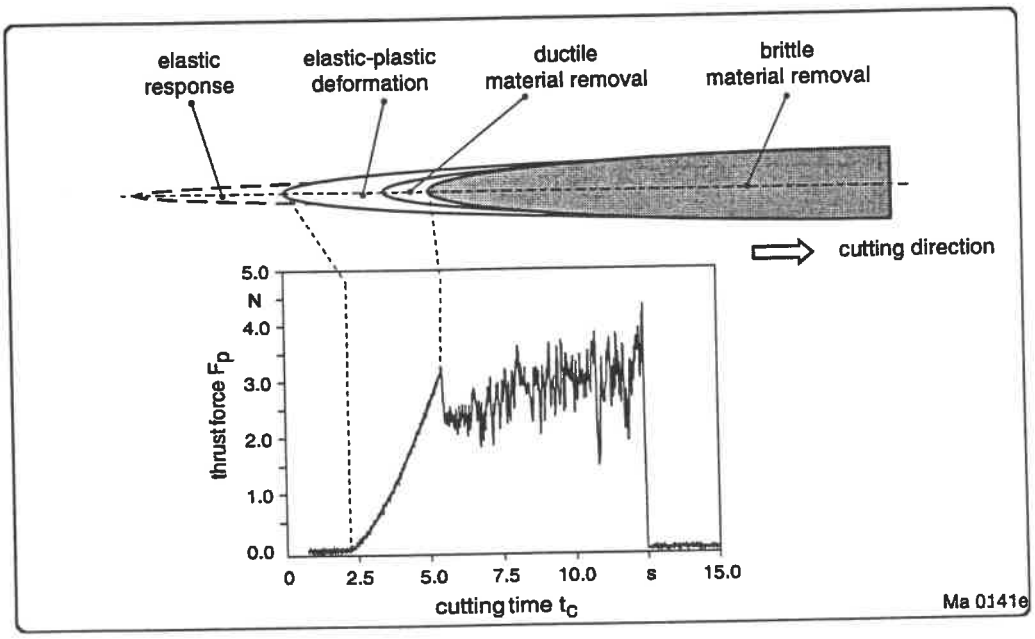


**Fig. 2:** Thrust force $F_p$ related to the four different regimes of material response.

Nomarski photographs of plunge-cut grooves obtained with negative rake tools along different crystallographic directions are shown in fig. 3. The values of the critical cutting and thrust forces, corresponding to the beginning of crack formation, are also indicated in fig. 3. Obviously, the {111}-surface is more susceptable to crack formation than the {100}-surface. The ductile mode is also favoured by a large tool nose radius. Note, that in the case of negative rake tools, there is a continuous transition from the ductile to the brittle mode.

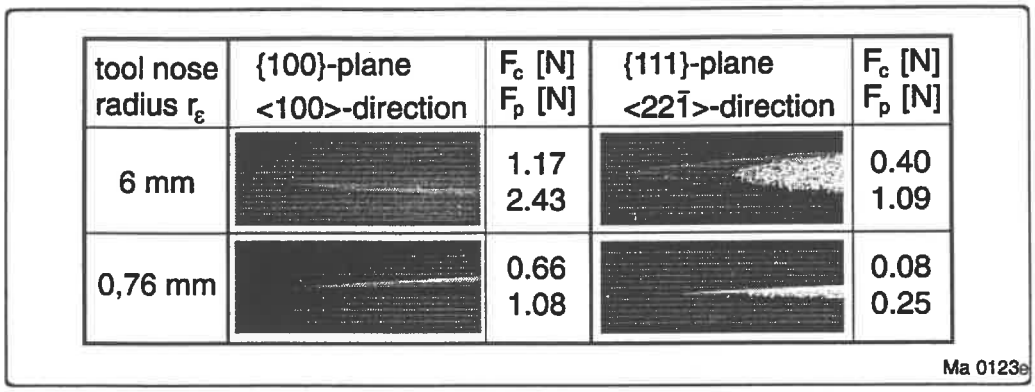


**Fig. 3:** Comparison of groove topography and critical cutting and thrust forces for two different crystallographic orientations and two different tool nose radii. Rake angle: $\gamma = -45^\circ$.

Generally, critical process forces are larger on the {100}-surface than on the {111}-surface. Moreover, critical thrust forces exceed critical cutting forces by a factor of two to three (cf. fig. 4).

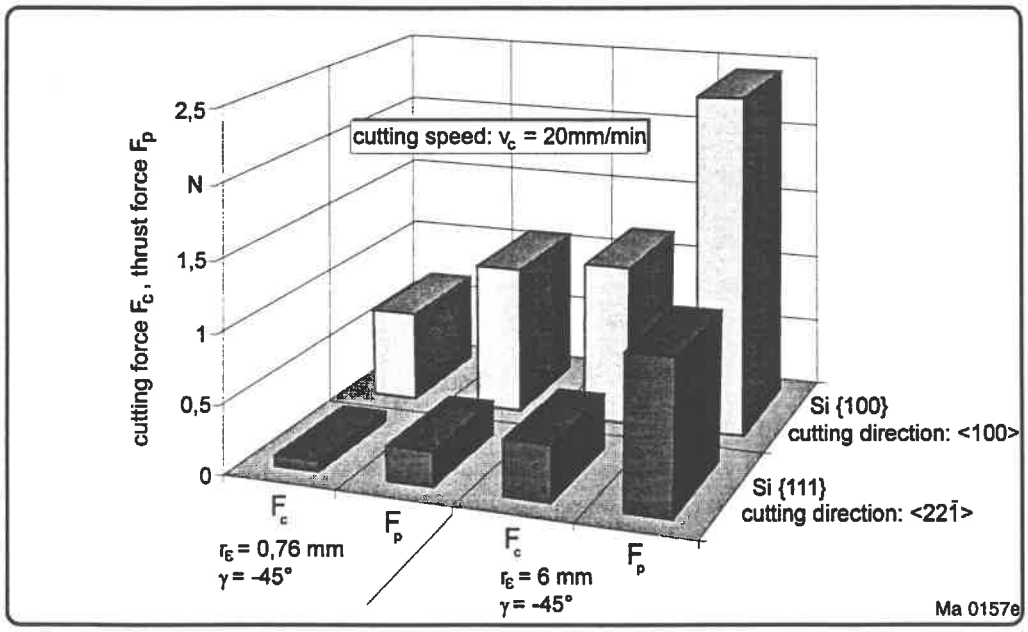


**Fig. 4:** Critical process forces at the beginning of the brittle zone.

AFM-images of the groove topography generated by a zero degree rake tool are shown in fig. 5. In contrast to negative rake tools, the transition from ductile to brittle material removal takes place almost instantaneously across the full width of the plunge-cut groove.

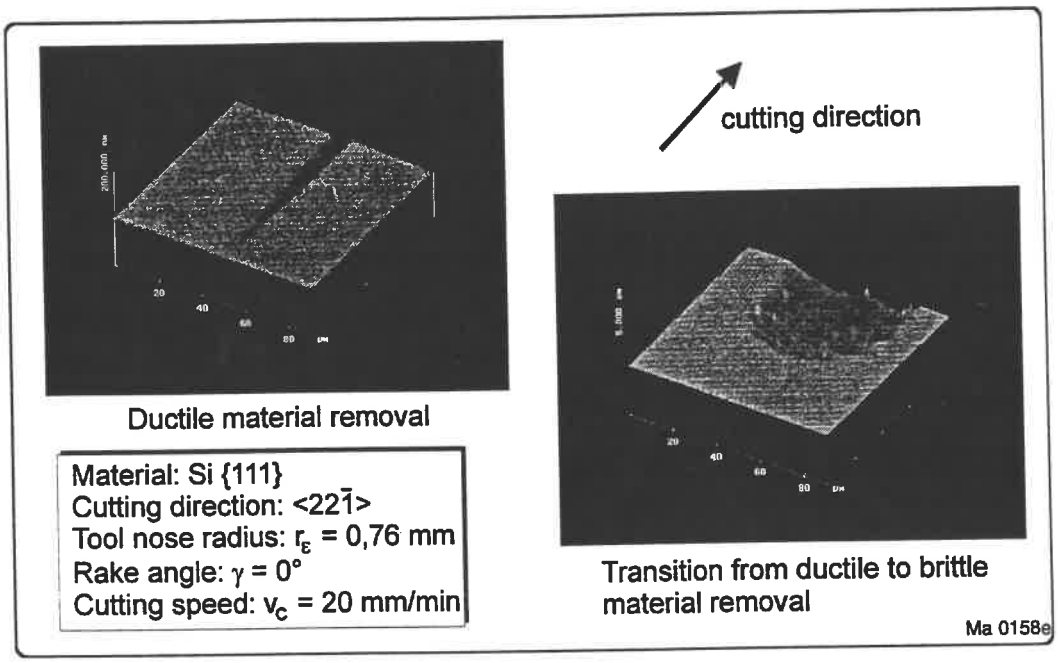
cutting direction
Ductile material removal
Material: Si {111}
Cutting direction: <22$\bar{1}$>
Tool nose radius: $r_\varepsilon$ = 0,76 mm
Rake angle: $\gamma$ = 0°
Cutting speed: $v_c$ = 20 mm/min
Transition from ductile to brittle material removal
Ma 0158e

**Fig. 5:** AFM-images of the groove topography generated by using a zero degree rake tool.

## 3 Conclusion

Inclined plunge-cut experiments in monocrystalline silicon performed with different diamond tools yield four regimes of material response. The characteristics of ductile to brittle transition strongly depend on material crystallographic orientation [2] and on the rake angle of the cutting tool. An explanation for the dependence on rake angle has been given by Blackley and Scattergood [3]. While tensile stresses behind the cutting edge are supposed to induce crack formation when zero degree rake tools are used, shear stresses and compressive stresses built up in front of the cutting edge dominate brittle material removal in the case of negative rake tools.

## References

[1] Brinksmeier, E.; W. Preuß; O. Riemer. "From Friction to Chip Removal. An Experimental Investigation of the Microcutting Process. Part I". Proceedings of the 3rd International Conference on Ultraprecision in Manufacturing Engineering, Aachen, Germany, May 1994: p. 393-400.

[2] Shibata, T.; S. Fujii; E. Makino; M. Ikeda. "Ductile-regime turning mechanism of single-crystal silicon." Precision Engineering, April/May 1996 Vol 18 No 2/3: p. 129-137.

[3] Blackley, W.S.; R.O. Scattergood. "Chip Topography for Ductile Regime Machining of Germanium". Trans. of the ASME, J. Eng. Ind., May 1994, Vol. 116: p. 263-266.

# Cutting Fluid Study for Single Crystal Silicon†

David Chargin‡
Lawrence Livermore National Laboratory
Livermore, CA

**Summary:**
An empirical study was conducted to evaluate cutting fluids for Single Point Diamond Turning (SPDT) of single crystal silicon. The pH of distilled water was adjusted with various additives to examine the effect of pH on cutting operations. Fluids which seemed to promote ductile cutting appeared to increase tool wear as well, an undesirable tradeoff. High pH sodium hydroxide solutions showed promise for further research, as they yielded the best combination of reduced tool wear and good surface finish in the ductile regime. Negative rake tools were verified to improve the surface finish, but the negative rake tools used in the experiments also showed much higher wear than conventional 0° rake tools. Effects of crystallographic orientation on SPDT, such as star patterns of fracture damage forming near the center of the samples, were observed to decrease with lower feedrates. Silicon chips were observed and photographed, indicative of a ductile material removal process.

**Experimental Setup:**
An experimental setup was selected to evaluate cutting fluids for the SPDT of silicon in the ductile regime. All machining was performed on the PERL-2 (Precision Engineering Research Lathe) at Lawrence Livermore National Laboratory, a horizontal spindle T-base lathe with microinch precision. Tools manufactured with a 1.52mm nose radius and 0° rake angle were used for most tests, while tools provided by a different manufacturer with negative rake angles were also evaluated. Four test samples of single crystal silicon, 95mm in diameter and 12.7mm thick with surface normals in the [100] direction, were vacuum chucked in the PERL-2 machine to 380mm Hg. Cutting fluid delivery was accomplished with a tank pressurized by compressed air, pushing the fluid out a 0.254mm diameter nozzle. The cutting fluid was directed at the intersection of the tool tip and sample, adjusted so the flow was between 2-3 liters per hour. The machine is enclosed, and both the spindle and enclosure are regulated to 20 ± 0.5° C.

**Test Procedure:**
Cutting parameters for the tests were chosen based on past experience for a ductile finishing cut. No special surface preparation, i.e. chemical etching to remove micro-fracture damage, was performed between tests. It was felt that 3 roughing cuts would be sufficient to level the surface of the sample and insure a repeatable surface between final cuts. Samples were machined from the inside out, shielding the tool from slow cutting speeds near the center when it is dull at the end of the cut, the centers of each disk previously having been relieved of material.

For the initial experiments, final cut parameters included: spindle speed 1000rpm, feedrate 1.91μm/rev, and cutting depth 2.54μm. This gave a cutting distance of 3.7 km and a cutting speed of 5 m/sec at the outer edge. Roughing cuts used identical parameters but with a feedrate of 2.54μm/rev. A second set of experiments then lengthened the cutting distance in the hope of accentuating the differences in the cutting fluids. Cutting parameters were the same, with the exception of the feedrate, which was decreased to 1.27μm/rev from 1.91μm/rev. This increased the cutting distance to 5.6 km. The lower feedrate should increase the ductility of the cut, and improve the initial surface finish. Spindle speed and depth of cut remained at 1000 rpm and 2.54μm respectively, and the roughing procedure was also unchanged.

**Results:**
Cutting fluids to test were then chosen for several reasons. First, the pH of the cuttings fluids was to be varied, as it should affect the silicon dioxide layer on the surface of the silicon. The semiconductor industry has had success with using alkaline solutions in polishing silicon[3]. A surfactant was chosen to find the influence of surface tension. Several other fluids, such as 25% ethylene glycol solution, were then also tested based on reports of success at other sites.

---

†This work was performed under the auspices of the U.S. DOE by Lawrence Livermore National Laboratory, Livermore, California under Contract No. W-7405-Eng-48.
‡ Currently at the Massachusetts Institute of Technology, Cambridge, MA

Initial baseline tests were run with distilled water which was approximately pH 6.0. Three tests established the baseline roughness and wear values seen in Table 1. Further tests were then conducted to evaluate the effectiveness of various water based cutting fluids. Ammonium hydroxide was added to the water to form an alkaline solution with pH 10.0. Surface roughness ranged from equivalent to worse than baseline. Tool wear was just appreciably greater than the baseline, not giving much hope for alkaline solutions. Castrol Safety-Cool 822C, a cutting fluid additive for water, produced slightly better surface finishes than water, but with more tool wear. A surfactant, ACT-ST5, was then used to examine the effects of surface tension on cutting fluid effectiveness. Two runs conducted with this solution produced nearly identical results to the baseline distilled water. For several of these tests, a cloudy four axis pattern appeared at the centers of the samples, consistent with past experiences of machining crystals grown in the [100] direction.

A non-water based cutting fluid was then evaluated, Shell Diala Oil AX. This oil greatly increased the wear on the tool and produced a much worse surface finish. Tool wear increased to 130-250nm. Roughness values at the outer edge were nearly three times that of the baseline water, at 150 Å RMS. A second test was then run with a new nozzle on the fluid delivery system. This nozzle was 0.51mm in diameter and angled in from the feed side of the tool, making a 15° angle with the test sample. The fluid was directed in at the side of the tool/chip interface, opposite the direction of feed. This fluid delivery setup greatly reduced the tool wear, down to 64 μm. However, the surface roughness also increased considerably, to 354.5 Å RMS at the outer edge. Future tests utilized the previous delivery system.

The final test of this initial study evaluated the negative rake tools. Three tools were provided, having rakes of -1°, -15°, and -30°. The tools did demonstrate the value of negative rakes, as the surface finish did improve with the increasing negative rake. The -30° tool also did not leave any stars or other crystallographic artifacts in the test sample. However, these tools did show much more tool edge recession than the conventional tools, about 100-150nm.

The new feedrate in the second set of tests greatly increased the tool wear in the distilled water baseline, up to 280nm from the previous baseline of 20-50nm. The surface finish, however, did not improve significantly, not even near the beginning of the cut, and was worse in the outer areas. Investigation of the effect of pH continued, now with a low pH solution. A 5% solution of acetic acid (commercial grade vinegar) was used with a pH of 2.4. Other water based cutting fluids consisted of ethylene glycol, Wafermate 1000 (a propylene glycol solution used in the semiconductor industry), the ACT-ST5 surfactant, Trim Clear (a commercial cutting fluid additive), and sodium hydroxide. These solutions were all generally alkaline, with the exception of the ethylene glycol, which close to neutral. While these solutions generally did not appreciably improve the measured parameters, scattered patches of fracture damage, visible optically, were substantially reduced in the ethylene glycol, acetic acid, sodium hydroxide, and Wafermate 1000 solutions. Increases in surface roughness were appeared to be entirely attributable to feed marks.

Sodium hydroxide proved to be the most interesting cutting fluid. It was used in a 0.005% solution with a pH of 11. The first trial resulted in tool wear quite comparable to the water at 180nm, and the finish actually improved towards the outer edge, unlike any of the other tests. Further tests were run with extended baths in the cutting fluid prior to cutting. During the second test, tool wear increased to 230nm, but the surface finish improved even more, giving the best overall finish of the study. Unfortunately, during the third test, the first 20mm was machined at a higher feedrate, 2.54 μm/rev, and lower cutting speed, because of an operator error. Lower wear was expected because of the higher feedrate, but it strangely increased to the highest measured wear, 550nm.

Two interesting anomolies during testing included silicon chips and tool chatter. Curly silicon chips were observed after several cuts. These were observed and photographed through optical microscopes clinging to the test sample after the cut. These chips are indicative of the ductile cutting taking place, and varied greatly in size, which was not quantitatively measured. This difference in size is probably due to the amount of fracture taking place varying as the crystal is rotated through different orientations. Chips were probably formed in all of the final cuts, but collecting them does not appear to be a repeatable process with the horizontal spindle, as they are washed with the cutting fluid and destroyed. A chatter phenomenon of unknown origin was observed during several roughing cuts and one final cut. The chatter was audible and estimated at 17 khz from the pattern in the finished part. The spindle speed could be varied and the pitch would rise and fall with spindle speed, even if the feed was stopped. Talystep scans indicate the peak to valley measurement of the hills to be ~200nm. This chatter helps account for the high surface roughness in one ethylene glycol test.

Table 1
Test Data – 1.91µm/rev. Final Cut

| Cutting Fluid | pH | Tool Wear (nm) | Surface Roughness (Å RMS) | | | Notes |
|---|---|---|---|---|---|---|
| | | | Radius 5mm | Radius 25mm | Radius 46mm | |
| Distilled Water | 6.0 | 20 to 50 | 29.1 | 33.1 | 30.3 | star |
| Distilled Water | 6.0 | chip | 22.7 | 50.4 | 61.6 | |
| Distilled Water | 6.0 | > 50 | 16.3 | 50.9 | 51.7 | |
| Ammonium Hydroxide | 10.0 | > 50 | 37.0 | 56.8 | 96.1 | |
| Ammonium Hydroxide | 10.5 | 50 to 80 | 30.2 | 40.2 | 58.3 | |
| Castrol 822C | 9.5 | 75 | 19.2 | 34.2 | 40.5 | star |
| ACT-ST5 | 8.3 | 20 to 50 | 26.0 | 31.4 | 53.3 | star |
| ACT-ST5 | 6.0 | > 20 | 22.5 | 32.4 | 50.5 | star |
| Shell Diala Oil AX | NA | 130 to 250 | 35.0 | 105.6 | 150.2 | |
| Shell Diala Oil AX | NA | 65 | 19.8 | 108.8 | 354.5 | angled nozzle |
| Edge Tech. Tool -1° | 9.5 | 130 to 150 | 20.5 | 55.0 | 71.2 | star |
| Edge Tech tool -15° | 9.5 | 100 to 130 | 27.9 | 42.7 | 55.4 | star |
| Edge Tech tool -30° | 9.5 | 100 to 130 | 11.8 | 33.9 | 47.7 | |

Table 2
Test Data – 1.27 µm/rev. Final Cut

| Cutting Fluid | pH | Tool Wear (nm.) | Surface Roughness (Å RMS) | | | Notes |
|---|---|---|---|---|---|---|
| | | | Radius 5mm | Radius 25m | Radius 46mm | |
| Distilled Water | 6.0 | 150 | 24.9 | 26.8 | 53.1 | Si Chips |
| Distilled Water | 6.0 | 150 to 180 | 18.0 | 30.6 | 142.1 | |
| 5% Acetic Acid | 2.4 | 150 to 180 | 34.3 | 35.7 | 54.8 | |
| 5% Acetic Acid | 2.4 | 280 | 25.8 | 51.1 | 89.5 | |
| 1:200 Ethylene Glycol | 6.2 | 280 | 18.8 | 30.4 | 72.7 | Si Chips |
| 25% Ethylene Glycol | 6.3 | 230 | 18.7 | 32.0 | 163.2 | |
| 25% Ethylene Glycol | 6.2 | 250 to 280 | 47.3 | 49.8 | 563.4 | |
| Sodium Hydroxide | 10.9 | 180 | 20.0 | 64.4 | 40.9 | |
| Sodium Hydroxide | 11.0 | 230 | 33.5 | 52.5 | 32.1 | Si Chips, Best overall finish |
| Sodium Hydroxide | 11.0 | 550 | 39.1 | 51.2 | 44.5 | Si Chips in 100µin/rev region |
| 25% Wafermate 1000 | 8.7 | 250 | 27.9 | 40.8 | 55.3 | |
| ACT-ST5 | 7.8 | 240 | 23.8 | 41.9 | 58.4 | Si chips in roughing cuts |
| ACT-ST5 | 7.8 | 220 | 29.2 | 44.3 | 82.3 | |
| 1% Trim Clear | 9.5 | 150 to 180 | 45.0 | 30.2 | 60.1 | |

**Discussion and Conclusions:**

Lower feedrates reduced the effects of crystallographic orientation. Star shaped patterns and cloudy areas common to the 1.91μm/rev feedrate disappeared when the feedrate was lowered to 1.27μm/rev. This is consistent with the results produced in previous studies, which found different critical chip thicknesses for different crystal orientations. The star-shaped patterns themselves followed the 4 or 2 fold symmetry caused by the intersection of planes in a crystal grown in the [100] direction. Strangely, such patterns would be revealed during a roughing cut and sometimes would not reappear during a subsequent roughing cut, even though it may have used the same tool edge and cutting parameters.

Negative rake tools confirmed the value of negative rake angles in improving surface finish. However, these tools had much higher wear rates than the conventional tools, lessening their usefulness. This is contrary to other reports showing the negative rake tools provided extended life[1]. The high wear rate may possibly be associated with the geometry of the cutting with the negative rake angle. In any case, the high wear would be unacceptable over the distances necessary for cutting larger parts.

No cutting fluid reduced tool wear over that of distilled water. The one non-water based fluid tested, Shell Diala Oil AX, proved to be inferior to distilled water in all respects. Generally, cutting fluids reducing the wear on the tool also increased the fracture damage in the sample, but still maintained low roughness values. Those cutting fluids that resulted in higher tool wear also appeared to enhance ductile cutting. There was often little or no apparent fracture damage, and the high roughness values were caused solely by the feed marks. The higher wear on some fluids may also be attributed to a more consistent depth of cut. The water provides evaporative cooling, which can affect the depth of cut as the workpiece retracts away from the tool. More thermally stable fluids might then suffer from higher wear, although they may encourage better figure accuracy. This effect was not quantified or measured here.

The sodium hydroxide cutting fluid was the only deviation from these observations. While it did exhibit higher tool wear in some tests, it was the only cutting fluid to demonstrate an improvement in surface finish as the tool wore. This improvement in the outer region is probably due to longer exposure time, as the spinning disk sends the cutting fluids to the outside. These results are most probably due to the high pH of the cutting fluid interacting with the $SiO_2$ layer on the surface , although it is not beyond possibility that the sodium itself had an effect. Other high pH fluids had much higher concentrations of other molecules, which may have affected the cutting process. The report recommending a 25% ethylene glycol solution may have used antifreeze as a source of the ethylene glycol, which has a much higher pH ( pH 10.2 in one sample tested.) This could have given the better results reported.

Cutting speed, not thought to be an important parameter in SPDT, may have greater effects when cutting fluid action is taken into account. The high tool wear experienced in the third sodium hydroxide test runs counter to the expectation of less wear due to higher feedrate. The low cutting speed may have been the cause of this effect.

One possibility is that water is an ideal cutting fluid for SC silicon. It has a very small molecule with a high dipole moment, which causes the molecules to clump together. The small molecular size may allow easier penetration to the cutting interface, while the dipole moment may enhance the lubricating action as the particles stick together[2]. This does not address the concerns of the thermal effects of water, which were not quantified here. Evaporative cooling from the cutting fluid can significantly distort the part to be manufactured[4]. A compromise solution might be developed that may reduce the thermal effects at the expense of a small amount of tool wear

**References:**


1. Buelow, Larry, et al, "Resonator Optics Materials Assessment - Technical Status Report 1992-1993", Martin Marietta Technologies, Inc.
2. Estabrook, Dr. Kent, LLNL
3. Shimura, Fumio, Semiconductor Silicon Crystal Technology. San Diego: Academic Press, 1989
4. Taylor, J. S, Syn, C. K., Donaldson, R. R., and S. Shimada, "Ductile-Brittle Transition of Cutting Behavior in Diamond Turning of Single Crystal Si", Lawrence Livermore National Laboratory

# Monitoring brittle/ductile material removal mechanisms in micro-machining using wavelet packet analysis and Green's function solutions of AE signals

Xuemei Chen and David Dornfeld
University of California, Berkeley, California, USA

**Keywords:** Brittle/Ductile Transition, Micro-Machining, Wavelet Packet Analysis, Green's Function, Acoustic Emission

## Introduction

Micro-machining of brittle materials such as silicon, glass and ceramics involves both plastic deformation and brittle fracture [1]. Monitoring and identifying the dominant material removal mechanisms in such processes is important for achieving high productivity and surface finish with controlled tool wear. As the transient elastic energy that is spontaneously released when materials undergo deformation or fracture, acoustic emission carries rich information on the type, location, severity, and other characteristics of the deformation mechanisms at a microscopic scale. Therefore, acoustic emission signals can be regarded as signatures of the source events occurring at the location of deformation. This study examines the different elastodynamic representations and characteristic waveforms for brittle and ductile material removal mechanisms based on Green's function solutions. Earlier work on this was done by Daniel [2]. A feature extraction scheme is then developed using wavelet packet analysis with best basis selected with respect to the characteristic waveforms to achieve high representation efficiency.

## Elastodynamic Representation of Brittle and Ductile AE Sources

From the theory of elastodynamics, solutions to wave propagation are presented in terms of Green's functions, which refer to the medium transfer tensors that represent the displacement in a structure at a sensor point $\mathbf{x}$ and time $t$ due to an impulsive force applied at point $\mathbf{x_0}$ at time $t_0$. Source events for the formation of a crack can be represented by a dipole source, i.e. a moment tensor. On the other hand, source events for plastic deformation can be described by a monopolar source, which refers to a concentrated force or traction [3]. For these two types of source events, Green's functions for an infinite plate contain distinctive characteristic waveforms. Figure 1 shows the typical Green's functions for an infinite plate at epicenter location due to monopolar and dipole impulses at various orientations. As could be seen, a dipole Green's function tends to have a doublet or triplet shape, whereas a monopole source tends to have a delta-like or doublet shape. Such observation implies that acoustic emission waveforms carry inherent information on brittle or ductile deformation mechanisms and could be used as signatures for identifying different source events.

In frequency domain, the Green's functions as shown in Figure 1 have high-pass filter characteristics. This implies that the plate structure tends to attenuate low frequency events and transfer high frequency events. As will be depicted later in the paper, wavelet bases form a well-constructed high-pass filter bank, therefore are very suitable for emulating the effects of Green's transfer function and characterizing acoustic emission signals. This link between Green's function and wavelet transform underlies the effectiveness of the representation scheme of AE being developed in this paper.

## Wavelet Packet Analysis of AE Signals

A wavelet packet is a function $W_n(2^j t-k)$, $j,k \in Z$, $n \in N$, formed by taking linear combinations of ordinary wavelets [4]:

$$W_0(t)=\phi(t),\ W_1(t)=\psi(t)$$

$$W_{2n}(t) = \sqrt{2}\sum_k h_k W_n(2t-k)$$

$$W_{2n+1}(t) = \sqrt{2}\sum_k g_k W_n(2t-k)$$

where $\phi(t)$ and $\psi(t)$ are the wavelet and scaling functions generated by a pair of quadratic mirror filters. The functions $2^{j/2}W_n(2^j t-k)$ constitute a wavelet packet library [4]. Among this vast library of wavelet packets, the best wavelet packet basis that captures the essential information in a signal with the highest representation efficiency can be selected based on an information cost function such as the Shanon entropy. Wavelet packet bases so constructed allow more flexibility in adapting the basis to the frequency contents of a signal and thus achieve better frequency localization.

## Characterization of Brittle/Ductile Material Removal Mechanisms using Wavelet Packet Analysis of AE Signals

Wavelet packet analysis with best basis selection is applied to acoustic emission signals from scratch tests of glasses at various depths of cuts. Figure 2 shows a wavelet packet analysis for AE signal from a single scratch. As could be seen, wavelet packet analysis tailors to the characteristic waveforms in the signal with high representation efficiency. Figure 3 shows the time-frequency spectrograms for scratches with increasing depths of cuts calculated by best-basis wavelet packet transform. The gradual transition of material removal mechanisms from ductile to brittle as the depths of cut increase is clearly illustrated. The spectrograms show more high frequency (small-scale) contents as the depths of cuts increase.

## Conclusion

In conclusion, wavelet packet analysis with basis functions tailored to the characteristic waveforms as predicted by Green's function solution is capable of extracting acoustic emission bursts of various scales with high representation efficiency. Therefore, the proposed representation scheme has great potential in monitoring the brittle/ductile phenomena in micro-machining of brittle materials.

## References


[1] Shimada, S. et. al., "Brittle-Ductile Transition Phenomena in Micro-indentation and Micro-machining", Annals of the CIRP, Vol. 44/1/1995, 523-526.

[2] Daniel, J. P., "Applications of Quantitative Acoustics in Monitoring Precision Manufacturing," Ph.D. Thesis, Department of Mechanical Engineering, University of California, Berkeley, 1996.

[3] Kim, K.Y. and Sachse, W., "Acoustic emissions from penny-shaped cracks in glass. II. Moment tensor and source-time function", J. Appl. Phys., 59/8/1986, 2711-2715.

[4] Coifman, R.R., et al., "Wavelet analysis and signal processing", Wavelets and their applications, M.B. Ruskai et al., Jones and Bartlett, Boston, 1992, 153-178.

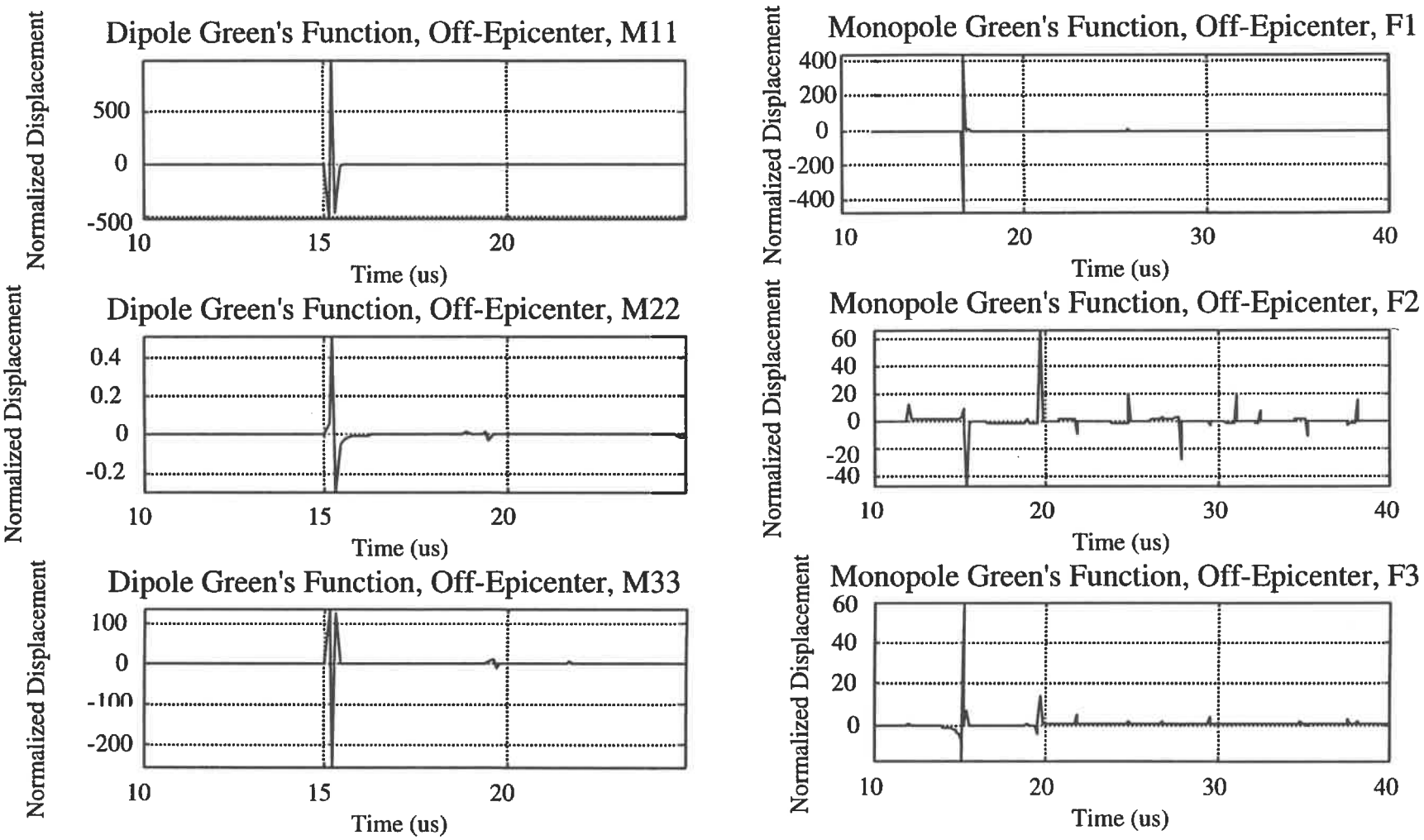


Figure 1. Green's functions in an infinite plate for dipole and monopole impulse events at epicenter location.

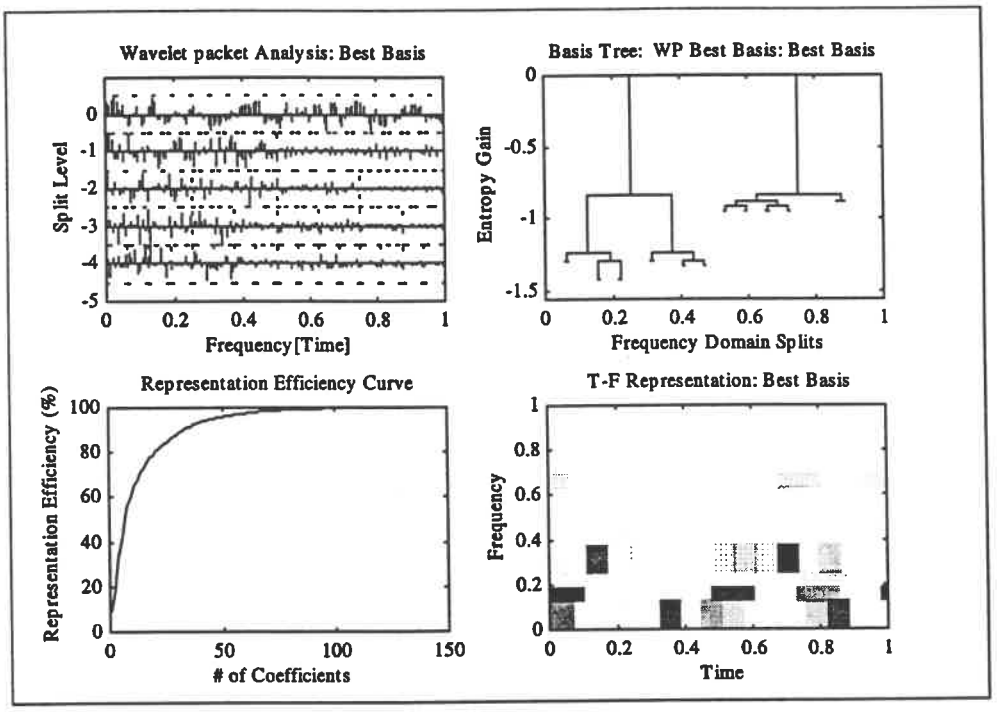


Figure 2. Wavelet packet analysis of an AE signal from a scratch test

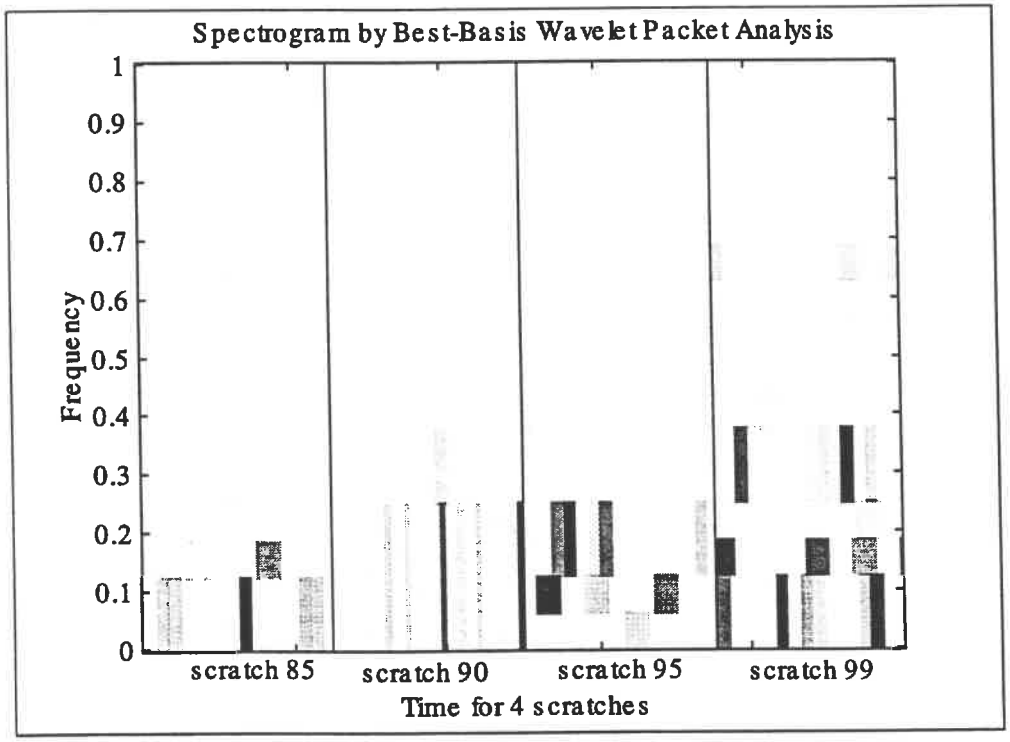


Figure 3. Time-frequency spectrograms calculated by best-basis wavelet packet transform for AE signals from scratch tests at increasing depths of cuts.

# Material Removal Rate Vs. Power in Silicon Wafer Dicing

Hagai Eshel, Process Development Engineer, Kulicke & Soffa Industries
Ilan Weisshaus, Dicing Process Development Manager, Kulicke & Soffa Industries

Dicing, the process of separating silicon wafers into individual dice, is the first step in semiconductor device assembly. Dicing is the mechanical process of cutting with an abrasive blade, and its mechanism is assumed to be similar to creep-grinding.

Optimizing the cut quality and reducing the process variations requires an understanding of the interaction between tool and material. Finding the interrelationships between the volume of silicon removed by the cutting blade, and the dynamics of the blade, provides means for building such an understanding.

The theory of brittle material grinding predicts linear proportionality between the material removal rate and the power input to the grinding wheel. Therefore, if the assumption about process similarity between dicing and creep grinding is valid, material removal behavior in dicing should demonstrate a linear dependence with the power input to the cutting blade.

In this research, the independent variable, material removal rate, was set by varying the feed rate, cut depth and blade thickness. Blade rpm and wafer type were used as the control variables. The measured variable used in this research, was the power used by the DC spindle motor, to keep the abrasive dicing blade rotating at a predetermined rotation speed (rpm).

A typical formula that relates the material removal rate with the addition of power input, above the base line that is needed to change the removal rate is:

**POWER = 0.12 + 0.67 MRR[$mm^3$/sec]**

MRR = Material Removal Rate = [Feed Rate]*[Kerf Width]*[Cut Depth]

This formula was obtained for a blade rotating at constant speed of 30 krpm. An increase in the spindle rotation speed decreases the slope of the curve. Interaction time of a single diamond with material is shortened as the rotation speed increases

The conclusion reached as a result of this study is that the silicon dicing process is characterized by a typical, linear relationship between the material removal rate and blade input power. Deviation from the linear rule, indicates the development of mechanisms or processes that cause damage and deteriorate cut quality by formation of cracks and chip outs.

## Introduction

During the manufacture of large scale integrated circuits, the array of the circuits is produced within the top layer of the silicon crystal. These integrated circuits are separated from the wafer by the dicing operation. The dicing, or silicon wafer cutting process, is performed by a rotating blade composed of diamond grits embedded in a nickel matrix. This removal of brittle (silicon) material by an abrasive wheel rotating at high speed, is assumed to be similar to the grinding of ceramic. The validity of this assumption is tested in this work.

The most accepted model for material removal by abrasion is presented by Evans and Marshall(1). This model predicts a threshold load that must be applied by the abrasive grain, to cause the fracture of the brittle ceramic. The cracks create localized fracture of the material in predicted directions. Material is removed as particles when some of these cracks join in three dimensions. Other cracks may remain in the material as damage.

From this model, a formula is derived that predicts a linear relation between the volume of the material removed, in the grooving process by an abrasive particle, and the load exerted by this particle. (1)

$$V = \alpha * \frac{P n}{M} * L$$

V - Volume of the material removed  Pn - Peak normal load  $\alpha$ - Material independent constant
M - Material properties dependent constant  L - Cut length, groove length

$$\frac{(E/H)^{4/5}}{Kc^{1/2}H^{5/8}} = M$$ (E - Young's modulus H - Material hardness Kc -Fracture toughness)

Further studies by Xu and Jahanmir (2) on material removal in scratching of polycrystalline alumina show that material removal rate is proportional to the load, $P^2$. The material removal mechanism suggested is by grain dislodgment resulting from grain boundary cracking .

In this work, the material removal rate, in the case of silicon single crystal, is tested and formulated as function of cutting blade torque, which is proportional to the load exerted by the cutting diamonds, and is expressed in units of spindle current. If we assume reciprocity of the formula, then the measured torque should have a linear relationship to the remove material (if the Evans Marshall model is applicable). This means that for removal of silicon at a known rate, a known torque value will be measured.

As shown by Malkin(3), a high percentage of the mechanical energy input turns to heat during the abrasive processes. Due to friction, excessive heat generation can cause damage to the workpiece and/or dicing blade. Heat may affect the bond strength of the material, and thus facilitate material cracking and disintegration and, as a result, change relation between torque and removal rate.

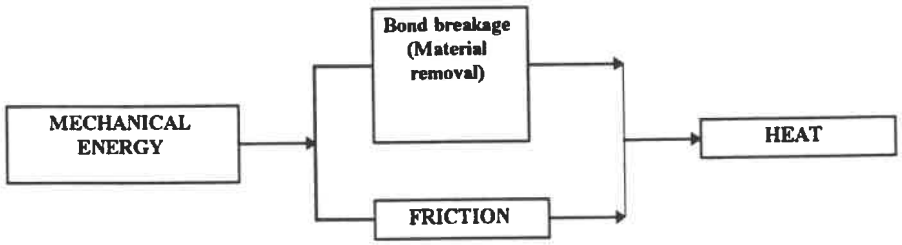


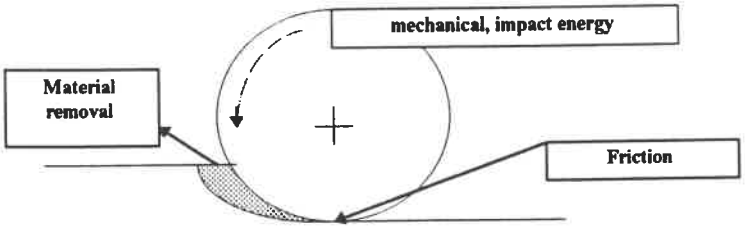


The Evans and Marshall model is based on mechanical interaction between the impacting abrasive grit and the workpiece, which causes fracture and material removal. Malkins model considers the sliding force as a component of the normal force. Since the linear relation between the normal force and removal rate is preserved, one should assume that either the effect of friction is negligible or that the load dependence on the friction is linear.

The linear approximation is highly significant in evaluating the mechanics of the dicing process. Deviation from linearity signifies changes in the mechanism and may be used as an indicator of process instability.

## EXPERIMENTAL

A system was designed to measure the current used by the spindle, of a K&S 7500 model, automatic dicing system during operation. The measurements are based on the feedback current that is required to keep a constant spindle speed.
The spindle current was calibrated against force, so when force was applied by a workpiece on the cutting blade that force could be calculated from the current measured.
The testing material used was blank silicon wafers. The test wafers were 150 mm in diameter "mirror" polished on one side and ground on the other. The wafers ranged from 508μm to 558μm in thickness. For dicing, all wafers were mounted on a frame with adhesive tape, Nitto SWT 20, and cured at 60°C for 30 minutes. For each cut line on the wafer, an average load value was determined from the current values recorded during the dicing. The term "load" represents the mean current values calculated from the recorded current data.

**Material Removal Rate**

To test the material removal rate the following set of experiments was carried out:

| Limits | Cut depth | Blade thickness | Feed rate |
|---|---|---|---|
| Low | 2 mils | 1.0 mils | 2 "/sec |
| High | 20 mils | 2.0 mils | 3 "/sec |

1)The spindle speed was maintained constant, during each testing series.
2) The cut depth was changed at increments of 2 mils.

## RESULTS AND DISCUSSION

The results of the experiments correlating the "load" with material removal rate are summarized in Fig. 2. The "load" values shown in this chart, are the values above the base line. The current consumed by spindle idle rotation and the current resulting from the interaction of coolant with the blade was calculated as base line, and was subtracted from the total value of the measured current.
The regression rule from the chart is: " **load** " = **0.12 + 0.67*{ material removed [mm^3/sec]}.**
- @ Confidence level: 95% and with Standard error: 0.06.
This typical, linear relationship between the load and the material removal rate was tested and recorded for a constant spindle speed of 30krpm.

**Figure 2**

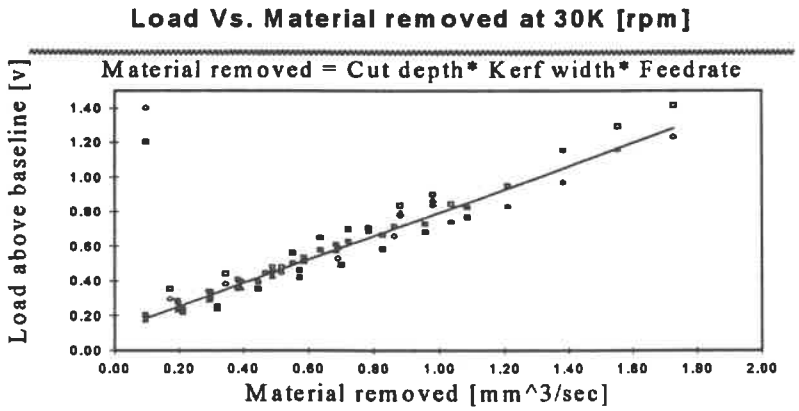

However, in certain cases there are distinct deviations from linear behavior, as shown in figure 3.

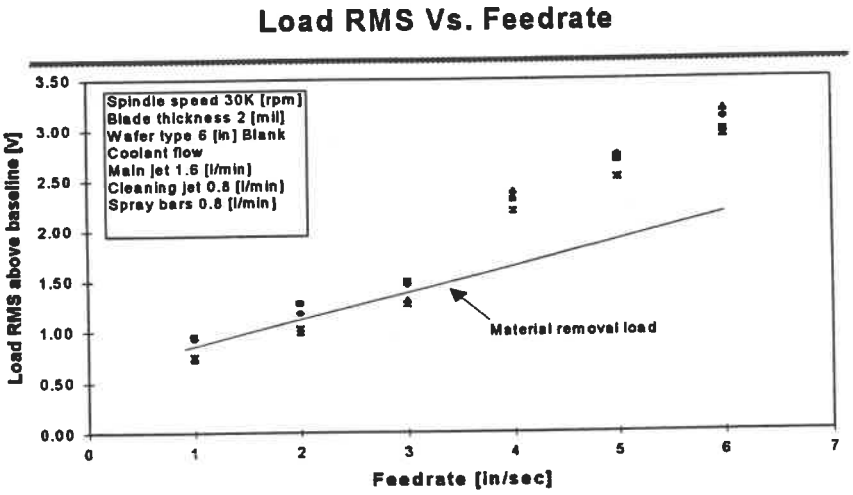


**Figure 3**

In Figure 3, the relation between "load" and dicing feed rate variation is presented. The blade properties were kept constant together with the spindle speed. Under test conditions a linear relation between the "load" and the feed rate is expected. However, when the feed rate increases above 3.5"/sec, a sharp increase is measured in "load" values and deviation from linearity is observed. An abrupt increase in measured values can result from changes in the mechanism of material removal. When all dicing process parameters are kept constant, the cut groove (kerf) is expected to stay at a constant width. Deviation of "load" values from the linear rule can reflect changes in the kerf width.

**Figure 4**

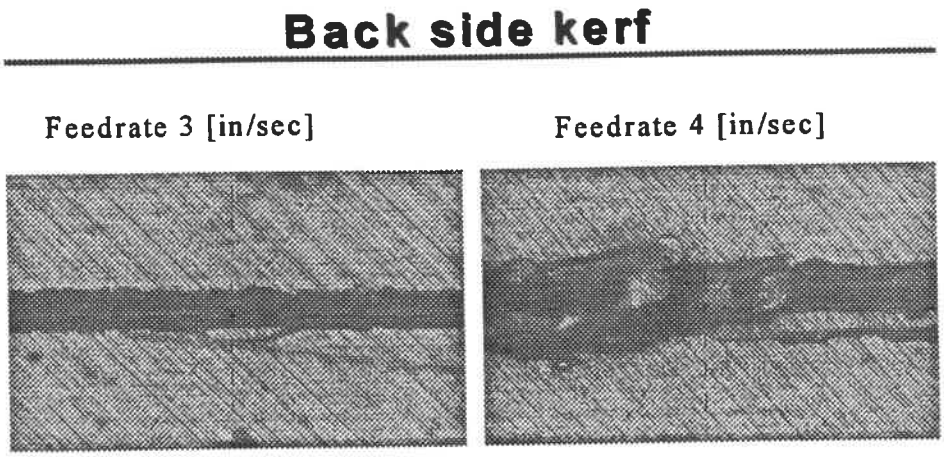

In Figure 4, the back side of the cut groove on the diced silicon wafer is shown, for two different feed rates. The first picture corresponds to a dicing feed rate of 3"/sec, while the second corresponds to dicing at 4"/sec. Simultaneously, with the widening of groove, the sharp increase in "load" is observed. Widening of the kerf means removal of more material. However, if the feed rate is not changed and more material is removed per unit of time, a non-linear increase in load could result. This can be seen in the load vs. feed rate charts.
The reason for the broadened, crushed kerf is the additional interaction between the blade and the material. A vibrating blade can be the source for an increase in the sliding force component of the normal force applied by the blade to the workpiece. An increase in sliding force generates additional heat and contributes to crack formation.

## CONCLUSIONS

1. When dicing silicon wafers, a linear relation exists between the torque measured on dicing blade and the material removal rate.
2. Deviations from linearity signify changes in material bond fracture, and eventually, material removal rate.
3. Material removal parameters that cause the measured torque values to deviate from a linear relation are accompanied by numerous cracks and heavy damage to cut edge integrity.

## REFERENCES


1. Evans, A.G., and Marshall, D.B., "Wear mechanisms in ceramics", Fundamentals of friction and wear of materials, ASME Press, New York, N.Y. pp.439-452 (1981)
2. Xu, H.H.K., and Jahanmir, S. "Microfracture and material removal in scratching of alumina" J. Mater. Science 29 (1994)
3. Malkin, S., "Grinding Technology" Ellis Horwood Ltd., (1989) pp. 129- 139

# Superpolishing by a Tin Polisher

**Honggang Gao, Bin Chen, Jianlin Cao**
State Key Lab. of Applied Optics, PO Box 1024, Changchun 130022,
P. R. China, 0086-0431-5684692. Email: wzs@public.cc.jl.cn

Along with the development of Soft X-ray optics, optical elements with ultrasmooth surfaces are demanded. Multilayered reflective mirrors are the most identical optics in the Soft X-ray region which require the surfaces of substrates to be supersmooth, that is, the surface roughness below 1 nm rms. Furthermore, the excellent reflectors usually take advantage of the substrates with surface roughness 0.1 nm rms.

Among the techniques for superpolishing which fabricate optics with ultrasmooth surfaces, Float Polishing is outstanding with its unusual character of making use of a tin polisher. We have developed a polishing machine (called Tin Polishing machine) to study the tin polisher. The basic structure of the polishing parts of the apparatus is similar to Float Polishing machine while the accuracy is much lower than that of the later one. The Tin Polishing machine has tin polisher of 200 mm in diameter. Grooves of concentric circles of 5 mm in pitch and a series of diamond turning fine spiral grooves are cut on the tin surface by an ordinary lathe. The final flatness of the tin polisher is not measured.

It is found that the tin polisher is directly contacted with the samples in the period of polishing because the contours of the samples change a lot and the tin surface wears obviously. This is the distinguished difference between the two methods of Tin Polishing and Float Polishing. Experiments have been carried out to explore the changes of surface roughness caused by the ware of the tin polisher and the fitness of the samples and the polisher. In the following experiments, BK7 glass plates are employed.

## 1. Polishing with diamond paste

Various sizes(from 0.5 to 2.5 um in diameter) of diamond pastes are employed, however the polished surfaces are not as smooth as supposed. It appears that the surfaces of sample become smoother after polishing while the smaller size of diamond paste applied, and that the tin polisher wears furiously due to diamond paste during the operation. When samples with smooth surfaces are being polished, the surfaces turns somewhat rougher after 1 hr., then tend to be smooth in the following 2 hrs. and then become rough again. The surface roughness changes from 4 nm (prepolishing) to 10 nm (1 hr. later) to 3 nm (3 hrs. later) to 18 nm (5 hrs. later) in the end. The surface roughness after nearly 5-hour-polishing is much higher than before polishing.

## 2. Polishing in liquid

The process of polishing in liquid is similar to Bowl Feed Polishing. Both of the samples and tin polisher are immersed in the polishing fluid of the mixture of the deionized water and various

abrasive powders such as CeO (0.5 um), SiO (of 7 nm) and colloidal silica (of 25 nm), and the pH value of fluid can be changed through dropping NaOH or HCl into it.

Polishing of samples with rougher surfaces (1.7 um p-v) shows that the surface roughness reduces from um degree to nm degree rapidly during the first 30 min., and increases slowly in the following 2 hrs. When the samples are prepolished to the surface of peak-valley roughness of 4-6 nm p-v, the superpolishing with a tin polisher exerts little influence on the improvement of surface roughness. Ultrasmooth surfaces are obtained by use of colloidal silica and prepolished samples. The polishing operation is carried on for 2 hrs. And the measurements of surface roughness show that the pH value of the polishing fluid is very important for superpolishing. The smoothest sample of 30 mm in diameter of surface roughness below 0.3 rms is obtained after 2-hour-polishing, and the concentration of polishing liquid is 3.5% wt. with pH value changing from 10 to 8.

It is concluded from the above experiments with a tin polisher that samples must be prepolished to a certain smooth degree (for example, 0.1 - 0.01 um Ra) by whatever methods before superpolishing. Tin polisher wears while the sample is superpolished. The wear of the tin-polisher, which is caused by several factors such as the hardness of the abrasive, the roughness of prepolished samples, pressure and polishing velocity in the superpolishing process, is very important for the fitness of the surfaces of polisher and sample which will result in the supersmooth surface of the sample, but the over-wear of the polisher will lead to the unfitness of the two surfaces, therefore damage the surfaces of the being polished samples. Samples of 30 mm in diameter of BK7 optical glass have been used in the experiments and the surface roughness of below 0.3 rms is reached after 2-hour superpolishing by a tin polisher.

**Key Words: ultrasmooth, polishing, tin, optics**

# Silicon Spheres for Gravity Probe B Experiment

Frane Marcelja, George M. Keiser
Stanford University, Hansen Experimental Physics Laboratory

## Introduction.

The General Theory of Relativity predicts two effects which should contribute to the drift of a gyroscope in a polar orbit around the earth: a "geodetic effect" and a "frame dragging". For a gyroscope in the form of a perfect homogeneous sphere the predicted drift rates are 6.6 arc sec per year for the geodetic effect and 0.042 arc sec per year for the frame dragging. The aim of the Gravity Probe B experiment is to detect and measure these two effects.

On the other hand, imperfections of the rotor spheres such as asphericity, inhomogeneity and mass imbalance also cause drifts due to classical torques. It it therefore essential that these unwanted drifts be negligible as compared to the effects which are to be measured.

From simulations it was determined that in order to reduce the drift rate due to asphericity to less than 0.0001 arc sec per year the rotor spheres have to be polished to 1 micro inch (25 nm) or to deviate no more than ± 0.5 micro-inch ( ± 12 nm) from a perfect sphere. Similar goals are also set for the other unwanted effects.

## Fabrication of the Gyroscope Rotor Spheres.

The almost perfect spheres for the experiment were manufactured at Hansen Experimental Physics Laboratory. The spheres are made of fused silica and of single crystal silicon. Fused silica was originally chosen for the rotors as it can be reliably manufactured with high homogeneity. In addition the homogeneity was verified by optical methods. Later, single crystal silicon was investigated. It can be manufactured with density homogeneity better than 1 part in 100,000. Silicon has the advantage of a significantly smaller thermal expansion at the operating temperature of 2°K and a higher thermal conductivity. Four gyroscopes will be used in the experiment. The present plan is to include two gyroscope rotors made of each material.

The polishing apparatus and the polishing technology used was first developed to polish fused silica spheres (Angele, ref. 1). The spheres, 1.5 inch (38 mm) in diameter, are

polished using four laps in a tetrahedral configuration. The three lower laps support the weight of the sphere and balance the pressure exerted by the upper lap, resulting in the upper lap pressure being smaller than the lower laps pressure. For a tetrahedral configuration, some asymmetry due to the weight of the sphere (67.3 g) can not be avoided. The motion of the four laps is programmed to provide, on average, a uniform polishing action over the sphere. The alignment of the polishing machine is found to be very critical. A special material was developed for the laps: a phenolic rosin filled with paper or wood. Pitch laps were tried and abandoned, as the sphericity obtained with pitch laps in the original experiments was not sufficient.

The experience gained in polishing fused silica spheres was very useful, since it was possible to perfect the polishing process in absence of the additional problems related to the crystalline structure of silicon. The anisotropic mechanical and chemical properties of single crystal silicon are used to advantage when polishing flat silicon wafers. However, when the same polishing technology was attempted on a sphere, it produced peak to valley heights of the order of 100 micro-inches (2.5 micro m) highlighting the crystalline structure. After reformulating the process and by using appropriate abrasive slurries and process controls, we were able to reduce the peak to valley heights to below 1 micro-inch globally.

The required sphericity and surface quality is achieved with a special combination of lap material and slurry, as well as a close control of the slurry acidity near pH 6.7 . The inadequate surface quality obtained on silicon with phenolic laps prompted us to return to pitch laps. Empirically, it was finally possible to identify a combination of factors which produced a particular condition on the silicon surface, leading in turn to a uniform polishing action. The best results were obtained with minimal surface wetting, which apparently minimizes chemical action.

Measurements of the sphericity.

The sphericity was measured with a Talyrond roundness measuring instrument. Seventeen great circles are measured (16 meridians and the equator, Lipa and Siddall, ref. 2). In order to achieve the accuracy required one has to correct for the spindle error which is repeatable and is of the same order of magnitude as the deviation of the rotor from a spherical surface: about 1 micro-inch (25 nm) peak to valley. These measurements are then used to represent the surface by an expansion in spherical harmonics up to the 16'th order. Using the expansion coefficients one can reconstruct and plot the sphere surface (see Fig. 1.)

Measurement of the diameter.

The diameter is measured by comparing with a standard fused silica sphere. If the temperature is different than "room temperature" ( 20°C ) a correction for the difference in thermal expansion between silicon and fused silica is applied. A tolerance of ± 5 micro-inch (127 nm) is achievable.

Results and Conclusion:

Various kinds of deviation from a perfect sphere have different effects on the gyroscope motion. To study and control these effects the shape of the rotor was expanded in spherical harmonics up to 16-th order. Simulations of the gyroscope motion were performed using spherical harmonics expansions. Also, using the coefficients obtained in the expansion, the surface of the rotor has been plotted (see Fig. 1). The even and odd harmonics and L=2 harmonic were separately specified, according to the estimated effects.

It was found that for silicon spheres the crystalline structure contributes mostly to even harmonics for L=4 and higher. These were required to be kept below 0.7 micro-inch (18 nm). The odd harmonics contribution was also specified to be less than 0.7 micro-inch (18 nm) and the L=2 harmonic contribution to be less than 1 micro inch (25 nm) peak to valley. The best results obtained for even and odd harmonics (L>2) were 0.3 to 0.4 micro inch (8 to 10 nm) with approximately 0.1 micro inch (2.5 nm) of the residual uncorrected spindle error included. For overall sphericity, the best results were 0.6 to 0.7 micro-inch (15 to 18 nm).

The eight fabricated silicon rotor spheres satisfy all the requirements for the experiment. After extensive testing of all completed gyroscopes on the ground, two silicon and two fused silica gyroscopes will be selected for the science mission.

References:

1.) W.Angele: Finishing high precision quartz balls. Precision Engineering Vol.2 N.3, 3 July 1980, pp. 119-122.
2.) J.A.Lipa, G.J.Siddall: High precision measurement of gyro rotor sphericity. Ibid. pp. 123-128.

Key words: polishing, precision metrology

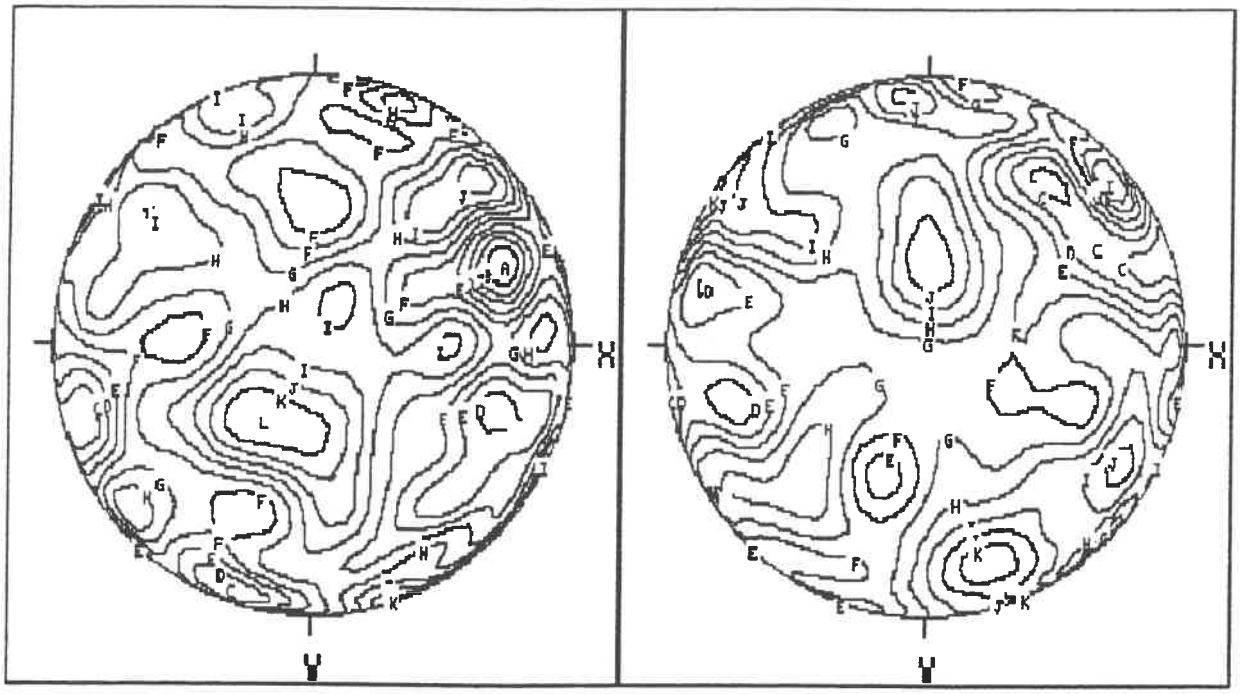

Fig. 1, Silicon rotor sphere 96S29; A=-.38 micro-inch (-10 nm), L=+.32 micro-inch (+8 nm).

# Investigation of the Relationship between Preston's Coefficient and Friction Coefficient in Chemical Mechanical Polishing(CMP) of Silicon

Yongsik Moon and David A. Dornfeld
Laboratory for Manufacturing Automation
Department of Mechanical Engineering
University of California at Berkeley
Berkeley, CA 94720-1740

**Abstract**

In this research, the relationship between Preston's coefficient and friction coefficient in chemical mechanical polishing(CMP) is investigated and a basic mathematical model of the polishing process, Preston's wear equation, is modified.

## 1. Introduction

Chemical mechanical polishing(CMP) process is known as a very effective polishing process to provide excellent global planarization which is critical in the production of integrated circuits(IC). It has been widely used for the planarization of interlevel dielectric(ILD), shallow trench isolation(STI), and the damascene metallization process[1][2].

Since the wider use of CMP for global planarization, many mathematical models of the CMP process have been developed. A model dealing with the degree of nonplanarity on material removal has been developed[3] and the actual pattern has also been considered for the polishing rate mainly based on a phenomenological study[4]. The effect of slurry on the removal rate was investigated using the solution of the Navier-Stokes equation[5][6]. More recently, the pattern density on the IC has been taken into account as a parameter to be considered for predicting the material removal rate[7].

The main objective of this research is first to derive a new model from Preston's equation, which was originally developed for glass polishing, using the relationship between Preston's coefficient and the measured friction coefficient. Second, after verifying the new model experimentally the significance of friction force on material removal rate will be considered. This study could apply to any process where behavior follows Preston's equation.

## 2. Preston's wear equation

The basis for the CMP process model developed here is Preston's wear equation[8]. Preston's equation states that the volumetric removal rate on a workpiece, due to the relative motion between surfaces, is proportional to the bearing load and the relative velocity. The equation has been accepted and utilized as a basic mathematical model for the CMP process, and has the form

$$\dot{h} = C \cdot P \cdot v, \tag{1}$$

*where $P$ = pressure, $v$ = relative velocity, $\dot{h}$ = average height removed/unit time, $C$ = Preston's coefficient.*

Preston's coefficient, C, is simply a proportionality constant and, so far, it has not been fully determined which physical variables can affect its value. What has been determined is that C depends on the properties of the polishing pad, and abrasive slurry as well as the material properties of the workpiece. Thus, C is highly dependent upon the different operating conditions used in the individual CMP process and it is unique for each process.

We can rewrite Equation (1) as[9],

$$\frac{\Delta h}{\Delta t} = C \cdot \frac{L}{A} \cdot \frac{\Delta s}{\Delta t} \tag{2}$$

$$\rightarrow \Delta h = C \cdot \frac{L}{A} \cdot \Delta s \tag{3}$$

$$\rightarrow \Delta h \cdot A = C \cdot L \cdot \Delta s \tag{4}$$

$$\rightarrow \Delta V = C \cdot L \cdot \Delta s, \tag{5}$$

*where $A$ = apparent contact area between workpiece and pad, $L(x)$ = contact load, $V$ = volume of material removed, $s(x)$ = sliding distance, $P(x)$ = pressure on workpiece, $t$ = time.*

By multiplying by the density of the workpiece, the mass removed can be obtained.

$$\rho \cdot \Delta V = \rho \cdot C \cdot L \cdot \Delta s \tag{6}$$

$$\rightarrow \Delta m = \rho \cdot C \cdot L \cdot \Delta s, \tag{7}$$

*where $\rho$ = density of workpiece, m = mass.*

Therefore, Preston's coefficient can be determined from Equation (7),

$$C = \frac{\Delta m}{\rho \cdot L \cdot \Delta s.} \tag{8}$$

If we consider the energy input, $\Delta Q$, it should be proportional to the volume of material removed.

$$\Delta Q = k_1 \cdot \Delta V, \tag{9}$$

*where $k_1$ = constant, $\Delta Q$ = energy input.*

The energy input is also proportional to the work done by friction, which is the product of the friction force, F and the displacement, $\Delta s$,

$$\Delta Q = k_2 \cdot F \cdot \Delta s, \tag{10}$$

*where $k_2$ = constant, F = friction force between workpiece and polishing pad.*

Therefore,

$$k_1 \cdot \Delta V = k_2 \cdot F \cdot \Delta s. \tag{11}$$

By using Equation (5),

$$k_1 \cdot C \cdot L \cdot \Delta s = k_2 \cdot F \cdot \Delta s \tag{12}$$

$$F = \frac{k_1}{k_2} \cdot C \cdot L. \tag{13}$$

For Coulomb friction, which is assumed in this case, the friction force is defined as the friction coefficient, $\mu$, times the normal load, L,

$$F = \mu \cdot L. \tag{14}$$

Therefore, we can obtain a mathematical relationship between Preston's coefficient and the friction coefficient as,

$$\frac{k_1}{k_2} \cdot C \cdot L = \mu \cdot L \tag{15}$$

$$C = \frac{k_2}{k_1} \cdot \mu \tag{16}$$

$$C = \alpha \cdot \mu, \tag{17}$$

*where $\alpha$ = constant of proportionality, $\mu$ = friction coefficient.*

Therefore, theoretically, Preston's coefficient should be proportional to the friction coefficient. This relationship needs to be evaluated and verified experimentally. Preston's coefficient in Equation (17) can be obtained by Equation (8) when the material removal is obtained experimentally. The friction coefficient in Equation (17) is calculated from the friction force measured in-situ during the CMP process.

## 3. Experiment

The objective of this experiment is to obtain the data from CMP process for estimating Preston's coefficient and the friction coefficient to verify Equation (17).

A schematic of the experimental setup is shown in Figure 1. A load cell with a 75 lb maximum capacity was mounted to the polishing plate holding the polishing pad and measured the friction force between the polishing pad and the workpiece. Three polished bare silicon wafers with <100> orientation and P-type were used as the workpieces. Polished wafers were used to eliminate the effect of surface roughness of the workpiece on the friction force between workpiece and polishing pad. Before each CMP test, the flatness was measured using a Taylor-Hobson profilometer to allow removal of the geometric effect on the material removal rate and the friction force.

The abrasive slurry used was Nalco 2352, and consisted of colloidal silica and an alkanobmine dispersion with 70 - 90 nm grain size. The dilution ratio was 10(DI water) to 1(slurry), which contains 4.5 % abrasives by weight in the slurry. The abrasive slurry was stirred by a magnetic mixer and supplied through a peristaltic pump onto the polishing pad at a 30 ml/min flow rate. The relative speed of the workpiece was 5 cm/s and the load on the workpiece was 45 N. The polishing time for each Si wafer was 5 hours.

Three polishing pads, IC60, SUBA500, and UR100 from Rodel, were used in this experiment. IC60 is a microporous polyurethane material and its small pore structure works effectively with slurry to minimize scratching and provide optimum polishing performance such as global planarization. SUBA500 is designed to maximize wafer flatness in process, operating in the 6-10 psi range. Increased removal rates and extended pad life are achieved through improved pad porosity and reduced compressibility due to a special impregnation technique. UR100 is

designed to be used for the final polishing process. It is a napped poromeric synthetic that features grown-in-place materials. The cross-section view of these three pads is shown in Figure 2.

The CMP tests were stopped every hour to measure the mass of workpiece. The Si wafer was cleaned first with an ultrasonic cleaner and its mass measured using a Sartorius electric balance with 0.1 mg resolution. A Zygo laser interferometer with 0.1 angstrom resolution was used to measure the surface roughness before and after each CMP process step.

The signal output from the load cell was amplified and sampled every 10 minutes using a PC with a Gagescope data acquisition system at a 100Hz sampling rate. The signal was calibrated to convert it to an equivalent friction force. Mass removal was measured every 1 hour. From Equation (8), Preston's coefficient was calculated and compared with the measured friction coefficient. All friction coefficients sampled every 10 minutes for each hour were averaged to get a medium value. In other words, if $c_1$, $c_2$, ..., $c_6$ are the friction coefficients sampled at ten minute intervals for an hour, the medium value c will be $(c_1+c_2+...+c_6)/6$.

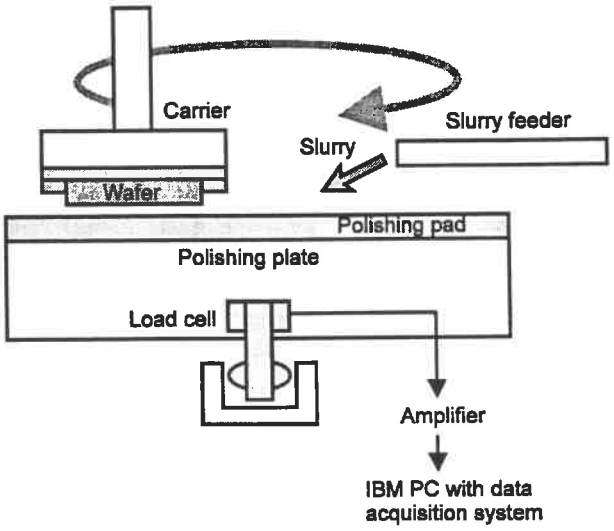


**Figure 1 Schematic of experimental setup**

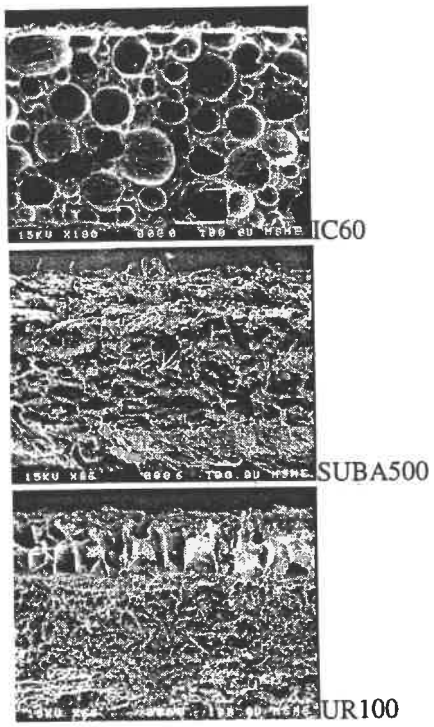


**Figure 2 Cross-section view of IC60, SUBA500, and UR100 polishing pads**

## 4. Results

### 4.1 Friction force and friction coefficient

Before considering the effect of the friction force on the workpiece, it was necessary to consider the effect of surface roughness variation of the workpiece. The surface roughness was measured before and after each CMP test for each Si wafer. Before CMP, the surface roughness of the three wafers was typically around 2nm Rms over a 235μm x 212μm area. After the CMP process, the surface roughness was measured again to determine the change. The final surface roughness for the three polished wafers was around 3nm Rms over a 235μm x 212μm area. Compared to the general surface roughness of a polishing pad(~ 100μm)[10], the effect of surface roughness variation of Si wafer on friction force was negligible.

The friction force on the Si wafer polished by UR100 was the highest of the polishing pads. The friction force for the IC60 pad was the lowest. This was also seen for the friction coefficient due to the constant normal load. The variation of friction coefficient over the tests is shown in Figure 3.

### 4.2 Material removal

The material removal variation for each Si wafer polished by the three polishing pads is shown in Figure 4. As with the result for the friction force measurement, the Si wafer polished by the UR100 had the highest material

removal and the Si wafer by IC60 had the lowest. This suggests that the material removal is proportional to the friction force between workpiece and polishing pad under otherwise constant condition.

The material removal rate was essentially constant over the 5 hour polishing time while those for UR100 and SUBA500 had 10% variation.

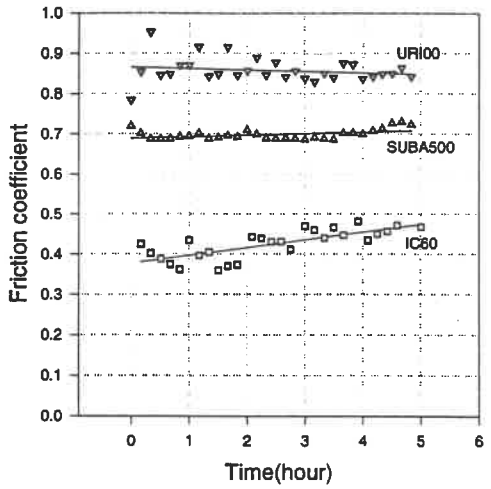


**Figure 3. Friction force variation during CMP process**

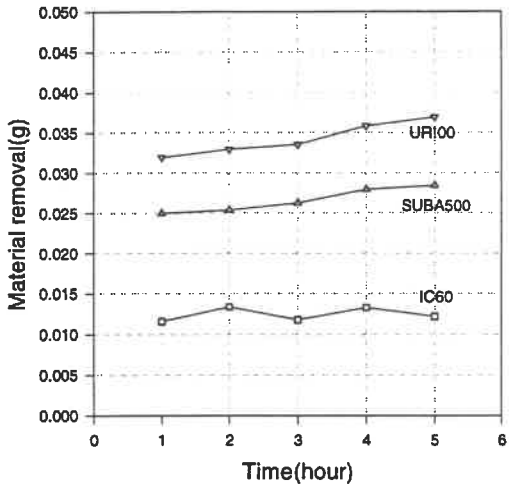


**Figure 4. Material removal variation during CMP process**

### 4.3 Preston's coefficient and proportionality constant α

Preston's coefficient was calculated from Equation (8) using the material removal for each hour, Figure 5. The relationship between Preston's coefficient and friction coefficient is shown in Figure 6. As expected from the analytical results, Preston's coefficient was linearly proportional to the friction coefficient. After plotting each data set, a first order interpolation was performed to calculate α as $2.4 \times 10^{-9}$ ($m^2/N$).

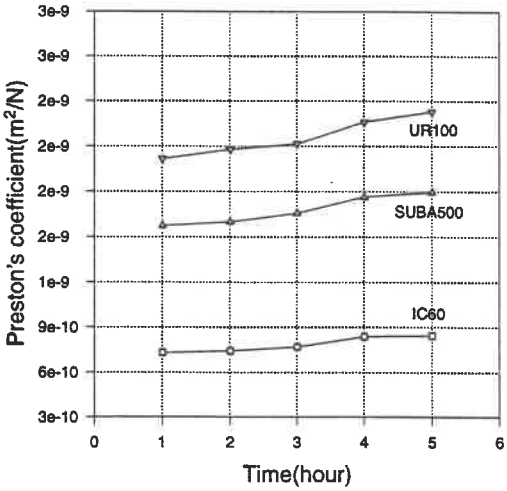


**Figure 5. Preston's coefficient variation during CMP process**

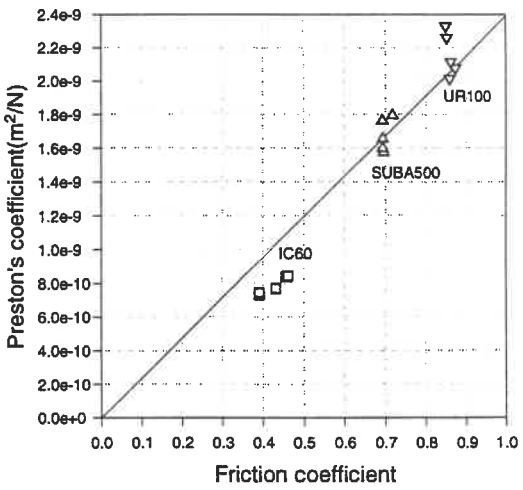


**Figure 6. Preston's coefficient variation with friction coefficient**

## 5. Discussion

The experiments verified that Preston's coefficient is linearly proportional to the friction coefficient with a proportionality constant, $\alpha$ ($=2.4\times10^{-9}$ m$^2$/N). Thus, a modified model for CMP process is proposed as

$$C = \alpha\cdot\mu = 2.4\times10^{-9}\cdot\mu \tag{18}$$

$$\dot{h} = C\cdot P\cdot v = \alpha\cdot\mu\cdot P\cdot v = 2.4\times10^{-9}\cdot\mu\cdot P\cdot v.. \tag{19}$$

If we apply Equation (17) for the volume removal, Equation (5),

$$\Delta V = C\cdot L\cdot\Delta s \tag{5}$$

$$\rightarrow \Delta V = \alpha\cdot\mu\cdot L\cdot\Delta s \tag{20}$$

$$\rightarrow \Delta V = \alpha\cdot F\cdot\Delta s \tag{21}$$

$$\rightarrow \Delta V = \alpha\cdot W_{friction}. \tag{22}$$

Thus, the volumetric removal is linearly proportional to the friction force between workpiece and polishing pad and also to the work by friction force during CMP process.

## 6. Conclusions

The following conclusions can be drawn from this analysis and experimental testing:

- Preston's coefficient was shown to be linearly proportional to the friction coefficient, during CMP with a constant of proportionality for silicon, $\alpha = 2.4\times10^{-9}$.
- Material removal rate can be estimated by the equation, $\dot{h} = 2.4\times10^{-9}\cdot\mu\cdot P\cdot v$.
- Material removal was linearly proportional to the friction force and the work done by the friction force on the workpiece for the CMP process with silicon.

The potential for using this quantitative relationship for process diagnostics or setup, e.g. estimating or observing variations in Preston's coefficient, is being evaluated.

## 7. Acknowledgments

This research is supported by the industrial affiliates of the Laboratory for Manufacturing Automation at the University of California at Berkeley.

The polishing machine on which the research was conducted was donated by Lawrence Livermore National Laboratory (LLNL). Our special thanks go to Dr. John Taylor of LLNL for his assistance and motivation in this research.

## 8. References

[1] I. Ali, et al., "Physical Characterization of Chemical Mechanical Planarized Surface for Trench Isolation," *Journal of Electrochemical Society*, Vol. 142, No. 9, pp. 3088-3092, 1995.

[2] F. B. Kaufman, et al., "Chemical Mechanical Polishing for Fabricating Patterned W Metal Features as Chip Interconnects," *Journal of Electrochemical Society*, Vol. 138, No. 11, pp. 3460-3465, November 1991.

[3] P. Burke, "Semi-empirical Modeling of SiO2 Chemical Mechanical Polishing," *Proc. VMIC Conf*, pp. 379-384, 1991.

[4] J. Warnock, "A Two-dimensional Process Model for Chemomechanical Polish Planarization," *Journal of Electrochemical Society*, Vol. 138, No. 8, pp. 2398-2402, August 1991.

[5] S. Runnels, " Feature Scale Fluid-based Erosion Modeling for Chemical Mechanical Polishing," *Journal of Electrochemical Society*, Vol. 141, No. 7, pp. 1900-1904, July 1994.

[6] S. Runnels, et al., "Tribology Analysis of Chemical Mechanical Polishing," *Journal of Electrochemical Society*, Vol. 141, No. 6, pp. 1698-1701, June 1994.

[7] B. E. Stine, et al., "Analysis and Decomposition of Spatial Variation in Integrated Circuit Processes and Devices," *IEEE Trans. Semi. Manufacturing*, V.10, No. 1, February 1997.

[8] Preston, F. W., "The Theory and Design of Plate Glass Polishing Machine," *Journal of The Society of Glass Technology*, Vol. 11, pp. 214-256, 1927.

[9] N. J. Brown, *Optical Fabrication*, Report *MISC-4476* Rev 1., Lawrence Livermore National Laboratory, September 1990.

[10] D. Stein, et al., "Optical Interferometry for Surface Measurements of CMP Pads," *Journal of Electronic Materials*, Vol. 25, No. 16, 1996.

[11] *Rodel Catalog*, pp. 1-9, 1994.

# Mechanical Properties and Relationship to Process Performance of the Polishing Pad in Chemical Mechanical Polishing(CMP) of Silicon

Yongsik Moon, Ilwhan Park, and David A. Dornfeld
Laboratory for Manufacturing Automation
Department of Mechanical Engineering
University of California at Berkeley
Berkeley, CA 94720-1740

**Abstract**

This study investigated the relationship between the material properties (density and compressibility) of the polishing pad and the CMP performance such as the material removal rate and the final surface roughness of the silicon wafer. The friction force between the silicon wafer and the polishing pad was measured and correlated with the material properties of the polishing pad and the material removal rate of the silicon wafer.

It was verified in this study that the material removal rate was inversely proportional to the density of polishing pad. It was proportional to the compressibility of polishing pad and to the friction force between the workpiece and the polishing pad. Also, the roughness of the final surface depended on the mechanical properties of polishing pad.

## 1. Introduction

Chemical mechanical polishing (CMP) has been used extensively in the polishing of silicon wafers and has become the process of choice for planarization of the dielectrics and the metal in IC fabrication.

In CMP, the polishing pad, which is principally polyurethane, is one of the most important elements and has a direct impact on CMP performance as measured by material removal rate and final surface roughness. The influence of polishing pad on CMP has been investigated by some researchers. Material removal rate is inversely proportional to the density and shear modulus of the polishing pad[1]. The shear modulus of polishing pad is affected by the variation of temperature[2]. The structure of the polishing pad is basically an open cell structure[3] and the mechanical properties of the cellular solids or foams are related to the properties of the cell wall material and to the cell geometry[4]. The polishing pad also has the ability to remove contaminants after polishing as a post-polishing process[5]. The polishing pad is deformed after being used for a long period of time, causing a decrease in the material removal rate[6].

This study will investigate the relationship between the polishing pad and the CMP performance and the effect of friction force applied on the workpiece on the material removal rate will be also identified.

## 2. Polishing pad in CMP

Three categories of polyurethane polishing pads are commonly used in the CMP process: (1) impregnated felt substrated-coagulated urethane in a fiber matrix, (2) microporous polyurethane polishing material and (3) napped poromerics-porous urethane layers on supporting substrates. The first type is used for stock removal or rough polishing. Increased removal rates and extended pad life are achieved because of the improved pad porosity and reduced compressibility due to a special impregnation technique. The second type is made to minimize scratching and provide optimum polishing performance such as global planarization. The third type is designed to remove only small amounts of surface irregularity and is most often used in the final polishing step.

In this research, SUBA500, IC60, and UR100 polishing pads from Rodel were used, representing type I, type II, and type III of pad, Figure 1.

The foam-structured polishing pad aids both the chemical action as well as the mechanical action. Although the pores cannot make the slurry reaction more active chemically, they can play a role in helping transport slurry to all parts of the wafer uniformly. Following the mechanical action by the abrasives in the slurry and chemical action, the pores in the pad facilitate the transportation of the removed material from the wafer surface. If pad materials do not have a sufficiently porous structure, the free flow of slurry in and out of the pad would be impossible and this would affect the removal of loose material from the wafer surface. Therefore, the highest material removal in CMP is obtained with pads with pores comprising a large percentage of pad volume (i.e. low density).

The fatigue behavior or mechanical deterioration of the polishing pad should not be ignored either. The process effectiveness will change if pad properties vary during processing. Pads with low density due to pores are more likely to collapse under the applied load and immediately begin to lose their effectiveness. With smaller

number of pores (high density), the pad can maintain its initial polishing rate longer due to its rigidity even though its initial polishing rate is considerably lower than more porous pads.

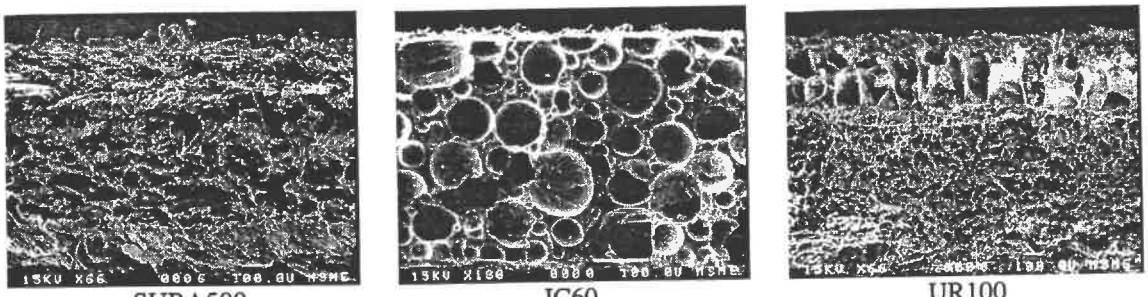

SUBA500 IC60 UR100

**Figure 1. Cross-sectional view of SUBA500, IC60, and UR100 polishing pads**

## 3. Experiment

CMP process experiments were conducted using three commercially available polishing pads(SUBA500, IC60, and UR100) to study the effects of the material properties(density and compressibility) of pad on CMP material removal rate and wafer surface roughness. Also the friction force between the silicon wafer and the polishing pad was measured in process and correlated with the material properties of the polishing pad and the CMP performance.

Three unpolished bare silicon wafers (<100> orientation and P-type) were used as the workpiece. The slurry used was Nalco 2352 consisting of 70 - 90 nm grain size colloidal silica. The dilution ratio was 10(DI water) to 1(slurry) which contains 4.5 % abrasives by weight in the slurry. The relative speed of the workpiece was 14.4 cm/s. A load of 15.1 N was applied for an equivalent pressure of 18.6 kPa.

In CMP, a wafer carrier holds and rotates the wafer against the polishing pad. The abrasive slurry (continuously stirred by a magnetic mixer) is supplied to the pad surface through a peristaltic pump with a 30 ml/min flow rate. A 75 lb maximum load cell is mounted on the polishing plate to measure the friction force between the polishing pad and the workpiece. The load cell was connected to an oscilloscope and PC with a Gagescope data acquisition system for data collection at a 100Hz sampling rate.

Data from the friction force sensor were collected every 5 minutes, and mass removal and surface roughness were measured every 20 minutes for the IC60 pad tests and every 40 minutes for the SUBA500 and UR100 pads tests. A Sartorius electric balance with 0.1 mg resolution and Zygo Maxim3D laser interferometer with 0.1 angstrom resolution were used to measure the mass and the surface roughness, respectively. Before each test, the wafer flatness was measured using a Taylor-Hobson profilometer to remove the geometric effect on the material removal rate and the friction force.

A schematic of experimental setup is shown in Figure 2. The material properties of each pad are given in Table 1.

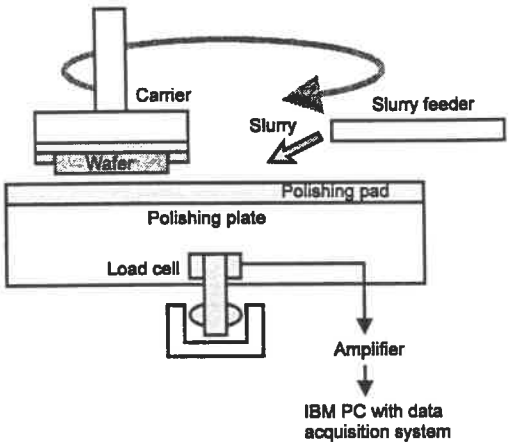


**Figure 2. Schematic of experimental setup**

| | SUBA500 | IC60 | UR100 |
|---|---|---|---|
| COMPRESSIBILITY(%) | 7 | 4 | 14 |
| MEAN THICKNESS(IN)[cm] | 0.05 [0.127] | 0.05 [0.127] | 0.059 [0.15] |
| WEIGHT DENSITY(g/cm$^3$) | 0.37 | 0.685 | 0.35 |
| HARDNESS (SHORE A) | 65-78 | 52-60 | |

**Table 1. Material Properties of SUBA500, IC60, and UR100(Rodel)**

## 4. Results

The variations in the material removal rate, friction force and surface roughness of the silicon wafer are detailed here for each polishing pad test.

The UR100 pad had the highest material removal rate for the workpiece among the three pads, and the IC60 pad had the smallest, Figure 3. The material removal rate was relatively stable after about 2 hours of polishing, which indicates that the final surface was obtained. The friction force shown in Figure 4, shows unique differences for each pad - UR100 had the highest friction force and IC60 had the lowest.

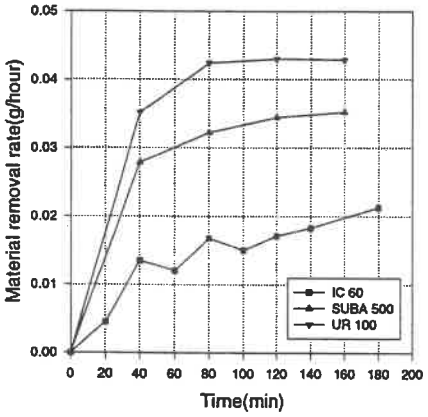


**Figure 3. The Material Removal Rate for Each Polishing Pad**

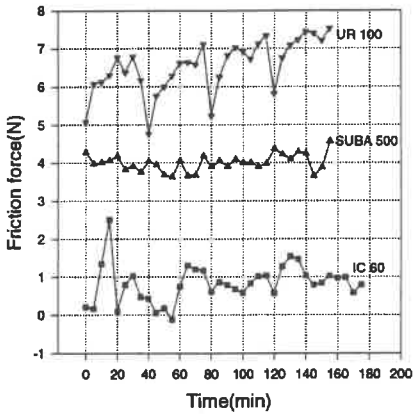


**Figure 4. Friction Force Variation on the Work Piece for Each Polishing Pad**

Two material properties of the pad, which are the density and the compressibility, were considered as a basis for comparison for CMP performance. The lower the pad density, the higher the material removal rate and the friction force are, Figure 5. For compressibility, the opposite effect is seen as lower compressibility reduces material removal and friction, Figure 6. The material removal rate and friction force were all averaged for the entire polishing time in Figures 5 and 6.

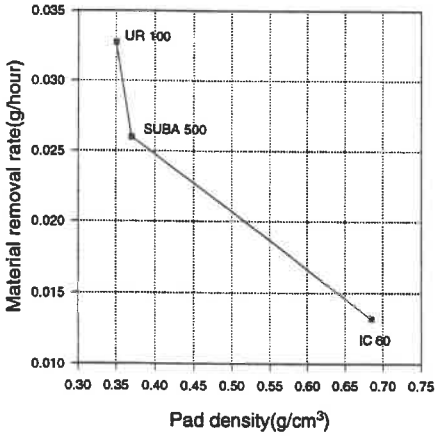


(a) Material Removal Rate Variation with Polishing Pad Density

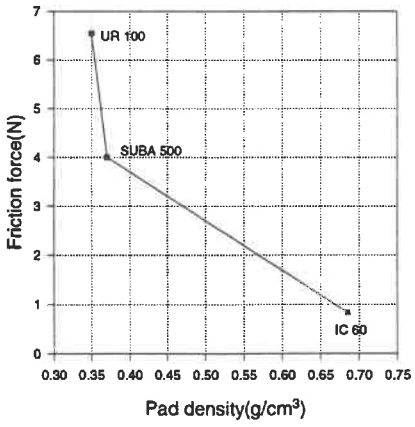


(b) Friction Force Variation with Polishing Pad Density

**Figure 5. Material Removal Rate and Friction Force Variation with Polishing Pad Density**

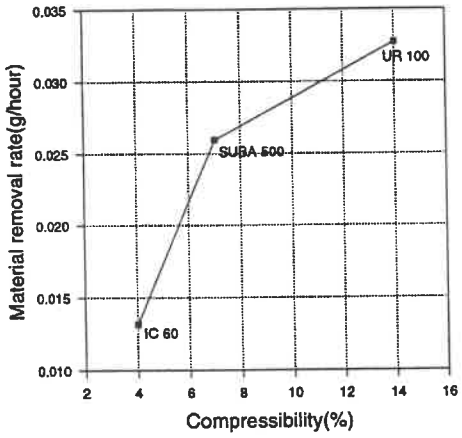


(a) Material Removal Rate Variation with Polishing Pad Compressibility

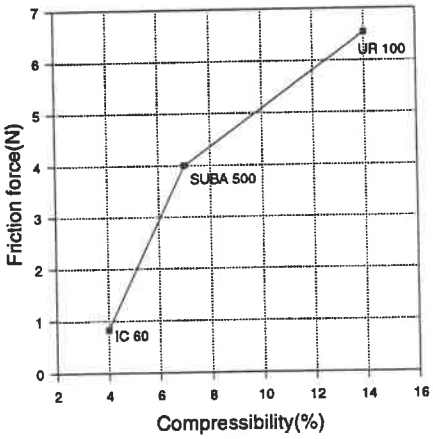


(a) Friction Force Variation with Polishing Pad Compressibility

**Figure 6. Material Removal Rate and Friction Force Variation with Polishing Pad Compressibility**

The final surface roughness of each silicon wafer was correlated with the density and the compressibility of polishing pads, Figure 7. Peak to Valley, Ra, and Rms surface roughness were calculated. The final surface from the UR100 pad was rougher than the surface from the SUBA500 and IC60 pads.

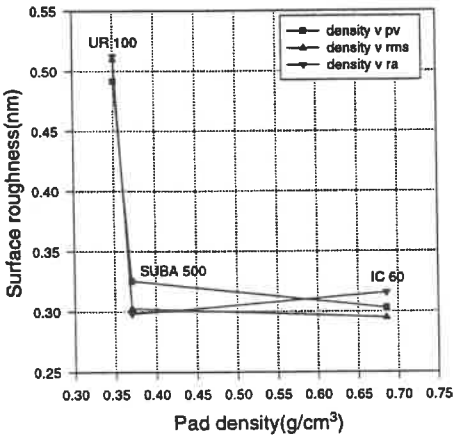


(a) Final Surface Roughness with Polishing Pad Density

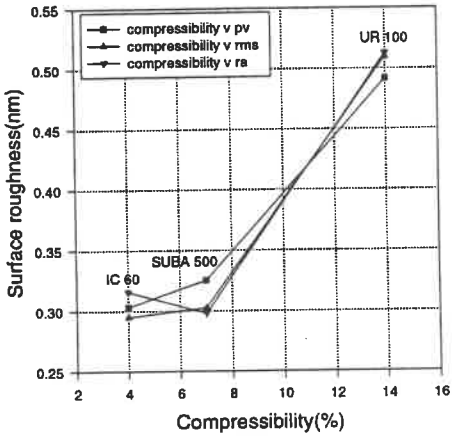


(b) Final Surface Roughness with Polishing Pad Compressibility

**Figure 7. Final Surface Roughness for Polishing Pad Density and Compressibility**

## 5. Discussion

These experiments verified that the material removal rate is inversely proportional to the pad density and proportional to the compressibility of the pad. Using the relationship of the pad density and its composition with its mechanical properties, it is believed that the material removal rate is inversely proportional to the elastic modulus and shear modulus of the pad[1].

$$Material\ removal\ rate \propto \frac{1}{\rho_{pad}} \tag{1}$$

$$\Rightarrow E \propto \left(\frac{\rho_{pad}}{\rho_{polymer}}\right)^2, \Rightarrow G \propto \left(\frac{\rho_{pad}}{\rho_{polymer}}\right)^2 \tag{2)(3}$$

$$\Rightarrow Material\ removal\ rate \propto \frac{1}{E}, \frac{1}{G}, \tag{4}$$

*where* $\rho_{pad}$ *= pad density,* $\rho_{polymer}$ *= polymer density, E = elastic modulus, G = shear modulus.*

From Preston's equation[7][8], material removal rate is a function of the relative velocity and the loading pressure of the workpiece against the pad. If the pressure and the velocity are constant, the material removal rate, theoretically, should also be constant. Thus, the pad density and compressibility are critical elements to control Preston's coefficient and the material removal rate. The pad density and compressibility have a strong relationship with the pore size and number of pores. If a pad has a large pore size and a large number of pores, the pad density will be low and the compressibility will be high. The pad density is inversely proportional to its compressibility and the effect of compressibility was the opposite of that of the density.

There is no material removal without the abrasive slurry. In other words, the polishing pad itself cannot remove material. It transports and supplies the abrasive slurry for the mechanical and chemical reaction. Material removal rate is high for low pad density, due to the influence of density on the shear modulus. If pad density is low, the elastic modulus and shear modulus, E and G, respectively, are going to be low. Large deformation of the pad surface will occur resulting in more contact area and more abrasive applied to the wafer surface. This also explains the reciprocal relationship between the friction force on the workpiece and the pad density. The increased contact area results in the higher friction.

The final surface roughness had a certain relationship with the pad density and compressibility. It was shown from this research that the lower the pad density, the rougher the final surface is and the lower the pad compressibility, the smoother the final surface is. The surface roughness is influenced by the structure of the polishing pad as well as by the density and compressibility since each pad structure has its unique density and compressibility. It is believed that one of the key elements controlling the final surface roughness is the contact mode between silicon wafer and polishing pad according to the pad structure. If the surface of the polishing pad is flat and smooth, the fluid film thickness between the wafer and the pad will increase, resulting in no contact with silicon wafer and a smooth final wafer surface from the dominant chemical action in CMP. If the surface of the polishing pad is irregular and rough, the fluid film thickness between the wafer and the pad will decrease, resulting in some contact with silicon wafer and a rough final wafer surface from the increased mechanical action in CMP.

## 6. Conclusions

Based on the polishing tests with the three polishing pads, the following conclusions can be drawn.

- It was verified that the material removal rate was inversely proportional to the pad density.
- Material removal rate is proportional to the compressibility of the polishing pad and to the friction force between the workpiece and the polishing pad.
- The friction force between the workpiece and the polishing pad is inversely proportional to the pad density and proportional to the pad compressibility.
- The roughness of the final surface depends on the polishing pad structure and mechanical properties.

## 7. Acknowledgments

This research is supported by the industrial affiliates of the Laboratory for Manufacturing Automation at the University of California at Berkeley. The polishing machine on which the research was conducted was donated by Lawrence Livermore National Laboratory(LLNL).

## 8. References

[1] R. Bajaj, "Effect of Polishing Pad Material Properties on Chemical Mechanical Polishing (CMP) Processes," *Material Research Society Symposium Proceeding*, Vol. 337, pp. 637–644, 1994.

[2] W. Li and D. W. Shin, "The Effect of the Polishing Pad Treatments on the Chemical Mechanical Polishing of $SiO_2$ Films," *Thin Solid Films*, 270, pp. 601–606, 1995.

[3] *Rodel Catalog*, pp. 1-9, 1994.

[4] M. F. Ashby, "The Mechanical Properties of Cellular Solids," *Metallurgical Transactions A*, Vol. 14A, pp. 755-769, Sept. 1983.

[5] P. Singer, "Chemical-Mechanical Polishing: A New Focus on Consumables," *Semiconductor International*, pp. 48-52, February 1994.

[6] M. Desai, R. Jairath, "Chemical Mechanical Polishing for Planarization in Manufacturing Environment," *Material Research Society Symposium Proceeding*, Vol. 337, pp. 99-104, 1994.

[7] F. W. Preston, "The Theory and Design of Plate Glass Polishing Machine," *Journal of the Society of Glass Technology*, 11 (44), pp. 214-256, December 1927.

[8] N. J. Brown, *Optical Fabrication*, Report *MISC-4476* Rev 1., Lawrence Livermore National Laboratory, September 1990.

# Cutting Tool Edge Radius and Depth of Cut Influence on the Generation of the High Pressure Phase Transformation during Ductile Machining

John Patten
University of North Carolina Charlotte

**Abstract:** The geometry of the cutting tool and the chip thickness are known to affect the brittle to ductile transition during silicon machining. These same machining parameters also influence the extent of the high pressure phase transformation during cutting. This paper will provide an explanation and analysis of the relationship between these conditions. Specifically, the cutting edge radius and depth of cut, or uncut chip thickness, establish the extent of the semiconductor to metallic high pressure phase transformed region in the vicinity of the tool tip. For a purely ductile cut, the high pressure phase transformed region must extend sufficiently throughout the chip to avoid a brittle response resulting in fracture. An analysis of the cutting edge radius, depth of cut, high pressure phase transformation, together with rubbing, cutting and fracture conditions results in a mechanism map which delineates the conditions necessary for ductile material removal. This mechanism map can be used to establish the necessary and sufficient conditions for producing ductile material removal. The model resulting from this analysis compares very well to an abundance of published experimental data. Comparable results include cutting, friction (sliding and rubbing), scratching, indenting and brittle-ductile transitions. A review of the pertinent experimental data with the subject model is provided in this paper. One important aspect of this model is that it defines two zones of potential brittle-ductile behavior. One is that normally associated with a trailing tensile stress field behind, or in the wake of, the tool. The other is associated with the leading stress field in front of the tool which acts to generate the chip. The model indicates that the latter stress field must be sufficient in magnitude and spacial extent to generate the high pressure phase transformation necessary to achieve a ductile response. If this condition is not achieved, brittle material removal will occur due to fracture ahead of the tool.

Keywords: Tool Geometry, Cutting Edge Radius, Rake Angle, Depth of cut, high pressure phase transformation, ductile machining

**Introduction:** The ductile response during silicon machining is related to the plastic deformation of the high pressure metallic phase of this semiconductor. The brittle response of silicon during machining is controlled by the fracture response of the semiconductor phase. Fracture can occur both in front of the tool, where the chip is being formed, or in the wake of the tool where tensile stresses act to propagate cracks. The brittle behavior associated with the trailing stress field is well

documented and understood. This paper presents an analysis of the conditions in front of the tool which can also lead to brittle behavior. The fracture behavior in front of the tool is well documented for metal cutting, i.e. segmented chips, but has not been fully explored as a process mechanism for the machining of semiconductors. The analysis presented in this paper indicates that if the material in front of the tool, in compression, is not sufficiently transformed to the high pressure "ductile" metallic phase then fracture will occur. Without the presence of the ductile phase, the deformation must occur within the brittle semiconductor phase, which results in fracture. If sufficient material in front of the tool, i.e. the chip, is transformed to the high pressure phase, then brittle behavior is avoided and ductile machining occurs. This paper will address the conditions under which ductile machining is possible.

**Theory:** Referring to Figure 1, the traditional orthogonal chip formation model is indicated along with two additional parameters.

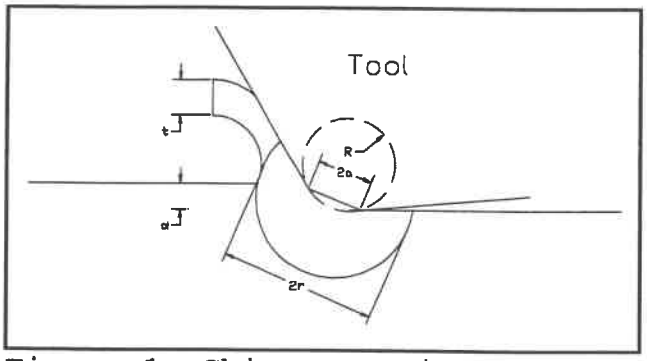

Figure 1: Chip Formation

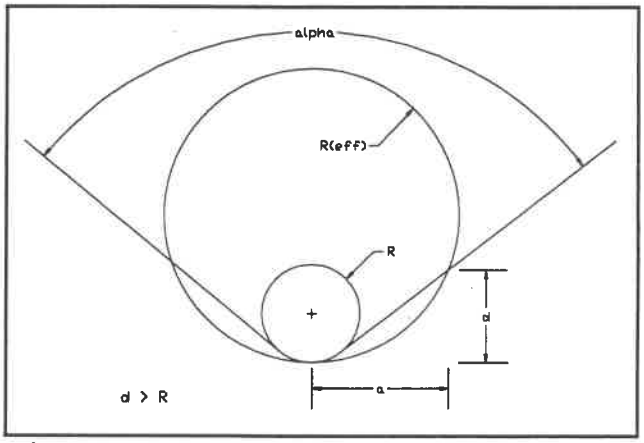

**Figure 2:** $R_{eff}$, Effective Cutting Edge Radius

The value "2*a" defines a diameter of high contact stress and the diameter "2*r" defines the region associated with the high pressure phase transformation (Patten, 1996). In Figure 2 an effective radius, $R_{eff}$ is defined based upon the rake angle (included angle alpha) and depth of cut (d). To insure that the chip is completely transformed into the high pressure metallic phase, the following must be true: For d > R and $R_{eff}$ > R, then

$$R_{eff}/d > 1$$

Where, referring to Figure 3:

$$R_{eff} = a = d/[2*\tan(.5*\text{alpha} + 45)$$

$$R_{eff}/d = 1/[2*\tan(.5*\text{alpha} + 45)]$$

This relation is derived by setting the transformed chip thickness, $T_a$ equal to the actual chip thickness $T_d$ :

$$T = T_a = T_d$$

$T_d$ is the chip thickness due to d and theta.

$$T_d = d*\sin(90-\text{theta} + \text{alpha})/\sin(\text{theta})$$

$T_a$ is the chip thickness which undergoes the phase transformation

$$T_a = ((r-a)(2r-(r-a)))^{.5}$$

For r = 1.44*a, where r is the extent or radius of the phase transformation region (Chiang, 1982, Beta = 2.5) then, $T_a = a$.

and

$$T_a = a = d*\cos(90-\text{theta}+\text{alpha})/[2*\sin(\text{theta})]$$

and

$$T_d / T_a = 2*\tan(45 + .5*\text{alpha}) < 1$$

therefore,

$$T_a > T_d$$

Theta, the shear angle, is related to alpha, the rake angle, by:

$$\text{theta} = .5 * \text{alpha} + 45$$

then,

$$R_{eff}/d = T_a / T_d > 1$$

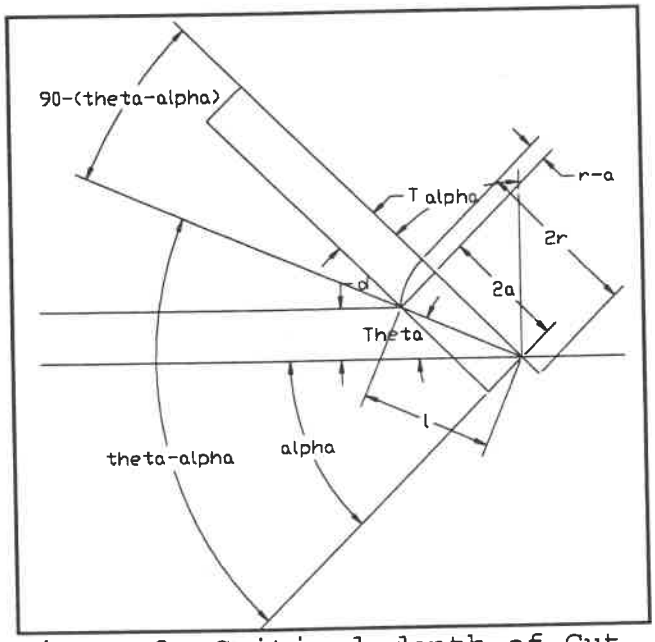


Figure 3: Critical depth of Cut

**Conclusions:** The determination of the high pressure phase transformation zone in front of the tool is based upon an analogy between machining and indenting (Leung, 1998). The cutting edge radius is equated to the indenter tip radius in this analysis. The high pressure phase transformed zone is correlated to the plastic zone of indentation studies and models by use of appropriate scaling criteria (Chiang, 1982). Several observables are consistent with the proposed model.

1. A sharp tool can obtain a larger critical depth of cut than a corresponding dull or worn tool.
2. A worn tool may perform better for smaller depths of cut than a sharp tool.
3. A more negative rake angle is generally preferred over a less negative rake.
4. Rubbing conditions have been reported for R/d = 25.
5. Ductile machining conditions have been reported for: 0.833 < R/d < 5.

The proposed model, $1 < R/d < 25$, is consistent with the observables. A minimum lower bound of $R/d = 0.75$ may exist for some cutting conditions. Figure 4 shows these bounds along with the fracture criterion of a = 670 nm. The area within these limits establishes the ductile machining conditions.

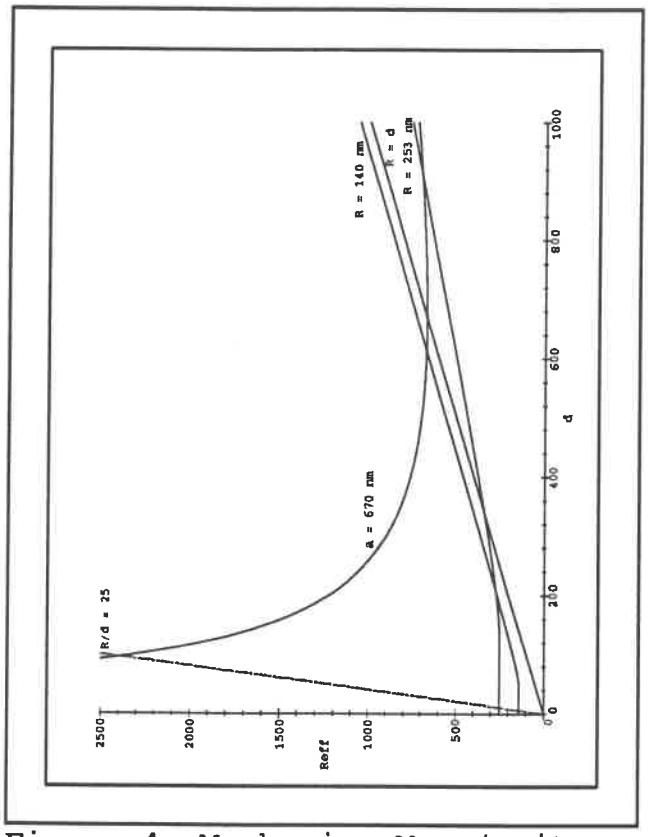


**Figure 4:** Mechanism Map (units in nm) Brittle-Ductile Zones (Patten, 1996)

**References:**


Chiang, S.S., D.B. Marshall, A.G.Evans, The response of solids to elastic plastic indentation 1. Stresses and residual stresses, *J. Appl. Phys.* 53 (1) Jan. 1982, p. 298

Leung, T.P., W.B., Lee, X.M. Lu, diamond turning of silicon substrates in ductile regime, *J. Mats. Proc. Tech.* 73 (1998) 42-48.

Notis, Michael R., Deformation Mechanism Maps - A review with applications, Materials Research Center and the Dept. of Metallurgy and Materials Science, Leheigh University, Bethlehem, Pa, 18015

Patten, John A., High Pressure Phase Transformation Analysis and Molecular Dynamics simulations of single point diamond turning of germanium, Ph.D. Dissertation, North Carolina State University, 1996.

# Evaluation of Effective CMP Conditions by Estimation of Pressure Distribution on Semiconductor Wafer

Yoshiaki SASAKI*, Hideki AOYAMA*, Ichiro INASAKI*
Hiroo MIYAIRI**, Hiroshi SHIBAYA**
* Department of Mechanical Engineering, Keio University
3-14-1 Hiyoshi, kohoku-ku, Yokohama, Kanagawa 223-8522, JAPAN
** Mitsubishi Materials Corporation
1-297, Kitabukuro-cho, Omiya, Saitama 330-0835, JAPAN

## 1. Introduction

In order to make a highly integrated LSI, the circuits of patterned metal layers are constructed on a semiconductor-wafer as three-dimensional structure. In the processes of constructing three-dimensional circuits, the insulating films made between the circuit layers have to be made planar before depositing patterned metal layers on it. CMP (Chemical Mechanical Polish) is the most effective technology for planarizing semiconductor-wafer surfaces. For improving the functions and performance of a CMP machine, the various conditions, such as polishing pressure, career form, polishing pad (hardness, elasticity, property of a pad surface, material, structure), ingredients of slurry (polishing grain, grain diameter, and PH), the edge shape of a wafer, the backing film, and so on, have to be taken into consideration. More efficient processing conditions for CMP are decided by know-how and knowledge obtained by repeating basic experiments. However, since it takes much time and manpower to determine the CMP conditions via experiments, it is required to narrow the conditions down by computer simulations. It is considered that polish of insulating films is mechanically caused than chemically with regard to CMP. Since pressure applied on a semiconductor-wafer surface is the most essential factor about the rate of mechanical polish, it is indispensable to obtain pressure distribution on the wafer surface in order to estimate the polishing rate.

In this paper, pressure distribution applied on the wafer surface from the polishing pad is computed by FEM (Finite Element method) in order to estimate the polishing rate on the various CMP conditions: the retainer ring, the shape of the wafer edge, the proportion of pressures applied on the wafer and the retainer ring, and materials of the backing film. Then, the CMP conditions are evaluated from the viewpoint of the polishing rate.

## 2. Analysis Results

Pressure distributions influenced by the shape of the wafer edge, utilization of the retainer ring, and the backing film are analyzed by FEM. The basic FEM model is described as follows:

- The diameter of the wafer is 8 inches.
- The upper and lower pads are disks with the double diameter for the wafer.
- The wafer and the pads are concentric and the bottom face of the lower pad is completely fixed.
- The friction coefficient between the wafer and the upper pad is 0.3.

### 2.1 Influence of the Shape of the Wafer Edge

A semiconductor-wafer has been chamfered although chamfering makes the area of a semiconductor-wafer small. Pressure distributions on the wafer surfaces with the different edge shapes as shown in Fig. 1 (a) and (b) are computed by FEM, and then influence of the shape of the wafer edge for the polishing rate is

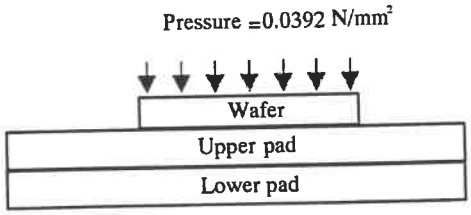

(a) Non-chamfered wafer model

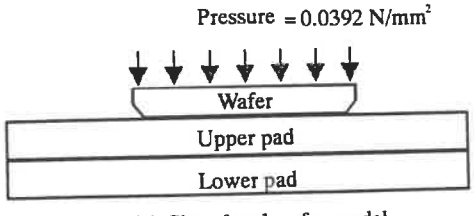

(b) Chamfered wafer model

Fig. 1 FEM model for investigating wafer chamfering

investigated.

In the FEM analysis, the chamfering widths of the models shown in Fig. 1 (a) and (b) are 0.0 and 0.3 mm, respectively. And the uniform pressure load of 0.0392 N/mm$^2$ (0.4 kgf/cm$^2$) is applied on the upper surface of the wafer. The poison's ratio and Young's modulus of the upper pad are 0.44 and 1900.0 N/mm$^2$, respectively, and, those of the lower pad are 0.49 and 200.0 N/mm$^2$, respectively.

The results of pressure distributions on the wafer surfaces are shown in Fig. 2. Since the chamfered wafer can get more uniform pressure distribution than the non-chamfered wafer, it is conformed that chamfering of the wafer edge is effective for obtaining more uniform polishing rate on the wafer surface.

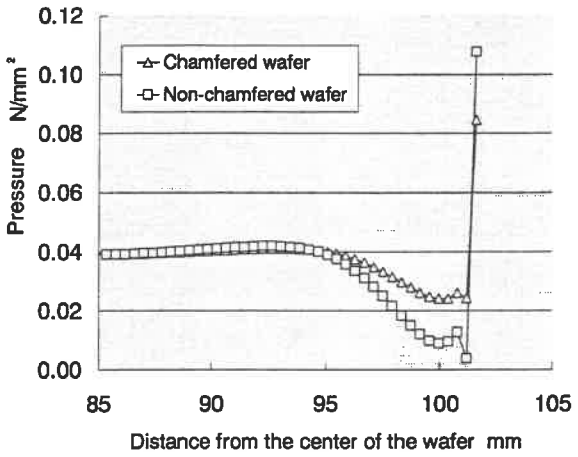


Fig. 2 The influence of pressure distribution by chamfering

## 2.2 Influence of Retainer Ring

One of the roles of the retainer ring is to control the position of a wafer in polishing processes. In addition, it is expected that the retainer ring will have effectiveness for making uniform pressure distribution on a wafer.

Figure 3 shows the FEM model for investigating influence of the retainer ring. Ideally, the inside diameter of the retainer ring should be definitely equal to the wafer diameter. However, actually, the inside diameter of the retainer ring is more than 0.4 mm for the wafer diameter under considering scatter of the wafer diameter and avoiding contact between the wafer and the retainer ring. In the FEM analysis, the pressure load applied on the wafer is fixed and the one applied on the retainer ring is changed. In specifically speaking, the pressure load of 0.0392 N/mm$^2$ (0.4 kgf/cm$^2$) is applied on the upper surface of the wafer and the pressure loads of 0.0196, 0.0392, and 0.0784 N/mm$^2$ are applied on the retainer ring. In other words, the proportion of pressure loads applied on the wafer and the retainer ring are 1:2, 1:1, and 2:1.

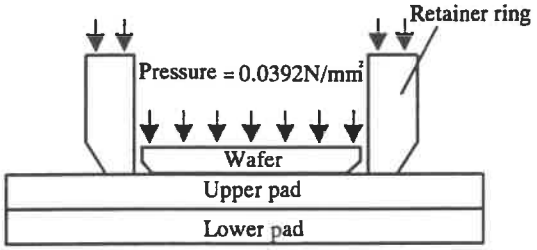


Fig. 3 FEM model for investigating retainer ring

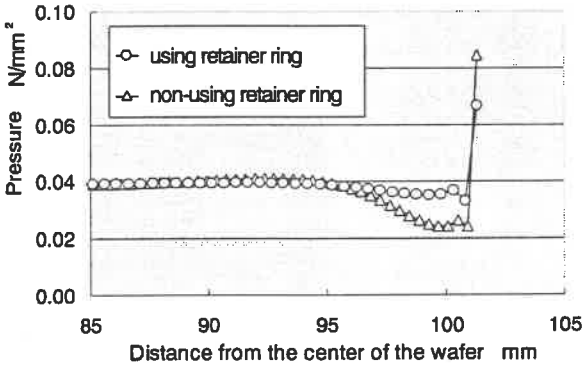


Fig. 4 The influence of retainer ring on pressure distribution

Figure 4 shows the pressure distribution on the wafer surface in the cases of using and non-using the retainer ring. In the case of using retainer ring, same pressure load with the wafer was given on the retainer ring. As in Fig. 4, more uniform pressure distribution is obtained by using the retainer ring. Thus, it is confirmed that the retainer ring is effective for the uniformity of the pressure distribution on the wafer surface. Figure 5 shows the results of the pressure distribution in changing the proportion of pressure loads applied on the wafer and the retainer ring. When the pressure loads applied on the wafer and the retainer ring remain the same; that is, the proportion of the pressure loads is 1:1, the pressure distribution is most uniform among the three pressure proportions (1:1, 2:1, and 1:2). Figure 6 shows the experimental results of remained film thickness after polishing in the cases of changing the pressure loads on the wafer and the retainer ring. As shown in Fig. 5 and Fig. 6, the pressure distributions computed by FEM have a close tendency to the distribution of the remained film thickness. Thus, it is understandable that the polishing rate in CMP can be estimated from the pressure distribution on the wafer surface.

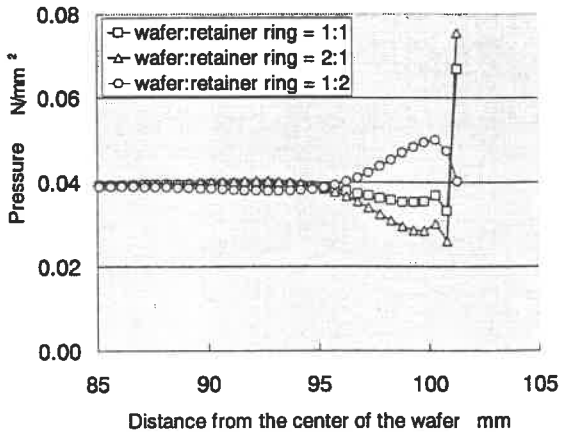


Fig. 5 The influence of pressure loads applied on the wafer and the retainer ring

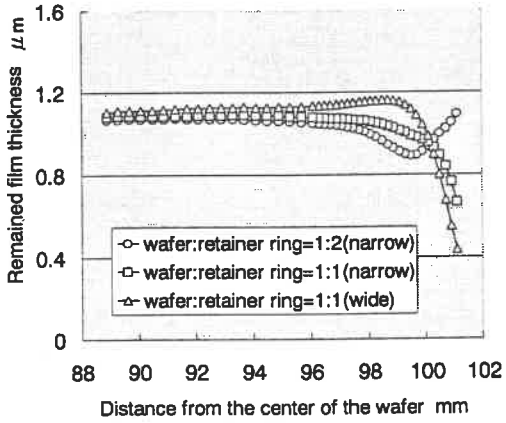


Fig. 6 The experimental results of remained-film thickness

## 2.3 Influence of Backing-film

The backing film is inserted between the wafer and the stiff carrier as shown in Fig. 7 in order to absorb the influence of undulation on the wafer surface and uneven thickness of the wafer for obtaining uniform pressure distribution on the wafer surface. For the purpose, polyurethane with very large elastic modulus is utilized as the material of the backing film. Since the elasticity of the backing film definitely affects on the pressure distribution of the wafer, the pressure distributions for the models shown in Fig. 7 with the different elastic modulus of the backing film are calculated. The elastic modulus was selected as 0.05, 10.0, 100.0, 200.0, 500.0 and 2000.0 N/mm$^2$. In the FEM analysis, two types of the models were considered. One is the analysis for the static model in which static pressure is given on the stiff carrier, and the other is the analysis for the dynamic model in which the wafer is transferred by applying force to the stiff carrier.

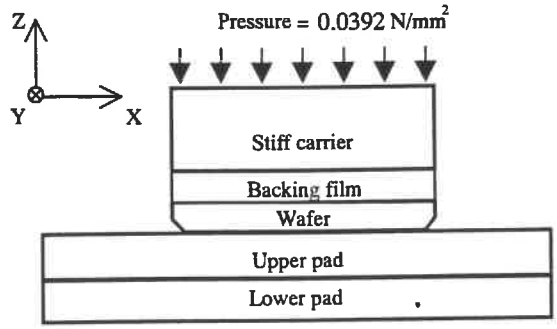


Fig. 7 FEM model with the backing film

Figures 8 and 9 show the pressure distributions on the wafer obtained for the static model and the dynamic model, respectively. In Fig. 8, there is no appreciable change in the pressure distribution even if the elasticity of the backing film is largely changed. On the other hand, as in Fig. 9 (a), the pressure distribution of the wafer in the transferring direction of the wafer is remarkably affected by the elasticity of the backing film. Figure 10 shows the displacement of the wafer surface in the Z-direction in the dynamic model. In the results, the deformation of the wafer is the smallest in the case that the Young's modulus is 100 N/mm$^2$. In addition, the diameter of the area in which pressure is within 90 - 110 % for the pressure on the wafer center is investigated in the dynamic model. Table 1 shows the diameter for the model with different young's modules of the backing film. From the results shown in Fig. 10 and Table 1, it seems to be clear that the backing film should have the Young's modulus of 100 N/mm$^2$ from the viewpoints of wafer deformation and uniformity of pressure distribution.

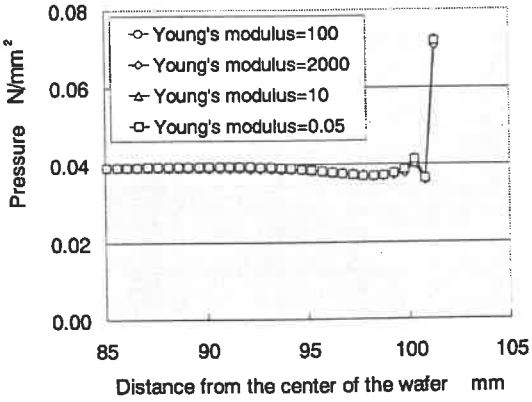


Fig. 8 Pressure distribution of the static model ( The wafer is fixed )

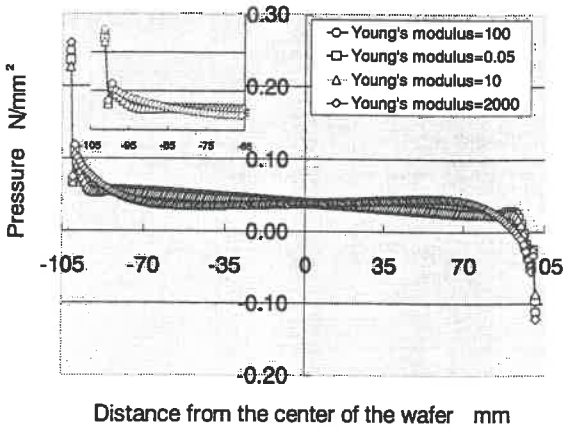


(a) The pressure distribution in the transferring direction

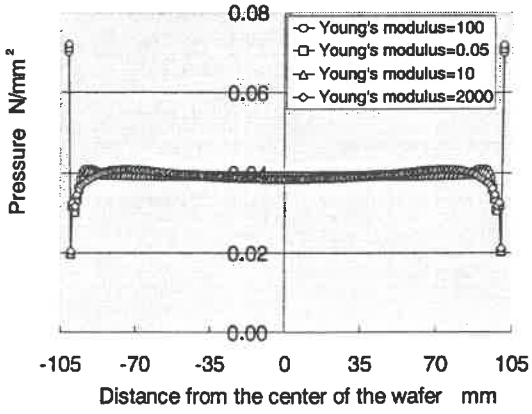


(b) The pressure distribution in the perpendicular direction for the transferring direction

Fig. 9 Pressure distribution of the dynamic model ( The wafer is transferred )

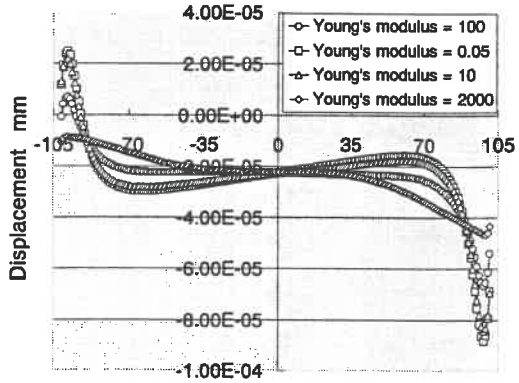


Fig. 10 The displacement in Z-direction in the transferring direction

Table. 1 Diameter of the area with the pressure of 90- 110 % for the pressure at the wafer center

| Young's modulus [N/mm²] | Diameter [mm] |
|---|---|
| 2000 | 42.5 |
| 500 | 46.6 |
| 200 | 67.9 |
| 100 | 120.5 |
| 10 | 24.3 |
| 0.05 | 16.2 |

## 3. Conclusion

In this study, pressure distribution on the wafer surface that is most important factor in CMP is calculated by the FEM analysis under the various conditions in order to estimate polishing rate of insulating films on a semiconductor-wafer and to evaluate CMP conditions. This study is summarized as follows:

- It is effective for the uniformity of the pressure distribution to chamfer semiconductor-wafers.
- The retainer ring is effective for the uniformity of the pressure distribution on the wafer surface.
- The pressure distributions on the wafer surface computed by FEM have close tendency to the distributions of the remained film thickness. Thus it makes clear that the polishing rate in CMP can be estimated from the pressure distribution on the wafer surface.
- It is effective for the uniformity of the pressure distribution to take the backing film with large elasticity into a CMP machine.

## References


1) *Sivaram, S. Proceeding Of The 1991 Symposium On Advanced Metallization And Processing For Semiconductor Devices And Circuits, April, 1992.*
2) *Rentein. P. Advanced Metallization For ULSI Applications In 1994, P. 153, 1995*

# Pressure Distribution at the Silicon/Polishing Pad Interface

Lei Shan, Joseph Levert and Steven Danyluk
The George W. Woodruff School of Mechanical Engineering
Georgia Institute of Technology
Atlanta, GA 30332-0405

## ABSTRACT

The polishing of silicon is typically a three-body abrasive problem, where the silicon is held against a compliant pad and drags a slurry into the interface. Our previous work (Ref.1) has shown that chemical-mechanical polishing of silicon wafers generates a suction force at certain regions of the interface, between the silicon wafer and the polishing pad. This suction force can be of the order of 50~100% of the normal load applied during polishing. The distribution of suction (negative) pressure has been measured over the typical range of normal loads and velocities used in the polishing of silicon wafers. The results show that the leading two-thirds of the wafer exhibits a negative pressure, and the trailing third a positive pressure. This pressure distribution could result in a non-uniform polished surface. The interfacial pressure has been modeled using the contact stress analysis, interfacial liquid film thickness calculation, and the fluid mechanics. The results of this model fit the experimental results to within a factor of two.

## INTRODUCTION

Chemical Mechanical Polishing (CMP) is an important integrated circuit fabrication process which produces smooth (~1nm), flat and uniform (~ 5μm) surfaces. The fundamental understanding of CMP mechanisms is limited, and reduces CMP predictability in manufacturing. One aspect of CMP for the planarization of IC interlayer dielectric involves the interface mechanics.

Previous research showed two trends of CMP interface mechanics. One trend suggested that the workpiece (silicon wafer) is separated from the polishing pad by a hydrodynamic film of slurry and polishing is done by abrasive collision. The other said that the hydrodynamic effect is not strong enough to separate workpiece from pad and pad abrasion dominates the polishing process. Our experiments on CMP could not confirm hydrodynamic polishing. Unexpectedly, suction (negative pressure) forces were always found in these experiments. To thoroughly understand the physical mechanism of the suction and model the CMP process to address the need of precise production prediction, interfacial pressure measurements were done and interface mechanics was closely studied. In the following parts of this paper, the experimental setup and methodology for pressure measurement, results, physical explanation, and modeling are described.

## EXPERIMENTAL DETAILS

The apparatus shown in Figure 1, was a commercial bench top polishing machine (Logitech model PM4 built in 1994) with custom-built additions. The polishing machine had a 305 mm (12 inch) diameter stainless steel turntable driven by a 1/3 horsepower speed controlled DC drive. Speed was controllable to within 1 rpm from 5 to 70 rpm and the turntable could withstand 450 N vertical loads as well as 450 N horizontal (frictional drag) loads. Polishing pads were bonded onto the turntable with sheets of double sided pressure sensitive adhesive. A custom-built overhead structure was added to support samples and to

mount instrumentation. The pressure of the slurry trapped at the 'wafer/pad' interface was measured with the fixture show in Figure 1, in place of a wafer. This diagram shows the top and side view of a 100 mm diameter, 25 mm thick, stainless steel disk with 16 – 0.4 mm diameter holes drilled through to the 'pad/wafer' interface. The array of holes of the pressure fixture can be aligned at any desired direction during CMP. Interfacial pressure was measured by connecting the holes with an electronic pressure transducer (Crystal, Inc. part no. 1522) which has a resolution of 2.5 mm (0.1 in) of water head pressure. Each pressure measurement was taken over a time period of up to 10 minutes to allow the readings to stabilize. Data was recorded manually. The typical polishing pad used in the experiments was a commercially available (Rodel IC1000), impermeable, void filled, cast polyurethane sheet approximately 1.25 mm thick. And after conditioned with 80μm grit tool, it has an average surface roughness of about 5μm. For comparison, a sheet of mylar tape was attached on the top of the pad which has an average surface roughness of about 0.5μm and decreases the friction coefficient from 0.4 to 0.1. During most of the pressure measurements, the pad was flooded with water .

## RESULTS AND DISCUSSION

1. **Pressure distribution (data interpolation)**
   Each measurement represents pressure data along two perpendicular lines across the pressure fixture, tangential and radial with respect to the motion of the turntable. The whole interface was meshed by 16x16 square cells, and based on the two sets of data (16x2=32), pressure values in other cells at the interface can be interpolated. Some random points were tested to verify the precision of the interpolation. Figure 2 shows a typical pressure distribution mapping at the interface. It is obvious that the leading two-thirds of the wafer exhibits a negative pressure, and the trailing third a positive pressure. Finally, an average value of the interface pressure can be easily obtained by summing up all the numbers in all cells and divided by 208. Negative average pressures were always obtained with the variation of magnitude depending on pad type, pad condition and surface roughness, and relative velocity (turntable speed). This suction force can be of the order of 50~100% of the normal load applied during polishing.

2. **Pressure vs. polishing variables**
   Although, in most cases, negative pressure can be measured during CMP, the pressure distribution and magnitude varies with polishing variables. We experimented on turntable speed, pad elasticity and surface roughness, and normal load, and tried to figure out the process dominants. Figure 3, 4, 5 are comparisons of pressure measurements with different input of variables. By elimination of the edge effects, for the same pad condition and normal load, the magnitude of the pressure is nearly proportional to the relative velocity. This can be monitored by either changing the turntable speed and looking at the pressure at a certain point, or keeping the turntable speed constant and looking at different location along the radial center line. Also, with the increase of turntable speed the zero pressure point shifts towards the trailing edge significantly (Figure 3). By comparing the results of the IC1000 pad (Ra=5μm) and the mylar tape topped pad (Ra=0.5μm), we can see that the roughness of pads contributes significantly to the generation of the negative pressure. For some turntable speeds and pad conditions, for example, when normal load is within a certain range, the interfacial pressure distribution is not affected (Figure 5).

## PHYSICAL EXPLAINATION AND MODELING

The contact stress between a rigid wafer and a compliant pad (Ref. 2) is not constant but has a bowl shape, i.e. high stress at the edge and low stress at the center. And with the motion of one part, due to the

shear stress caused by the friction force, the contact stress distribution shifts backwards, behind the leading edge of the moving surface (Figure 6). The applied load between the two surfaces is supported by asperities and there exists a liquid film at the interface, which varies with the contact stress, i.e. thicker film at the center and thinner film at the edge (Figure 7). We know from Ref. 3 that a divergent gap always leads to negative pressure and a convergent gap always leads to positive pressure. This is the reason for the negative pressure at the leading edge and positive pressure at the trailing edge. The pressure magnitude and distribution vary with relative velocity, pad elasticity and roughness, and other variables.

By using the above physical model, the pressure distribution along the tangential central line can be calculated as follow:

$$p(x) = 6\mu U\left(\int_{-a}^{x}\frac{dx}{h^2} - \frac{\int_{-a}^{a}\frac{dx}{h^2}}{\int_{-a}^{a}\frac{dx}{h^3}}\int_{-a}^{x}\frac{dx}{h^3}\right)$$

where, h is the liquid film thickness,

$$h(x) = -\sigma\ln\left(\frac{1.13(1-\nu^2)s(x)}{\eta E R^{1/2}\sigma^{3/2}}\right)$$

and s is the contact stress,

$$s(x) = \frac{P\cos\pi\gamma}{\pi(a^2-x^2)^{1/2}}\left(\frac{a+x}{a-x}\right)^{\gamma}, \qquad \cot\pi\gamma = -\frac{2(1-\nu)}{f(1-2\nu)}$$

Refer to Figure 8 for an example pressure distribution obtained by this model.

## CONCLUSION

The results show that the leading two-thirds of the wafer/pad interface exhibits a negative pressure, and the trailing third a positive pressure. This pressure distribution could result in a non-uniform polished surface. However, by understanding the interface mechanics and handling process parameters properly, this non-uniform effect can be moderated or eliminated.

Although the results and conclusions here discussed are derived from CMP process analysis, it can also be applied to other similar problems, such as machining and other elasto-hydrodynamic problems.

## REFERENCE


1. J. Levert, R. Baker, F. Mess, R. Salant and S. Danyluk, "*Mechanisms of Chemical-Mechanical Polishing of $SiO_2$ dielectric on Integrated Circuits*", to be published in Tribology Transactions, 1998

2. K. L. Johnson, "*Contact Mechanics*", P41, Cambridge University Press, Cambridge, UK, 1985

3. Bernard J. Hamrock, "*Fundamentals of Fluid Film Lubrication*", P141-165, McGraw-Hill, 1994

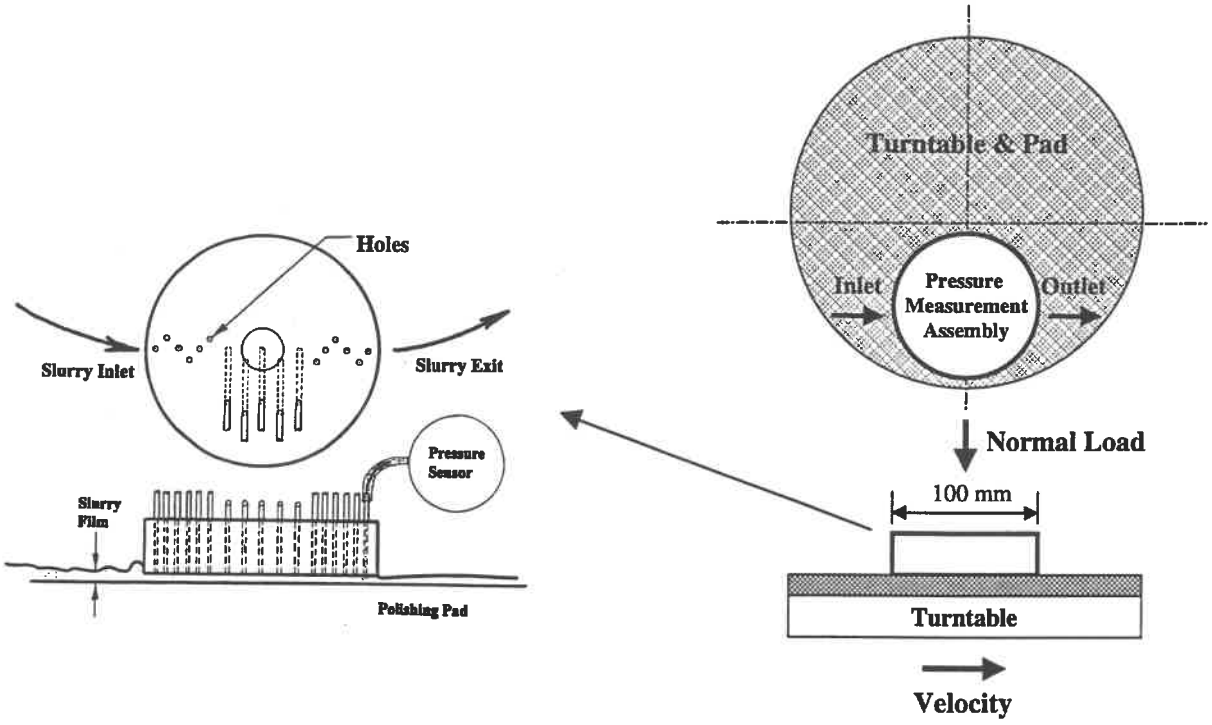


Figure 1. Experimental setup and schematic diagram of top and side view of the slurry pressure measurement fixture. The sample fabricated from stainless steel has 16-0.4 mm diameter holes at the pad interface.

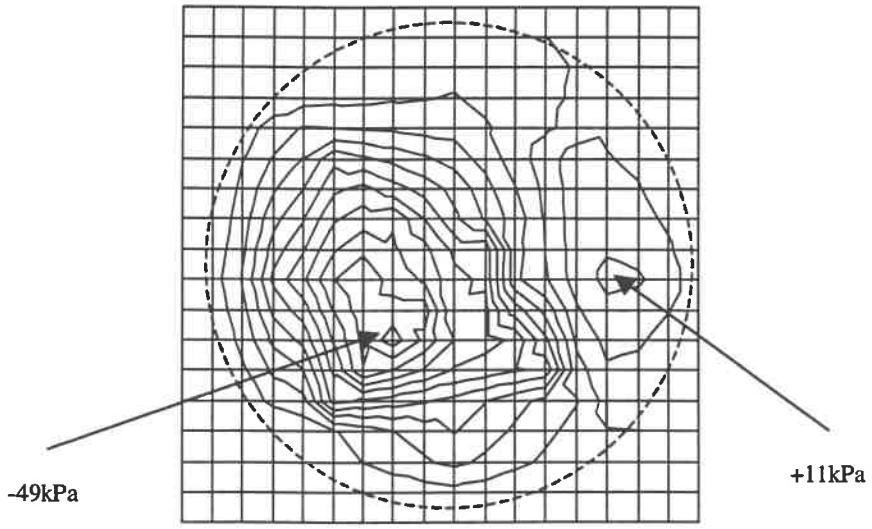


Figure 2. A typical pressure distribution at the interface (20kPa normal load, IC1000 pad, 0.43m/sec)

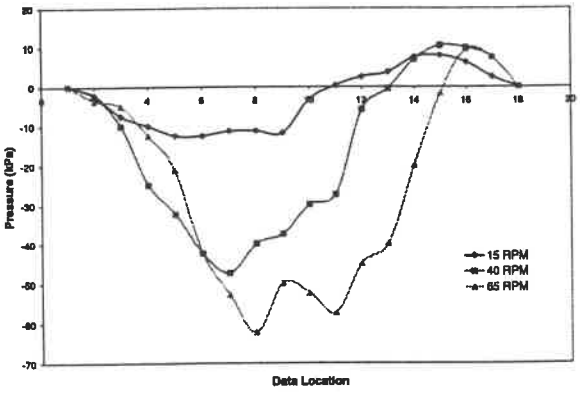


Figure 3. Tangential pressure distribution vs. velocity

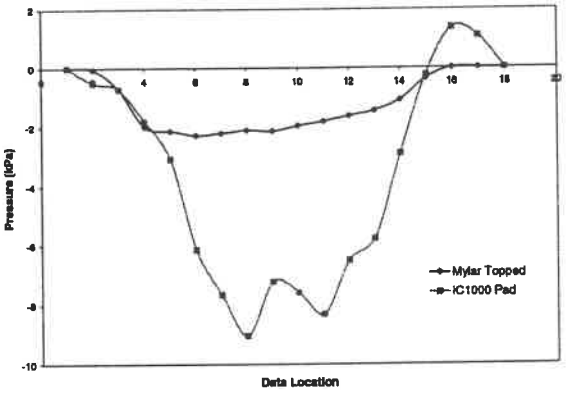


Figure 4. Tangential pressure distribution vs. pad types

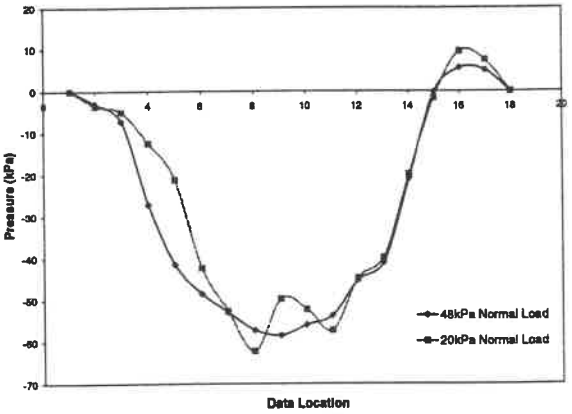


Figure 5. Tangential pressure distribution vs. loads

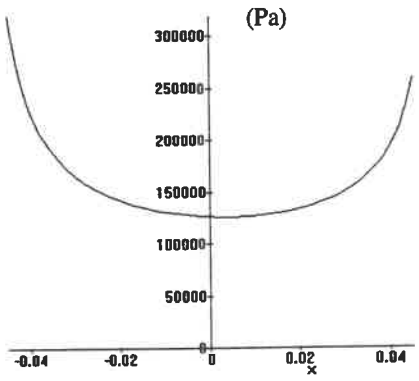


Figure 6. Contact stress distribution along the central line

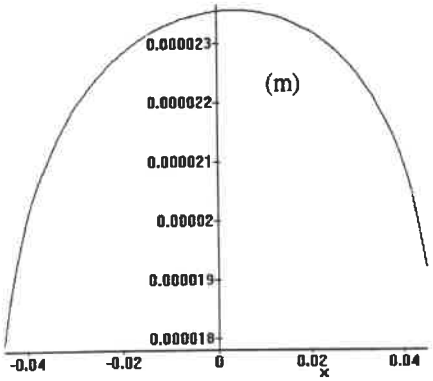


Figure 7. Liquid film thickness along the central line

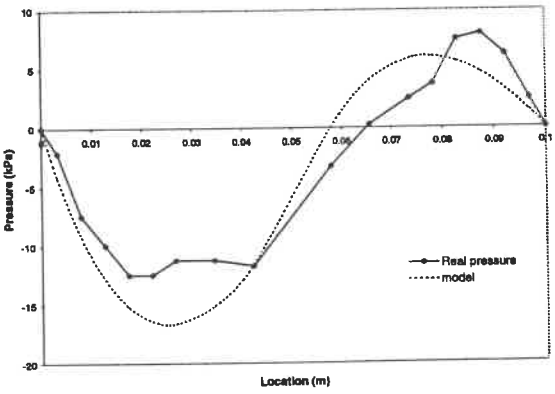


Figure 8. Pressure modeling result vs. real value (0.16m/sec, 20kPa load, IC1000 pad)

# FABRICATION OF 1KG SINGLE CRYSTAL SILICON SUPER-PRECISION SPHERES (BALLS) FOR THE AVOGADRO'S EXPERIMENT

Achim J. Leistner
CSIRO Telecommunications and Industrial Physics
PO-Box 218 Lindfield NSW 2070 Australia

## ABSTRACT

One kilogram balls of hyper-pure single crystal silicon (SCS) have become an essential artefact in the redetermination of the Avogadro constant, and the redefinition of the international standard of mass, the kilogram. A ball is the most suitable three dimensional artefact, because, to determine the volume of a near perfect ball with a negligible error of sphericity, requires one measurement only, its diameter. The volume of a near perfect ball of known deviation from sphericity on the other hand, may be calculated numerically. Cubes and cylinders are unsuitable, as they have sharpe edges and corners which are sucepteble to damage and many measurements are necessary to establish their volume which can lead to a large error budget.

The Avogadro's experiment involves the measurement of three quantities, the density, the lattice parameter, and the molar mass of a suitable single crystal, to enable the Avogadro's constant to be determined to an accuracy of about one part in $10^8$. Silicon has so far proved to be the best material for the experiment. The SCS balls that are required must be of extraordinary precision and quality. The balls should weigh 1 kg within ± 50 mg, have an error of roundness ( total sphericity error TSE) of <100 nm peak to valley (P-V), and a surface that is macroscopically and microscopically smooth, free of scratches, residual grinding marks and any subsurface damage. A formidable challange.

Considerable expertise in the fabrication and measurements of balls was developed in our Laboratory over many years. Hollow and solid balls have been fabricated from fused silica, Zerodur and glass over a number of years for use in experiments to measure the density of water. Balls of about 94 mm diameter and a nominal weight of 1 kg made of fused silica, Zerodur and SCS, have since been produced for a number of laboratories - the PTB (Germany), the NRLM (Japan), the IMGC (Italy), the OFMET (Switzerland) and the KRISS (Rep. of Korea). A SCS ball was fabricated in 1987 for researchers at IMGC (Italy) to be used in the experiment to measure the Avogadro constsant [1]. The experience gained from successful completion of this ball formed the basis for further substantial improvements in the fabrication process and measurements of roundness, bringing the accuracy of the balls within the error bars which satisfied the requirements for the Avogadro experiment.

The stages of grinding and polishing in the fabrication of SCS balls are much the same as for other precision optical component made from crystalline or amorphous materials:

(a) rough shaping, using diamond grinding tools and coarse loose silicon carbide abrasives,

(b) fine grinding, using aluminium oxide loose abrasives,

(c) polishing, using a matrix such as pitch and a suitable oxide.

The ball fabrication begins with a cylindrical ingot of hyper-pure SCS, 100 mm in diameter and 100 mm long. A universal two vertical spindle (2VS) glass grinding machine and a cup wheel diamond cutter are used for the first grinding (preshaping) operation, followed by manual rough grinding in a conical tool of mild steel which rotates on a suitable spindle. Conical shaped grinding and polishing tools as shown in Fig.1 are used for all the loose abrasive grinding and polishing operations. The conical tool adjusts continously as the ball grinds its way towards the smaller end. While grinding operations are carried out manually in a single conical tool that rotates on a spindle, polishing is performend between two conical tools and is assisted manually [1].

A high level of symmetry in the ball's shape must be maintained right from the beginning of generating roundness. After preshaping, rough grinding using loose abrasives begins with 120-grit silicon carbide and finishes with 400-grit. The operation takes several days and produces a ball with a P-V error of 1 μm to 4 μm, representing a combination of out of roundness and surface roughness. Eight areas of high specularity can be observed on the ball surface at this stage. These are produced by the different fracture modes of the abrasive due to the non uniform elastic properties (hardness) variations of the silicon crystal. The centre of each area of high-specularity shows them to be positioned at the imaginary corners of a cube located inside the ball so that its corners just reach the surface of the ball. A measurement of the total sphericity error (TSE) of the ball at this stage indicated that the eight spots of high specularity were coincident with the

sphericity error surface in the order low-to-high. Laue backscatter x-ray tests of the ball normal to the centre of the spots of high specularity were consistant with the orientation of the spots along the <111> axes, indicating alignment with the corners of the silicon cubic structure.

With fine grinding begins the more critical process that determines the final precision of roundness and surface quality of the ball. Six grades of successively finer powders of Microgrit aluminum oxide from 25 μm to 1μm are used. Non corroding and in general more forgiving (less chance of scratches) brass conical tools are used for the first two grades of 25 μm and 15 μm grits, producing a substantially rounder ball with a P-V error between 100 nm and 300 nm TSE. When grinding with abrasive particle sizes below 10 μm it becomes increasingly difficult to prevent the 1 kg ball from making contact with the relatively small surface of the grinding tool, with the result that metal is picked up by the ball surface which causes scratching. Control of the ball's diameter at all stages of grinding from the coarser to the finer grits is crucial, because only a predetermined amount of material can be removed with each grit size in order to achieve the final correct size and mass of the ball.

The problem of scratching can largely be overcome with the use of grinding tools made from glass. A special Pyrex glass ring grinding tool arrangement was constructed which is submersed in a bowl containing the aluminium abrasive slurry, that is providing continous and uniform feed. Fine grinding with 1μm aluminum oxide prior to polishing is important for three reasons: (a) it optimises and maintains roundness and symmetry of the shape of the ball to <100 nm (b) it minimises the residual roughness and sub-surface damage (SSD) of the surface and (c) substantially reduces the time to completely polish the ball. These conditions are important prerequisits in determining more accurately the final size, roundness and quality of the ball. Also, a ball ground with 1μm-grit produces a specular surface at normal incidence and can be tested using the WYKO TOPO 3D noncontact surface profiler: a typical result shows an rms value of 0.344 μm. To avoid (SSD) a sufficiently thick layer is removed from the ball surface with every grit size down to 1 μm (surface layer removed = three times everage grit size). This amount has proved to be adequate as has been shown by Scanning Transmission Electron Microscope (STEM) examination. Fracture depth damage from 1μm grit was shown to be around 0.3 μm.

After fine grinding with 1μm-grit a systematic inspection is made of the surface for scratches using a stereo microscope with X20 magnification, followed by a comprehensive measurement of roundness to establish the TSE. Balls invariably have a strong cubic symmetry and a TSE of between 100 nm to 200 nm as shown in Fig 2 a&b. It is interesting to note that the low-to-high regions are now clearly reversed from the measurement in the rough surface condition and are ordered faces-edges-corners [2].

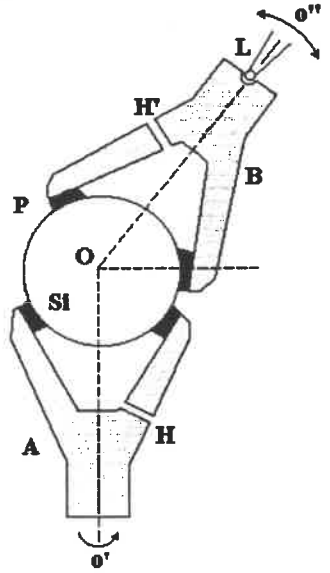


**Figure 1.** Polishing arrangement of cone A and B. Cone A is rotating about axis O-o'; and cone B around axis O-o″, which is driven by a ball and socked L of an oscillating arm (not shown). H' and H are polishing slurry feed and drain holes respectively. P shows the pitch ring and Si is the SCS sphere.

A surface layer of 0,004μm to 0.006 μm is removed to produce a completely polished ball free of all residual grinding marks and sub-surface damage. To eliminate the possibility of introducing subsurface damage that may be caused by polishing, a super-polishing process is used from start to finish, employing pitch as the polisher matrix. A narrow 15 mm wide ring of pitch about 4 mm thick is placed over the part of the conical lap surface which previously was the grinding face. Two or three 2 mm wide circular groves and three radial slots spaced at 120 degree are cut in to the pitch to accomodate slurry and pitch flow. The hardness of pitch is not critical, however, when polishing SCS two parameters are of great importance in achieving a completly polished, scratch free and supersmooth surface: (a) substantial polishing pressure for effective removal of material and (b) maintaining good contact between the lap and ball at all times for producing a high quality surface finish, hence a harder pitch is the more desireable. To maintain a good contact between lap and sample, the polishing of the silicon ball is carried out between two conical laps, the lower one rotating on a spindle, the upper one mounted on an

oscillating arm with a ball-and-socked connection as shown in Fig.1. Numerous conditions during polishing contribute to an imbalance of friction experienced by the two conical pitch laps against the ball, and this requires the ball to be manipulated by hand for achieving and maintaining a true random rotation, a process that cannot be overstated in its importance for achiving a round ball. The process requires much stamina, since the load on the polishing arm is gradually increased from 5 kg to 15 kg during each polishing cycle of 20 to 30 minutes.

It takes 10 hours to completly polish a ball free of all residual grinding marks, which reduces its diameter by 0.008 mm to 0.012 mm. The polishing agents used are *ULTRASOL 200A* colloidal alumina [4] and a colloidal suspension of titanium dioxide (A-E) [5], having a pH of 3.5 and 7-8 respectively. *ULTRASOL 200A* is used for the first 5 hours of polishing or until the ball is about 75% polished. The final polishing is carried out with titanium dioxide, which reduces the risk of surface marks.

The finished balls appear overall spherically with only small asymmetric features like ovality present as shown in Fig 3. However, close inspection reveals the presence of identifiable and repeatably measureable topographical features on the surface. In at least one case good correspondence between the angular separation of surface peaks and the corners and edges of a cube was noticed, indicating that the final topography of the error surface is still correlated with the silicon crystal latice. According to J.G.Collins et al [6] the predicted effect of Young's modulus variations on roundness of the silicon ball during fabrication is in remarkable agreement with the observed shape of the ball. If uniform grinding and polishing conditions exist on the surface of the silicon ball, the number of atoms removed will vary in any direction as the inverse of Young's modulus, ie wear will be least along the <111> direction and greatest along the <100> direction. The cubic pattern superimposed on the sphere and observed experimentally is explained in terms of the variation of Young's modulus with crystal orientation and the relationship between Young's modulus and fracture energy.

The two-dimensional high-precision roundness measurement is based on the excellent repeatability of the Talyrond 73 spindle, high-resolution automated data collection, and the subsequent application of error sepparation and data reduction algorithms [2,3].

The Talyrond 73 is operated in a well controlled laboratory environment, with shielding to reduce air currents and thermal drift, and a temperature of 20°C with a ±0.1 C° stability over a two hour period. Geometrically the radial signal that is collected is a combination of the out-of-roundness of the ball, the out-of-roundness of the spindle and the eccentricity between their symmetry axes.

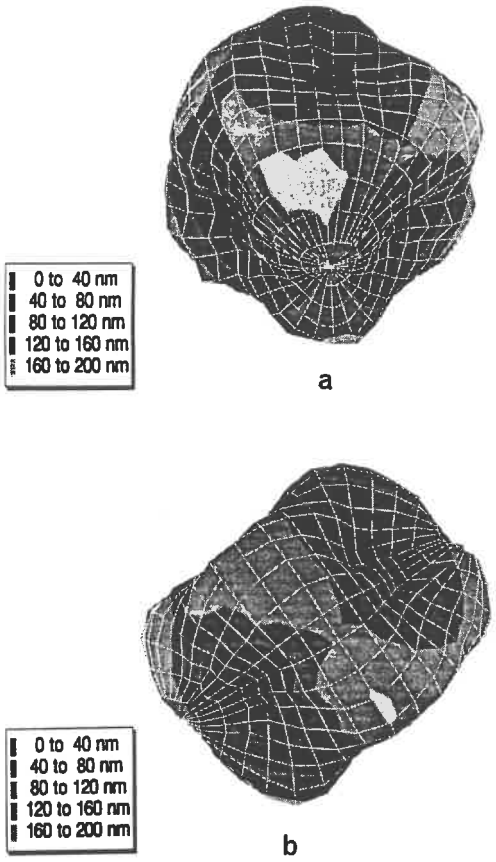


**Figure 2.** Showing two 3D views a and b of a fine ground SCS ball (1µm grit finish) with least-square sphere error P-V of 178 nm: (a) facing a cube corner, (b) facing a cube edge.

For a sphericity measurement consisting of multible profiles of the ball, the spindle error is first measured using a multistep method, profiling of 12 angular orientations at 30° intervals around a vertical axis of symmetry, and the data analysed to separate the spindle and the ball equator out-of-roundness errors. Following the multistep method of accuratly characterising the spindle, 18 meridians from 0° to 170° in 10° intervals are determined by subtracting the known spindle error. The set of 2D profiles is then formed into a 3D data set including the equator (from an arbitrary position) and each meridian (starting from the equatorial line) all running from 0° to 359°. The standard uncertainty in measurement of P-V sphericity for balls of around 50 nm error is typically 4 nm with 500 degrees of freedom. Shape characterization of the topography of the balls by precise measurements of roundnes was instrumental in the optimization of

parameters during the grinding and polishing process and led to rounder and smoother SCS balls. In turn we had clear evidence that measurement accuracy is a function of ball quality because the ultimate minimum value of the Sphericity Test Function used to fit the 2D profiles together to generate the 3D data becomes smaller with the total sphericity error and surface smoothness. Figure 4 shows a 2D noncontact surface profile analysis of a random sample of a ball's surface with a typical microroughness value of around 0.1 nm rms.

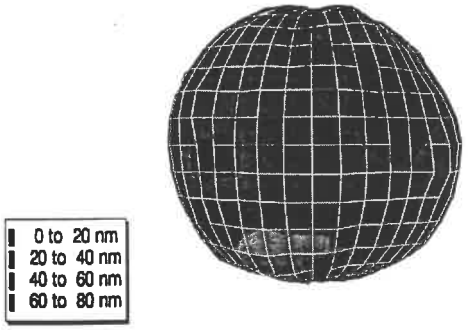


**Figure 3.** 3D error surface view of completed SCS ball.

After polishing, the balls have a relatively thick surface oxide layer in the range of 5 nm to 12 nm thick, which so far has defied explanation. Flat surface samples of SCS polished using identical polishing conditions to the ones used for polishing the balls have an oxide layer thickness of only 0.15 nm to 0.20 nm. Work continues to quantitatively and precisely determine all surface conditions and parameters of the ball such as the surface chemical composition, possible SSD and surface modification caused by polishing and a possible amorphous interface layer between the oxide layer and the silicon bulk material.

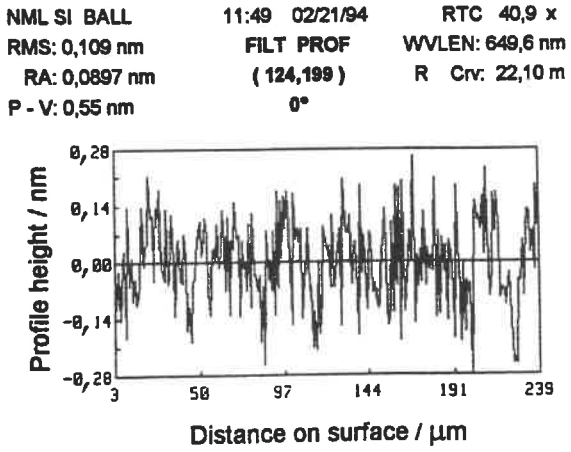


**Figure 4.** Typical *WYKO TOPO* 2D line profile analysis of completely polished SCS ball surface.

We accept that a cubic symmetry will exist in a finished SCS ball no matter how close to perfectly round the ball may be. However, it could also be that the perfect symmetry and the nonuniform elastic properties of the SCS will be the guiding parameters which will make a near perfect spherical ball the ultimate reality.

Key Words: single crystal silicon sphere (ball), Avogadro constant, roundness measurements, super-polishing SCS

References

[1] Leistner A.J. and Zosi G.: Polishing a 1-kg silicon sphere for a density standard. Appl. Opt., Vol.26, 4.Feb. **15,** 1987.

[2] Leistner A.J. and Giardini W.J.: Fabrication and Sphericity Measurement of Single-crystal silicon spheres, Metrologia, 1994, 31. INVITED PAPER International meeting on "The Avogadro Constant and the Representation of the Silicon Mole." March 1994. IMGC, Turino, Italy

[3] Giardini W.J., Miles J.R.: The Precision Measurement of Roundness at DAP - Melbourne Branch, Technical Memorandum M 12, CSIRO Division of Applied Physics, June 1991.

[4] Solution Technology, INC., Matthews, N.C. 28106, USA.

[5] Seckold J.A.: Optical Polishing with Titanium Dioxide, Appl. Opt., 1976, **15**, 1693.

[6] Collins J.G., Giardini W.J., Leistner A.J., Kenny M.J.: The Influence of Young's Modulus on Roundness in Silicon Sphere Fabrication, IEEE Transactions on Instrumentation and Measurements, Vol. 46, **2**, 1997, 572.

# Acoustic Emission Sensing as a Tool for Manufacturing Process Control

David A. Dornfeld
Professor of Mechanical Engineering, University of California
Berkeley CA 94720-1740

## 1. The Need for In-Process Monitoring and Control

New demands are being placed on monitoring systems in the manufacturing environment because of recent developments and trends in machining technology and machine tool design (high speed machining, hard turning, "nano-machining", precision polishing, for example). In-process sensors play a significant role in assisting manufacturing systems in producing products at a cost affordable to the mass consumer market. In-process sensors are used to generate control signals to improve both the control and productivity of manufacturing systems. For example, acoustic emission sensors are used in many precision machining processes to monitor the degree of tool wear, chip formation, surface features, etc., and in precision grinding, acoustic emission sensors are used to detect both the near approach of the grinding wheel to the work surface, and the initial wheel contact with the work [1, 2]. In the precision grinding, stock removal can be just a few tens of microns or less, and a human operator has limited ability to monitor and control material removal in this regime. Further, consistency dictates more quantitative techniques for process monitoring and control. Incorporation of an in-process sensor requires a high level of engineering confidence in the ability of the sensor to reliably detect the desired process characteristic. Without this confidence, manufacturers justifiably do not leverage in-process sensor technology to achieve the higher levels of process productivity they offer.

Numerous different sensor types are available for monitoring and control of the manufacturing and machining environments [3]. The most common sensors in the industrial machining environment are force, power and acoustic emission sensors. This paper first discusses the requirements for sensor technology for precision manufacturing process monitoring and control in general. Then, background and details are given about acoustic emission (AE) and the application of AE sensing to process characterization and monitoring, primarily in material removal processes. A review of the source of AE in metal cutting, signal processing of acoustic and other sensor signals is included.

## 2. Requirements for Sensor Technology for Precision Manufacturing

Precision machining takes place at the sub-micron to nano scale dimensions (with respect to the uncut chip thickness, for example.) At these levels, the machining process, surface finish and chip formation are more intimately affected by the material properties such as ductile/brittle behavior or transitions in grinding or single point turning of brittle materials. These effects can adversely affect the surface quality or integrity of the machined component. Critical sensor information in precision machining is required mostly for assessing material removal at the sub-micron level, surface finish and subsurface damage. In addition, it is of interest to track for control purposes the variation in process parameters such as material removal rate (MRR), tool condition (e.g. wheel in grinding, abrasive in lapping, pad in chemical mechanical polishing) as well as process cycle related characteristics (e.g. contact or sparkout in grinding, air time in machining). These parameters are generally measured using sensors with very high sensitivity and with effective frequencies ranging to several MHz. In precision processes, sensor feedback information is critical for higher yields and process throughput.

Not surprisingly, different sensors have different applicability at different levels of precision, or displacement or MRR. Figure 1 below [4] shows a schematic diagram of different types of sensor applications for different precision levels and control parameters. The boundary represents the approximate range of usage with the shaded area emphasizing the core application range. Acoustic emission as illustrated here shows the greatest sensitivity (with the lowest noise level, i.e. highest signal to noise ratio) to the most critical process conditions in precision machining. Precision machining requires an attention to a number of work characteristics in addition to

tolerance on dimension and, as the control parameters approach subsurface damage, the conventional sensing technlologies from conventional manufacturing are less suitable. There are, of course, a host of other techniques for assessing roughness and subsurface damage but they are not usually considered to be useful "on line."

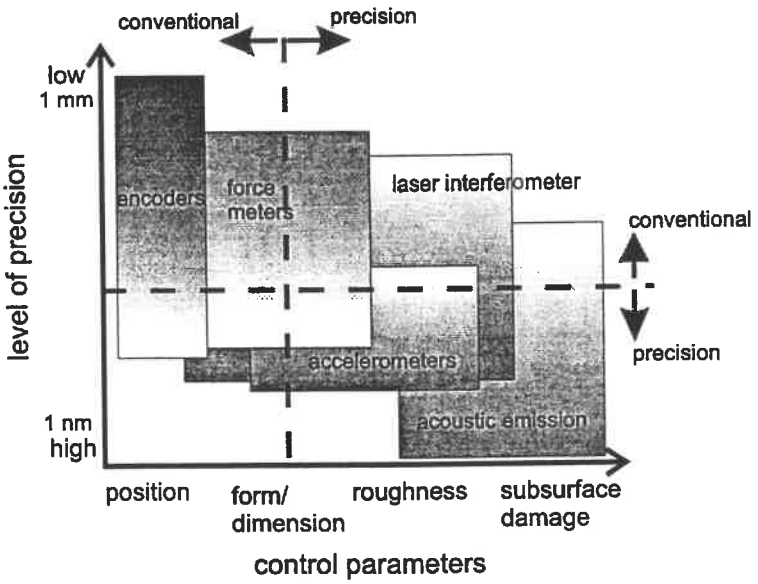


Figure 1 Sensor application vs. level of precision and error control parameters, [4]

3. Acoustic Emission in Manufacturing

Acoustic Emission Sources- Normally, for most effective diagnostic application in manufacturing, the variation of only the source must be insured. The reliability of the AE-based diagnostic system is dependent on the designer's ability to consider all of the potential process sources. In many cases, the major factors affecting the AE signal are sufficiently dominant as to render the "second order" effects inconsequential. These sources include material deformation and fracture, contact of tooling with work, phase change of materials, electrical signals or noise, boiling, fluid flow and turbulence, etc. Details on the characterization of AE sources in manufacturing can be found in a number of references including [5, 6].

Acoustic Emission Sources-Process Monitoring The use of acoustic emission-based sensing for manufacturing process monitoring is much better documented. Whether or not it has been much more successful is not clear as many applications are complex and ones in which competing technology either does not exist or has not been effective either. Traditionally, the bulk of the processes monitored are drilling, milling and turning. The most potential for acoustic emission-based monitoring are material deformation-based manufacturing processes. They use either continuous or discontinuous application of energy to reform or remove material in one way or another. The process monitoring or product defect monitoring scheme is based on either deformation (including friction and rubbing) or fracture derived AE. In some cases material metallurgical transformation is an AE source. Thus, depending on the type of the AE source, and whether the source is expected to be steady or non-steady, on must use the appropriate signal processing methodology. Sensor location and signal processing are not always straightforward considerations.

Acoustic Emission in Machining Research over the past several years has established the effectiveness of AE based sensing methodologies for machine tool condition monitoring and process analysis. The sensitivity of the AE signal to the various contact areas and deformation regions in the cutting and chip formation process has led to the analysis of AE signals as a basic tool for the analysis of the cutting process. Principal areas of interest with respect to AE signal generation are in the primary generation zone ahead of the tool where the initial shearing occurs during chip formation, the secondary deformation zone along the chip-tool rake face interface where sliding and bulk deformation occurs, and the tertiary zone along the tool flank face-work surface interface. Finally, there is a fourth

area of interest, that associated with the fracture of chips during the formation of discontinuous chips. If one is studying the milling process (or other interrupted cutting) an additional source of AE is the impact of the tools on the workpiece and the noise due to the swarf motion on the tool and work.

## 4. Applications of AE in Precision Manufacturing

Diamond turning and lapping- The acoustic emission energy and specific energy has been shown to scale with the uncut chip thickness. $AE_{RMS}$ is directly proportional to the chip thickness defined as $t_{emax}$ in Figure 2 below. Here f, d and V represent feed, depth of cut and cutting speed, respectively. Figure 3 shows the sensitivity of specific $AE_{RMS}$ to uncut chip thickness for both worn and sharp diamond tools for single point turning. Sensitivity down to less than 0.01 micron is seen [7].

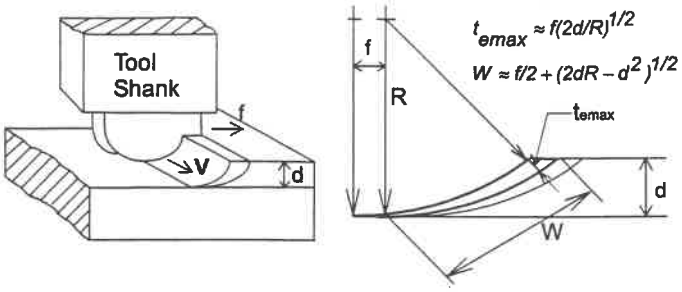


Figure 2 Tool-chip geometry and uncut chip thickness

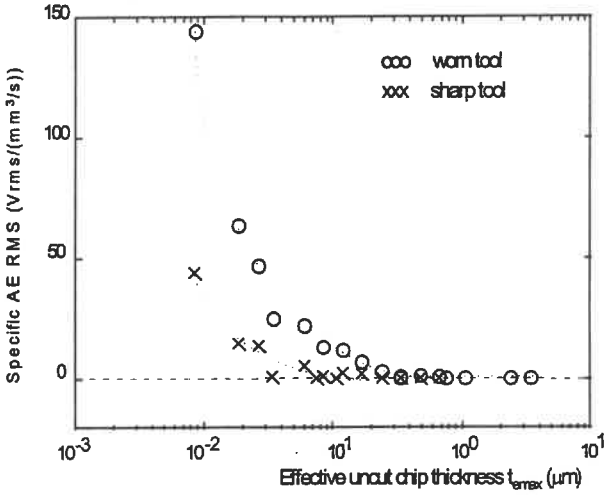


Figure 3 Specific AE-RMS vs. uncut chip thickness

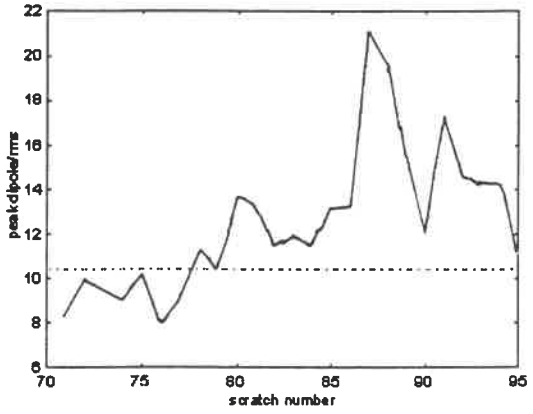


Figure 4 Peak dipole to AE RMS ratio vs. scratch number; ductile/ brittle transition at scratch 77.

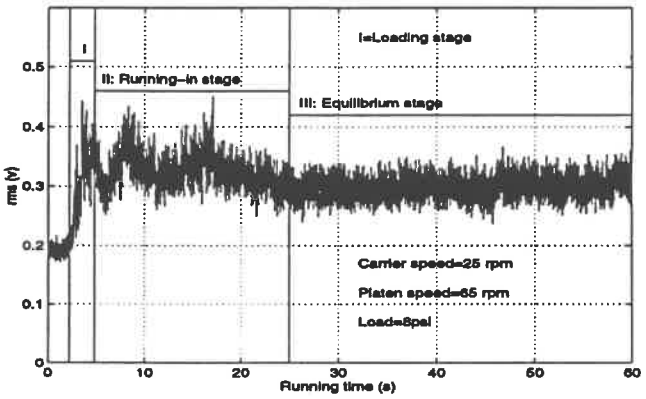


Figure 5 AE signal during CMP process stages.

This similar sensitivity was seen in the surface texturing monitoring research of Liu [8] where a correlation between friction coefficent and abrasive conditions was determined during tape burnishing or magnetic disk substrate and the lapping work of Chang [9] where AE was used to assess the degradation of abrasive size during the process and as a basis for re-freshing the slurry supply.

The ductile-brittle transition was analyzed with AE signals by Daniel [10]. This work showed that the basic migration from plasticity dominated ductile removal mechanisms to fracture dominated brittle mode material removal can be observed by using acoustic emission. Surface displacements from representative ductile and brittle acoustic source functions are calculated using a Green's function approach. The predicted displacement waveforms for ductile and brittle acoustic source functions were verified experimentally using a specially designed AE transducer sensitive in the 1-3 MHz range. The ratio of peak dipole of the AE signal to RMS AE voltage showed a clear transition in machining from ductile to brittle. Figure 4 above illustrates this ratio as a function of number of test scratch with the transition from ductile to brittle mode removal occurring at scratch number 77.

Finally, in chemical mechanical polishing (CMP), a critical planarization step in the fabrication of semiconductor devices, the process stages, pad condition, end point, slurry characteristics and frictional interactions, scratching, etc. can be monitored using AE. Figure 5 above, from Tang *et al* [11] shows the AE RMS signal variation during three distinct stages of CMP with a 200 mm bare silicon wafer polished with SC112 slurry, IC1000 pad and Strasbaugh CMP machine. Any scratches in the wafer surface generated due to abrasive action during the process are visible as spikes of AE activity on top of the basic signal during steady state polishing. This will also be useful in the development process models including the fluid and abrasive interactions.

## 5. Summary

It is difficult to summarize in a short paper the results of over a decade of research in many laboratories around the world investigating the application of acoustic emission in precision manufacturing processes. As workpieces require finer and finer surfaces, tighter tolerances and stringent requirements on sub-surface damage, sensing systems must be able to ensure that the sensitivity of the sensor must be consistent with the magnitude of the phenomenon under investigation. Uniquely, acoustic emission is capable to meet these requirements, specially for material removal process parameters like material removal rates (and very low rates by comparison to conventional processes) and very small uncut chip thicknesses.

## 6. References


1. Dornfeld, D. A. and Cai, H. G., "An Investigation of Grinding and Wheel Loading using Acoustic Emission," *Trans. ASME, J. Eng. Ind.*, 106, 1, 1984, 28-33.
2. Gomes de Oliveira, J. F., Dornfeld, D. A. and Winter, B., "Dimensional Characterization of Grinding Wheel Surface through Acoustic Emission," *Annals CIRP*, 43, 1, 1994, 291-294.
3. Byrne, G., Dornfeld, D., Inasaki, I., Ketteler, G., Konig, W. and Teti, R., "Tool Condition Monitoring (TCM)-Status of Research and Industrial Application," *Annals CIRP*, 44, 2, 1995, pp. 541-567.
4. Lee, Y. X. and Dornfeld, D. A., "Application of Open Architecture Control System in Precision Machining," *31st CIRP International Seminar on Manufacturing Systems*, Berkeley, CA, May, 1998 (to appear).
5. Dornfeld, D. A., "Monitoring the Machining Process by Means of Acoustic Emission Sensors," *Acoustic Emission: Current Practice and Future Directions*, ASTM, STP 1077, W. Sachse, J. Roget and K. Yamaguchi, Eds., American Society of Testing and Materials, Philadelphia, 1991, pp. 328-344.
6. Dornfeld, D. A., "Design and Implementation of In-Process Sensors for the Conrol of Precision Manufacturing Processes," chapter in *Advanced NDE Techniques for Process Sensing and Control*, ASNT, 1998, in press.
7. Liu, J. J. and Dornfeld, D. A., "Modelling and Analysis of Acoustic Emission in Diamond Turning," *Precision Machining: Technology and Machine Development and Improvement*, PED-Vol. 58, ASME, 1992, pp.43-58.
8. Liu, J. J., Liu, C., and Dornfeld, D., "Optimization of Texturing Process via Sensor Feedback in Manufacturing of Thin-film Rigid Disks," *Proc. Japan-USA Sym. on Flexible Automation, ASME*, 1992, pp. 1591-1597.
9. Chang, Y. P., Hashimura, M., and Dornfeld, D. A., "An Investigation of the AE Signals in the Lapping Process, *CIRP Annals*, Vol. 45, No. 1, 1996, pp. 331-334.
10. Daniel, J. and Dornfeld, D. A., "In-process Detection of the Ductile-Brittle Transition in High Speed Scratching of Glass- Theory and Experiment," *Proceedings of ASPE Annual Meeting*, 1996, Monterey CA, pp. 561-565.
11. Tang, J. S., Dornfeld, D. A., Pangrele, S. and Dangca, A., "In-Process Detection of Micro-scratching during CMP using Acoustic Emission Sensing Technology," *Proc. TMS Annual Meeting*, San Antonio TX, TMS, February, 1998.

# DESIGN CONCEPT OF MULTI-WIRE SAW FOR 400mm DIAMETER SILICON INGOT SLICING

H.Oishi, K.Asakawa, J.Matsuzaki
Super Silicon Crystal Research Institute Corp., 555-1, Nakanoya, Annaka, Gumma, 379-0125, Japan

ABSTRACT

This paper presents the design concept of SSi's multi-wire saw for 400mm diameter silicon ingot slicing. The wire saw was designed so that the various parameters were 2～3 times as widely variable as standard machines for the purposes to test the optimum slicing conditions for 400mm, and to collect the basic experimental data on the wire saw slicing in general. A few technical issues to realize the machine specifications are explained, too.

**Introduction.** As integration and performance of semiconductor devices (DRAM, MPU) advance, the design rule has become smaller, and the chip size has become larger at the same time. Therefore increasing diameter of silicon substrate wafers, the raw material for the device chips, has been the only way to produce larger chips without increasing their production cost. Silicon wafers which started at 10mm diameter have now reached 200mm, and 300mm is also close to our hand. Super Silicon Crystal Research Institute Corp. (SSi) was founded by Japan Key Technology Center and 7 Japanese silicon wafer manufacturers in 1996. SSi aims at establishing the key technologies to serve as the production basis of 400mm diameter, the next generation silicon wafers by 2001.

In the wafer shaping process, SSi uses the multi-wire saw to slice a 400mm ingot in place of ID-saw that has been used for 200mm or smaller diameters. Table 1 shows a rough comparison of various slicing methods for 400mm silicon. At this moment, the wire saw seems the best choice for 400mm. Although the multi-wire saw had been used exclusively for small diameter crystalline materials for about 20 years, it was applied for the first time to 200mm silicon ingot slicing in the mass production scale a few years ago, and is now beginning to be used for 300mm silicon, too. However, there is no experience for 400mm silicon slicing, and there is little basic study on wire or slurry themselves in conjunction with the wire saw performance either. In this paper, the concept of the newly designed 400mm wire saw and a few technical issues to realize the machine specifications are explained.

**Design concept of 400mm wire saw.** SSi's wire saw was designed for the purposes to test the optimum slicing conditions (for quality, productivity, and cost) for 400mm wafers, and to collect the basic experimental data on the wire-saw slicing in general, including characteristics of the wire and the slurry. For these purposes, various machine parameters are more widely variable than standard machines.

Figure 1 shows schematically the kinetic factors affecting the wire saw slicing. Relationship among the ingot feed rate (V), the wire tension (T), the wire speed (U), the slurry abrasive size (S), the wire deflection in Y-direction ($\delta_Y$), and the wire displacement in X-direction ($\delta_X$) is shown in the following equation [1] . This equation was obtained half theoretically and half empirically.

$$\delta_Y \propto \frac{V}{T \times U \times S} \qquad \text{Eq. (1)}$$

$$\propto \delta_X$$

$\delta_X$ is the out-of-plane component of the wire deflection arising from an asymmetrical wire cross-section and slurry flow, and becomes a cause of the wafer warpage or the surface waviness. In equation (1), increasing the wire tension or the wire speed can increase the ingot feed rate and decrease $\delta_X$. Based on this relationship, the major machine specifications were decided as follows;

(1) **Large diameter slicing.** The wire saw can slice up to 400mm in diameter, 400mm in length, and 120kg in weight.

(2) **High wire tension.** The wire tension is available up to 7 kgf (70 N )/wire, which is approx. 3 times as large as conventional machines. It is expected that high wire tension can suppress the wafer warpage or the surface waviness while maintaining the ingot feed rate for a large ingot.

In order to secure the machine stiffness against high wire tension and cutting resistance, the groove roller spindles and the machine frame were designed to have enough rigidity. Figure 2 shows a schematic drawing of the wire saw's rib structure. The loop rigidity between the ingot holder and the spindle mounting base is approx. 60 kgf (600 N)/$\mu$m.

(3) **High wire speed.** The wire speed is available up to 1,000 m/min, which is about twice as fast as conventional machines, to improve the ingot feed rate. And the maximum reciprocation cycle of the wire is 4 cycle/min. The 7 axes synchronous control was adopted for the groove rollers, the wire spools, and the traversers so as to improve the fluctuation of wire tension. Figure 3 shows schematically the tensioning system of the wire saw.

(4) **Stabilization of machine operating conditions.** As it will take a long time (goal 24 hrs) to complete a 400mm ingot slicing, a stabilization of the machine conditions during the slicing is essential to maintain the ingot feed rate and the sliced wafer qualities. For the stabilization, the following measures were taken;

① Total wire length of 600 km (for 0.18mm diameter wire, 120 kg equivalent) is available.

② The large slurry tank with 400 litter capacity is prepared to minimize a change of abrasives wear.

③ To stabilize a temperature fluctuation of the groove roller spindles and to minimize the spindle axis expansion which becomes a cause of the wafer warpage, the spindle cooler was adopted.

(5) **Automatic data logging and remote monitoring.** The automatic multiple-point data logging and the remote monitoring systems are available so as to ease the experimental data collection and to reduce an machine operator's trouble.

**A few technical issues.** There were a few technical issues to realize the machine specifications.

(1) **Groove roller driving motor, wire spool driving motors.** For SSi's wire saw, we

had the specially designed small sized-high power motor for the groove roller driving and the built-in type wire spool driving motor developed. The AC-servo motor for the groove roller driving has 85 kW output in its 30cm cube. A weight increase of the groove rollers due to their increased stiffness, an increase in the wire speed and the reciprocation cycle required such a high output. However, a volume of the motor is approx. 1/6 of that of conventional ones, and helped ease the design of machine weight balance.

(2) **Groove roller spindles.** In order to support the groove rollers on which the high wire tension of 7 kgf (70 N)/wire is applied, the spindles have the bearing configuration that bears 6,400 kgf (63,000 N) load and is suitable for a long life operation.

**Water - soluble coolant.** For conventional wire saw slicing, the slurry with the oil-based coolant has been used. However, for 400mm diameter ingot slicing, the slurry with the water-soluble coolant is planned to be adopted. We want to make the best use of merits of the water-soluble coolant such as "Non-inflammability", "Good bio-degradability", and "Easiness of post-slice cleaning". We have several candidates for water-soluble coolant which will meet the requirements of wire saw slicing such as "Good abrasives suspension", "Low viscosity change", and "Low foaming characteristic". The capacity of the slurry heat exchanger was designed on the assumption of using the water-soluble coolant.

**Test schedule.** Upon the receipt of 400mm ingots from the ingot growth laboratory (of SSi), the wire saw slicing is scheduled to start in Mar. 1998.

**Acknowledgement.** The authors would like to thank Mr.Yasunaga and Mr.Nagatsuka of Tokyo Seimitsu Co. Ltd. for their extended cooperation in discussion and actual machine designing.

**Reference.** (1) M. Fujisawa, High Efficiency and High Precision Slicing for Brittle Materials (in Japanese), p188, IPC, Tokyo, (1995)

| Method | Current status and expectations for 400mm slicing |
|---|---|
| ID saw | (Current) 1,600mm width blade core, essential for 400mm slicing, is not available. If available, kerf loss will be approx. 500$\mu$m.<br>(Productivity) 4.0 pcs/hr. |
| Wire saw | (Yield) Kerf loss will be 240~250$\mu$m. Yield will be 115~125%, compared to ID saw.<br>(Productivity) 7.0 pcs/hr (assuming ingot length of 300mm).<br>(Cost) − $14 /pc, compared to ID saw. (cost = machine depreciation + expendables + kerf loss cost of silicon crystal) |
| Others | (Electric discharge cutting) Not applicable to normal resistivity silicon.<br>(Plasma CVM) No better than basic research level.<br>(Band saw) No advantage over wire saw. |

Table 1. Comparison of various slicing methods for 400mm diameter silicon.

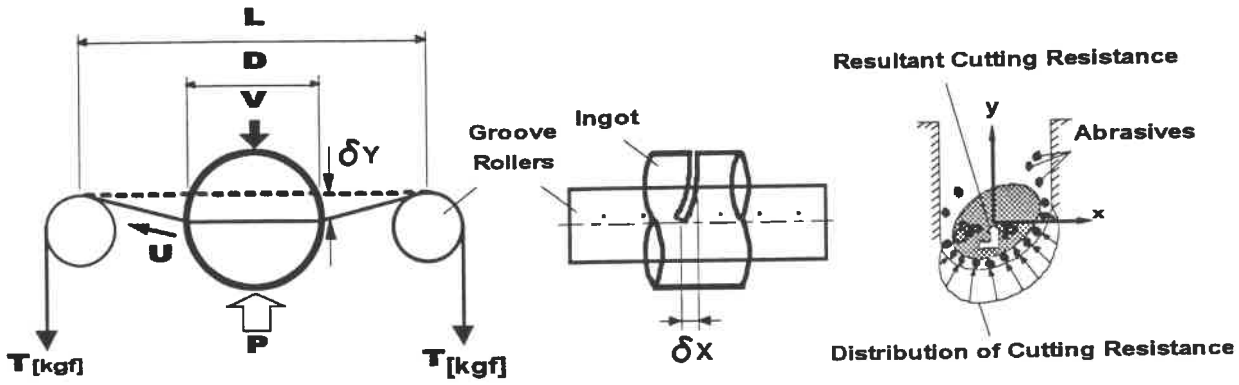


Figure 1. Cutting resistance and wire deflection in wire saw slicing (Reference (1)).

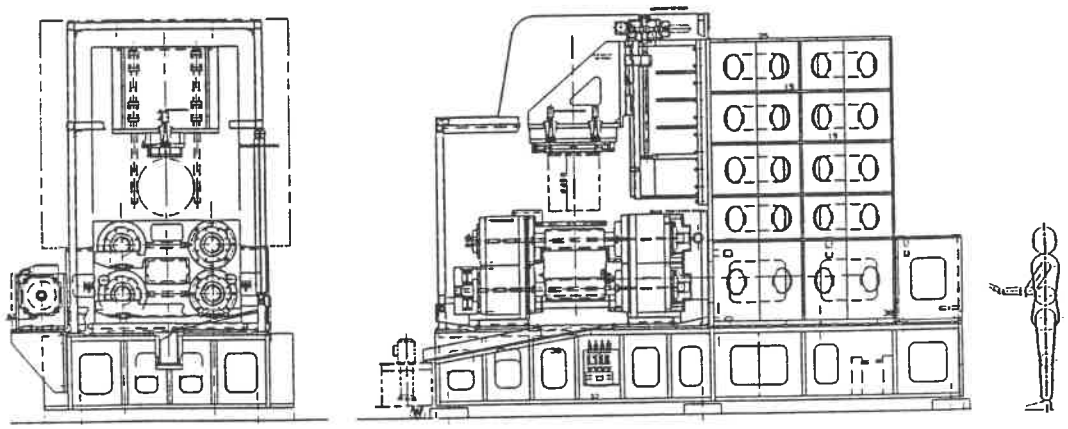

Figure 2. The rib structure of 400mm wire saw frame.

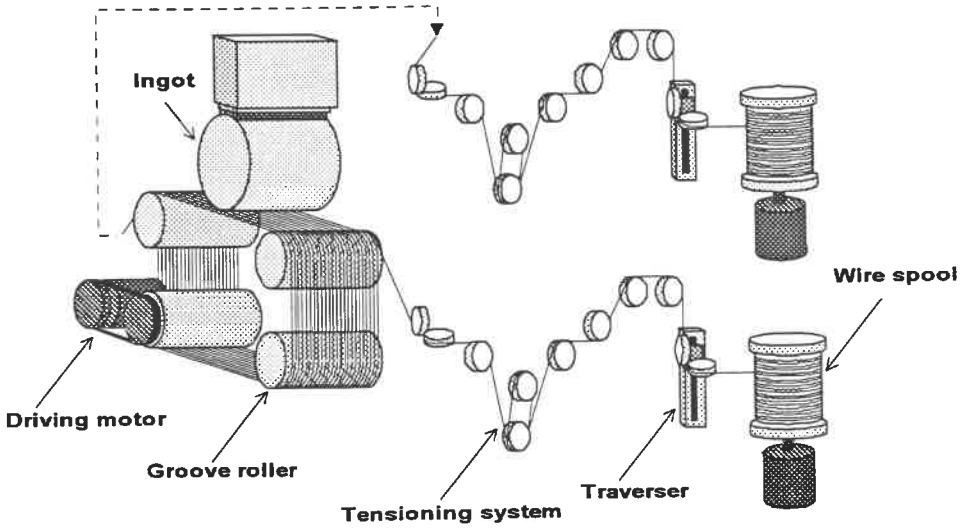


Figure 3. Schematic diagram of wire tensioning system for 400mm wire saw.

# Development of an Ultraprecision Grinding Machine for Super-Large and Super-Flat Silicon Wafer

## — Proposal of Trigonal Prism Type Pentahedral Structure —

*Kohzo Abe, *Shinji Okawa, **Yutaka Koma, **Kazuhisa Arai
*Super Silicon Crystal Research Institute Corp.(SSi), **DISCO CORPORATION
*555-1 Nakanoya, Annaka, Gumma, 379-0125, Japan
**14-3 Higashi kojiya 2-chome, Ota-ku Tokyo 144 Japan

----- Abstract -----

This paper proposes the trigonal prism type pentahedral structure which consists of three columns as the new wafer grinding machine design for realizing the extremely high stiffness and withstanding the bending moment caused by heavy grinding load. The trigonal prism structure will generate the 0.1 $\mu$m order flatness on the further super-large wafer as post-$\phi$300mm generation in the giga-bits semiconductor device manufacturing of the 21st century.

And furthermore, the ultraprecision grinding has been expected as the next technology realizing etching-less process. To realize etching-less process, a sophisticated ultra-precision grinding machine based on the trigonal prism structure concept is under development in the SSi project as a joint research program of 7 wafer manufacturers supported by the Japanese government.

### 1. Introduction

The conventional wafer shaping process consists of lapping, etching and polishing as shown in Fig.1-1. It has been becoming difficult to guarantee 0.1 $\mu$m order flatness because these processes do not have high potential for producing super-flat wafers, excellent controllability and repeatability. And, etching itself is too sensitive to the environment concerned.

The ultraprecision grinding based on the principle of motion copying[1] is suitable as the solution for realizing high flatness and etching-less process. Here, the both faces of super-large wafer will be required to be mirror polished. So, both faces should be ground in the grinding process as shown in Fig. 1-2. Not only the high flatness but also high quality roughness and less subsurface damage will be obtained at the grinding process.

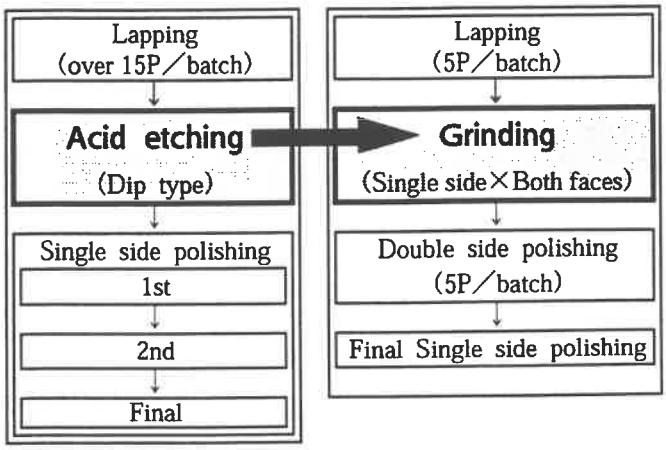


1-1. Conventional $\phi$200mm 1-2. Super-large wafer

Fig 1. Comparison of wafer shaping process

## 2. Problems expected in super-large and super-flat wafer grinding

To develop the machine, the following subjects should be resolved.

1) **Stiffness** : The grinding load will be over 300N which is twice as much as that of $\phi$200mm wafer. The cantilever type single column structure as shown Fig.2-1 will easily pitch (D2) and yaw (D1) against such a heavy load. In case of bridge type double column structure as shown in Fig.2-2, it will not be suitable for minimizing pitching (D4).

2) **Feeding mechanism** : The conventional linear guide for infeeding the grinding spindle unit on the column surface does not work suitably for nanometer-feeding.

3) **Bearings** : The conventional aerostatic bearing will generate chatter marks on the ground surface because of its poor damping performance.

4) **Accuracy** : The bolt screw adjusting mechanism for the axial parallelism between the grinding spindle and the chuck table requires much time to obtain better accuracy than half micro-radian.

## 3. Design concept of the next generation ultra-precision wafer grinding machine

The machine will be constructed based on the following advanced design concept and machine tool technologies.

1) **Stiffness : The trigonal prism type pentahedral structure which consists of three columns**

The trigonal prism structure will be adopted as the grinding frame as shown in Fig.3. Basic thinking is the trigonal prism consisted of an equilateral triangle (Fig.3-1). At the corner of trigonal prism, three columns are arranged on the bed as shown in Fig.3-2. Along the center of trigonal prism, grinding spindle, saddle and linear actuator are installed for minimizing Abbe's error as shown in Fig.4-1.

2) **Feeding mechanism : The vertical double-V guide-way system**

The vertical double-V guide-way system with pressurizing mechanism in the second brace will be used for guaranteeing 10 nm feeding accuracy as shown in Fig. 4-3. The V-groove is located at each side of the saddle which holds the grinding spindle. In case of this, the center of the double-V guide is also along the center of trigonal prism.

3) **Bearings : The deionized-water hydrostatic bearing system**

The deionized-water hydrostatic bearing system will be introduced for realizing the extremely high damping performance and keeping cleanness in the wafer manufacturing process. The design value of stiffness are shown in Table 1. These are over twice as much as that of ultraprecision grinding equipment for $\phi$200mm wafer[2]. We estimate the loop stiffness of the trigonal prism type machine at over 300 N/$\mu$m.

4) **Accuracy : The gap control system**

The gap control system of the hydrostatic thrust bearing will be installed into the chuck table. This is for the accurate adjustment and the easy setting of the axial parallelism between the grinding spindle and the chuck table to obtain 0.1$\mu$m order wafer flatness.

5) **Single spindle structure : Advanced grinding wheel technology**

Single grinding spindle design will be applied for the machine. This is based on the DISCO's high performance fine grinding wheel technology which needs not coarse grinding process. For the single spindle, there are two chuck tables as shown in the Fig. 4-2. This is for realizing high throughput productivity (Fig.5) even if this machine is for research equipment.

The ultraprecision grinding machine based on the above advanced technologies will be installed to SSi this May. The designed performance will have been confirmed until that time.


## 4.Acknowledgment

The authors would like to thank Prof. Masakazu Miyashita, Prof. Nobuo Yasunaga, Prof. Akira Kanai, Mr. Katsutoshi Tanaka and Mr. Masahide Katsuki of TOSHIBA MACHINE CO.,LTD., Takashi Koda of TECHNO DESIGN-LIMITED and Mr. Motomi Kitano of DISCO CORPORATION for their extended cooperation in the discussing and designing the machine.


## 5. Reference


1) Masakazu Miyashita, Journal of the JSPE,56,5(1990)782

2) Kohzo Abe, Nobuo Yasunaga, Masakazu Miyashita, Jun-ichi Yoshioka, Michimasa Daito, Development of an Ultraprecision Grinding Equipment for Ductile Mode Surface Finishing of Brittle Materials, 7th IPES Proceedings (1993,Kobe) p153


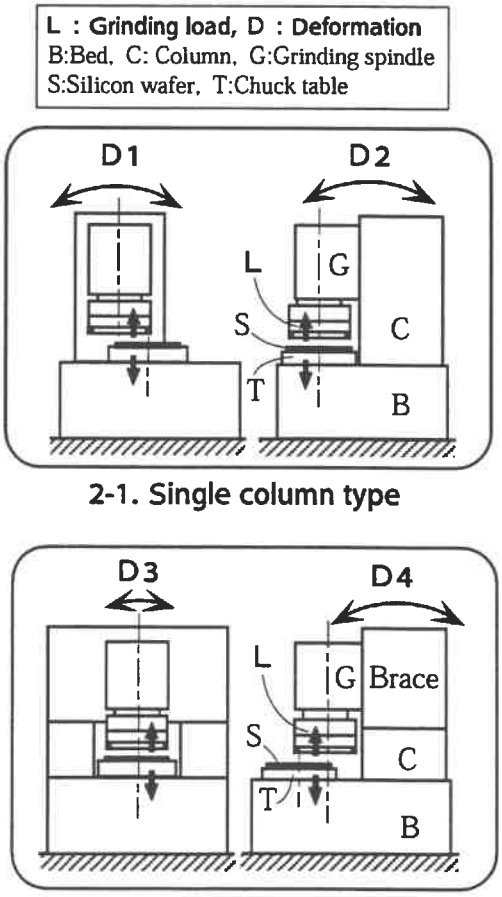


2-1. Single column type

2-2. Double column type

Fig.2 Conventional structure of wafer grinder

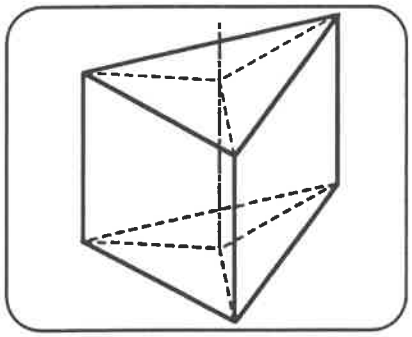

3-1. Trigonal prism type pentahedron consisted of an equilateral triangle

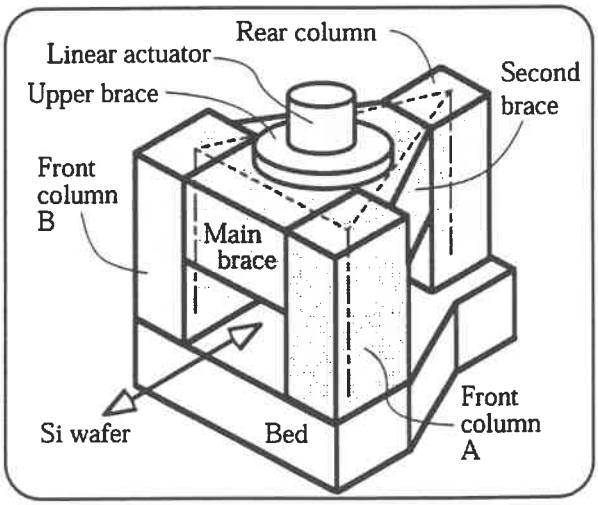


3-2. Machine image

Fig.3 Basic concept of the trigonal prism type pentahedral structure consisted of 3 columns

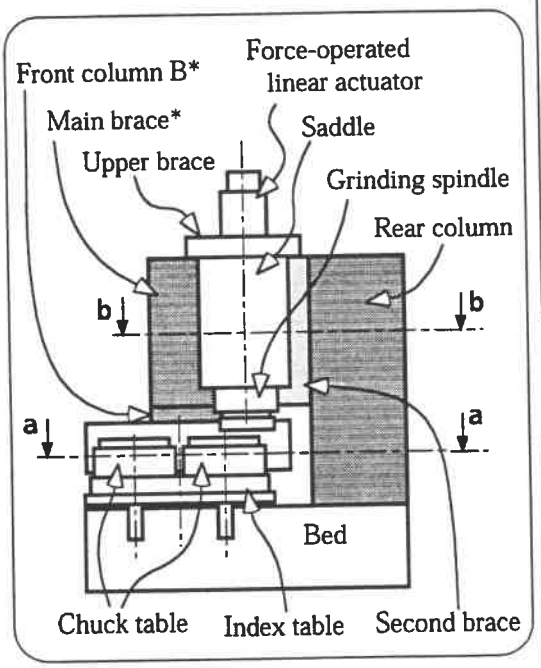


4-1. Side view

* Main brace and front column A & B are cast as one pcomponent

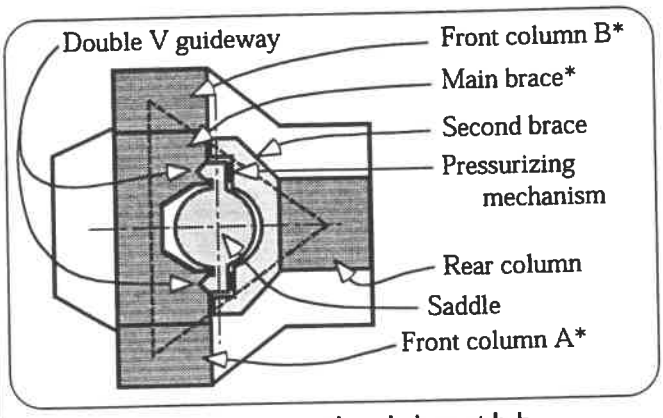


4-3. Cross sectional view at b-b

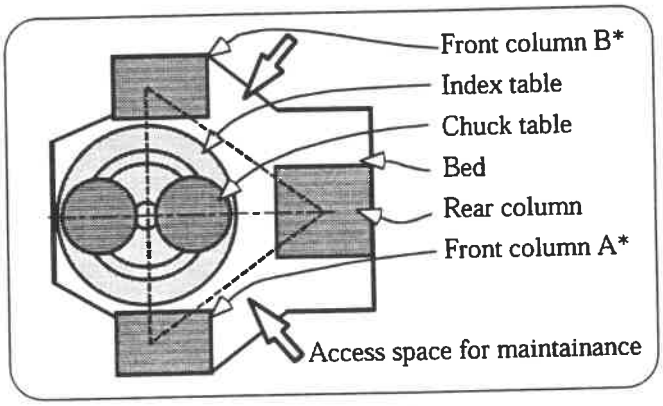


4-2. Cross sectional view at a-a

Fig.4 Structure of Ultraprecision grinding machine

Table 1 Spindle stiffness : design value

| | Thrust | Radial |
|---|---|---|
| Grinding spindle | 2400 | 1400 |
| Chuck table | 3000 | 1500 |

Unit : N/$\mu$m

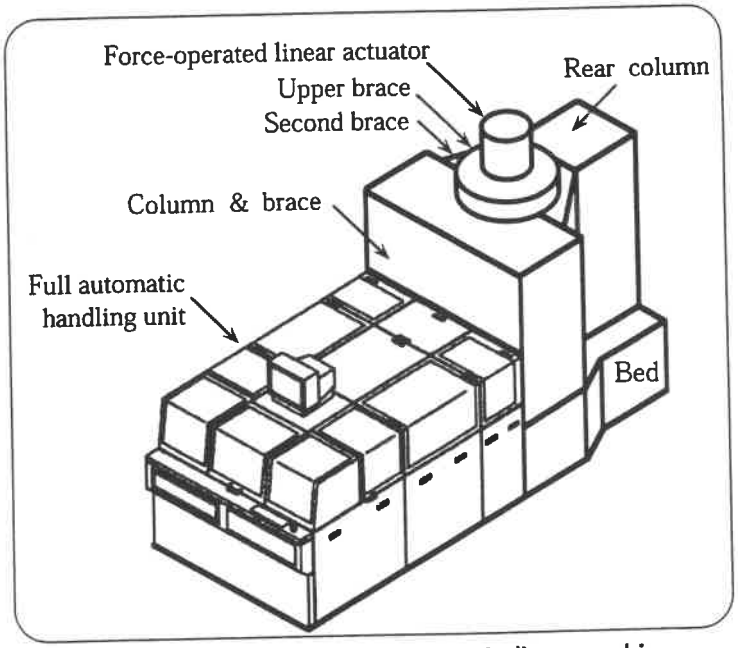


Fig.5 Schematic of ultraprecision grinding machine for super-large and super-flat silicon wafer

# DUCTILE MODE CUTTING OF SILICON MICROPARTS

Thomas Hellmold, Lars P. Ruhbach, Jeihad Zeadan, Hans H. Gatzen
Institute for Microtechnology, Hanover University

**Keywords -- Ductile Mode Cutting, Sidewall Effects, Edge Chipping**

***Abstract*** **-- Silicon is a dominant wafer material for semiconductor microdevices and micro electro-mechanical systems (MEMS). Silicon is a brittle material therefore, a brittle fracture mode cutting is the most likely machining mode to occur. This mode is undesirable, since the workpiece suffers the induction of substantial subsurface damages which may result in a failure of the finished part due to crack formation. By choosing machining conditions resulting in a ductile mode cutting, these damages may be minimized. This paper presents experiments with hard resin and metal blades clarifying what conditions have to be met to machine silicon in a ductile mode. It discusses furthermore silicon dicing phenomena and provides proof that ductile machining has been achieved during the experiments.**

## I. Introduction

Silicon not only is the most dominant wafer material used in semiconductor microdevices, it also is seeing a widespread use in micro electro-mechanical systems (MEMS). In both cases, the devices built up on a wafer need to be separated in a dicing process. For some applications in MEMS, profiling might also be required. Silicon is a brittle material, brittle fracture mode cutting therefore is the most common cutting mode. However, this mode is undesirable, since it causes substantial subsurface damages resulting in crystalline microcracks and chipping. For dicing microelectronic chips, side wall microcracks become less and less acceptable. They may initiate fractures that could result in a mechanical failure of the component due to fatigue when exposed to a dynamic mechanical or thermal load after packaging. Whatever allowance for chipping has to be set aside eats into the real estate available for components on a wafer surface.

## II. Cutting Mode Considerations

Investigations performed on advanced ceramics have shown that subsurface damages on brittle materials may be minimized if a predominantly ductile mode of cutting is achieved [1]. Ductile mode cutting is based on a submicron depth of cut, as well as on an appropriate cutting energy. Due to the likeliness of the atomic bond, advanced ceramics and semiconductor materials display similar machining behavior. Therefore, the application of ductile machining to silicon promises a solution to the issues mentioned above by avoiding (or at least minimizing) subsurface damages [2]. To achieve a predominantly ductile cutting mode, Bifano's equation (1) has to be fulfilled: the depth of cut $h_{cu}$ has to meet a critical value $h_{cu,crit}$ [1].

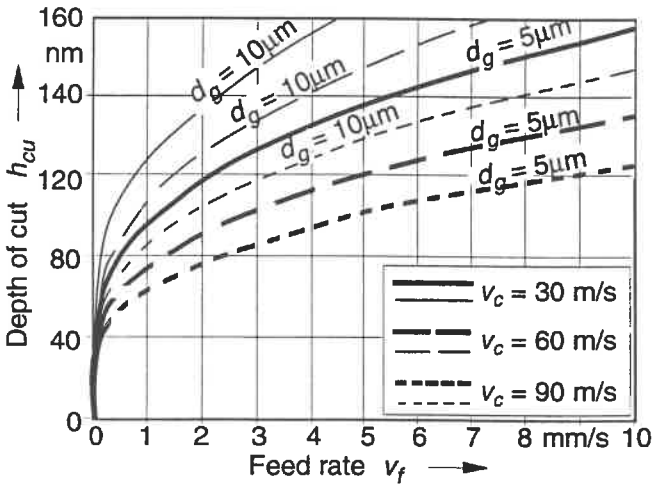


$$h_{cu,crit} = \Psi \cdot \left(\frac{E}{HV}\right) \cdot \left(\frac{K_{Ic}}{HV}\right)^2 \quad [1]$$

$E$ - Young's modulus
$HV$ - Vickers hardness
$K_{Ic}$ - Critical stress intensity factor
$\Psi$ - Surface damage factor

Fig. 1: Relation between process parameters and depth of cut.

Fig. 1 depicts the actual depth of cut as a function of the process parameters [3, 4]. The greatest changes in the depth of cut occur at low feed rates. According to Bifano's equation, for silicon the critical average depth of cut $h_{cu,crit}$ is 15 nm. Therefore, Bifano's equation predicts that only low feed rates will yield ductile mode cutting.

## III. Dicing Experiments

To investigate what kind of cutting conditions result in ductile machining, a set of dicing experiments was carried out. The two key cutting parameters studied were the blades' binder material and the feed rate.The experiments were carried out using a high precision dicing saw equipped with an air bearing spindle and located in a temperature controlled environment (20 ± 1°C). The dicing wheels used in the experiments were hubless diamond blades, mounted between a pair of flanges. Two types of binder, resin and metal, are in use. Using a resin bond, which is available in different hardnesses, typically a better edge quality is achieved, but metal bonded wheels wear at a slower rate. The two binder materials investigated were hard resin and metal. The feed rate $v_f$ was varied between 0.1 mm/s and 10 mm/s. The remaining blade and cutting conditions were chosen as follows: for all blades, the average diamond grain size $d_g$ was 5 to 6 µm, the blade width $a_b$ was 100 µm, and the blade exposure $e$ was 0.6 mm. The cut speed $v_c$ was 86.4 m/s. As coolant liquid water was used and as the coolant velocity $v_w$ was 19 m/s. Table I summarizes the test conditions for the experiments performed.

When machining a silicon wafer one of its unique conditions, its crystal structure, needs to be taken into account. In general, silicon wafers are a single crystal material, with the crystal orientation at the surface either {110} or {100}. In these investigations, {100} wafers were cut in [100] and [110] direction.

Table I

Silicon Dicing Experiments Process Parameters

| | | |
|---|---|---|
| Blade type / binder | Hubless; metal | Hubless; resin, hard |
| Diamond grain size | 6 µm | 5 µm |
| Feed rate | 0.1 – 10 mm/s | 0.1 – 10 mm/s |
| Cut speed | 86 m/s | 86 m/s |
| Cutting direction | [100], [110] | [100], [110] |
| Cut depth | 0.55 mm | 0.55 mm |
| Feed direction | Down cut | Down cut, up cut |
| Coolant | Water | Water |

## IV. Experimental Results

### A. Edge Quality

An excellent parameter for judging if a predominantly ductile machining has been achieved is the amount of edge chipping that occurs during machining.

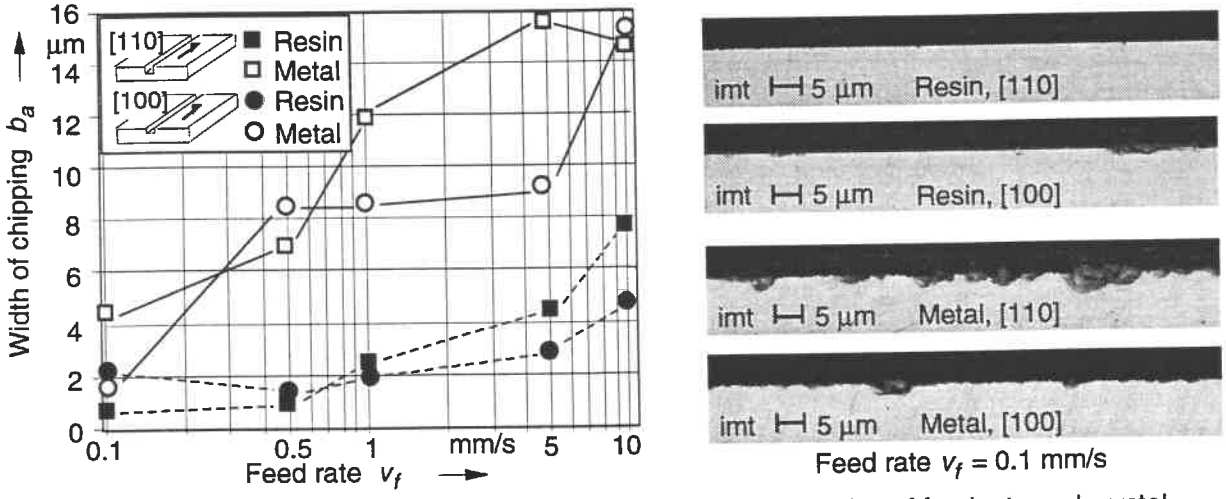


Fig. 2: Width of chipping for resin and metal bonded blades as a function of feed rate and crystal orientation (left). OM images of edge contours (right).

Fig. 2, left, depicts the average width of chipping (i.e. the depth of chip penetration) for the two binder variations and the range of feed rates. Fig. 2, right, shows SEM micrographs for the dominant cutting conditions. Minimum chipping occurs for the lowest feed rates; the further the feed rate is decreased, the higher is the percentage of ductile mode cutting. Furthermore, the hard resin bonded blade achieves better results than the metal blade. Better damping and self sharpening capabilities of the resin blade are the main reasons for the resin blade's superiority. However, the usage of resin bonded blades at feed rates $v_f$ above 10 mm/s cause an excessive radial wheel wear and even result in blade-damages.

*B. Up Cut vs. Down Cut*

Cutting mode and edge quality are influenced by the direction of cutting, i.e choosing the down cut or up cut mode for dicing. Fig. 3, left, depicts the cutting conditions for down vs. up cut. For this experiment, a hard resin bonded blade was selected; cutting was executed in the [110] crystal direction. Fig. 3, right depicts the findings: a down cut results in substantially less chipping than an up cut. A diamond grain entering the work piece at the maximal depth (down cut) yields better results than starting out with a cut depth of zero (up cut).

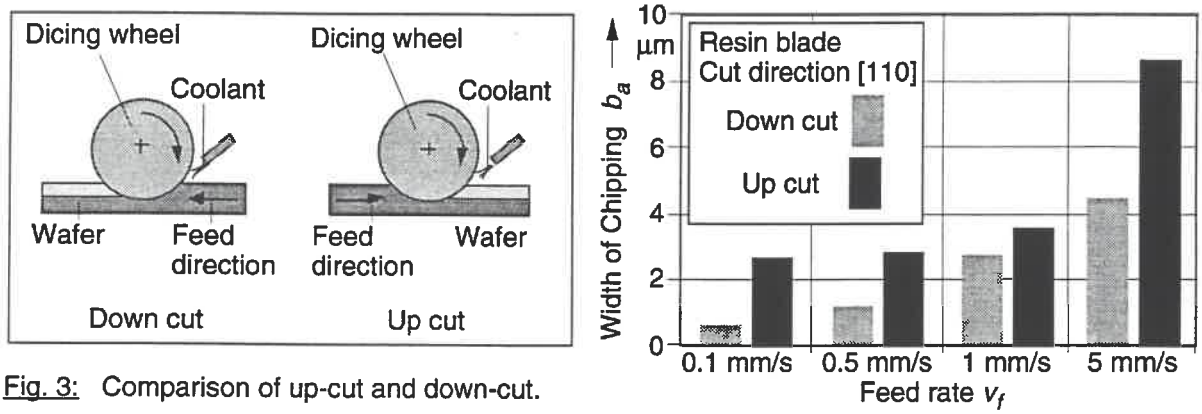


Fig. 3: Comparison of up-cut and down-cut.

*C. Sidewall Phenomena*

While the main material removal is performed by the diamond grains located at the blade's circumference, phenomena resulting in creation of the sidewall are of a higher complexity. Due to the frictional effects at the sidewall to blade interface, smoothening effects may occur. These effects apparently are aggravated by loose diamonds, as well as the abrasive products transported in the space between blade and sidewall. If a material cutting does occur, the depth of cut of the individual grain will be extremely small, a case typically not resulting in optimal cutting conditions.

Using a Stylus Profiler with a 2.5 µm radius tip allows an analysis of the kerf's sidewall roughness. The analysis is only of qualitative nature due to the cutoff of short wavelength topography features caused by the comparatively large tip radius. Fig. 4 depicts the results.

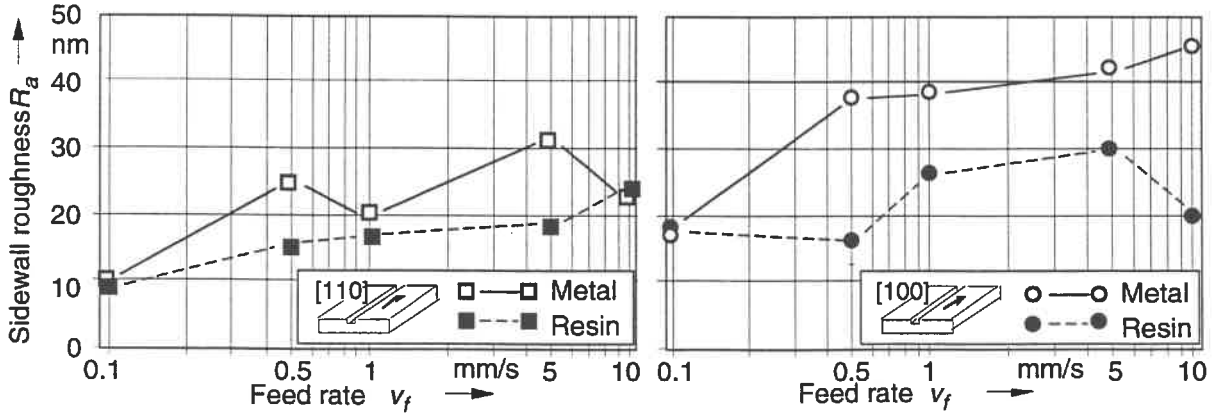


Fig. 4: Sidewall roughness for resin and metal bonded blades. Cut directions [110], left, and [100], right.

The resin bonded blades achieve a better sidewall quality, which may be contributed to a self-sharpening effect due to dull diamonds breaking out. Therefore, at all times a great number of sharp diamond grains is engaged. Thus, resin bonded blades achieve better surface finish and are more likely to reach a ductile cutting mode, but they also wear much more rapidly than metal bonded wheels. Resin bonded blades also show less sensitivity regarding the surface roughness due to crystal directional influences. Metal bonded blades achieve a better surface roughness when cutting in [110] direction which has a higher atomic packing density rather than [100]. In [110] direction, the glide planes correspond with the cut direction and favor a plastic deformation of the material [5].

Fig. 5 depicts SEM micrographs of the kerf's sidewall created by a resin (left) and a metal bonded (right) blade at the two extreme feed rates $v_f$ (0.1 mm/s and 10 mm/s). As a result, ductile mode cutting at the sidewall will most likely occur when sharp diamonds are engaged and the depth of cut (and therefore the feed rate) is small. Deep parallel scratches show the influence of single diamond grains with an excessive protrusion. Fig. 5, c, provides us with an indication of sidewall effects taking place due to friction: plastic deformation and smearing of material. The local flash temperatures during these processes may be substantial: the melting temperature of silicon is 1412°C.

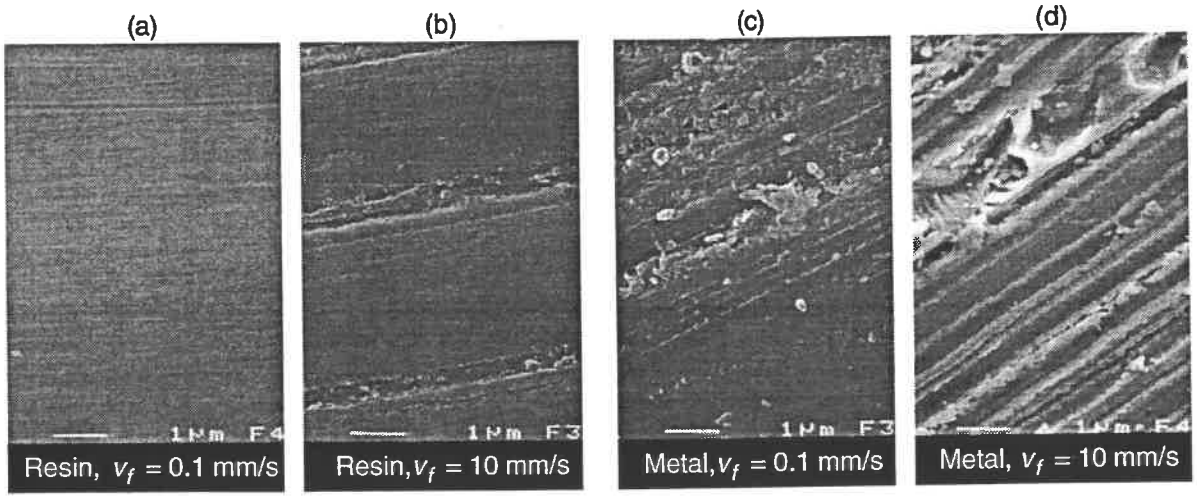


Fig. 5: SEM-micrographs of the kerf sidewall for resin and metal bonded blades and different feed speeds (a-d).

Another kerf phenomenon occurring occasionally is 'sidewall lines'. The most likely cause for them may be found in the blades' fabrication process. When the blades are fabricated, the final step is a lapping of each blade to thickness. Occasionally, singular diamond grains are still protruding from the sidewalls after lapping. They will cause steps in the kerf's sidewall which look like lines parallel to the workpiece's top surface. Fig. 6 depicts an AFM 3-D plot and a 2-D profile of a silicon side wall containing two such steps. In general, the steps are not detrimental.

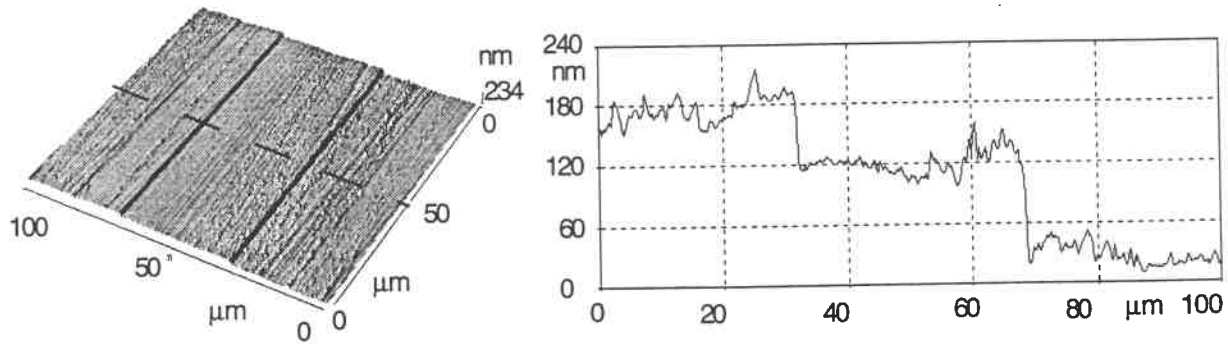


Fig. 6: Side wall steps in a silicon cut side wall (AFM image and line scan).

*D. Chip Analysis*

So far, the ductile mode cutting was assumed to occur when the surface roughness and edge chipping were at an optimum. However, the ultimate proof for the occurrence of ductile mode cutting is to find chips showing ductile deformation. To perform such an analysis, chips were filtered out of the dicing saw's used coolant water. Fig. 7 depicts the results. The left micrograph shows chips created by crystalline microfractures typical for brittle fracture mode cutting and occurring at a high feed $v_{f2}$ (10 mm/s). When analyzing chips created at low feed rates $v_{f1}$ (0.1 mm/s), the chips are substantially different (Fig. 7, right). The dominating helical or bent abrasive products are an indication of the plastic chip formation instead of material microbreakage. The thickness of the chips formed through ductile cutting is in the same order of magnitude as the theoretical determined values in Chapter II.

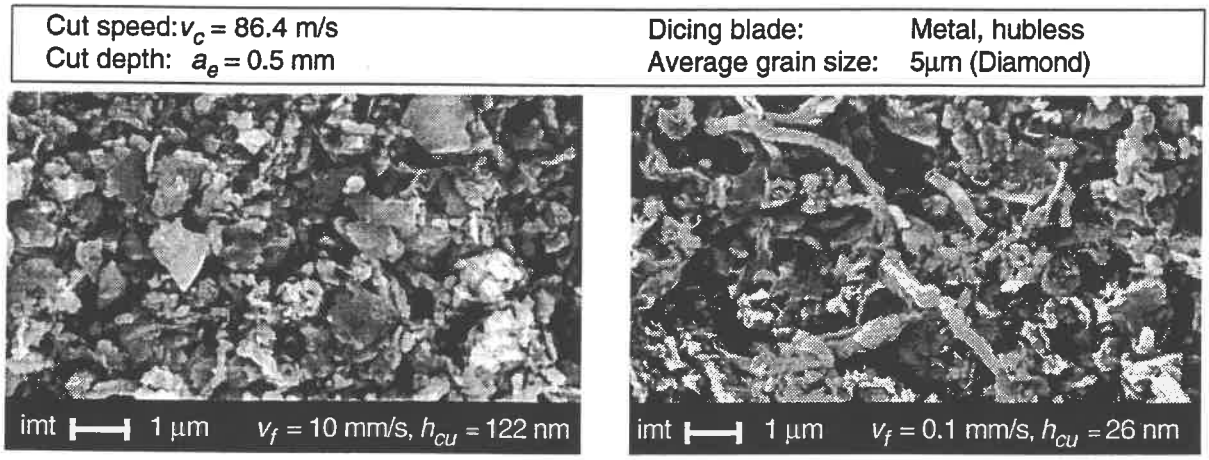
Cut speed: $v_c$ = 86.4 m/s
Cut depth: $a_e$ = 0.5 mm
Dicing blade: Metal, hubless
Average grain size: 5µm (Diamond)
imt 1 µm $v_f$ = 10 mm/s, $h_{cu}$ = 122 nm
imt 1 µm $v_f$ = 0.1 mm/s, $h_{cu}$ = 26 nm

Fig. 7: Abrasive product analysis, metal bonded blade (SEM-micrographs). Left: block chips caused by brittle mode cutting. Right: helical and bended chips caused by ductile mode cutting.

## V. Conclusion

For the manufacturing of high quality silicon microparts, subsurface damages like cracks and induced residual stresses can be minimized if cutting conditions resulting in predominantly ductile mode cutting are chosen. Optimal results are achieved if a diamond blade with a grain size in the 5 µm range and a hard resin bond is operated at low feed rates $v_{f1}$ (0.1 mm/s). The two drawbacks of this approach are relatively high wheel wear and low machining rates. The proof for actually having achieved a ductile mode cutting are helical chips filtered from the spent coolant water.

## References

[1] Bifano, T.G.: "Ductile Regime Grinding: A New Technology for Machining Brittle Materials", Transactions of the ASME, Vol. 112, pp. 184-189, 1991

[2] Gatzen, H.H.; Maetzig, J.C.: "Nanogrinding", Journal of the American Society for Precision Engineering (ASPE), Vol. 21, No. 2/3, pp. 134-139, 1997

[3] Ruhbach, L.: "Erzeugung hochgenauer Kanten beim Präzisions-Trennschleifen von Keramik", Ph.D. Thesis, Hanover University, Hanover, (1998)

[4] Tönshoff, H. K.: "Spanen" Springer Verlag, Berlin, 1995

[5] Schatt, W.: "Werkstoffwissenschaften", Deutscher Verlag für Grundstoffindustrie, Stuttgart, 1996

# TECHNICAL DETAILS OF SILICON MACHINING BEHAVIOR FROM A DIAMOND TOOLMAKER'S PERSPECTIVE
( A Tutorial Presentation )

George A.Kim
Edge Technologies, Inc.
Indianapolis, Indiana

Abstract

Diamond tool makers are intimately aware of the abrasive anisotropic machining behavior of single crystal diamond and of past investigators, studies, models and explanations of such behavior. However, it is not generally understood that silicon, with its diamond atomic and crystalline structure may machine in a similar way. Diamond literature generally accepts that abrasive diamond machining takes place by brittle-fracture chipping, principally along (111) planes, and is systematically related to crystal structure. A review of abrasive diamond machining and a perspective of abrasive silicon machining, similar to diamond, is presented.

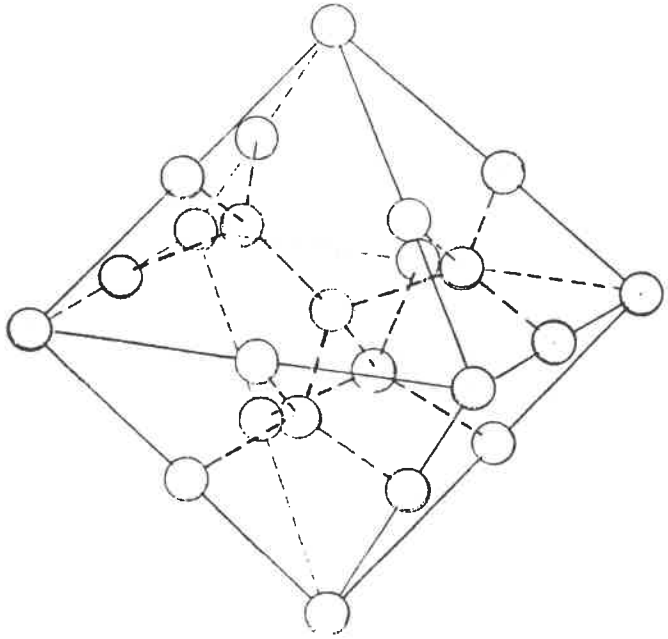

Atomic and Crystalline Structure for Diamond and Silicon

## 1. Introduction

The atomic chart indicates group four elements have four valence electrons and that carbon (diamond), silicon and germanium form tetrahedral bonded diamond structures.
The atomic structures and crystal morphologies for diamond, silicon and germanium are the same but have different internuclear distances, sizes, strengths and fracture energies.

Fig 1 shows Wilks & Wilks' model that describes the anisotropic grinding behavior of diamond. The abrasive machining of diamond occurs primarily through (111) plane brittle-fracture mechanics and chipping [1]. However, recent work indicates plastic grooving and/or sp3 to sp2 rehibridization may be present [2,3].

## 2. Discussion

Fig 2 superimposes Wilks & Wilks empirical results on (111) silicon and explains the revealed three-way material distress pattern when single point turning.

Putting silicon in a closely packed structure (either by applying pressure or by melting) makes it a metal.[4] Could the difficulty of silicon machining approach the ease of aluminum machining as pressure/heat is increased ?

## 3. Summary

Silicon and germanium are diamond-type crystals that tend to brittle-fracture-machine similar to diamond. An awareness of crystal orientation can help achieve optimum abrasive machining results, especially with directional processes like flycutting, grinding and lapping.

## 4. References


1. E.M.Wilks and J.Wilks, Clarendon Laboratory, Oxford 1961
2. W.J.P.Van Enckevort, M.S.Couto, and M.Seal, IDR, Volume 53, #559, 6/93
3. F.M.vanBouwelen, L.M.Brown and J.E. Field, IDR, Volume 57, #572, 1/97
4. W.A.Harrison, Electronic Structures and Properties of Solids, Dover, 1989, p61


## 5. Figures

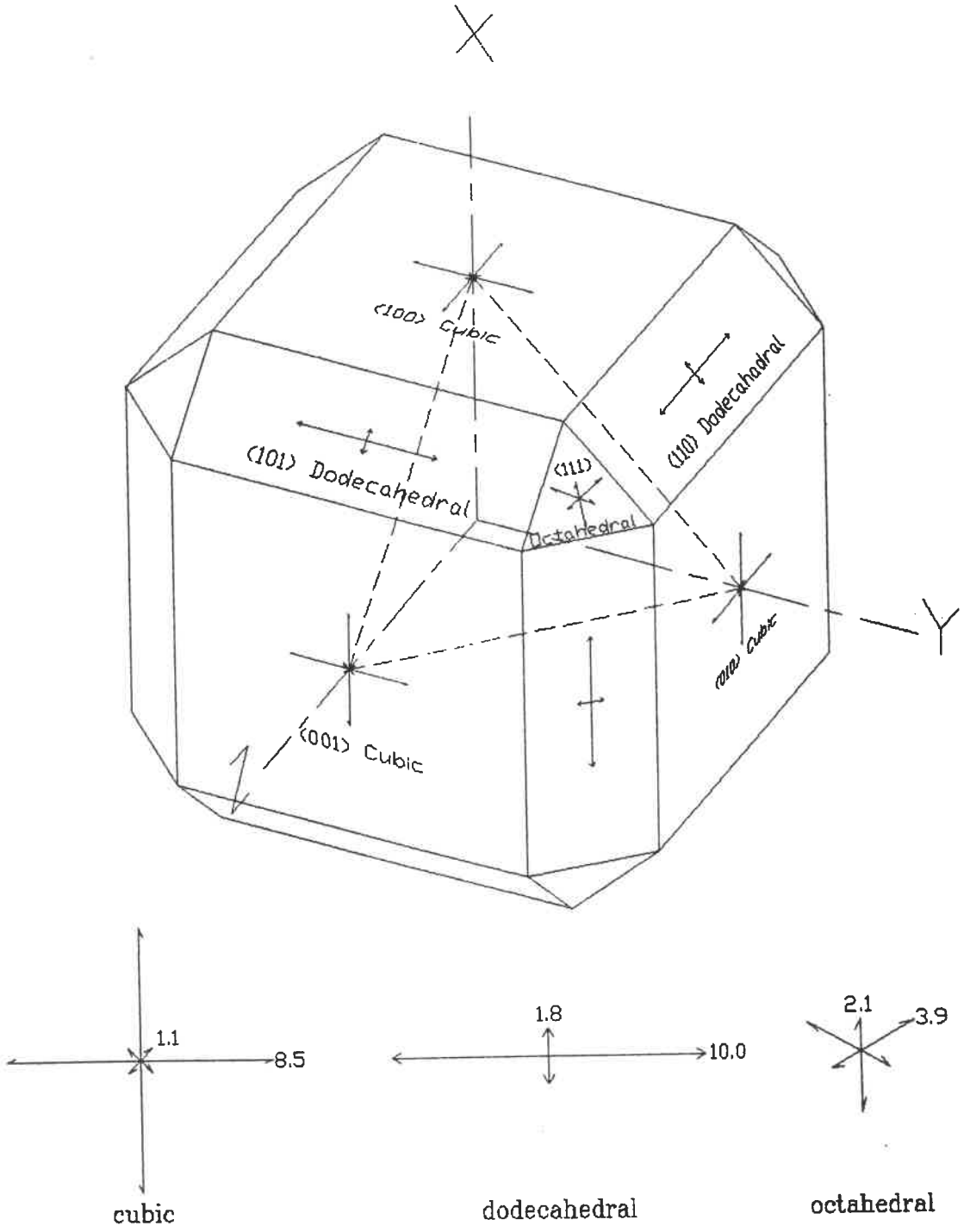


Fig. 1. Anisotropic grinding behavior of diamond was determined by grinding grooves in different directions on the principle diamond faces. The arrow length indicates the depth of cut, or ease of grinding in the direction the arrow points. (E.M. Wilkes and J.Wilkes, Clarenden Laboratory, Oxford 1961)

Wilkes & WIlkes
Diamond octahedral plane (111) anisotropic depths of cut

Towards the cubic plane

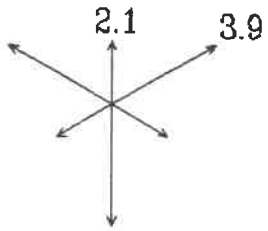


Towards the dodecahedral plane

Octahedral plane (111) anisotropic depths of cut superimposed on a rotating part

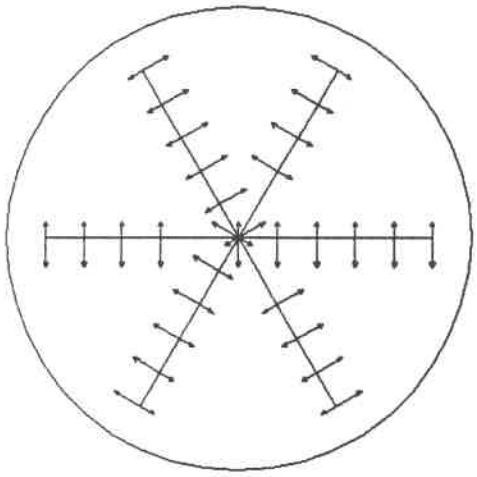

machining/grinding on octahedral (111) planes of silicon, germanium, and diamond.

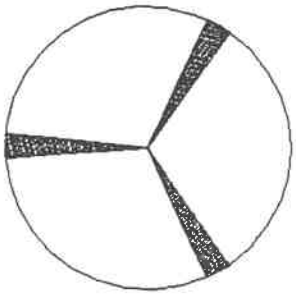

CCW Rotation

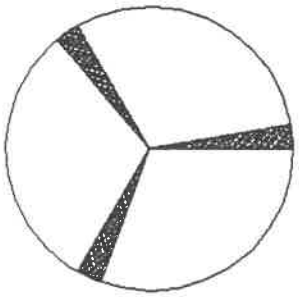

CW Rotation

Fig. 2. Superimpose Wilkes & Wilkes emperical results on (111) silicon and simulate diamond turning to reveal a three-way material distress pattern

# Proposal to the National Science Foundation (NSF) to Research Silicon Machining

John Patten
University of North Carolina Charlotte

**Abstract:** A proposal was submitted to the National Science Foundation (NSF) to study the high pressure phase transformations of silicon, germanium and silicon nitride during manufacturing processes, such as machining. The original proposal was submitted April 1, 1997, a revised proposal, based upon reviewers' feedback from the original, is planned for submission in 1998. This paper reviews the details associated with the research plan for this proposal. The paper also describes contributors, individuals and organizations, to the proposal and research plan. The goals, milestones, and deliverables of the proposed research are also discussed. The purpose of this paper is to generate additional interest, discussion and feedback regarding the proposed research. The proposed research includes experimental work on indenting, scratching and machining (including the effects of temperature and fluid environment). Numerical and analytical modeling, including atomistic and FEA of high pressure phase transformations and machining respectively. Researchers participating in the proposal include professors from Georgia Institute of Technology (GIT), Rice University, North Carolina State University and UNC Charlotte. The expertise of these researchers includes backgrounds in physics, material science, mechanical engineering and manufacturing. Discussion of the proposed research will hopefully alert interested persons to this activity and serve to introduce other researchers to this work. It is hoped that additional industrial organizations will be attracted to, and participate in the proposed research activity.

Keywords: NSF, High Pressure Phase Transformations, Silicon, Machining

**Summary:** Research on a "collection" of related issues has provided the accumulated knowledge from which we have identified that the high pressure phase transformations of Si and Ge are responsible for their ductile material behavior during mechanical deformation-based manufacturing processes. The proposed team-based project will provide the direction, focus and synergy needed to successfully bring our knowledge, of the influence of the high pressure phase transformation, to the forefront of research activities in such areas as materials, tribology and precision engineering. Through the proposed multi-university group effort our effectiveness is enhanced by providing for the substantial extension of the basic knowledge and potential applications of the high pressure phase of these materials to such processes as friction, wear and precision machining. The assembled group of researchers will provide a coordinated and

integrated resource group to industry. We will serve as a single one-stop reference source for information and expertise on processing of silicon and germanium and related work on ceramics. This effort will be a natural extension of the "Silicon Machining Workshop" (ASPE, 1998). The ASPE workshop was initiated to focus on research that will help to overcome the present limiting constraints involved with fabricating Si devices. The workshop format is also included in this proposal as the mechanism to bring together researchers from academe, industry and government laboratories who have a common interest and need for information necessary to manufacture components from these materials.

**Introduction:** The objective of the proposed research program is to establish an interdisciplinary group of researchers with the necessary range of expertise to characterize the role and influence of the high pressure phase transformations of silicon, germanium and ceramics during manufacturing processes. It is envisaged that this material behavior may be exploited to improve the manufacturing processes by increasing yields, decreasing defects and reducing the manufacturing costs of devices and products manufactured from these materials. The research plan proposes to extend significantly the understanding of the fundamental principles and mechanics of the deformation and machining of these materials. The high pressure phase transformations which occur during machining of Si and Ge are a recently discovered manufacturing process mechanism. Existing scientific and engineering models do not include this important effect. In an article by Cahn (Cahn, R.W., Metallic solid silicon, Nature, 357, 645-646, 1992) it is suggested that the knowledge of the existence of the high pressure metallic phase of silicon "has about it the unmistakable scent of a major advance: it is likely to lead to a host of consequential researches". This knowledge is a major breakthrough for the semiconducting and optical research and manufacturing community. The use of the high pressure phase transformations of these materials to improve the manufacturing process is a strategic change in the basic conception of the fundamental manufacturing process mechanisms. This fact is apparently realized by only a handful of researchers. Some members of the present research group (Patten and Scattergood) studied the effects of the high pressure phase transformation of germanium during machining (Morris et al., 1995). The proposed work is an outgrowth of this original collaboration. This research will advance the knowledge of manufacturing mechanics of these materials and permit manufactures to hurdle the present obstacles that confront them as they attempt to manufacture products of higher precision and lower cost. The high pressure phase transformation work on Si/Ge promises to be applicable to engineering ceramics, such as silicon nitride, and to manufacturing processes such as slicing, grinding, lapping and polishing. The high pressure phase transformation represents a new means for controlling manufacturing processes and equipment to produce the desired end effect or product. This proposal provides for the integration of the expertise and resources drawn from several engineering and

scientific fields to work on a problem-focused research agenda that is broader than what any single investigator could accomplish individually. The necessary conditions for exploiting the high pressure phase transformation of semiconductors and ceramics will be evaluated. This team effort includes researchers from solid state physics, materials science, mechanical engineering and manufacturing. The interaction provided by a small group research award will allow the investigators to add significant breadth and depth to their existing work and enhance the proposed research program.

Experimental Program:

| | 1, Indenting, Scratching, Machining | 2. Modeling | 3. Instruments | 4. Material Property Data |
|---|---|---|---|---|
| UNCC | Patten, Smith | Cherukuri, Patten | Patten, Smith | Patten |
| Rice | Pharr | | | |
| NCSU | Scattergood | Bernholc, Roland | Nemanich | Scattergood |
| GIT | Danyluk | | Danyluk | |

1. Experimental (wet and dry)
   - Indenting
   - Scratching
   - Machining
     - I. Single Point Diamond Turning (SPDT)
     - II. Scanning Electron Microscope (SEM)
2. Theoretical Modeling
   - Analytic Models
   - Numerical Models
     - I. Finite Element Machining Model
     - II. Atomistic/Ab-initio/Molecular Dynamics
3. Instrumentation Evaluation:
   - Infra-red Detection
   - Electrical Conductivity
4. Material Property Data

Conclusions: The proposed research will be integrated throughout the three year project. Some of the individual tasks are accomplished in series while other occur in parallel. All of the proposed work is necessary and critical for a complete understanding of the significance of the high pressure phase transformation of these materials relative to their manufacturability. The important conclusions or results which will be achieved include:

- -Material property data which includes the effect of the high pressure phase transformation and the influence of the fluid environment.
- -Manufacturing process optimization to:
  - -minimize defects and damage such as fracture, dislocations and amorphous material.

-Provide an integrated model for material behavior including the size effect.
-Develop process control strategies which implement optimization routines to simultaneously minimize damage and maximize material removal, minimize tool wear, and generate the desired surface quality in terms of roughness.

There is a significant opportunity to use the results of this research to improve the manufacturing processes based upon the knowledge of the existence of both the amorphous phase and the crystalline phase of these materials which are present after processing. As a result of the proposed research, processing research can be proposed that would take advantage of these material structures to optimize process variables or steps. As an example, the amorphous phase of these materials also transforms to the high pressure metallic phase, but this occurs under different conditions than the crystalline phase. It is also known that the various crystalline planes may have differing transformation pressures. This information could be useful to control the manufacturing process to optimize performance. It is conceivable that the surface layer of amorphous material could be removed, either mechanically, chemically and electrically, or in combination, without affecting the underlying substrate. The extent of the amorphous phase is a critical parameter which will be obtained from the proposed research program. One outcome of this research will be to define the conditions under which the extent of the damaged surface and subsurface layers can be minimized through proper selection of process parameters. Controlling the extent of the total damaged layer, both the amorphous surface and subsurface dislocations, can have economic benefits in terms of minimizing processing costs through a reduction in processing time and a reduction in waste material. Previous brittle-ductile transition work has focused on the brittle behavior and the resultant fracture damage. Research was aimed at determining the damage threshold and avoiding brittle failure. Here we propose to take a fundamentally new approach and study the ductile characteristics of the process. The ductile response of Si and Ge is a result of high pressure phase transformation which occurs during processing at the contact interface. This knowledge and understanding will lead to process modifications which enhance the ductile processes. This ductile processing approach is in contrast to the fracture approach which attempts to suppress the brittle behavior. Optimizing material removal, possibly through closed loop control by monitoring of measurable phenomenalogical changes, will improve existing manufacturing processes and potentially lead to entirely new processes. We believe that enhanced ductility, by taking advantage of the high pressure phase transformations of these materials, is a fundamentally new approach and complements the vast amount of previous research on the fracture and brittle behavior of these materials.

# Author Index


Abdel-Aal, Hisham A. . . . . 19
Abe, Kohzo . . . . . 113
Aoyama, Hideki . . . . . 92
Arai, Kazuhisa . . . . . 113
Asakawa, K. . . . . 109
Ball, Matthew J. . . . . 50
Beinert, Joachim . . . . . 32
Blaedel, Kenneth L. . . . . 44
Brinksmeier, Ekkard . . . . . 55
Burns, Stephen J. . . . . 11
Cao, Jianlin . . . . . 72
Carlisle, Keith . . . . . 50
Chargin, David. . . . . 59
Chen, Bin. . . . . 72
Chen, Kang-Hua . . . . . 11
Chen, Xuemei . . . . . 63
Ciarlo, Dino R. . . . . *
Daito, Masamichi. . . . . 40
Danyluk, Steven. . . . . *, 96
Davis, Pete J. . . . . 44
Döll, Walter . . . . . 32
Dornfeld, David A. . . . . 63, 78, 83, 105
DuPuy, Peter C. . . . . 44
Ehlert, A. . . . . 32
Eshel, Hagai . . . . . 67
Evans, Chris J. . . . . *
Faulk, Scott C. . . . . *
Gao, Honggang. . . . . 72
Gatzen, Hans H. . . . . 117
Gee, Anthony E. . . . . 15
Goodman, William A. . . . . 3
Goorsky, Mark S. . . . . *
Hashimoto, Hiroshi . . . . . 36
Hellmold, Thomas . . . . . 117
Helmreich, Dieter. . . . . 32
Huber, A. . . . . 32
Imai, Kenichiro. . . . . 36
Inasaki, Ichiro . . . . . 92
Inoue, T. . . . . 24
Jacobs, Stephen D. . . . . 11
Jeynes, Chris. . . . . 15
Kanai, Akira . . . . . 40
Keiser, G. M. . . . . 74
Kerstan, Michael . . . . . 32
Kim, George A. . . . . 122
Knight, Stephen. . . . . 10
Koma, Yutaka . . . . . 113
Krulewich, Debra A. . . . . 44
Lambropoulos, John C. . . . . 11
Leistner, Achim J. . . . . 101
Levert, Joseph A. . . . . 96
Malz, Rüdiger . . . . . 55
Marcelja, Frane . . . . . 74
Matsuzaki, J. . . . . 109
McClellan, Michael R. . . . . 44, *
McGlauflin, Michael L. . . . . *
Mess, Francis M. . . . . *
Miyairi, Hiroo . . . . . 92
Miyashita, Masakazu. . . . . 40
Moon, Yongsik . . . . . 78, 83
Narayanan, C. . . . . *
Neil, David J. . . . . *
Oishi, Hiroshi . . . . . 109
Okawa, Shinji . . . . . 113
Park, Ilwhan. . . . . 83
Parks, Robert E. . . . . *
Patten, John A. . . . . 28, 88, 126
Pharr, Gearge M. . . . . *
Preuß, Werner R. . . . . 55
Puttick, Keith E. . . . . 15, *
Riemer, O. . . . . 55
Roderick, D. J. . . . . *
Ruhbach, Lars P. . . . . 117
Sasaki, Yoshiaki . . . . . 92
Schinker, Martin G. . . . . 32
Shan, Lei . . . . . 96
Shibaya, Hiroshi . . . . . 92
Shillito, Keith R. . . . . *
Skolnik, Lyn H. . . . . *
Smith, Stuart T. . . . . 19
Stocker, M. A. . . . . 50
Syn, Chol K. . . . . 44
Takashina, M. . . . . 24
Tanaka, S. . . . . 24
Wall, M. A. . . . . 44
Weisshaus, Ilan. . . . . 67
Yamamoto, Y. . . . . 24
Yasunaga, Nobuo . . . . . 24
Zeadan, Jeihad . . . . . 117


* *Abstract not available at press time*